



PhD Thesis  
University Paris Diderot, Sorbonne Paris Cité

by

**Audrey Ducourthial**

*Submitted in fulfillment of the requirements for the degree of*

DOCTEUR ES SCIENCES  
OF THE UNIVERSITY DENIS DIDEROT

*Specialty :*

Physics of the Universe  
Doctoral school of Geo and Environment Sciences and of Physics of the Universe, Paris

# Upgrade of the ATLAS experiment Inner Tracker and related physics perspectives of the Higgs boson decay into two b quarks

Defended the 26<sup>th</sup> of October 2018 in front of the jury :

Mr	Didier Contardo (IPNL)	DR	Referee
Mr	Fares Djama (CPPM)	IR	Referee
Mrs	Paula Collins (CERN)	Senior physicist	Member of the jury
Mrs	Lydia Fayard (LAL)	DR	Member of the jury
Mr	Michael Moll (CERN)	Senior physicist	Member of the jury
Mr	José Ocariz (LPNHE-UPD)	Professor	Member of the jury
Mr	Marco Bomben (LPNHE-UPD)	MdC	PhD advisor







THESE DE DOCTORAT  
Université Paris Diderot, Sorbonne Paris Cité

*présentée par*

**Audrey Ducourthial**

*Pour obtenir le grade de*

DOCTEUR ES SCIENCES  
DE L'UNIVERSITE DENIS DIDEROT

*Spécialité :*

Physique de l'Univers

Ecole doctorale des Sciences de la Terre et de l'Environnement et Physique de l'Univers, Paris

# **Amélioration du trajectographe de l'expérience ATLAS et impact sur l'étude de la désintégration du boson de Higgs en deux quarks $b$**

Soutenue le 26 Octobre 2018 devant le jury composé de :

Mr	Didier Contardo (IPNL)	DR	Rapporteur
Mr	Fares Djama (CPPM)	IR	Rapporteur
Mme	Paula Collins (CERN)	Senior physicist	Examinatrice
Mme	Lydia Fayard (LAL)	DR	Examinatrice
Mr	Michael Moll (CERN)	Senior physicist	Examineur
Mr	José Ocariz (LPNHE-UPD)	Professeur	Examineur
Mr	Marco Bomben (LPNHE-UPD)	MdC	Directeur de thèse







# Contents

<b>1</b>	<b>The Standard Model of particle physics and Higgs boson production at LHC</b>	<b>9</b>
1.1	Introduction . . . . .	9
1.1.1	Theoretical framework . . . . .	10
1.2	Elementary particles: state of the art . . . . .	16
1.3	Higgs boson production at LHC . . . . .	17
1.3.1	Higgs production . . . . .	17
1.3.2	Higgs decay . . . . .	19
<b>2</b>	<b>The LHC and the ATLAS experiment</b>	<b>21</b>
2.1	The Large Hadron Collider . . . . .	22
2.2	The ATLAS experiment . . . . .	24
2.2.1	The ATLAS detector . . . . .	26
2.2.2	Reconstruction and simulation of physics objects . . . . .	33
2.3	Conclusions . . . . .	39
<b>3</b>	<b>Silicon detectors and ATLAS pixels sensors</b>	<b>41</b>
3.1	Silicon detector physics . . . . .	42
3.1.1	Silicon charge carriers concentration . . . . .	42
3.1.2	PN junction . . . . .	44
3.2	Signal formation . . . . .	45

3.2.1	Electron-hole pair creation . . . . .	45
3.2.2	Signal development inside the sensors . . . . .	46
3.2.3	Signal induction . . . . .	47
3.3	Pixel sensors technologies . . . . .	49
3.3.1	Hybrid pixel sensors . . . . .	49
3.3.2	Monolithic pixel sensors . . . . .	53
3.4	Radiation damage effects in silicon . . . . .	53
3.4.1	Microscopic defects in silicon . . . . .	53
3.4.2	Macroscopic impact of radiation damages in silicon . . . . .	54
<b>4</b>	<b>ATLAS radiation damage digitizer</b>	<b>59</b>
4.1	Modeling radiation damage . . . . .	60
4.1.1	Determination of the fluence . . . . .	61
4.1.2	Electric fields maps . . . . .	61
4.1.3	Diffusion study: Cluster size dependency on temperature and bias voltage: testbeam results . . . . .	68
4.1.4	Charge chunking and trapping . . . . .	69
4.1.5	Ramo potential and Induced Charge . . . . .	70
4.2	Validation of the model and perspectives . . . . .	71
4.2.1	Validation of the standalone framework . . . . .	71
4.2.2	Validation of the Athena framework . . . . .	72
4.2.3	Cluster properties . . . . .	72
4.2.4	Charge collection efficiency . . . . .	78
4.2.5	Tracking properties . . . . .	80
4.3	Conclusions and perspectives . . . . .	85
<b>5</b>	<b>ATLAS during the High Luminosity LHC</b>	<b>87</b>
5.1	The High Luminosity LHC . . . . .	87

5.2	ATLAS HL-LHC upgrade . . . . .	88
5.3	ATLAS Inner Tracker (ITk) . . . . .	89
5.3.1	ITk pixels . . . . .	91
5.3.2	ITk Performance . . . . .	95
5.3.3	Physics perspectives at HL-LHC . . . . .	97
<b>6</b>	<b>Silicon pixel sensors for ATLAS ITk</b>	<b>101</b>
6.1	FBK-LPNHE Productions . . . . .	101
6.1.1	Production 1: Active edge sensors . . . . .	105
6.1.2	Production 2: Thin sensors . . . . .	107
6.1.3	Irradiation of the second production . . . . .	108
6.1.4	Production 3: Thin and Active edge sensors . . . . .	112
6.1.5	RD53A compatible sensors . . . . .	115
6.2	Pixel module tuning . . . . .	116
<b>7</b>	<b>Performance on beam of pixel detectors</b>	<b>119</b>
7.1	Data taking at Testbeam . . . . .	120
7.2	Observables . . . . .	122
7.2.1	Charge collection efficiency . . . . .	122
7.2.2	Hit efficiency . . . . .	123
7.2.3	Hit residuals and spatial resolution . . . . .	125
7.3	Performance of un-irradiated sensors of the first production . . . . .	128
7.4	Performance of irradiated thin sensors . . . . .	129
7.4.1	Irradiation fluence peak constraint . . . . .	129
7.4.2	Charge collection efficiency of W80 . . . . .	133
7.4.3	Global hit efficiency . . . . .	142
7.4.4	Conclusion on thin and irradiated sensors . . . . .	145

7.5	Active edge performance . . . . .	145
7.5.1	Standard active edge performance . . . . .	146
7.5.2	Staggered active edge performance . . . . .	149
7.5.3	Conclusions on Active edges sensors . . . . .	154
7.6	Biasing structure and implant design . . . . .	157
7.7	Conclusions on the pixel R&D for ITk . . . . .	158
<b>8</b>	<b>B-tagging upgrade for ITk</b>	<b>159</b>
8.1	B-tagging . . . . .	160
8.1.1	Introduction . . . . .	160
8.1.2	B-tagging algorithms . . . . .	161
8.2	B-tagging optimization for ATLAS ITk . . . . .	163
8.2.1	Layouts comparison . . . . .	164
8.2.2	SV1 optimization . . . . .	166
8.2.3	B-tagging extrapolation for high $p_T$ jets . . . . .	176
8.3	Conclusions . . . . .	178
	<b>Conclusions and Perspectives</b>	<b>179</b>
	<b>Appendices</b>	<b>181</b>
<b>A</b>	<b>Appendix: Simulation details</b>	<b>183</b>
<b>B</b>	<b>Résumé</b>	<b>187</b>
	<b>List of figures</b>	<b>201</b>
	<b>Bibliography</b>	<b>213</b>

# Abstract

By 2026, the LHC will enter its high luminosity regime, providing protons protons collisions at an unprecedented rate. The LHC experiments will have to be upgraded to cope with this higher data rate. The new ATLAS Inner Tracker (ITk) will allow a better identification of b-quarks and interesting physics signature with b-quarks in the final states such as the Higgs trilinear coupling will be reachable.

The work performed during this thesis consisted in testing planar pixel sensors for the ITk, as well as optimizing b-tagging algorithms. In parallel, a study on the radiation damage on silicon pixel sensors have been performed.

The radiation hardness of silicon sensors plays a determinant role as it allows them to be efficient in the highly radiative environment at LHC. Understanding the impact of radiation in silicon sensors is a major challenge and a radiation damage digitizer which models radiation damage effects in ATLAS Monte Carlo simulations is currently developed by the ATLAS experiment.

Three ITk silicon planar pixel sensors productions of LPNHE and FBK have been developed, produced and tested on beam. Sensors from these three productions aim to be part of the ITk and have to demonstrate good performance after being irradiated at high fluences. Several technological designs have been investigated, such as temporary metal biasing option and active edges which maximize the geometrical acceptance of the sensors.

The optimization of b-tagging SV1 algorithm (a secondary-vertex based algorithm) will be presented as well as a study on the extrapolation of b-tagging performances at high pT.

**Keywords:** ATLAS experiment, ATLAS ITk, Planar Pixel sensors, Silicon, Active edge, Radiation damage, B-tagging



# Abstract

Le LHC entrera dans sa phase à haute luminosité vers 2026 et pour profiter de l'augmentation importante du taux de collisions, ATLAS, et plus particulièrement son trajectographe doivent être améliorés en terme de résistance aux radiations et traitement de données à un taux accru.

Grace au nouveau design du trajectographe et à l'amélioration d'algorithmes d'étiquetage des saveurs de jets, l'identification de jets issus de la désintégration de B hadrons sera facilitée et des canaux de physique possédant des quarks b dans leurs états finaux seront plus facilement accessibles, parmi lesquels le couplage trilinéaire du boson de Higgs.

La résistance aux raditions des capteurs à pixels en silicium joue un rôle primordial dans leur utilisation auprès des expériences LHC. La quantification de l'impact des rayonnements sur les capteurs silicium est une enjeu crucial : un outil de digitisation des dommages des rayonnements a été développé pour modéliser l'impact des radiations dans les simulations Monte Carlo d'ATLAS.

Le test de capteurs à pixels planaires, développés par le LPNHE et la fonderie FBK, constitue la partie principale de cette thèse. Les trois productions de capteurs testées possèdent plusieurs designs technologiques. Pour maximiser l'acceptance géométrique du détecteur, des capteurs à bord mince ont été développés. Deux options de polarisation durant les phases de test ont aussi été étudiées. Les capteurs ont été testés à plusieurs phases d'irradiation.

L'optimisation d'algorithme de b-tagging basé sur la reconstruction de vertex secondaire sera aussi présentée, ainsi qu'une étude concernant les performances du b-tagging à haut  $p_T$ .

**Keywords:** ATLAS, ATLAS ITk, Capteurs à bords minces, Silicium, Dommage des rayonnements, B-tagging





# Remerciements

I would like to thank the all LPNHE group for the three last years: it has been a truly passionating journey. I am specially grateful to my PhD advisor Marco Bomben and the all ATLAS group. My deepest gratitude to the LPNHE PhD students and their constant "bonne humeur": Anissa, Dilia, Ilaria, Jad, Louis, Simon and all the others ;) Merci également aux très sympathiques services administratifs et techniques du LPNHE: en particulier Bernard, Véronique, Eduardo, François et Patricia. My deepest gratitude to the Atlas testbeam group, especially Natascha, Julian, Reem, David, Mareike, Dmytro and Tasneem. A special thanks to Tobias Bisanz for all the help provided to master Eutelescope and TBMon2. I would also like to thank Ben, Alessandro and Sasha for providing a lot of answer to my often annoying and technical questions. Thanks to all the member of the jury for the nice discussion, a special thanks to my two referees, Farès and Didier, for the extremely useful exchanges on the manuscript. Merci à ma famille élargie et à mes amis. Merci infiniment à mes parents, Bernard et Marie Odile ainsi qu'à mes frères Thibault et Adrien et à mes deux grand mères. Enfin merci à Hugo Abraham, l'amour de ma vie, qui a su rendre cette expérience merveilleuse par son soutien constant.



# Introduction

The ATLAS experiment has recently been able to document at five sigma level the couplings of the Higgs bosons with the third generation family of quarks (top [1] and b quarks [2]). Those discoveries have been greatly eased by the addition in 2015 of a fourth pixel layer in the tracker, namely the Insertable B-Layer (IBL), and by the improvements of flavour tagging algorithms capable of identifying b-jets.

By 2026, the LHC will enter its high luminosity regime, providing protons protons collisions at an unprecedented rate. This implies an increase in the discovery potential of the LHC experiment, which have to be upgraded to cope with this higher data rate. ATLAS and especially its Inner Tracker will be upgraded. The new ATLAS Inner Tracker (ITk) will allow a better identification of b-quarks and interesting channels with b-quarks in the final states will be reachable. The Higgs trilinear couplings with at least one of the Higgs boson decaying into two b-quarks is among those promising channels.

Silicon pixel sensors play a key role in actual tracker at LHC experiments. The work performed during this thesis<sup>1</sup> consisted in analyzing the performance of planar pixel sensors for the ITk, as well as optimizing b-tagging algorithms for the ITk. In parallel, a study on the radiation damage on silicon pixel sensors have been performed, which can also help to do predictions for the ITk performance.

After a brief review of the Higgs boson production at LHC, the ATLAS detector will be presented with a special focus on its Inner Detector and on its pixel sensors. The following Chapter (3) will describe the physics of silicon pixel sensors and review the various pixel technologies. Among the interesting features of silicon pixel sensors their radiation hardness plays a determinant role as it allows pixel sensors to be efficient in the highly radiative environment at LHC. Consequently, it is a major challenge to quantify and understand the impact of radiations on the actual Inner Detector. In order to address this question, a radiation damage digitizer which models radiation damage effects in the ATLAS Monte Carlo simulations is currently developed by the ATLAS collaboration.

---

<sup>1</sup>In this thesis, natural units will be used  $c = \hbar = 1$  as well as ATLAS coordinates system. ATLAS uses a right-handed coordinate system with its origin at the nominal interaction point (IP) in the center of the detector and the z-axis coinciding with the axis of the beam pipe. The x-axis points towards the centre of the LHC ring, and the y -axis points upward. Cylindrical coordinates  $(r, \phi)$  are used  $\phi$  being the azimuthal angle around the z-axis. The pseudorapidity  $\eta$  is defined in terms of the polar angle  $\theta$  such as  $\eta = -\ln(\tan(\theta/2))$ . Other ATLAS common notations are the transverse momentum  $p_T = p \sin(\theta)$  and transverse energy  $E_T = E \sin(\theta)$ .  $\Delta R = \sqrt{\Delta\eta^2 + \Delta\phi^2}$  is used to define cone size.

Chapter 4 describes the current radiation damage digitizer effort of ATLAS. My first personal contribution to this study was to generate electric field maps inside planar pixel sensors for various fluences and bias voltages as well as uncertainties study on those electric field profiles. I have also contributed to the effort by carrying study on diffusion obtained from testbeam data. The main work I have performed in the radiation damage digitizer framework was to confront the model with collision data and to analyze the cluster and tracks properties at various steps of the digitizer development. On the near future, the impact of radiation damage on b-tagging variables and on the  $Vh \rightarrow b\bar{b}$  analysis will also be considered.

Chapter 5 presents the ATLAS Inner Tracker (ITk) upgrade for the High Luminosity LHC phase. To cope with higher data rate, a new detector has been designed. The innermost detector will be a pixel detector comprising 5 silicon pixel barrel layers. Chapters 6 and 7 presents the three ITk silicon planar pixel sensor productions of LPNHE and FBK foundry<sup>2</sup>. Sensors from these three productions aim to be part of the ITk and have to demonstrate good performance after being irradiated at high fluences. Several technological designs have been investigated, such as temporary metal biasing option and active edges. To maximize the geometrical acceptance of the inner tracker, sensors with a reduced inactive part at their borders, namely active edge pixel sensors were tested. I tested those three productions during testbeams at various steps of irradiations and various tuning points. Performance in term of sensor power dissipation, charge collection efficiency and hit efficiency will be presented. Results from testbeam of active-edge sensors have been compared to TCAD simulations. At the end of this chapter some conclusions on the LPNHE productions and the potential use by ITk of the various designs investigated will be drawn.

The last Chapter (8) is dedicated to the optimization of b-tagging algorithms which are the algorithms allowing identification of jets from b-quarks. The optimization of the SV1 algorithm (a secondary-vertex based algorithm) will be presented as well as a study on the extrapolation of b-tagging performance at high  $p_T$ .

Eventually, a summary of the work addressed and some perspectives will be given in the final part.

---

<sup>2</sup>FBK-CMM (Trento, Italy): <http://cmm.fbk.eu/>

# Chapter 1

## The Standard Model of particle physics and Higgs boson production at LHC

### Contents

---

<b>1.1</b>	<b>Introduction . . . . .</b>	<b>9</b>
1.1.1	Theoretical framework . . . . .	10
<b>1.2</b>	<b>Elementary particles: state of the art . . . . .</b>	<b>16</b>
<b>1.3</b>	<b>Higgs boson production at LHC . . . . .</b>	<b>17</b>
1.3.1	Higgs production . . . . .	17
1.3.2	Higgs decay . . . . .	19

---

### 1.1 Introduction

The physics of particles is an extraordinary construction relying on the quantum theory of field which has been built on the shoulders of the two main theories of the early 20<sup>th</sup> century, quantum physics and special relativity. It has been nourished and enriched by advanced mathematical tools and concepts such as group theory, symmetries and broken symmetries, field theory and by technological advancements in electronics and solid-state physics, cryogenics, acceleration technologies and many more.

The history of particle physics is truly passionating and a brilliant illustration of the creation of a new science: it has been created over epistemological ruptures [3] with pre-established scientific dogma (e.g quantum mechanics vs classical mechanics).

By the 1970's years, the physics of particles, both on its theoretical and experimental fronts, had created a coherent model explaining the particles and their interactions: the Standard Model (SM) of particles and interactions.

The SM is not complete, as it lacks a dark matter candidate, gravitation can not be modeled as a gauge interaction and masses hierarchy is not understood, which pushes the scientific community to investigate further and to continue the quest towards a unified model of particles and interactions.

The experiments based at CERN [4] (Centre Européen de la Recherche Nucléaire) LHC (Large Hadron Collider [5]) and the ATLAS (A Toroidal LHC Apparatus [6]) experiment in particular, are designed to further characterize the already discovered particles and to fathom the sub-atomical world as far as possible to increase our global understanding of the universe.

In the upcoming sections an overview of the already known particles will be given with a special emphasis on the Higgs physics. Finally the Higgs boson physics results from LHC experiments will be described.

### 1.1.1 Theoretical framework

The Standard Model (SM)[7, 8] of elementary particles describes the electromagnetic, strong and weak interactions and the elementary particles of matter (fermions). The fermions are divided in leptons and quarks, both organized in three generations. The SM is based on the gauge group  $SU(3) \times SU(2) \times U(1)$ , describing the exchange of boson fields for each interaction: gluons for the strong interaction (see next paragraph on QCD lagrangian),  $W^+$  and  $W^-$  and  $Z$  bosons for the weak interactions and photons for the electromagnetic interactions. The particles acquire masses via electroweak symmetry breaking and the addition of a new scalar field: the Higgs field.

In the following, some theoretical basis of the standard model will be developed: after a brief description of the QCD lagrangian, the electroweak sector and the Higgs mechanism will be described.

### The Quantum Chromo Dynamics (QCD)

QCD relies on the idea of quarks as particles and  $SU(3)$  color symmetry, as it describes the interactions of quarks and gluons. As opposed to Quantum Electro Dynamics (QED), QCD is a non-Abelian theory which leads to the self coupling of gluons (trilinear and quartic self couplings). Quarks can have three different colors and six flavors. The gluons which are the massless mediator of the strong force are of eight types (8 generators of the  $SU(3)$  color group). The hadrons have the property to be color neutral, either by combining the three colors or by combining a color and an anti-color, the former are called baryons and are composed of three quarks, the latter are called mesons and are formed of a quark-antiquark pair. The quarks and gluons cannot be found alone: they hadronize, which means they become part of a color-less hadron. The heaviest quark, the top quark, is so massive that it decays before it can become part of a hadron. The main parameter of QCD are the quarks masses and the coupling constant  $g_s$  which determine the strength of the interaction between colored quarks and gluons.

The QCD Lagrangian density is given by the sum over the 6 flavors (q) and the 3 colors (j,k,l):

$$\mathcal{L} = \sum_q \bar{\psi}_{q,j} (i(\gamma^\mu D_\mu)_{jk} - m_q \delta_{jk}) \psi_{q,k} - \frac{1}{4} F_{\mu\nu}^a F_a^{\mu\nu} \quad (1.1)$$

where  $\psi_{q,j}$  is the quark field,  $F_{\mu\nu}^c$  is the field strength tensor which is found from the gluon field  $A_\mu^a$ , with the index  $a$  ranking from 1 to 8:

$$F_{\mu\nu}^a = \partial_\mu A_\nu^a - \partial_\nu A_\mu^a - \underbrace{g_s f^{abc} A_\mu^b A_\nu^c}_{\text{non abelian term}} \quad (1.2)$$

where  $f^{ABC}$  are the structure constants of the SU(3) color group. The non-abelian term in the field strength tensors is responsible for the gluon trilinear and quartic self-interactions.

## Electroweak lagrangian

In the following, the electroweak sector, the electroweak symmetry breaking and the Higgs mechanism will be described. For more detailed discussion, one can refer to [7, 8].

The electroweak unification was proposed by Glashow [9], Weinberg [10] and Salam [11] in the early 1970's years. The electroweak lagrangian expresses the interactions between the right handed singlet and left handed leptons doublet. The left handed doublet  $\psi_L = \begin{pmatrix} \psi_{\nu,L} \\ \psi_{l,L} \end{pmatrix}$  has two components, the left handed lepton component  $\psi_{l,L}$  and the left handed neutrino component  $\psi_{\nu,L}$ . The right handed component is a singlet  $\Psi_R = \Psi_{l,R}$  because no right handed neutrinos has ever been observed. Glashow proposed the symmetry gauge group  $SU(2)_L \times U(1)$  to unify the electromagnetism and weak interactions. The invariance under  $SU(2)_L \times U(1)$  lead to the introduction of a massless isovector triplet field  $W_\mu = (W_\mu^1, W_\mu^2, W_\mu^3)$  and a neutral vector field  $B_\mu$ .

The transformations on the left and right handed fermions and the covariant derivative expressions are the following

$$\psi_L \rightarrow \psi'_L = \exp(i\theta \cdot \tau + i\alpha Y) \psi_L, \quad Y = -1 \quad (1.3)$$

$$\psi_R \rightarrow \psi'_R = \exp(i\alpha Y) \psi_R, \quad Y = -2 \quad (1.4)$$

$$D_\mu = \partial_\mu - ig \frac{\tau_i}{2} W_\mu^i - ig' \frac{Y}{2} B_\mu \quad (1.5)$$

where  $g$  and  $g'$  are the SU(2) and U(1) gauge couplings,  $\frac{\tau_i}{2}$  are the SU(2) generators,  $Y$  is the weak hyper charge and  $\theta$  is a vector of Pauli matrices.

The obtained lagrangian is:

$$\mathcal{L}_{int} = \bar{\psi}_L \gamma^\mu \left( i\partial_\mu - g \frac{1}{2} \tau \cdot W_\mu - g' \frac{Y}{2} B_\mu \right) \psi_L + \bar{\psi}_R \gamma^\mu \left( i\partial_\mu - g' \frac{Y}{2} B_\mu \right) \psi_R \quad (1.6)$$

The physical  $W^+$  and  $W^-$  bosons are an admixture of  $W_\mu^1$  and  $W_\mu^2$ :  $W_\mu^\pm = \frac{1}{\sqrt{2}}(W_\mu^1 \mp iW_\mu^2)$ . The neutral weak boson  $Z$  and the electromagnetic boson  $A$  can be recovered when a rotation of  $\theta_W$  is performed, mixing  $W_\mu^3$  and  $B_\mu$ , such as:

$$\begin{pmatrix} Z \\ A \end{pmatrix} = \begin{pmatrix} \cos(\theta_W) & -\sin(\theta_W) \\ \sin(\theta_W) & \cos(\theta_W) \end{pmatrix} \begin{pmatrix} W^3 \\ B \end{pmatrix} \quad \begin{array}{l} \text{with } \cos(\theta_W) = \frac{g}{\sqrt{g^2 + g'^2}} \\ \text{with } \sin(\theta_W) = \frac{g'}{\sqrt{g^2 + g'^2}} \end{array}$$

The leptonic currents can be formulated as:

$$\begin{array}{ll} J^{+, \mu} = \bar{\psi}_{\nu_l, L} \gamma^\mu \psi_{l, L} & \} \text{ Charged leptonic currents} \\ J^{-, \mu} = \bar{\psi}_{l, L} \gamma^\mu \psi_{\nu_l, L} & \\ J^{3, \mu} = \bar{\psi}_L \gamma^\mu \psi_L & \} \text{ Leptonic weak isospin currents} \\ J^{Y, \mu} = -\frac{1}{2} \bar{\psi}_L \gamma^\mu \frac{\tau_3}{2} \psi_L - \bar{\psi}_R \gamma^\mu \psi_R & \} \text{ Weak hypercharge currents} \\ J^{EM, \mu} = -(\bar{\psi}_{e, L} \gamma^\mu \psi_{e, L} + \bar{\psi}_{e, R} \gamma^\mu \psi_{e, R}) & \} \text{ Electromagnetic currents} \end{array}$$

The electroweak lagrangian can then be expressed in terms of physical bosons and currents

$$\mathcal{L}_{int} = \frac{g}{\sqrt{2}} J^{+, \mu} W_\mu^+ + \frac{g}{\cos \theta_W} (J^{3, \mu} - \sin \theta_W J^{EM, \mu}) Z_\mu + g \sin \theta_W J^{EM, \mu} A_\mu \quad (1.7)$$

The lagrangian in equation (1.7) contains all interactions terms but no mass term. Particles acquire masses via electroweak symmetry breaking and the Higgs mechanism which are described in the subsequent paragraph.

### Electroweak symmetry breaking and Higgs mechanism

The main idea of symmetry breaking is that the lagrangian is invariant under  $SU(2) \times U(1)$  but its vacuum value is not [8]. One complex scalar doublet  $\Phi$  is considered, with the following most common gauge invariant form:

$$\Phi = \begin{pmatrix} \phi^+ \\ \phi^0 \end{pmatrix} = \frac{1}{\sqrt{2}} \begin{pmatrix} \phi_1 + i\phi_2 \\ \phi_3 + i\phi_4 \end{pmatrix}$$

where  $\phi_j$  with  $j$  running from 1 to 4 are scalar fields.

The lagrangian of  $\Phi$  is of the form:

$$\mathcal{L}_\Phi = (D_\mu \Phi^\dagger)(D^\mu \Phi) - V(\Phi) + \mathcal{L}_{Yukawa} \quad (1.8)$$



where the potential  $V(\Phi)$  is:

$$V(\Phi) = -\mu^2 \Phi^\dagger \Phi + \lambda (\Phi^\dagger \Phi)^2 \quad (1.9)$$

where  $\mu$  and  $\lambda$  are two constants and  $\mathcal{L}_{Yukawa}$  is the Yukawa lagrangian (described in the following paragraph).

The potential shape depends on the signs of  $\lambda$  and  $-\mu^2$ . If  $-\mu^2$  and  $\lambda$  are both positive, the potential minimum which corresponds to the vacuum state is obtained for  $|\Phi| = \sqrt{\Phi^\dagger \Phi} = 0$ , the electroweak symmetry in this case is not broken, as a gauge transformation acting on  $|\Phi| = 0$  does not change the vacuum state [8].

In the case where  $-\mu^2 < 0$  and  $-\lambda > 0$  the potential shape becomes the one presented in Figure 1.1. The minimum value of the potential is obtained for  $|\Phi| = \sqrt{\frac{\mu^2}{2\lambda}}$ , which is not invariant under  $SU(2) \times U(1)$ : the electroweak symmetry is broken.

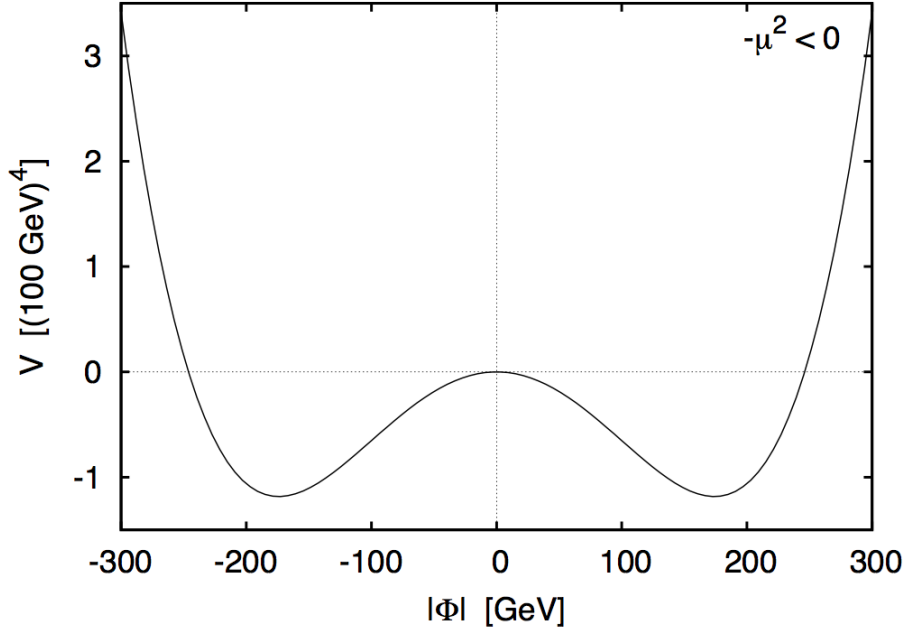


Figure 1.1 – From [8] Higgs potential for a 125 GeV higgs boson with a vacuum expectation value (vev) of  $v = 246$  GeV.  $-\mu^2 < 0, \lambda > 0$ , the minimum of the potential is at  $|\Phi| = \frac{v}{\sqrt{2}} \simeq 174$  GeV.

Around the vacuum one can choose  $\langle \phi_3 \rangle \equiv v = \sqrt{\frac{\mu^2}{\lambda}}$  with  $v$  the vacuum expectation value (vev) and  $\langle \phi_1 \rangle = \langle \phi_2 \rangle = \langle \phi_4 \rangle = 0$ . A new real scalar field  $h$ , which vacuum value is zero  $\langle h \rangle = 0$  can also be added. For infinitesimal fluctuations around the vacuum, the potential  $\Phi$  becomes:

$$\Phi = \frac{1}{\sqrt{2}} \exp\left(\frac{i\epsilon^a \sigma^a}{v}\right) \begin{pmatrix} 0 \\ v + h \end{pmatrix}$$

with  $a$  an index running between 1 and 3,  $\sigma^a$  the Pauli matrices, and  $\epsilon^a$  some fields from Goldstone bosons. By selecting an appropriate gauge, the Goldstone bosons fields can be eliminated. Under  $SU(2)$ , the field is transformed as  $\Phi \rightarrow \Phi' = \exp\left(i\lambda_L^a(x)\frac{\sigma^a}{2}\right)\Phi$ . If one choose  $\lambda_L^a(x) = -2\frac{\epsilon^a}{v}$ , it leads to:

$$\Phi = \exp\left(-i\frac{\epsilon^a\sigma^a}{v}\right)\exp\left(i\frac{\epsilon^a\sigma^a}{v}\right)\begin{pmatrix} 0 \\ v+h \end{pmatrix} = \frac{1}{\sqrt{2}}\begin{pmatrix} 0 \\ v+h \end{pmatrix}$$

Hence using the covariant derivative from, the gauge kinetic term gives:

$$(D_\mu\Phi^\dagger)(D^\mu\Phi) = \underbrace{\frac{1}{2}\delta_\mu h\delta^\mu h}_{\text{Kinetic h field}} + \underbrace{\frac{1}{8}g^2(v+h)^2(W_\mu^1 - iW_\mu^2)(W_\mu^1 + iW_\mu^2)}_{\text{W term}} + \underbrace{\frac{1}{8}g^2(v+h)^2(-g'B_\mu + gW_\mu^3)^2}_{\text{Z term}} \quad (1.10)$$

By introducing the physical boson fields ( $W_\mu^+$ ,  $W_\mu^-$  and  $Z_\mu$ ), the boson mass terms and couplings to the Higgs boson appear:

$$\text{W term} = \underbrace{\frac{g^2v^2}{4}W_\mu^+W_\mu^-}_{\text{W mass term}} + \underbrace{\frac{g^2v}{4}hW_\mu^+W_\mu^-}_{\text{WW h coupling}} + \underbrace{\frac{g^2}{4}hhW_\mu^+W_\mu^-}_{\text{WW h h coupling}} \quad (1.11)$$

$$\text{Z term} = \underbrace{\frac{(g^2+g'^2)v^2}{8}Z_\mu Z^\mu}_{\text{Z mass term}} + \underbrace{\frac{(g^2+g'^2)v}{4}hZ_\mu Z^\mu}_{\text{ZZ h coupling}} + \underbrace{\frac{(g^2+g'^2)}{4}hhZ_\mu Z^\mu}_{\text{ZZ h h coupling}} \quad (1.12)$$

If we consider now the Higgs potential, we can extract its self couplings:

$$-V(\Phi) = \mu^2\Phi^\dagger\Phi - \lambda(\Phi^\dagger\Phi)^2 - V(\Phi) = -\lambda v^2h^2 - \lambda v h^3 - \frac{\lambda}{4}vh^3 \quad (1.13)$$

## Higgs and fermions

The coupling of fermions to the Higgs bosons are described by the Yukawa lagrangian [12, 13, 14]. In the following, the couplings to leptons will be described [8].

$$\mathcal{L}_{Yukawa}^{leptons} = -y_e\bar{e}_R\phi^\dagger\Psi_L - y_e^*\bar{\psi}_L\Phi e_R \quad (1.14)$$

By using the expression of  $\Phi$  and  $\Psi_L$ , one obtains:

$$\mathcal{L}_{Yukawa}^{leptons} = -y_e\frac{1}{\sqrt{2}}((v+h)\bar{e}_R e_L + (v+h)\bar{e}_L e_R) \quad (1.15)$$

$$\mathcal{L}_{Yukawa}^{leptons} = - \underbrace{\frac{y_e v}{\sqrt{2}} \bar{e} e}_{\text{e mass term}} - \underbrace{\frac{y_e}{\sqrt{2}} h \bar{e} e}_{\text{hee couplings}} \quad (1.16)$$

$y_e$  are complex couplings,  $e$  is the lepton index, it can be  $e, \mu, \tau$ .  $e_R$  is the right handed  $SU(2)_R$  singlet fermion field,  $\Psi_L = \begin{pmatrix} \nu_{e,L} \\ e_L \end{pmatrix}$  is the  $SU(2)_L$  doublet fermion field and  $\Phi = \begin{pmatrix} 0 \\ (v+h)/\sqrt{2} \end{pmatrix}$  is the Higgs doublet field in unitary gauge.

As stated in the QCD paragraph, there are 3 generations of quarks. The components are the left handed weak isospin quark doublet  $Q_{Lj}$ , an the singlet  $d_{Rj}$  and  $u_{Lj}$ , with  $j$  the generation index running from 1 to 3. Let's introduce the conjugate Higgs doublet  $\tilde{\Phi}^\dagger$ . The most general form of the quark Yukawa lagrangian [8] is

$$\mathcal{L}_{Yukawa}^{quarks} = \sum_{i=1}^3 \sum_{j=1}^3 y_{ij}^u \bar{u}_{Ri} \tilde{\Phi}^\dagger Q_{Lj} + y_{ij}^d \bar{d}_{Ri} \Phi^\dagger Q_{Lj} + h.c \quad (1.17)$$

$y_{ij}^u$  and  $y_{ij}^d$  are the Yukawa matrices components and "hc" stands for hermitian conjugate. By replacing  $\Phi$  by its vacuum value, one obtain [8]:

$$\mathcal{L}_{Yukawa}^{quarks} = -(\bar{u}_1, \bar{u}_2, \bar{u}_3)_R M^u \begin{pmatrix} u_1 \\ u_2 \\ u_3 \end{pmatrix}_L - (\bar{d}_1, \bar{d}_2, \bar{d}_3)_R M^d \begin{pmatrix} u_1 \\ u_2 \\ u_3 \end{pmatrix}_L + h.c \quad (1.18)$$

where  $M^u = \frac{v}{\sqrt{2}} y^u$  and  $M^d = \frac{v}{\sqrt{2}} y^d$  are the quark mass matrices in the generation space. They are not diagonal. To find the mass eigenstates, we need to diagonalize the two matrices, which can be done by multiplying it on both sides by unitary matrices  $(U_R, U_L, D_R, D_L)$ .

$$\begin{pmatrix} u_1 \\ u_2 \\ u_3 \end{pmatrix}_{L,R} = U_{L,R} \begin{pmatrix} u \\ c \\ t \end{pmatrix}_{L,R}, \quad \begin{pmatrix} d_1 \\ d_2 \\ d_3 \end{pmatrix}_{L,R} = D_{L,R} \begin{pmatrix} d \\ s \\ b \end{pmatrix}_{L,R} \quad (1.19)$$

$$U_R^{-1} M^u U_L = \begin{pmatrix} m_u & 0 & 0 \\ 0 & m_c & 0 \\ 0 & 0 & m_t \end{pmatrix}, \quad D_R^{-1} M^d D_L = \begin{pmatrix} m_d & 0 & 0 \\ 0 & m_s & 0 \\ 0 & 0 & m_b \end{pmatrix} \quad (1.20)$$

$m_u, m_d, m_c, m_s, m_t, m_b$  are the masses of the quarks.

The couplings of Higgs boson to quarks are then equal to  $\frac{-iy_q}{\sqrt{2}} = \frac{-im_q}{v}$ , as  $m_q$  are the mass eigen-values.

## 1.2 Elementary particles: state of the art

There are two types of elementary particles: the fermions which possess a half integer spin and behave according to the Fermi-Dirac statistics, and the bosons, the interactions mediators whose spin is an integer and which behave according to the Bose-Einstein statistics. The fermions are divided into two families: the leptons which are sensitive only to the weak and electromagnetic interactions, and the quarks, see Table 1.1. Both the quarks and the leptons are classified in three generations families so there are 6 quarks with different masses (up, down, charm, strange, beauty and top) and 6 leptons (electron, muon, taus and associated neutrini).

Table 1.1 – Fermions table. From [15].

Fermions (spin 1/2)				
	<u>Quarks</u>		<u>Leptons</u>	
<b>Generation 1</b>	<b>u</b>	<b>d</b>	<b>e</b>	<b><math>\nu_e</math></b>
mass (MeV)	$2.2^{+0.6}_{-0.4}$	$4.7^{+0.5}_{-0.4}$	0.511	<2eV
Charge (q)	+2/3	-1/3	-1	0
<b>Generation 2</b>	<b>c</b>	<b>s</b>	<b><math>\mu</math></b>	<b><math>\nu_\mu</math></b>
Mass (MeV)	$1280 \pm 30$	$96^{+8}_{-4}$	105.6	<2eV
Charge (q)	+2/3	-1/3	-1	0
<b>Generation 3</b>	<b>b</b>	<b>t</b>	<b><math>\tau</math></b>	<b><math>\nu_\tau</math></b>
Mass (GeV)	$173.1 \pm 0.6$	$4.18^{+0.04}_{-0.03}$	1.776	<2eV
Charge (q)	+2/3	-1/3	-1	0

The bosons, except from the Higgs boson, are the mediators of three gauge interactions: the photon is the mediator of electromagnetism, the W and Z bosons are the mediators of the weak interaction and the gluons are the mediator of the strong force. Their characteristics are compiled in the Table 1.2. No evidence of a gravitation mediator has ever been made.

Table 1.2 – Bosons table. From [15].

Type	$W^+, W^-$	Z	$\gamma$	gluon	Higgs boson
Interaction	Weak		Electromagnetism	Strong	-
Charge (q)	$\pm 1$	0	0	0	0
Mass (GeV)	80.399	91.188	$< 10^{-24}$	0	125.3
Spin	+1		+1	+1	0
Interactions with:	quarks, leptons and Higgs boson		charged leptons and quarks	quarks	massive particles

The quarks can combine in the SM framework (if their combination is color neutral) and their combinations (hadrons) by 2 (mesons [15]), 3 (baryons [15]), 4 (tetraquarks [16, 17]), 5 (pentaquarks [18]) has already been observed; in particular the last two ones have been observed recently by the LHCb collaboration [19].

### 1.3 Higgs boson production at LHC

The LHC and its experiments were built to allow within five years of data taking to either observe or discard at  $5\sigma$  level a not too heavy Higgs boson. The Higgs boson was indeed discovered in 2012 by ATLAS and CMS [20, 21]. The following section will present the Higgs boson production mechanism and the Higgs boson decay channels considered at LHC. The various plots shown on this section are produced by the Higgs cross sections working group [22] and documented in their CERN yellow reports [23].

#### 1.3.1 Higgs production

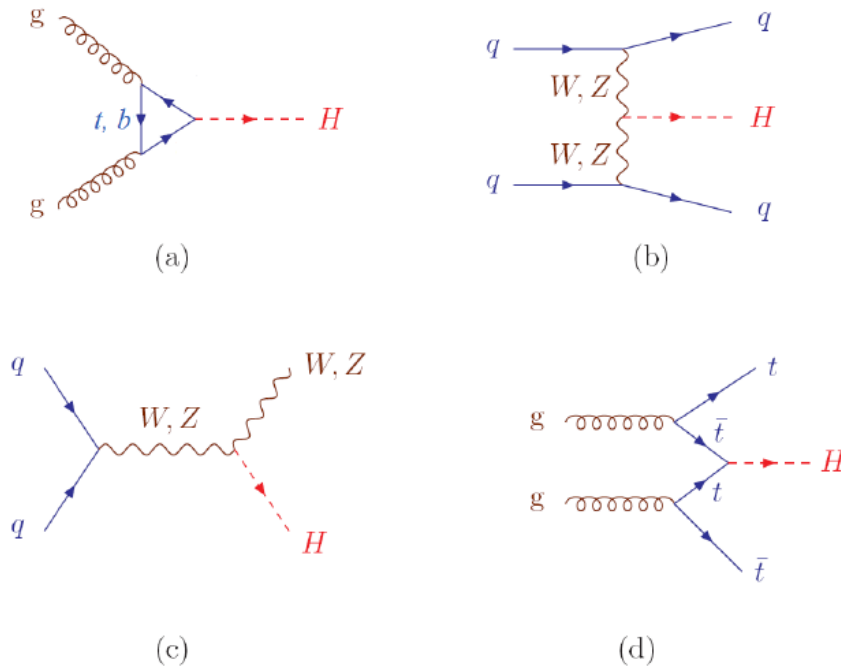


Figure 1.2 – Higgs production channels considered at LHC. [22, 23]

At the LHC the Higgs boson can be produced in several production channels, represented in Figure 1.2. The four main production channels explored at LHC are listed below from the most to the least frequent:

- Gluon gluon fusion (ggF): fusion of two gluons in a top or b loop which gives a Higgs boson. As shown on the Figure 1.3a ggF is by far the dominant production channel, but is polluted by a lot of QCD activity. Consequently it is more interesting when associated to clean Higgs decay such as  $\gamma\gamma$  or four leptons final states.
- Vector Boson Fusion (VBF): VBF has the second largest cross-section, it consists of two quarks exchanging two vector bosons creating then a Higgs boson. The VBF is the electroweak production of the Higgs boson with two associated jets. This channel has a reduced QCD activity [23].
- VH: Production of a Higgs boson in association with a vector boson (third and fourth highest cross sections respectively for W and Z). The vector boson can then decay leptonically in three channels: 0 leptons ( $Z \rightarrow \nu\bar{\nu}$ ), 2 leptons ( $Z \rightarrow l\bar{l}$ ), 1 lepton ( $W \rightarrow l\nu_l$ ). This is an interesting production channel to investigate the coupling of the Higgs boson with a vector boson and also to study Higgs final states with b quarks.
- ttH: Production of a Higgs boson in association with a  $t\bar{t}$  pair. This channel has the lowest cross section among the four. This decay channel has recently been observed at LHC [1] and it constitutes a direct observation of the Yukawa coupling between the Higgs boson and the top quark.

Other channels such as bbH (production of a Higgs boson in association with two quarks) and tH (production in association with a top quark) have even lower cross sections and are not presented here.

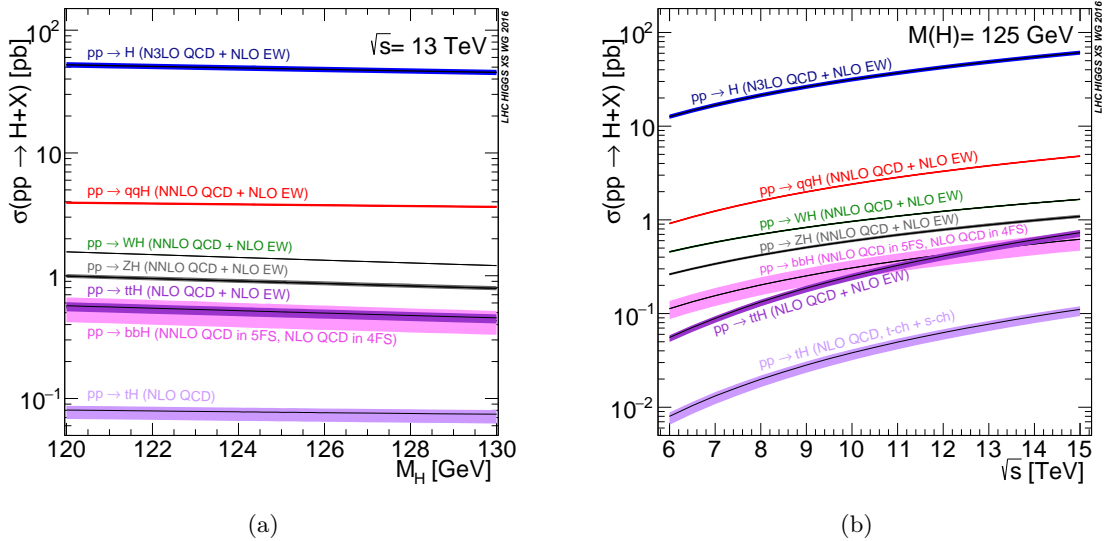


Figure 1.3 – (a) Higgs cross section at 13 TeV proton-proton energy collision for various Higgs masses. (b) Higgs cross sections for a 125 GeV Higgs for different  $\sqrt{s}$  [22].

### 1.3.2 Higgs decay

One of the main goal of the ATLAS experiment is to describe the Higgs interactions with other particles by measuring its couplings. In the following, the Higgs decays channels of interest at LHC will be documented. The Figure 1.4 presents the Higgs branching ratios.

The historical Higgs boson discovery channels [20, 21](for which the discovery significance is greater than  $5\sigma$ ) are  $h \rightarrow \gamma\gamma$  and  $h \rightarrow ZZ \rightarrow 4$  leptons.  $h \rightarrow \gamma\gamma$  has a low branching ratio (close to  $10^{-3}$ ) but it does not involve a QCD interaction so it is rather a clean channel.  $h \rightarrow ZZ \rightarrow 4$  leptons has a branching ratio which is an order of magnitude higher than  $h \rightarrow \gamma\gamma$  and is also a discovery channels thanks to the excellent muon reconstruction efficiency of ATLAS and CMS.

For a 125 GeV Higgs boson, the dominant channel is the  $h \rightarrow b\bar{b}$  channel. The b quarks are abundantly produced at LHC [24] with a cross section more than 7 orders of magnitude than the Higgs boson and their identification is quite challenging (there is a probability that jets from c-hadrons,  $\tau$  or light-flavored hadrons end mis-tagged as jets originated from b-hadrons decays). To have a chance to observe a Higgs boson decay into two b quarks, it is better to look at Higgs production in association with a vector boson. The observation of Higgs decay into two b-quarks has been reported by ATLAS and CMS experiment in 2018 [2].

Other decay channels such as  $H \rightarrow WW$ ,  $H \rightarrow gg$  and  $H \rightarrow \tau\tau$  are also considered. The Higgs decay into two Higgs boson is also a challenging channel, as it is the only way to access the Higgs trilinear self-couplings. The luminosity increase of the HL-LHC will maybe help to assess this phenomenon, more details in the Chapter 5.

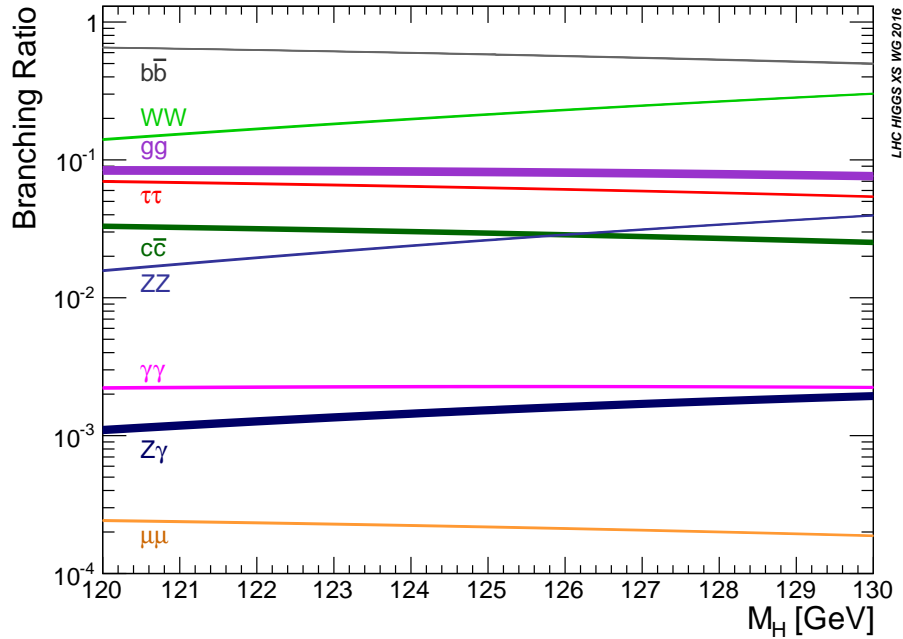


Figure 1.4 – Higgs branching ratios [23].

## Conclusion

The Standard model of the particles and their interactions has been presented in this chapter, with a special emphasis on the Higgs sector (the Higgs boson production and decays considered at LHC have also been documented). In the following, the ATLAS experiment, which have played a major part in the Higgs boson discovery and which continues to investigate further the Higgs boson characteristics, will be thoroughly described.



## Chapter 2

# The LHC and the ATLAS experiment

### Contents

---

<b>2.1</b>	<b>The Large Hadron Collider . . . . .</b>	<b>22</b>
<b>2.2</b>	<b>The ATLAS experiment . . . . .</b>	<b>24</b>
2.2.1	The ATLAS detector . . . . .	26
2.2.1.1	The Inner Detector . . . . .	28
2.2.1.2	The Electromagnetic Calorimeter . . . . .	30
2.2.1.3	The Hadronic Tile Calorimeter . . . . .	30
2.2.1.4	The Muon Spectrometer . . . . .	31
2.2.1.5	The Trigger system . . . . .	32
2.2.2	Reconstruction and simulation of physics objects . . . . .	33
2.2.2.1	Tracking in ATLAS . . . . .	33
2.2.2.2	B-Tagging . . . . .	37
2.2.2.3	Simulation chain in ATLAS . . . . .	38
<b>2.3</b>	<b>Conclusions . . . . .</b>	<b>39</b>

---

The ATLAS experiment [6] (A Toroidal LHC ApparatuS) is a multi purposed particle physics experiment based at CERN [4] (Conseil Européen de la Recherche Nucléaire). It is installed at one of the convergent point of the two beam lines of the Large Hadron Collider [5] (LHC), the 27 km long proton-proton collider accelerator of CERN. In the following chapter the LHC and the ATLAS experiment will be described. A second section will focus on the reconstruction of physics objects, with a special emphasize on tracking, flavor jet identification and event simulation.

The CERN current accelerator complex (see Figure 2.1) includes many particle accelerators which are used in a wide range of particle experiments, from LHC experiments to anti-

matter experiment such as AEGIS [25] which test the gravity of antiprotons and nuclear physics experiment such as ISOLDE [26]. The North Area of CERN is also a testbeam area where detectors prototypes are tested thanks to secondary beams from the Super Proton Synchrotron (SPS).

The LHC protons [27] delivered to LHC experiments are originated from a hydrogen bottle. The hydrogen atoms are ionized and the resulting protons are injected in a first accelerator, the LINAC 2 which accelerate them to an energy of 50 MeV. Then they reach the Booster synchrotron and are accelerated to 1.4 GeV. Later, in the Proton Synchrotron (PS), protons reach an energy of 25 GeV and acquire their bunch structure: 81 bunches packets with 25 ns spacing. Then triplets of 81 bunches are sent to the SPS which accelerate protons to 450 GeV. Eventually, the LHC is filled with about 2808 bunches per beam and accelerate each proton up to 6.5 TeV. Each bunch is made of about  $1 \times 10^{11}$  protons.

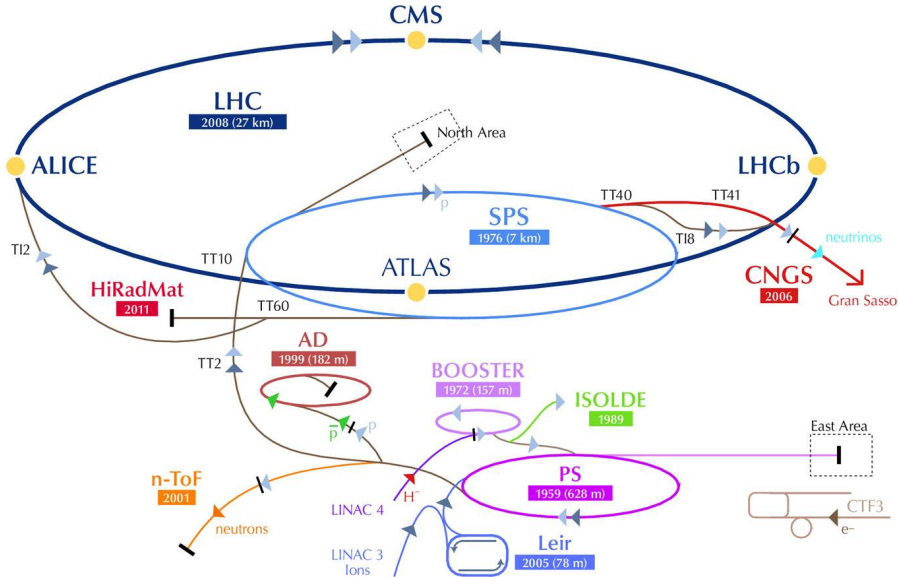


Figure 2.1 – Scheme of the CERN accelerator complex [28]

## 2.1 The Large Hadron Collider

The LHC is the current most powerful particle accelerator producing proton-proton collisions at the center of mass energy  $\sqrt{s} = 13$  TeV in several points where its main experiments, ATLAS, CMS [29], ALICE [30] and LHCb [19] are located. ATLAS and CMS are both generally purposed detectors which possess a quasi  $4\pi$  angular coverage. They investigate a wide range of particle physics question, from the Higgs boson to the search of beyond the standard model particles. LHCb focuses on the study of B-Hadrons and CP violation. ALICE focuses on the study of strong interaction at the highest energy by investigating the outcome of lead-lead ions collisions.

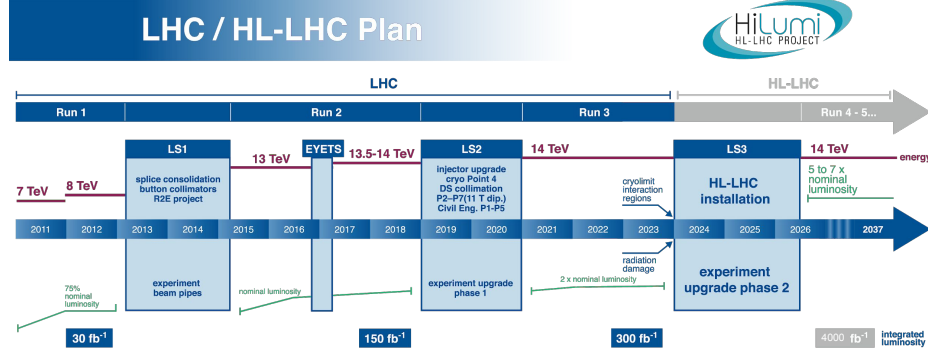


Figure 2.2 – LHC and High Luminosity LHC (HL-LHC) timeline [31].

The LHC (see Figure 2.2) have started to collide protons in 2008 ( $\sqrt{s} = 7$  TeV). Since 2008 it has ramp up twice in terms of energy:  $\sqrt{s} = 8$  TeV in 2012 and  $\sqrt{s} = 13$  TeV in 2015. This ramping up in energy has allowed ATLAS and CMS to increase their discovery potential.

### Instantaneous and integrated Luminosity

The instantaneous luminosity  $L$  is the ratio of event rate  $\frac{dN_{events}}{dt}$  over the interaction cross section  $\sigma$ . It is expressed in units of  $cm^{-2}s^{-1}$  or  $b^{-1}s^{-1}$  ( $1b = 10^{-24}cm^2$ ). The luminosity depends on beam parameters in the following way [32, 15]:

$$L = F \frac{N^2 n_b f_{rev} \gamma_r}{4\pi \sigma_x \sigma_y} \quad (2.1)$$

where  $N$  is the number of particles per bunch,  $n_b$  is the number of bunches,  $f_{rev}$  is the LHC revolution frequency,  $\gamma_r$  the relativistic gamma factor,  $\sigma_x$  and  $\sigma_y$  are the transverse beam profiles at the interaction point and  $F$  a geometrical reduction factor taking into account that all the protons in the bunch do not collide.

The integrated luminosity expressed in  $b^{-1}$  is the luminosity integrated over time. The nominal design of the LHC in terms of integrated luminosity is  $300 fb^{-1}$  that will be reached by the end of the LHC run time in 2023. In terms of luminosity, the LHC has provided so far more than  $100 fb^{-1}$  of stable beams protons (see Figure 2.3 - Left), considering the 7, 8 and 13 TeV energy in the center of mass datasets.

### Pile-up and mean number of interactions per bunch crossing

The mean number of interactions per bunch crossing ( $\langle \mu \rangle$ ) correspond to the mean of the poissonian distribution of the number of interactions per crossing calculated for each bunch.

$$\mu = \frac{L_{bunch} \times \sigma_{inel}}{f} \quad \text{with } L_{bunch} \text{ the luminosity per bunch, } \sigma_{inel} \text{ the inelastic cross section}$$

(about 80 mb at 13 TeV) and  $f$  the LHC revolution frequency. The current bunch frequency is 40 MHz.  $L_{int}$  is increasing each year, leading to an acceleration of the collected statistics (see Figure 2.3 - Left) but also of the pile-up  $\langle\mu\rangle$ . The pile-up increase implies that it is harder to spatially disentangle two events.

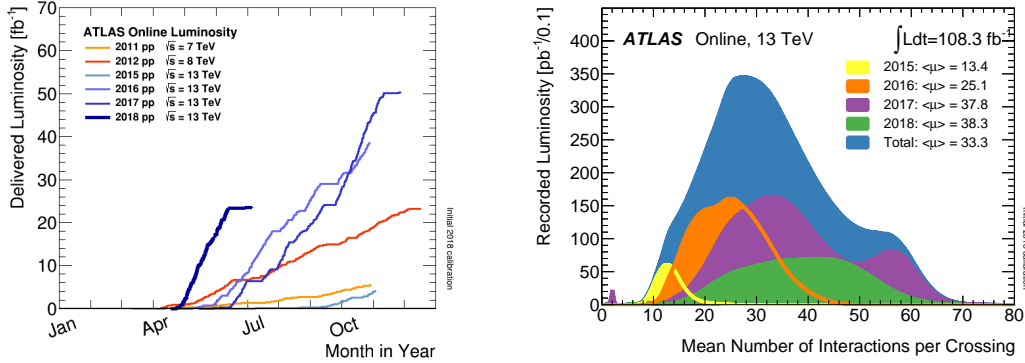


Figure 2.3 – Left: Integrated luminosity for each year with also referenced the energy in the center of mass. Right: Distribution of the mean number of interactions per bunch crossing vs luminosity for the 2015-2018 (up to the 12<sup>th</sup> of June) pp collision data at  $\sqrt{s}=13$  TeV. [33]

After 2023, the LHC will be upgraded into a high luminosity machine, the High Luminosity LHC (HL-LHC). The instantaneous luminosity will increase by a factor of 5 to 7. As a consequence, the mean number of interactions per bunch crossing  $\langle\mu\rangle$  will rise to 200, to be compared to the actual average value of the LHC which is less than 40. This increase in luminosity will allow to accumulate a lot more statistics, close to  $4000\text{fb}^{-1}$  at the end of the data-taking period, 10 times what will be collected at the end of the LHC run time. Further information on the HL-LHC can be found in the Chapter 5, dedicated to the HL-LHC and the upgrades of the ATLAS detector.

## 2.2 The ATLAS experiment

The goal of the ATLAS experiment is to observe and study the particles produced by the collisions of very energetic protons (from  $\sqrt{s} = 7$  to 13 TeV). The first motivation of the ATLAS experiment was the search of the Higgs boson, which was indeed discovered in 2012 [20, 21]. The actual efforts are orientated towards search of Beyond the Standard Model (BSM) particles and precise measurement of characteristics of already known particles and interactions. ATLAS has already produced a lot of highly remarkable scientific results. For example the cross section measurements of particles is in excellent agreement with the SM theory as shown on Figure 2.4.

Some of ATLAS many successful achievements include a precise measurement of the Higgs boson mass (see Figure 2.5). The Higgs boson has been discovered first in two channels,  $H \rightarrow \gamma\gamma$  and  $H \rightarrow ZZ \rightarrow 4$  leptons with the 7 and 8 TeV Run1 dataset. The search in other channels, especially in the  $H \rightarrow b\bar{b}$  channel which possesses the higher branching ratios but is

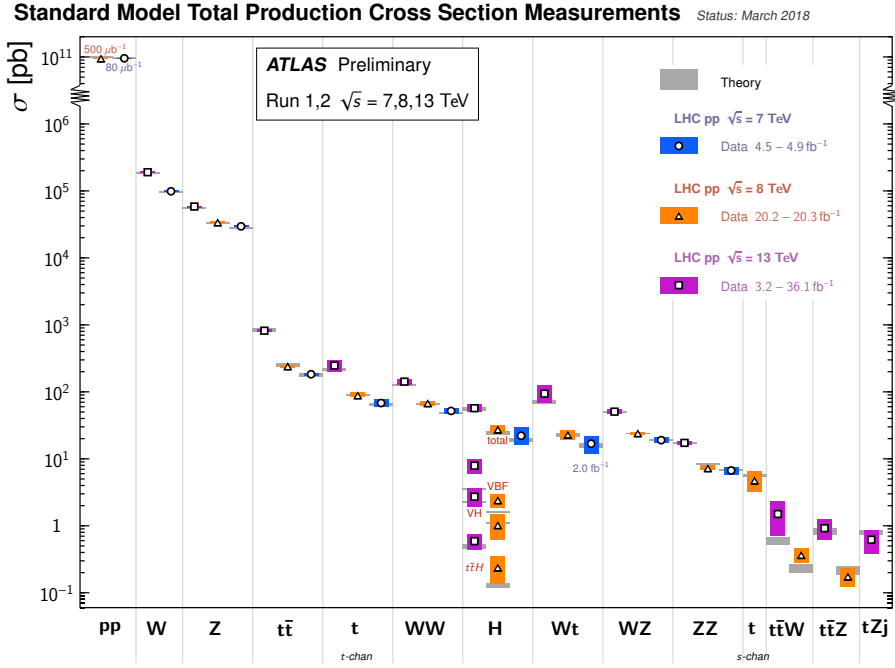
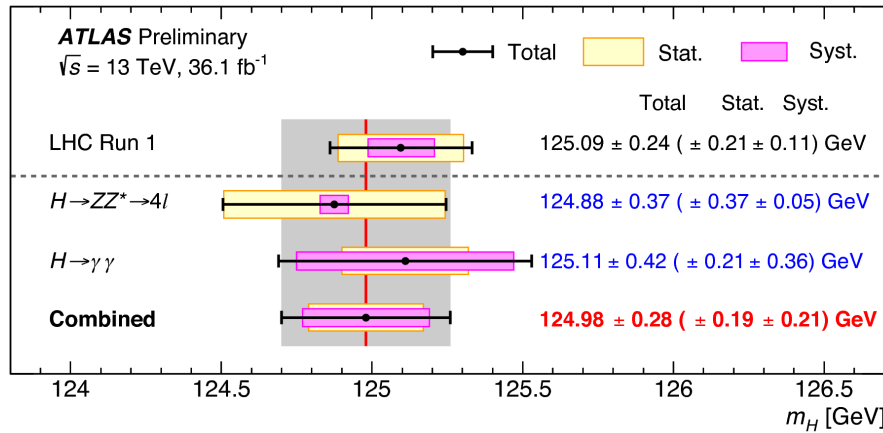


Figure 2.4 – SM cross section production for several final states [34]

a challenging channel due to the difficulty of identifying b-jets and the large  $b\bar{b}$  background, are ongoing and observation of the  $H \rightarrow b\bar{b}$  at  $5\sigma$  significance has recently been published [2, 35]. The results between the Run 1 and Run 2 are consistent and the Run 2 Higgs boson mass is measured at  $124.98 \pm 0.28$  ( $\pm 0.19 \pm 0.21$ ) GeV.

Concerning the search of BSM phenomena, no discoveries have been made by ATLAS so far but thanks to the huge statistics accumulated and to the refinement of the data analysis, a multitude of constraints on the mass and couplings of BSM models candidates have been set.

Figure 2.5 – Mass of the Higgs boson obtained by ATLAS experiment with the dataset collected in Run1 and Run2 on the two channels  $H \rightarrow \gamma\gamma$  and  $H \rightarrow ZZ \rightarrow 4l$  [36].

To be able to investigate such large and exciting fundamental physics question, the ATLAS detector is equipped with precise detectors whose salient features will be presented in the following section.

### 2.2.1 The ATLAS detector

The ATLAS detector (see Figure 2.6) is built at one of the interaction point of the LHC, 100 meters under the ground, which helps in stopping a large fraction of cosmic rays. The ATLAS detector is capable of detecting a large variety of particles, in an unprecedented range of energies, produced by the collision of partons inside the protons. It possesses a cylindrical symmetry and it covers almost all the  $4\pi$  solid angle surrounding the collision point, except from a small volume around the beam pipe.

ATLAS uses a right-handed coordinate system with its origin at the nominal interaction point (IP) in the center of the detector and the z-axis coinciding with the axis of the beam pipe. The x-axis points towards the centre of the LHC ring, and the y -axis points upward. Cylindrical coordinates  $(r, \phi)$  are used  $\phi$  being the azimuthal angle around the z-axis. The pseudorapidity  $\eta$  is defined in terms of the polar angle  $\theta$  such as  $\eta = -\ln(\tan(\theta/2))$ . Other ATLAS common notations are the transverse momentum  $p_T = p \sin(\theta)$  and transverse energy  $E_T = E \sin(\theta)$ .  $\Delta R = \sqrt{\Delta\eta^2 + \Delta\phi^2}$  is used to define cone size.

The various detectors of the ATLAS experiment are nested in a cylindrical way. Starting from the interaction point, one can find:

- The Inner Detector (ID): it is dedicated to the measurements of tracks momentum and vertices reconstruction. The ID is encapsulated in a 2 T magnetic field provided by a solenoid magnet, which helps to estimate the momentum of charged particles. It is composed of a pixel detector, a micro strips detector the SemiConductor Tracker (SCT) and a Transition Radiation Tracker (TRT).
- The Electromagnetic Calorimeter (EC): it reconstructs the energy loss by electrons and photons which cross it. It is the crucial tool for energy and identification of electrons and photons.
- The Hadronic Calorimeter (HC) which measure showers from the interaction of hadrons with its absorbers layers.
- The Muon Spectrometer (MS) which is a tracking device recording the trajectory of muons.

The ATLAS detector is immersed in a non homogeneous magnetic field [38] (see Figure 2.7) which bends the charged particles tracks and gives access to momentum of particles. It is ensured by three magnetic devices:

- a barrel toroidal magnet providing a magnetic field of maximum 4 T,
- two end-caps toroidal magnet providing a magnetic field of maximum 4 T,

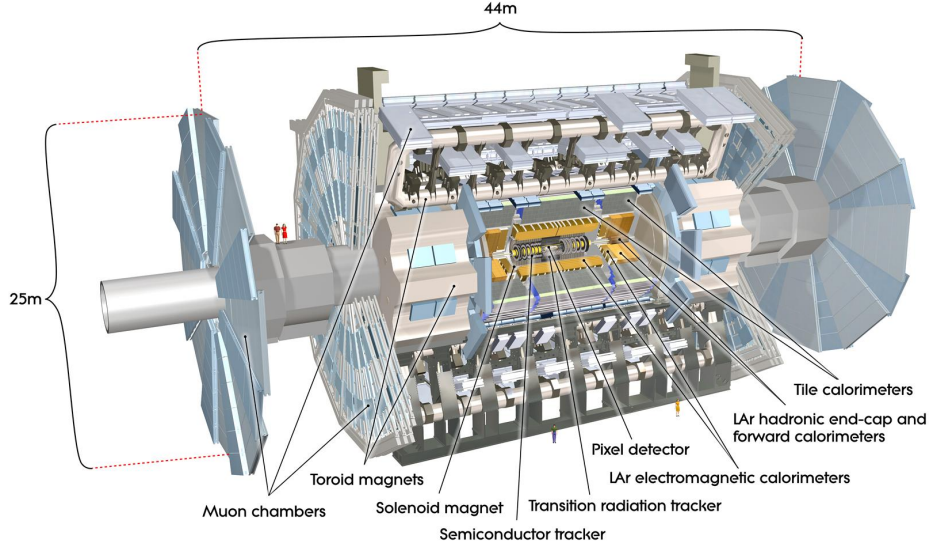


Figure 2.6 – The ATLAS detector [37]

- a central solenoid magnet providing a 2 T magnetic field.

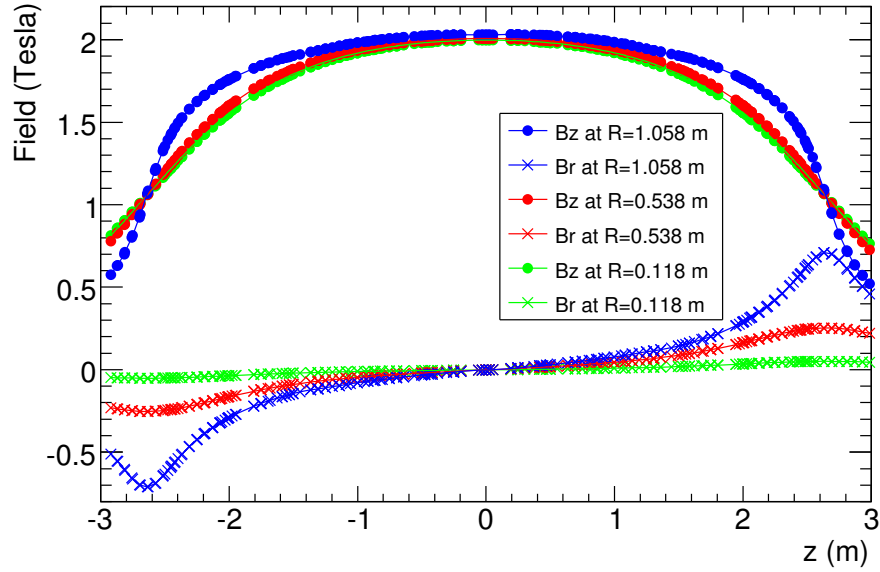


Figure 2.7 – r and z dependency of the radial (Br) and axial (Bz) magnetic field components in the inner detector cavity, at fixed azimuth. (From [6]).

To ensure an optimal data taking and to monitor the proton beam collisions, two dedicated detectors, the Beam Conditions Monitor (BCM) and the Beam Loss Monitor are used [32]. The BCM, which is composed of 500  $\mu\text{m}$  thick diamond sensor, monitor the beam conditions close to the interaction point. It can detect dangerous conditions and trigger an abort in the detector and accelerator system. Luminosity detectors, including a Diamond Beam Monitor (DBM)[39] which will measure luminosity and beam background, a zero-degree calorimeter



(ZDC [40]) that sits 140 m from the interaction point, a detector that performs a luminosity measurement using Cherenkov integration (LUCID [41]) and an absolute luminosity detector (ALFA [41]) for ATLAS are also used.

In the following sections, the ATLAS sub-detectors will be presented, starting with the ID.

### 2.2.1.1 The Inner Detector

The goal of the Inner Detector (ID) is to measure the trajectory of charged particles and associated production/decay vertices. To achieve this goal it detects hits inside its sub-detectors which are then fitted into helicoidal tracks. It is composed of three encapsulated sub-detectors as presented in Figure 2.8. From the beam pipe to the outer part, one can find the Pixel Detector, the Semi Conductor Tracker (SCT) and the Transition Radiation Tracker (TRT). All the three sub-detectors are divided into a central barrel part and two end-caps. The  $\eta$  coverage of the actual ID is  $|\eta| < 2.5$ . The two first detectors (pixel and SCT) rely on silicon detectors to study tracks. The TRT is composed of drift tubes. The momentum resolution of the ID is  $\frac{\sigma(p_T)}{p_T} \simeq 3.8 \times 10^{-4} p_T \text{ (GeV)} \oplus 0.015$ .

In what follows the three sub-detectors are going to be described, starting from the Pixel Detector.

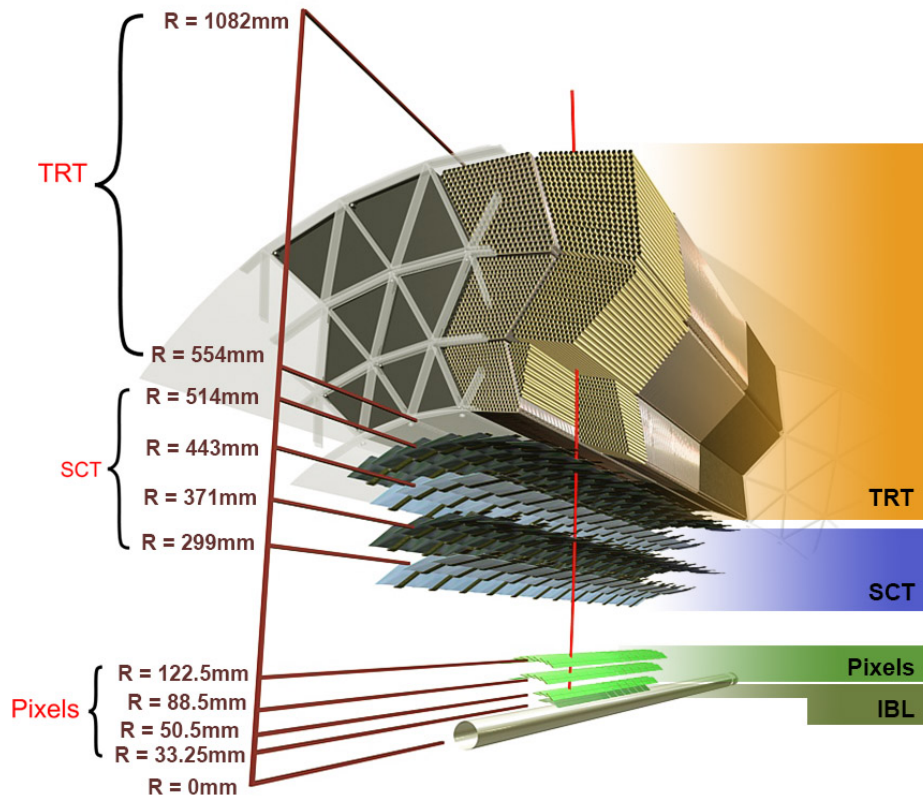


Figure 2.8 – Inner Detector barrel section [37]



### The Pixel Detector

The Pixel Detector [42] is the closest detector to the collision point, surrounding the beryllium beam-pipe. It is composed of one barrel part subdivided in 4 concentric cylinder of pixel sensors and of two end caps composed of 3 disks of pixels on each sides. The first layer, namely the Insertable B Layer (IBL, see [43, 44]) has been added in 2014 to help the reconstruction of displaced vertices from heavy flavour particle, which is relevant for many physics analyses. Its proximity to the interaction point makes this detector particularly exposed to radiation damage; further details on this topic can be found in Chapter 4 which is dedicated to the implementation of a radiation damage digitizer in the ATLAS Monte Carlo simulations. The three outer layers and 75% of the IBL sensing area are equipped with planar pixel sensors. The remaining IBL areas, at the extremity of the staves, consist of module based on the 3D technology [45]. Pixel sensors are highly segmented detectors: the pitch of the IBL pixels is  $250\text{ }\mu\text{m} \times 50\text{ }\mu\text{m}$  and the pitch of the other pixel layers is  $400\text{ }\mu\text{m} \times 50\text{ }\mu\text{m}$ . This implies a high spatial resolution of the order of  $10\text{ }\mu\text{m}$  in the  $(r - \phi)$  direction and  $100\text{ }\mu\text{m}$  in the  $z$  direction. The electronic read-out chip which is bonded to the IBL sensor is the FEI4 chip [46] whose clock is of 25 ns (corresponding to one LHC bunch crossing). For the other pixel layers, the corresponding chip is the FE-I3 chip [47]. The detection mechanism is the following: when a charged particle crosses the inner tracker, it interacts in the silicon according to Bethe Bloch formula, creating approximately 80 electron-hole pairs per micrometer crossed. These charge carriers drift towards the collection electrode and induce a signal on it. A more detailed description of pixels and silicon sensors will be given in Chapter 3.

### The SemiConductor Tracker

The SemiConductor Tracker (SCT) [48] is a silicon micro strips detector. The detection mechanism is analog to the pixel detector one, with the exception that the good spatial resolution only occurs in one direction. The barrel is composed of eight layers of strips which dimensions are  $80\text{ }\mu\text{m}$  in the  $(r - \phi)$  direction by  $6.4\text{ cm}$  in the  $z$  direction. The spatial resolution is of about  $17\text{ }\mu\text{m}$  in the  $(r - \phi)$  direction by  $580\text{ }\mu\text{m}$  in the  $z$  direction in the barrel and in the  $r$  direction in the end-caps. A module is composed of four detectors: two on each side of the modules which are rotated by a small stereo angle of  $40\text{ mRad}$ . Such rotation allow more precise measurements in  $z$ .

### The Transition Radiation Tracker

The Transition Radiation Tracker (TRT) [49]) is divided into a barrel ( $|\eta| < 0.7$ ) and two end-caps ( $0.7 < |\eta| < 2.0$ ). This detector, which is the outermost part of the current ID, is composed of  $4\text{ mm}$  diameter proportional drift tubes (or straws). It is designed to ensure that a particle crossing it in the  $[-2:2]$   $\eta$  range will cross at least 35 straws. The tubes consists of  $1\text{ m}$  long Kapton cathode coated with alumina and mechanically reinforced by carbon layers. In the center of the cylinder, there is a  $30\text{ }\mu\text{m}$  wide tungsten anode coated with gold. The tubes are filled with a gas mixture of Xenon (70 %),  $\text{CO}_2$  (27 %) and  $\text{O}_2$  (3 %). When a particle crosses the detector, it ionizes the gas mixture and the created electrons

drift, thanks to the applied high voltage, towards the anode where they are collected. The induced signal allows a particle to be detected with a spatial resolution of 130  $\mu\text{m}$ .

The TRT, more than just being a tracking device, served also as a particle identification detector: by looking at the transition radiation emission of passing through particles it can distinguish between electrons and pions. Polymers foils are interleaved with tubes to provoke transition radiation emission when a charge particles crosses through.

### 2.2.1.2 The Electromagnetic Calorimeter

The Electromagnetic Calorimeter (EC) [50, 51] is a liquid Argon calorimeter whose goal is to precisely measure the energy of electrons, positrons and photons produced in the collisions. It is composed of accordion shaped lead absorbers interleaved with copper electrodes. The gap between absorber and electrode is filled with liquid Argon (LAr). When a particle crosses the LAr, an output signal, proportional to its energy, is created by the drift of ionization electrons under high voltage. The EC is subdivided into a barrel and two end-caps, its  $\eta$  coverage is  $|\eta| \leq 3.2$ . The barrel calorimeter is embedded in a barrel cryostats, which surrounds the ID and hosts the solenoid magnet. Two end-caps cryostats house the end-cap electromagnetic calorimeter as well as the end-caps hadronic calorimeter. It contains also a pre-sampler on its inner radii, whose goal is to improve the energy resolution by correcting from the energy loss in the material upstream of the calorimeter. The presampler evaluates and reconstructs the energy of particles who have started the shower process before the EC, in the ID or in the service area (cables, cryogenic or mechanical support).

The EC energy resolution  $\sigma_E$  is well described by:  $\frac{\sigma_E}{E} = \frac{a}{E} \oplus \frac{b}{\sqrt{E}} \oplus c$  where  $a$  is the noise term,  $b$  the sampling term and  $c$  the constant term. The constant term  $c$ , which dominates at high energy, accounts for the depth of detector, cracks, dead materials and non uniformities. The noise term  $a$  accounts for the signal pile-up and the electronic noise and it dominates at low energy. The sampling term  $b$  dominates between 10 to 100 GeV and it accounts for the choice of absorbers, active material, the thickness and other minor effects.

The calorimeter is segmented in  $\phi$ ,  $r$  and  $\eta$ . Its total depth in  $r$  is greater than 22 radiation lengths in the barrel and greater than 24 radiation lengths in the end-caps. It is segmented in 3 layers (front, middle and back from the beam axis) in the  $r$  direction. The various granularities  $\Delta\phi \times \Delta\eta$  are documented in the Figure 2.9.

### 2.2.1.3 The Hadronic Tile Calorimeter

Surrounding the EC, the Hadronic tile Calorimeter (HC) [52] is its hadronic counterpart: it provides good measurements of the energy and direction of hadronic showers. The hadronic jets are originated from hadronization of gluons and quarks or originate from hadronic decays of  $\tau$  leptons. The HC is divided into a barrel part, the tile calorimeter (itself divided in central barrel and two extended barrels), and two end-caps forming the hadronic end-cap

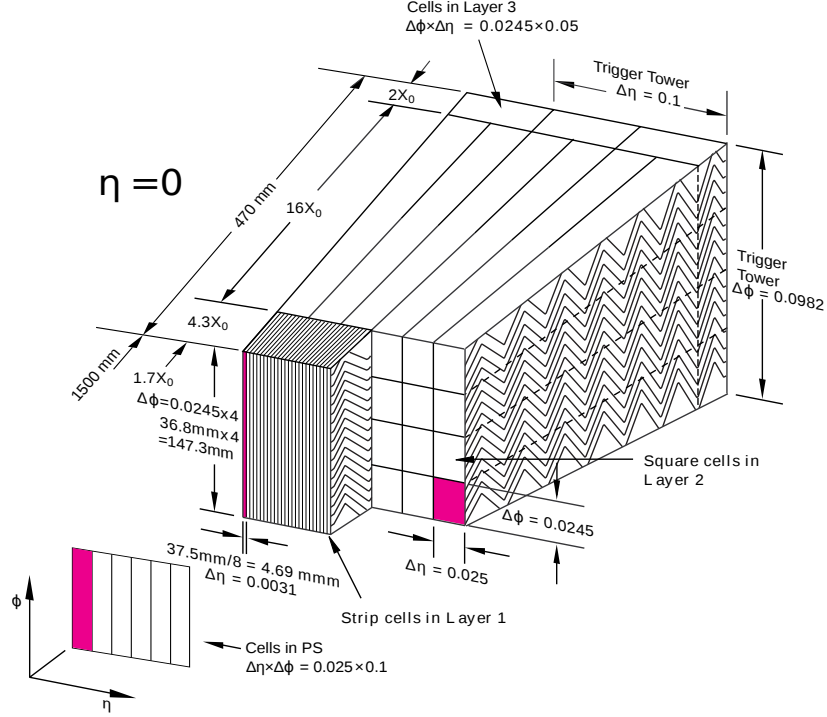


Figure 2.9 – Scheme of a barrel module of the electromagnetic calorimeter [50].

calorimeter (HEC) ( $1.5 < \eta < 3.2$ ). It is a sampling calorimeter, thicker than the electromagnetic calorimeter as the hadronic showers are longer and wider than the electromagnetic shower. The absorber of the tile calorimeter is steel and the active part is made of scintillating tiles. The HEC is composed of copper plates and liquid argon. The tile calorimeter has a granularity of  $\Delta\phi \times \Delta\eta = 0.1 \times 0.1$ .

#### 2.2.1.4 The Muon Spectrometer

The Muon Spectrometer (MS) [53] is a stand-alone tracking detector for muons within the toroidal magnetic field. Four different detector technologies are used: Monitored Drift Tubes (MDT), Cathode Strip Chambers (CSC), Resistive Plate Chambers (RPC) and Thin Gap Chambers (TGC).

MDTs are composed of an assembly of 6 layers of cylindrical aluminum drift tubes of 30 mm diameter each and a central wire of 50  $\mu\text{m}$  diameter; each tube is filled with a gas mixture of Ar,  $N_2$  and  $CH_4$ . It provides precision tracking in the central region with a spatial resolution of 35  $\mu\text{m}$  along  $z$  axis; on the contrary, the drift time is quite long ( $O(100)$  ns), so the triggering is not assured by this detector but by the RPC and the TGC.

CSCs are multi-wire proportional chambers with cathode strip. They cover the forward region, as the muon flux is higher in the forward region, they allow bi-dimensional measurements to minimize the track ambiguity. Their spatial resolution is 40  $\mu\text{m}$  in  $z$  and 5 mm resolution in the radial position.

RPCs are parallel plate capacitors filled with gas and separated radially for a fast momentum measurement in the central region. They provide triggering in the barrel part, their

time resolution being of the order of 1.5 ns.

TGCs are multi-wire proportional chambers with a finer granularity than RPCs in order to cope with the higher multiplicity and reduced track bending (for a fixed  $p_T$ ) in the forward region. They assure the triggering in the end-caps part with a time resolution of about 4 ns.

### 2.2.1.5 The Trigger system

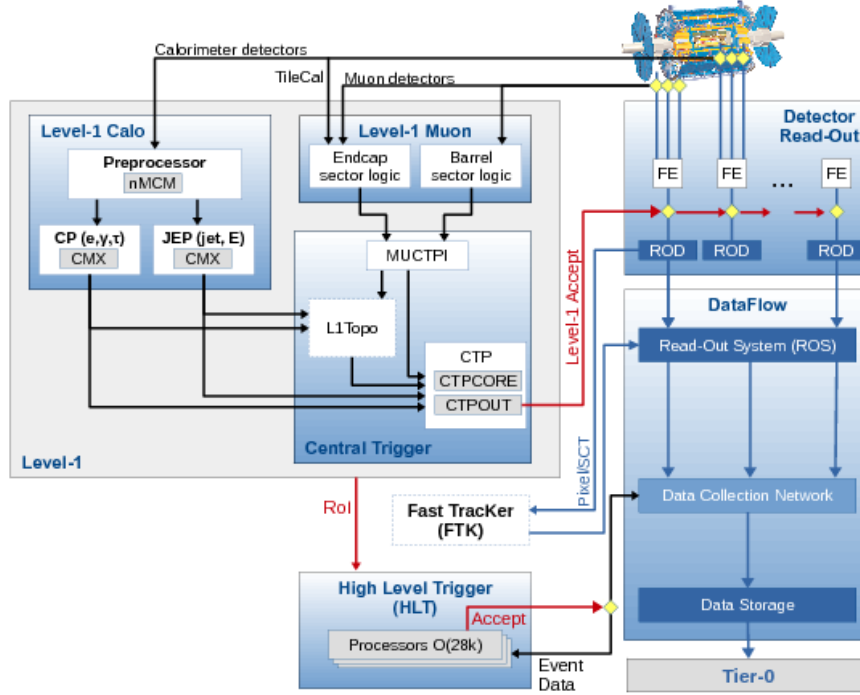


Figure 2.10 – Run2 Trigger overview [54].

The trigger system [54] task is to select interesting physics collisions in a short amount of time with a good efficiency and purity. It has to deal with an extremely high data rate, so it has to decide in a really short amount of time whether to keep or to throw out an information to keep a reasonable fraction of interesting events which can be stored offline. The ATLAS trigger system represented in Figure 2.10 has now 3 components: the Level-1 trigger (L1), the High Level Trigger and the Fast TracKer (FTK) [55] which is under commissioning. L1 provides a first selection based on inputs from the calorimeter and the muon spectrometer. In 2017, the Topological trigger, an additional FPGA-based hardware part which exploit the topological observables (invariant mass, angular selection) had been integrated to the L1. The L1 reduces the data rate from 40 MHz to less than 100 kHz by selecting interesting events passing a set of selection criteria. The second part of the trigger, the software based HLT, reduces the data rate from L1 (100 kHz) to approximately 1 kHz. The FTK is still under commissioning. It will provide the full detector tracking to the HLT by using a pattern recognition method to identify tracks by matching pixels and SCT hits to a bank of track patterns.

### 2.2.2 Reconstruction and simulation of physics objects

The offline reconstruction consists in assembling the various inputs (such as hits in the ID or energy deposits in the EC) to form higher level objects, closer to the final physics objects. Thanks to the ID inputs, charged particles trajectories or *tracks* are reconstructed and vertices are found during the tracking and vertexing phases. The energy deposits in the calorimeters allow the reconstruction of jets and missing transverse energy. Another step is the identification of particles (photons, electrons muons and  $\tau$ ). To identify jets from b-hadrons decay, a special set of algorithm collectively known as b-tagging are used (*e.g* Chapter 8).

The comparison of those higher level objects properties with Monte-Carlo simulated events is necessary to assess the good behavior of the detector and the relevance of the reconstruction of particles. In this section, the tracking and b-tagging will be emphasized as they are strongly bounded to the future Inner Tracker (ITK) development and  $H \rightarrow b\bar{b}$  analysis. A short introduction to the simulation in ATLAS will also be given.

#### 2.2.2.1 Tracking in ATLAS

The tracking [56, 57] is an essential part of High Energy Physics experiment. When a charged particle crosses the ATLAS ID, it leaves hits on the various layers of the detector. The collection of hits are then assembled in tracks through pattern recognition. Track candidates are then fitted and track parameters are estimated. The tracking relies on the ID geometry and on the number of hits or space points it can measure. Due to its actual geometry, the ID requires at least 7 Silicon hits (sum of the the Pixel detector and SCT detector hits). Such requirement ensures a good discrimination between true and fake tracks and a high resolution of tracks. Since the ID is immersed in a 2 T magnetic field, charged particles have helicoidal trajectories. One track can be described by 5 track parameters (2 local parameters:  $d_0$  and  $z_0$ ; 3 global parameters  $q/p_T$ ,  $\phi$  and  $\theta$ ) in the so called Perigée representation (see Figure 2.11). The five tracks parameters are:

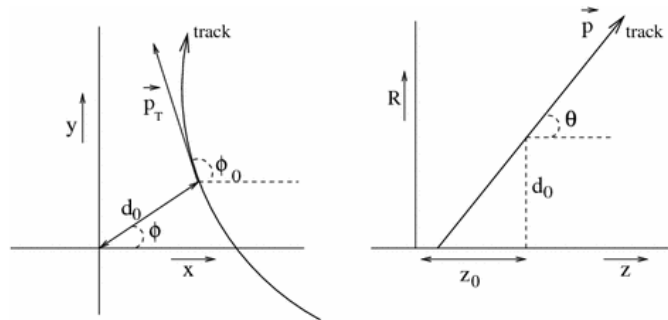


Figure 2.11 – Perigée representation [58]

- Transverse impact parameter  $d_0$ : it is the projection of the point of closest approach in the transverse direction. The transverse impact parameter resolution depends on

the pixel layer radius and space point precision as well as on the multiple scattering effect. For the ATLAS ID it is approximately  $\sigma(d_0) = \frac{90 \mu\text{m GeV}/c}{p} \oplus 12.5 \mu\text{m}$  [59]. The Figure 2.12 represents  $\sigma(d_0)$  vs  $\eta$  and vs  $p_T$  in ATLAS. The addition of a fourth layer in 2015 has allowed a better resolution, which is more or less divided by two at low  $p_T$  ( $< 1\text{GeV}$ ) in the full  $\eta$  range.

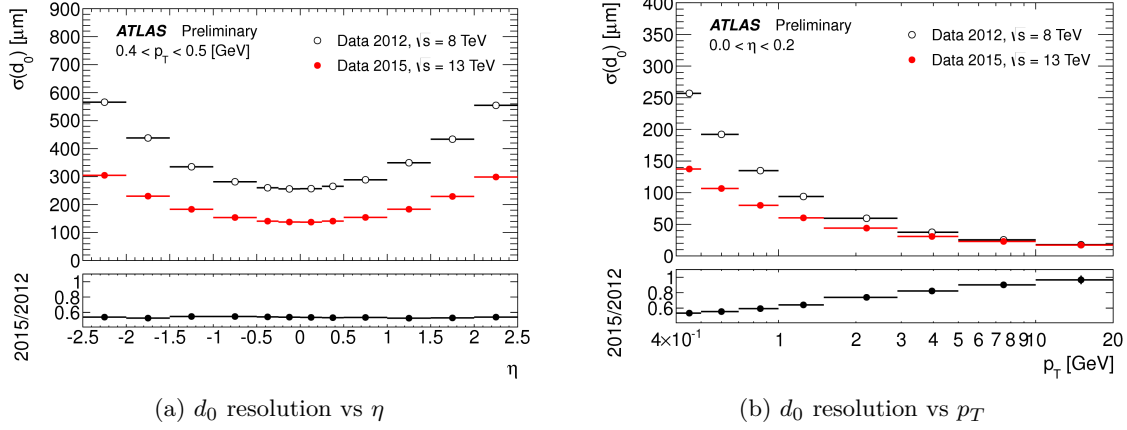


Figure 2.12 – Comparison of  $d_0$  resolution with and without the IBL over the full  $\eta$  range (a) and at low  $p_T$  (0.4 GeV to 20 GeV)(b). From [60].

- The longitudinal impact parameter  $z_0 \sin(\theta)$  which is the projection of the point of closest approach in the z-axis direction. The Figure 2.13 represents  $\sigma(z_0)$  vs  $\eta$  and vs  $p_T$  in ATLAS. The resolution is plotted for 2012 and 2015, which allows to evaluate the impact of the IBL addition. The 2015 conditions results in a better resolution over the full  $\eta$  and  $p_T$  ranges. The improvement is particularly emphasized at high  $|\eta|$  and low  $p_T$  ( $< 1 \text{ GeV}$ ).

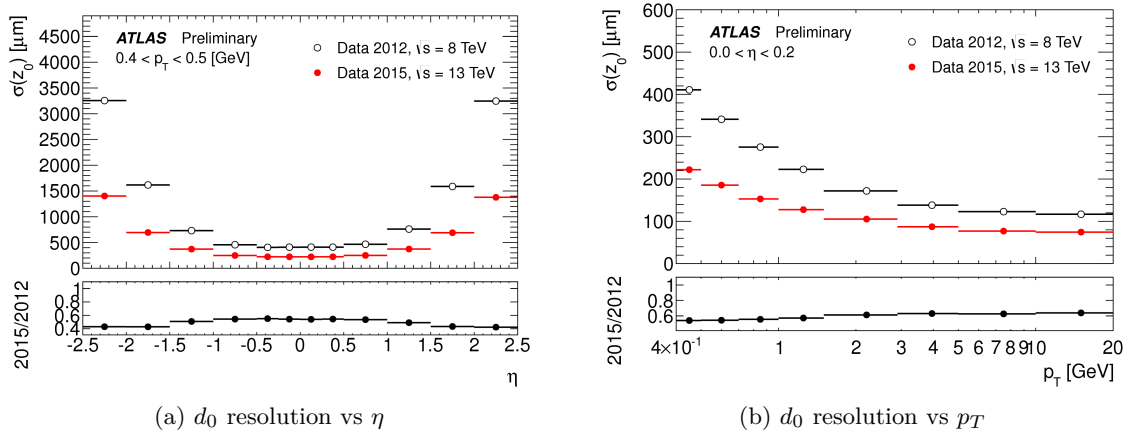


Figure 2.13 – Comparison of  $z_0$  resolution with and without the IBL over the full  $\eta$  range (a) and at low  $p_T$  (0.4 GeV to 20 GeV)(b). From [60].

- The inverse transverse momentum ( $q/p_T$ ) which give details about the curvature of the particle track. The transverse momentum  $p_T$ , which is expressed in  $\text{GeV}/c$ , is a crucial observable as it is Lorentz invariant. The transverse momentum resolution  $\sigma(p_T)$  [59]

depends on the space point measurement precision and on the multiple scattering contribution (described in details in Section 7.2.3), as well as on the magnetic field  $B$  (in Tesla) and on the radial length  $L$  (in m). The following formula expresses this dependency:

$$\frac{\sigma(p_T)}{p_T} = \underbrace{\frac{p_T}{0.3|z|} \frac{\sigma_{point}}{L^2 B} \sqrt{\frac{720}{N+4}}}_{\text{Space point measurement contribution}} \oplus \underbrace{\frac{0.054}{\beta B L} \sqrt{\frac{x/\sin\theta}{X_0}}}_{\text{Multiple scattering contribution}}$$

$N$  is the number of detector planes,  $\sigma_{point}$  the point resolution in m,  $|z|$  is the particle electrical charge,  $p_T$  is in GeV. For the multiple scattering component,  $\theta$  is the incident angle,  $X_0$  is the radiation length,  $x$  is the transversed material length.

- The track azimuthal angle ( $\phi$ ) which represents the direction of the track in the  $r\phi$  plane at the point of closest approach,  $\phi$  varies between  $[-\pi; \pi]$
- The track polar angle ( $\theta$ ), which varies between  $[0; \pi]$

The track reconstruction [56] happens in 3 steps: clusterisation, track finding and track fitting. Afterward, vertices (confluence point of several tracks) are reconstructed. In the following, the three steps will be presented.

### Clusterisation

When a particle crosses a sensor, the energy it losses can lead to the formation of multiple signals (or *hits*) in neighboring cells; those energy deposits have to be merged into one cluster to correctly describe the position of the particle crossing the sensor. The *clusterisation* in the pixel detector and in the SCT is the grouping of neighboring and simultaneous hits in one cluster. In the TRT the equivalent of the clusterisation is the formation of calibrated drift circle. From the clusters, three dimensional measurements, or *space-points* are created. In dense environments where boosted objects are collimated, some tracks can be detected simultaneously by adjacent pixels and merge into a *merged pixel cluster* as represented on Figure 2.14. To mitigate such effect, a neural network merging discrimination has been developed and is now used in the pixel detector [57].

### Track finding

The first step of the track finding is the *seeding* of space-points in short tracks of three or four hits of successive detector planes in the ID. The seeding uses pattern recognition and a combinatorial filter. Thanks to the addition of the IBL, the seeding performance was improved, a fourth point being added. Since 2012 [61], it is possible to recover electron losses from bremsstrahlung, thanks to an electron-specific pattern recognition and track fit, which enhances the tracking efficiency at low  $p_T$ . A combinatorial Kalman filter is applied to search for roads, which means adding to the seed track-compatible remaining space-points from the Pixel detector and the SCT.



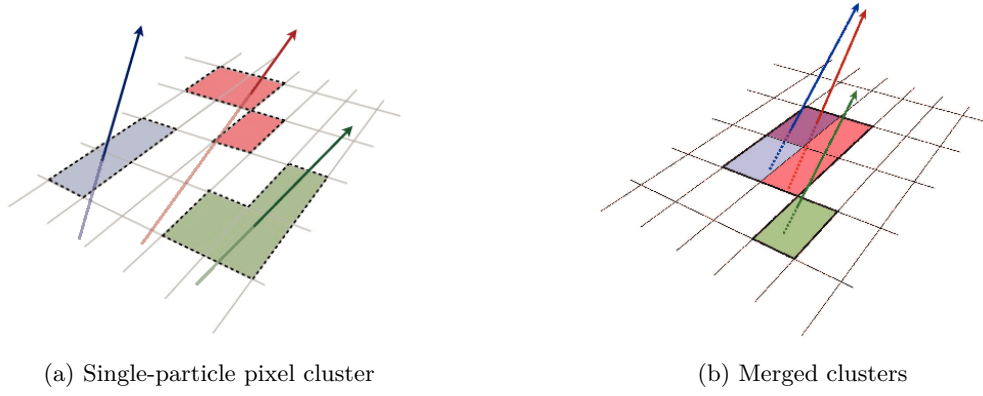


Figure 2.14 – Illustration of merged cluster phenomenon. The different colors account for signals from the passage of different charged particles. From [57].

At this step, some corrections have to be applied. The first issue is the un-homogeneous magnetic field, resulting in non strictly helicoidal tracks. The ATLAS ID can also be deformed due to mechanical and thermal constraints. This results in plane mis-alignment as detectors planes can be rotated, shifted or even bended. The alignment happens at the beginning of each run using a global fitting method which minimizes the track-hit residuals in each detector plane (track-hit residuals are the differences between the hit in the detector and the intersection of the detector with the track extrapolation) of all the tracks at the same time.

### Ambiguity solving and Track fitting

The goal of the track fitting is to determine the best track among candidates found during the finding steps. First an ambiguity solver is used and scores are given to the tracks. The scoring procedure relies on number of clusters (minimum 7 pixel and SCT clusters, 12 are expected), nature of the clusters (shared, merged, unambiguous),  $\chi^2$  value (bad track fitting implies that it is certainly a wrong assignment), track energy (suppression of low  $p_T$  tracks -  $p_T < 400$  MeV), cuts on the impact parameters ( $d_0 < 2.0$  mm and  $z_0 \sin\theta < 3.0$  mm). The first step discard the tracks which did not pass the requirements. The other candidates are ordered and then fitted using a Kalman filter. Tracks with a bad  $\chi^2$  are discarded or some marginal space points associated to these tracks are discarded and the remanent tracks are re-scored and re-fitted.

### Vertex finding and vertex fitting

Tracks can be originated from a primary vertex, the genuine colliding point between two partons, or from a secondary/tertiary vertex from particles decays, photon conversion or hadronic interactions. Secondary vertices are the signature of heavy flavour particles and long lived hadrons, especially b-hadrons which decays at a hundred of micrometers ( $\tau_b \simeq 1.5$  ps,



$c\tau_b \simeq 0.5$  mm) from the primary vertex. The primary vertex reconstruction is performed using an imaging algorithm described in [62].

### Track reconstruction performance

To evaluate the tracking performance, three criteria are retained:

- The track efficiency: it is the fraction of prompt particles which are associated to tracks which have passed a track selection *i.e.* the ratio of reconstructed tracks over truth tracks in simulation. The Figure 2.15 presents the track reconstruction efficiency for two track selection cut criteria. For more stringent cuts (for example on the number of pixel hits or the number of SCT hits), the reconstruction efficiency decreases significantly. The expected efficiency varies with the particle type and the track selection criteria. For example, muons are not strongly interacting hence their track efficiency is supposed to be close to 100 %. Electrons, which interact with the detector material via Bremsstrahlung, or pions, which are subject to hadronic inelastic interactions, have a lower track efficiency
- The track fake rate: fake tracks originate from a mis-association of genuine clusters and/or noise hits.
- The track parameters resolution: comparison of reconstructed values with simulated truth values. The Figures 2.12 and 2.13 from [60] show the  $d_0$  resolution and  $z_0$  resolution from the Run 1 compare to the Run 2 in the full  $p_T$  and  $\eta$  range. The addition of the IBL has clearly increased those parameters resolutions.

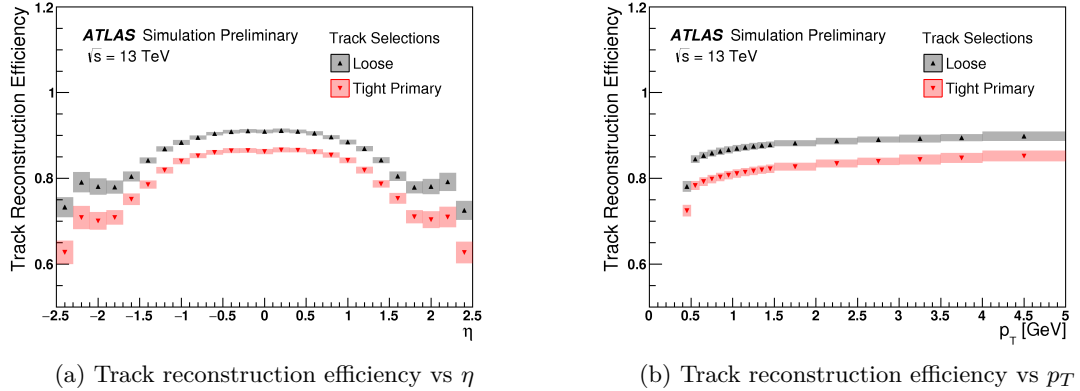


Figure 2.15 – Comparison of track reconstruction efficiency for two track criteria over the full  $\eta$  range (a) and  $p_T$  range (b). From [60].

#### 2.2.2.2 B-Tagging

B-hadrons production at LHC is substantial and one of the main challenges of the ATLAS analysis chain is to be able to identify those B hadrons and their decay products. The identification of jets containing b-hadrons (or "b-jets") is called b-tagging [63]. Due to the large

QCD  $b\bar{b}$  production, the b-tagging is a challenging task which is a fundamental ingredient for important final states such as  $H \rightarrow b\bar{b}$ . Some characteristics of the b-jets can be exploited to improve b-tagging, especially the presence of a secondary vertex. B-hadrons disintegrate mainly via the electroweak channel, the dominant decay diagram being  $b \rightarrow cW$  with W decaying leptonically or hadronically. The lifetime of b-hadrons is long (e.g 1.4 ps for the  $\Lambda_b^0$  [64]), hence the presence of secondary vertices at hundreds of micrometers from the primary vertex can be exploited for tagging.

Jets from light-flavour and charm decays can be mismatched and tagged as b-jets, hence the ATLAS b-tagging performance relies not only on the b-tagging efficiency but also on its ability to correctly identify light-flavour or charm jets; the performance are measured as light-flavour or c mis-tag rate.

Three families of algorithms are used to tag b-jets: secondary vertex based algorithms, impact parameters based algorithms and jet's topology based algorithms. Each of these algorithms provide a b-tag weight which is used to discriminate between b-, c- and light-flavour jets. The outputs of these low level algorithms can be combined in multivariate algorithms, which enhance greatly the b-tagging performance. Further details on b-tagging will be given in Chapter 8.

### 2.2.2.3 Simulation chain in ATLAS

The Monte Carlo production simulates the processes and the detector behavior in ATLAS. The simulation chain consists of various steps, from the physical proton-proton collision generation to the analysis of reconstructed objects.

The first step is the event generation, which will use generators such as Pythia [65], to simulate proton-proton collisions and its products. The hadronization and the decay of resulting hadrons are also simulated.

The second step is the simulation of the detector geometry using Geant 4 [66]. Detectors and materials are simulated, as well as the interaction of simulated particles with them.

The next step is the digitization which transforms signals in the detectors in binary outputs. Pile-up events are added at this step. The inclusion of radiation damages mechanisms in the digitization step is one part of the thesis; a dedicated Chapter (4) can be found in this thesis. After this step the format is similar to the one used with data.

The fourth step is the reconstruction of physics object from detectors inputs. They are store in several formats. In the last step data are saved in Root files [67].

## 2.3 Conclusions

The ATLAS detector and its Inner Detector have been described in this Chapter, as well as the tracking and b-tagging which heavily rely on the Inner Detector and especially with the pixel detector, whose sensors and physics will be described in the next Chapter [3](#). The high performance of the detector allowed to make significant discoveries especially in the Higgs sector. To increase its discovery potential and deal with the high data rate of the HL-LHC, ATLAS and its Inner Tracker will be upgraded; this will be discussed in Chapter [5](#).



## Chapter 3

# Silicon detectors and ATLAS pixels sensors

### Contents

---

<b>3.1</b>	<b>Silicon detector physics . . . . .</b>	<b>42</b>
3.1.1	Silicon charge carriers concentration . . . . .	42
3.1.2	PN junction . . . . .	44
<b>3.2</b>	<b>Signal formation . . . . .</b>	<b>45</b>
3.2.1	Electron-hole pair creation . . . . .	45
3.2.2	Signal development inside the sensors . . . . .	46
3.2.2.1	Carriers drift . . . . .	46
3.2.2.2	Diffusion . . . . .	46
3.2.2.3	Generation and recombination . . . . .	47
3.2.2.4	Lorentz angle . . . . .	47
3.2.3	Signal induction . . . . .	47
<b>3.3</b>	<b>Pixel sensors technologies . . . . .</b>	<b>49</b>
3.3.1	Hybrid pixel sensors . . . . .	49
3.3.2	Monolithic pixel sensors . . . . .	53
<b>3.4</b>	<b>Radiation damage effects in silicon . . . . .</b>	<b>53</b>
3.4.1	Microscopic defects in silicon . . . . .	53
3.4.1.1	Defects overview . . . . .	53
3.4.1.2	Non Ionizing Energy Loss (NIEL) . . . . .	54
3.4.2	Macroscopic impact of radiation damages in silicon . . . . .	54
3.4.2.1	Leakage current . . . . .	56
3.4.2.2	Change in operational depletion voltage - Effective doping concentration . . . . .	56
3.4.2.3	Charge trapping . . . . .	56
3.4.2.4	Conclusions on radiation damage in silicon . . . . .	57

Silicon is the material used to build pixel and strip sensors of the ATLAS experiment. It plays a major part in High Energy Physics (HEP) as it is a well known semiconductor, largely used in the industrial sector. It possesses interesting physical properties such as fast charge carriers collection, large signal over noise ratio and high density which translates into compact detectors, a crucial point for detectors as dense as ATLAS. In this chapter the basics of silicon detector physics will be reviewed, from PN junction to charge carriers dynamics. Later, the radiation damage effects in silicon will be discussed. Eventually an overview of the various detectors used for particle tracking with a special emphasis on ATLAS current ones will be discussed.

### 3.1 Silicon detector physics

Doped silicon is the key ingredient to build silicon sensors. In this section, the charged carriers concentration in intrinsic and extrinsic silicon will be studied. PN junction, the basis structure of silicon radiation detectors, will be described in the second section. The dynamics of charge carriers will also be presented.

#### 3.1.1 Silicon charge carriers concentration

##### Intrinsic silicon

Intrinsic silicon consists of raw Silicon material, without any added doping. The impurities concentration is considered negligible compared to thermally generated free electrons and holes (vacancy of electrons) [68]. In thermal equilibrium, the occupation probability of a state in silicon  $F(E)$  follows the Fermi-Dirac statistics:

$$F(E) = \frac{1}{1 + \exp \frac{E - E_F}{kT}} \quad (3.1)$$

where  $E$  is the state energy,  $E_F$  is the Fermi energy,  $k$  the Boltzmann constant and  $T$  the temperature. At room temperature the Fermi Dirac-distribution reduces to the Maxwell-Boltzmann distribution, which gives for electrons,  $F_n(E) = \exp(-\frac{E - E_F}{kT})$  and for holes  $F_p(E) = \exp(-\frac{E_F - E}{kT})$ . The densities of free electrons ( $n$ ) and free holes ( $p$ ) are obtained by integrating the effective density of states in the conduction band ( $N_c$ ) for electrons and in the valence band ( $N_v$ ) for holes with the Fermi-Dirac probability density function over the energy range:

$$n = \int_{E_c}^{\infty} N_c F_n(E) dE \quad ; \quad p = \int_{-\infty}^{E_v} N_v F_p(E) dE \quad (3.2)$$

The density of states  $N_{c,v}$  is given by  $N_{c,v} = \frac{(2m_{e,h})^{3/2}}{h^2} 4\pi E^{1/2}$  [69], where  $m_{e,h}$  is the carrier mass,  $h$  the Planck constant and  $E$  the state energy. The density of free electrons  $n$  and holes  $p$  are:

$$n = 2 \times \left( (kT)^{3/2} \frac{(2\pi m_e^* kT)}{h^2} \right)^{3/2} \exp\left(-\frac{E_c - E_F}{kT}\right) = N_c \exp\left(-\frac{E_c - E_F}{kT}\right) \quad (3.3)$$

$$p = 2 \times \left( (kT)^{3/2} \frac{(2\pi m_h^* kT)}{h^2} \right)^{3/2} \exp\left(-\frac{E_F - E_v}{kT}\right) = N_v \exp\left(-\frac{E_F - E_v}{kT}\right) \quad (3.4)$$

with  $m_h^*$  and  $m_e^*$  the effective masses of holes and electrons. For intrinsic silicon, as there is no doping, the material is electrically neutral and the density of electrons and holes have to be equal:  $n = p = n_i$  with  $n_i$  the intrinsic concentration:

$$n_i = \sqrt{N_c N_v} \exp\left(-\frac{E_G}{2kT}\right) \quad (3.5)$$

with  $E_G = E_c - E_v$  the band gap energy (1.1 eV for Silicon at room temperature).

The intrinsic Fermi level  $E_i$  is defined as:  $E_i = \frac{E_c + E_v}{2} + \frac{3kT}{4} \log(m_h^*/m_e^*)$ .

### Extrinsic silicon

For HEP applications, the silicon sensor is usually doped, meaning that some other materials are added to change the electrical properties of the raw material. There are two kind of dopants:

- **Donors:** Donor dopants have one extra electron in the valence band compared to Silicon (4 valence electrons). They are mainly atoms of the group V such as Phosphorus. When introduced in the silicon lattice, the additional valence electrons is weakly bound and with a small amount of energy (at room temperature for example) it can move freely in the crystal conduction band. The remaining dopant consist of a positive ion, stuck in the silicon lattice which modify the space charge. As electrons are the majority charge carriers, donor doped silicon is called n-doped silicon.  $N_D$  indicates the donor concentration.
- **Acceptors:** Acceptors dopants have one electron less than Silicon in the valence band (e.g Boron), which lead to an electron vacancy or hole inside the silicon structure. With a bit of energy, the hole become free in the valence band. As holes are the majority charge carriers, acceptor doped silicon is called p-doped silicon.  $N_A$  indicates the acceptor concentration.

The densities of electrons  $n$  and holes  $p$  in doped material are different. The mass action law,  $n_i^2 = n \times p$ , can be used to evaluate  $p$  and  $n$

$$n = n_i \exp\left(\frac{E_F - E_i}{kT}\right) \quad ; \quad p = n_i \exp\left(\frac{E_i - E_F}{kT}\right) \quad (3.6)$$

The Fermi level is modified by the addition of dopants in the silicon bulk. For donors it is shifted towards the conduction band:  $E_F = E_i + kT \ln \frac{N_D}{n_i}$ ; for acceptors it is shifted towards the valence band:  $E_F = E_i - kT \ln \frac{N_A}{n_i}$ .

### 3.1.2 PN junction

The PN junction [69] is the basic concept behind silicon detectors. It consists in the juxtaposition of a n-doped silicon part with a p-doped silicon part. At the interface, the energy bands are deformed as Fermi levels are different for n-doped and p-doped materials. As shown in Figure 3.1, the majority charge carriers from n-doped material are diffusing towards the p-doped region and vice-versa. Once the charge carriers migration is over, the area surrounding the junction is depleted of free charge carriers. In this area, called the depletion zone, the donor and acceptor ions are left without their free charge carriers counterparts, hence the zone is no more electrically neutral and is called the space charge region. The electric field caused by the space charge region leads to the appearance of the built-in voltage  $V_{bi}$  across the junction.

When an external voltage is applied across the P-N junction, the depleted region can either shrink if the bias is applied opposite to the built-in voltage (forward bias) or increase if it is applied in the same direction as the built-in voltage, which is called reverse bias. Increasing the depleted area is fundamental for the use of silicon sensor in HEP experiment. The basis particle detection mechanism is the drift of charge carriers created by the passage of a charged particle through the silicon sensor (more details on the signal generation can be found in the next section). This drift can only happen when the sensor is depleted, when a resulting electric field in the sensor is present. Once reversely biased, there is a net generation of carriers in the depleted area, hence a net current flows, commonly termed as leakage current ( $I_{leak}$ ). The depletion voltage is the reversed bias voltage necessary to deplete the entire P-N junction thickness ( $d$ ), which maximize the charge collection volume. It is given by

$$V_{dep} = \frac{q|N_{eff}|d^2}{2\epsilon\epsilon_0} \quad (3.7)$$

with  $q$  the elementary electrical charge,  $|N_{eff}| = |N_D - N_A|$  the effective doping concentration,  $\epsilon$  the silicon permittivity and  $\epsilon_0$  the vacuum permittivity.

The depletion voltage can be found experimentally by looking at a  $C^{-2}$  vs  $V$  curve: before depletion, the capacitance  $C$  depends on the inverse of the square root of the voltage  $V$ , after the depletion,  $C$  become almost independent of  $V$ .



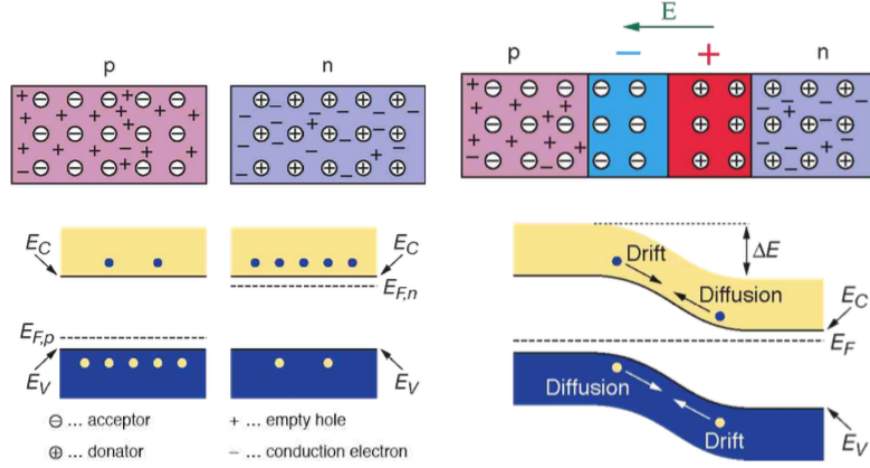


Figure 3.1 – PN junction. Scheme from [70].

The sensor can be biased with a higher voltage compared to the depletion voltage, it is then over-depleted: the electric field inside the sensor is increased and the free charge carriers are faster than if they were just in a depleted sensor. The collection time is consequently reduced.

The reverse bias is nevertheless limited by a breakdown voltage  $V_{BD}$  when an avalanche phenomenon is triggered. It is experimentally characterized by a sudden increase in the leakage current. Above the breakdown voltage, the sensor is extremely noisy and true signal cannot be distinguished from the avalanche current.

## 3.2 Signal formation

The previous part enlightened the P-N junction and the depletion mechanism. In the following section the signal formation, from the passage of a particle through the sensor to the signal collection by the electrode and its electronic processing will be discussed.

### 3.2.1 Electron-hole pair creation

When a charged particle crosses the depleted sensor's bulk thickness, electron hole pairs are created by ionization along its path. The number of produced pairs depend of the crossing particle energy and of the material type, the mean energy induced by this crossing follows the Bethe-Bloch distribution [15].

The amount of energy which is necessary to create a electron-hole pair in silicon is about 3.6 eV, which corresponds to the energy for moving an electron from the valence band to the conduction band at room temperature (1.1 eV), plus the excitation of a phonon to balance the crystal momentum.

In HEP experiments, as the particles crossing the sensor are highly energetic, most of the particle crossing the sensor are Minimum Ionizing Particles (MIP). The energy loss spectrum of crossing MIP signal in the silicon can be described by a Landau-Vavilov [71] distribution. The long tail is due to the possibility of energy transfers in which a  $\delta$  ray or a knock on electrons are generated [72, 73]. For thin sensors (O(200 $\mu$ m) or thinner), the signal is best described by the convolution of a Landau distribution with a gaussian distribution [74, 75]. The Most Probable Value (MPV) of such distribution is 80 electron-hole pairs per  $\mu$ m. The MPV is usually preferred to the Mean of the distribution to measure the deposited charge, as the mean is biased by the high energy transfers from  $\delta$  rays [72].

### 3.2.2 Signal development inside the sensors

Once free charge carriers are created, they will move into the sensors according to several effects: electrical drift, thermal diffusion, generation and recombination and Lorentz angle deflection; they will be described in the following section.

#### 3.2.2.1 Carriers drift

As the sensor is depleted, the charge carriers created by the passage of a charged particle crossing the sensor are going to drift towards the collecting electrode, following the electric field  $\vec{E}$ . As already stated, charge carriers in an over-depleted sensor will move faster than in a just depleted sensor. The drift is characterized by the charge carriers velocity:  $\vec{v}_e$  for the electrons and  $\vec{v}_h$  for the holes. The charge carrier velocity depends on the mobility of electrons and holes in the silicon (respectively  $\mu_e$  and  $\mu_h$ ):

$$\text{For electrons: } \vec{v}_e = -\mu_e \vec{E} \quad ; \quad \text{For holes: } \vec{v}_h = \mu_h \vec{E} \quad (3.8)$$

#### 3.2.2.2 Diffusion

In case of a gradient in the carrier concentration, an additional diffusion component has to be added to the thermal diffusion. The diffusion current per unit area of electrons/holes (respectively  $\vec{F}_e$  and  $\vec{F}_h$ ) [68] are described by:

$$\text{For electrons: } \vec{F}_e = -D_e \nabla n \quad ; \quad \text{For holes: } \vec{F}_h = -D_h \nabla p \quad (3.9)$$

with  $D_e$  and  $D_h$  the diffusion constants which can be expressed as a function of the mobility using the Einstein relation:

$$\text{For electrons: } D_e = \frac{kT}{q} \mu_e \quad ; \quad \text{For holes: } D_h = \frac{kT}{q} \mu_h \quad (3.10)$$

A typical value of  $D_e$  is  $\simeq 30 \text{ cm}^2/\text{s}$ . The diffusion spread is given by  $\sigma_{diff} = \sqrt{2Dt_{coll}}$  with  $t_{coll}$  the time travelled by the carrier until collection by the electrode. Silicon sensors are often operated cold (around  $-10^\circ\text{C}$ ), so the thermal diffusion is limited and  $\sigma_{diff}$  is of the order of few micrometers for thin sensors (thickness between 100 and 300  $\mu\text{m}$ ).

### 3.2.2.3 Generation and recombination

In Silicon, as the energy gap is quite low (1.1 eV at room temperature), the generation of holes and electrons is frequent at room temperature. The recombination is the annihilation of one electron with one hole. There are two possible recombination mechanisms:

- Direct recombination: an electron in the conduction band transit directly into a vacancy in the valence band
- Recombination through recombination centers: this is the most common mechanism in indirect semi conductors<sup>1</sup> such as silicon: holes and electrons recombine via intermediary states in the band gap. This is particularly common when the material has been irradiated, where a lot of defects have been introduced deeply in the band gap (close to the middle of the band gap). The section 3.4.2.3 will describe in detail the radiation damage.

### 3.2.2.4 Lorentz angle

If a sensor is immersed in a magnetic field, the free charge carriers will also be moved depending on the direction of the magnetic field. In the current ATLAS detector, the ID planar pixels are immersed in a solenoidal 2 T magnetic field which direction is perpendicular to the direction of the bulk thickness. The free charge carriers move in planar sensors with an angle compared to the electrical field ( $E$ ) direction called the Lorentz angle which is  $\tan\theta_L = r\mu(E)B$  with  $r$  the Hall scattering factor,  $\mu(E)$  the mobility and  $B$  the magnetic field. Before irradiation (using cosmic rays) the Lorentz angle in one ATLAS IBL pixel module is estimated to be of the order of 220 mRad [76].

## 3.2.3 Signal induction

### Ramo potential

The movement of charge carriers in the sensor creates a signal in the electrodes and the induced charge can be calculated thanks to the Ramo potential [77]: the amount of induced

---

<sup>1</sup>Electrons in an indirect semi conductor can move from the valence band to the conduction band by exchanging the band gap energy plus the energy required for the excitation of a phonon to balance the crystal momentum.

charge  $Q$  is the particle charge  $q$  multiplied by the difference between the Ramo potential  $V_{Ramo}(x)$  at its starting point ( $V_{Ramo}(x_i)$ ) and its ending point ( $V_{Ramo}(x_f)$ ).

$$Q = q((V_{Ramo}(x_i)) - (V_{Ramo}(x_f))) \quad (3.11)$$

The Ramo potential  $V_{Ramo}(x)$  can be calculated from the Shockley-Ramo theorem, which states that the current  $i$  induced on a electrode by a moving charge  $q$  is given by  $i(t) = q\vec{v} \cdot \vec{E}_{Ramo}$ , where  $\vec{v}$  is the charge carrier velocity at time  $t$  and  $\vec{E}_{Ramo} = -\nabla V_{Ramo}$ . By integrating this equation over the time of charge collection ( $t_f - t_i$ ), one can find the previous equation.

### Signal processing - FEI4 case

The ATLAS pixel sensors are bonded to the electronic front-end read out via bump-bonding (more details on the chip to sensor bonding in the pixel sensor technology section). The signal induced by the movement of charge carriers (from the MIP passage) on the electrode is digitized into Time over Threshold (ToT) [78] by the front-end chip FEI4B [46] (for IBL pixel sensors <sup>2</sup>); the FEI4B block diagram is presented in Figure 3.2. The FEI4B chip is intrinsically radiation hard as it is build in 130 nm technology. The pad which is where the charge from the sensor is collected is connected to the pixel through bump-bonding. It is followed by an injection circuit ( $V_{cal}$ ) which is used to inject charge, mimicking the passage of particles in the sensor, and to calibrate the response of the chip.

In the case of ATLAS pixels sensors [42, 43, 44], the electronics treats the signal as follow:

1. Charge amplification: Amplification step which usually implies a pre amplifier and a shaping of the signal. For the FEI4B, the preamplifier is associated with a feedback part which allow a fast shaping (return to baseline). The second amplifier provides a sufficient gain in voltage such that the signal can pass to the discriminator and be compared with a threshold value.
2. Signal discrimination: comparison with threshold value. The threshold is applied after the amplifier and its value is given as an equivalent input collected charge in units of electrons. When choosing the threshold, a compromise has to be found between a high threshold, which decreases the number of noise hits but decreases the signal efficiency as well, and a low threshold, with opposite effects.
3. Hit storage and retrieval: storage on a 4 bit ToT register for the IBL (8 bit for the other pixel layers).
4. Read-out for the events selected by the trigger logic: comparison with the trigger event identifier.

---

<sup>2</sup>The other ATLAS pixel layers are read-out by the FEI3 chip [42] which also uses a ToT mechanism to record pulse height

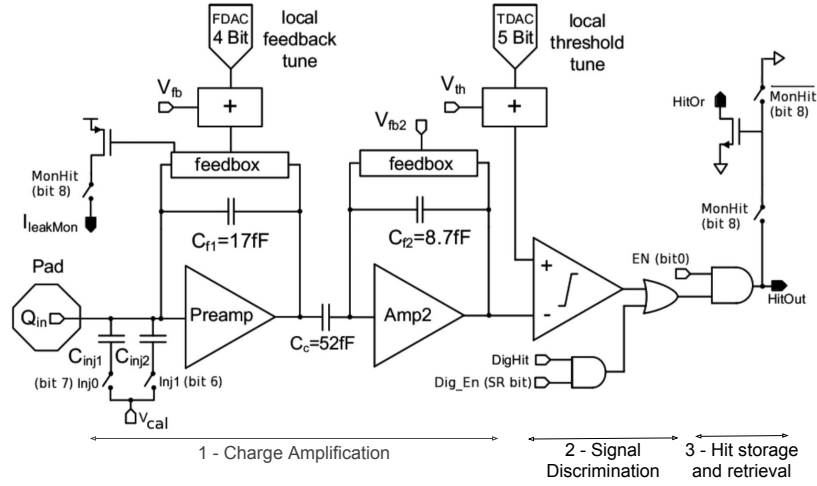


Figure 3.2 – FEI4 Block diagram of the analog processing of the signal (from [46])

### 3.3 Pixel sensors technologies

The silicon sensor processing starts with a silicon ingot which is cut with circular rotative diamond saw in few mm thick wafers. The raw material can be doped to modify its properties. It is also common to enrich silicon with oxygen, which helps to mitigate the irradiation effects of pions and protons [79]. Float Zone silicon (Float zone is a vertical crystal growth techniques which results in high purity silicon ingot) is the material of choice in HEP thanks to its purity. The wafers are then lapped down to their required thickness (hundreds of micrometers). Several lithographic steps follows, from the oxide passivation, the opening in the passivation, the high doping implantation on top of the bulk to create the PN junction and aluminum deposition to create ohmic contacts. In this section, after having briefly discussed 3D pixel sensors, a special emphasis will be put on planar pixel sensors features, exploited in the current ATLAS pixel sensors or foreseen for the ITk pixel productions. Eventually, CMOS sensors will be briefly described.

#### 3.3.1 Hybrid pixel sensors

Hybrid pixel sensors (3D or planar, see Figure 3.3) are the standard choice of pixel sensors in HEP at the moment. Hybrid refers to their property of being coupled to their electronic read out via small metallic bond, in contrast to monolithic sensors (such as CMOS sensors) whose electronics and sensors are processed on the same wafer.

Pixel sensors consists of a 2D dimensional array of small cells (pixels), which are separated one from another. The standard dimension of pixel are the tens or hundreds of micrometers (*e.g* IBL ATLAS pixels sensors pitch size is  $250\text{ }\mu\text{m} \times 50\text{ }\mu\text{m}$ ). This fine granularity ensures a good spatial resolution of the order of tens of micrometers. The tracking performance heavily relies on a good spatial resolution. Small pixel pitch assures also low occupancy per channels, small capacitance and leakage current.

The sensors are built from low doped material (few  $10^{11}$ -few  $10^{12}$  dopants per  $\text{cm}^3$ ) to ensure that they will be fully depleted at a reasonable depletion voltage ( $\sim 50\text{V}$ - $100\text{V}$  for a  $150\text{-}300\ \mu\text{m}$  thick sensor).

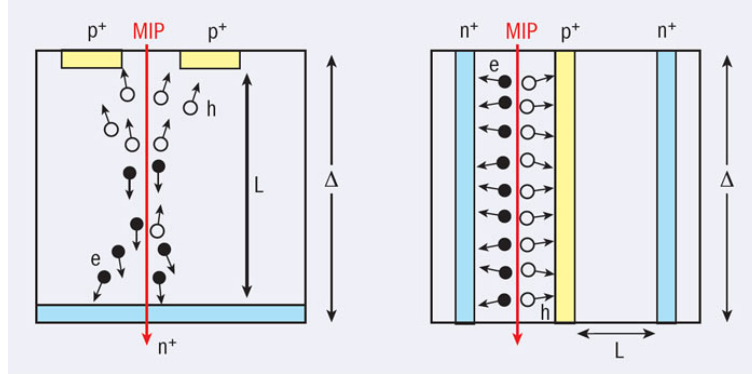


Figure 3.3 – Charge collection mechanism of an hybrid planar pixel sensor (left) and of a 3D pixel sensor (right).

### 3D pixel sensors

3D pixel sensors are composed of heavily doped pillars passing through a low-doped silicon bulk. In the IBL [43, 44] both full passing through column and partially passing through column solutions have been implemented. The IBL 3D sensors have  $250\ \mu\text{m} \times 50\ \mu\text{m}$  pitch and a thickness of  $230\ \mu\text{m}$ . The 3D technology is known to be radiation hard with the main advantage of short collection distance allowing operation with relatively low supply voltage of less than  $200\ \text{V}$  after heavy irradiation [80]. In the ATLAS barrel geometry, an other advantage of 3D sensors is that the E field and the B field are collinear, hence the Lorentz angle shift is negligible.

### Planar pixel sensors

Planar pixel sensors consist of a bulk (n-type or p-type) on top of which a segmented heavily doped n or p implant is implemented.

ATLAS planar pixel sensors are built on high-resistivity n-type silicon bulk; segmented heavily n-doped implants are formed at one surface, to collect electrons (n-on-n pixels). The bulk thickness is  $200\ \mu\text{m}$  for the IBL and  $250\ \mu\text{m}$  for the other layers. The top implant is highly segmented into pixels with dimensions of  $400\ \mu\text{m} \times 50\ \mu\text{m}$  for the outer layers and of  $250\ \mu\text{m} \times 50\ \mu\text{m}$  for the IBL.

The actual preferred design for the upgrade of the ATLAS Inner Tracker (ITk at HL-LHC) is n-on-p sensors, which are single sided sensors, biased by the backplane and more radiation hard as the bulk is of p type and hence will not undergo type inversion (inversion of n type doping into p type doping with the fluence, see dedicated part on radiation damage in silicon in the next section). The Figure 3.4 presents a schematic view of a planar pixel sensors with the different part which will be described in the following.

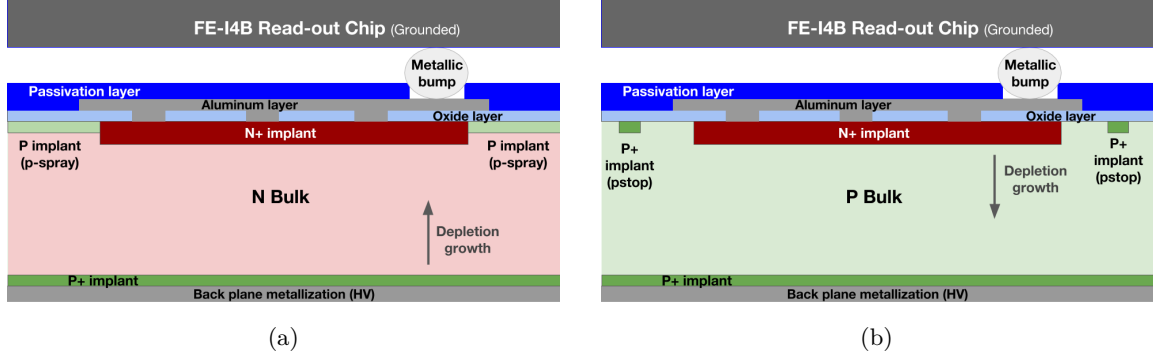


Figure 3.4 – Sections (not to scale) of an IBL-like n-in-n hybrid planar pixel sensor (a) and of an ITk-like n-in-p hybrid planar pixel sensor (b). For the IBL like module, the thickness of the sensor is  $200\text{ }\mu\text{m}$  and the pitch  $250\text{ }\mu\text{m} \times 50\text{ }\mu\text{m}$ ; For the ITk-like module, the thickness of the sensor will be around  $100\text{ }\mu\text{m}$  and the pitch will be either  $50\text{ }\mu\text{m} \times 50\text{ }\mu\text{m}$  or  $25\text{ }\mu\text{m} \times 100\text{ }\mu\text{m}$ .

### Pixel isolation

The pixel isolation prevents the formation of an electron layer just underneath the oxide which could short together two pixels; this would imply a critical loss in terms of resolution. For n-on-p and n-on-n sensors the pixel isolation can be achieved either using p-spray (low dose p-implantation on all the sensor) or p-stop (high dose p-implantation between pixels).

### Edges and guard rings

The traditional cut performed by diamond saw on the silicon wafers to separate sensors creates cracks at the sensors edges and hence defects in the lattice. This implies that a sensor can not be depleted up to its edges. Hence the use of guard rings to gradually decrease the voltage and hence the electric field at the sensor edge is necessary. One limitation to the use of guard ring as they take a considerable space, reducing the detector acceptance.

### Active edges

The active edge technology allows to reduce the insensitive area at the border of the sensor thanks to an ion etched trench which avoids the crystal damage produced by the standard mechanical dicing process (see Figure 3.5). The etched trench is afterward filled with doped poly-silicon to assure it will be equipotential with the backside. The number of guard rings can also be considerably reduced or active edge sensor can even be produced without guard rings. The use of active edges allow to reduce the un-instrumented area at the border of the sensor up to  $50\text{ }\mu\text{m}$ , as there is no need to add in this zone multiple guard rings. It has been shown that for un-irradiated sensors, the sensor lateral depletion can be extended up to a few micrometers from the sensors edge [81]. Chapters 6 and 7 will extensively present active edge sensors and their performance in beam.

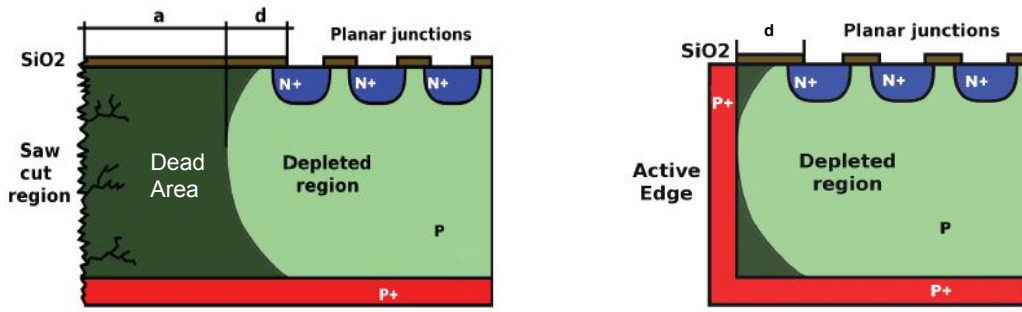


Figure 3.5 – Scheme of the edge of a sensor without Active edge (Left) and with Active edge (Right).  $a$  is the size of the dead area and  $d$  represents the distance between the last pixel and the end of the lateral depletion.

### Protection layers

The passivation is mandatory for single-sided sensors which have to be irradiated. It helps to prevent discharges between the sensor area with high voltage (edges and guard rings) and the readout-chip, which is in close proximity (of the order of  $O(10\text{ }\mu\text{m})$ ). The passivation material can be either parylene or BCB (Benzocyclobutene). With this passivation coating, the sensor can be biased at a higher voltage (of the order of 600 V for a  $O(100\text{ }\mu\text{m})$  wide sensor) to ensure high efficiency even if irradiated.

### Bonding

The connection between the sensor and the read out chip is performed via bump bonding: a bump of metal contact the opening in the passivation of the sensor on one side and the front chip on the other side. Standard bump material are indium or lead-tin alloy. The solid bumps are submit to a reflow process to melt and ensure the electrical connection between the pixel opening and the read-out chip pads.

### Biasing structures

Before bump bonding, it is necessary to test the quality of the sensor as HEP experiment are dealing with a large number of sensor. In order to bias the sensor, two kind of biasing strategies are adopted: bias dots/grids or temporary metal. The punch through mechanism [69] is exploited by the bias dots and grids approach; it consists in adding an additional biasing structure on one corner of each pixels, the punch-through dot. The punch through dot is connected to a bias rail, which is a metal layer running across all the inter-pixel area. The bias rail is kept at ground, which is transmitted to the punch through and consequently to the implant via punch-through mechanism [69]. The drawbacks of such approach is that the addition of a punch through dot usually degrades the performance of the sensor in terms of hit efficiency in the punch-through region. The temporary metal approach consist in shorting all pixels of a column together thanks to a temporary metal line. The temporary metal line is afterward removed, via chemical etching. The hit efficiency is then more homogeneous as



no permanent structures are present after bump bonding. Biasing structures options will be detailed in Chapters 6 and 7.

### 3.3.2 Monolithic pixel sensors

CMOS pixels sensors are monolithic sensors: the sensor and the electronics are processed on the same wafer, which is an advantage compared to hybrid sensors which have to deal with an additional bump bonding process and more material which spoils the spatial resolution due to the multiple scattering effect (see Section 7.2.3). CMOS sensors are widely used in the industry and High resistivity CMOS are especially interesting candidates for trackers at future colliders even if they have not demonstrated at the moment the level of radiation hardness of hybrid pixel sensors [43].

## 3.4 Radiation damage effects in silicon

Silicon detectors are extensively used in HEP experiments, especially in the LHC experiments which have to deal with a large number of collisions. In terms of the detector, the important flux of particles crossing the sensors (received fluence of the order of  $10^{14}$  to  $10^{16}$   $n_{eq}/cm^2$  for ATLAS during LHC and extrapolated for HL-LHC data taking periods) provokes damages inside the silicon lattice. These radiation-induced microscopic modifications imply some macroscopic effects at the sensor level which have to be taken into account to enable sensors to reach their best performance. In the following a description of the radiation induced microscopic alteration of the silicon [82] will be followed by a section on the observed macroscopic effects.

### 3.4.1 Microscopic defects in silicon

Radiation produces damages in the silicon bulk, at the surface and at the interface between the silicon and the oxide. Surface defects are linked to electronics and can be mitigated in sensor by the use of surface isolation (p-spray or p-stop), to prevent accumulation of electron in the oxide layers. In the following, radiation induced damages in the bulk will be studied.

#### 3.4.1.1 Defects overview

When an incoming particle provokes a collision with one Silicon atom in the lattice, the displaced atom is considered as a microscopic radiation damage and is called an interstitial defect. The hole left by the displaced atom is called a vacancy. A vacancy and an adjacent interstitial site in interaction form a Frenkel defect pair.

Depending on the energy and type of the impinging particles, the defects can be point defects (vacancy or interstitial defects) or clusters of defects, *i.e.* a combination of multiple point defects. In the band gap, the point defects act as intermediate states which can be charged and consequently influence the effective doping concentration  $N_{eff}$ .

The Figure 3.6 shows an overview of the various defects in Silicon with known impact on the detector performance. For comparison the states induced by the Phosphorus and Boron doping are shown; they are much closer respectively to the conduction and valence band.

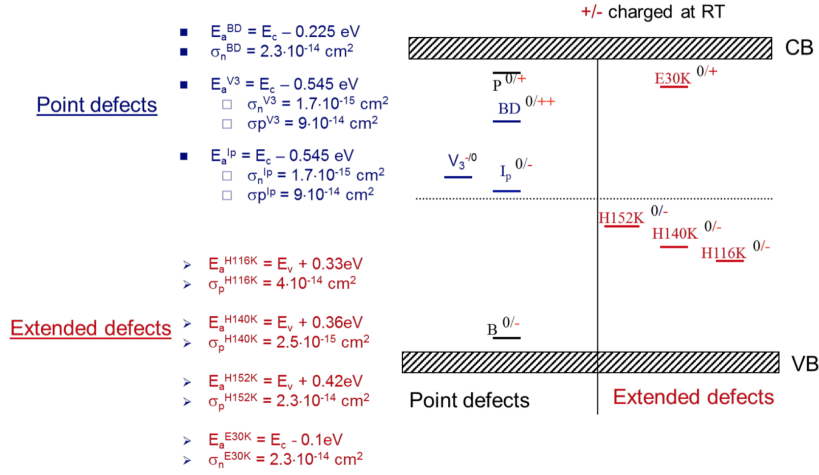


Figure 3.6 – Defect overview from [83]. The +/– legend indicates if the defect is charged at room temperature. Contributions of the point defects are represented in blue and cluster contributions (extended defects) are represented in red.

### 3.4.1.2 Non Ionizing Energy Loss (NIEL)

The defects produced by radiation inside the silicon bulk depends of the type of particles and their energy. The first challenge towards an understanding of the behavior of irradiated sensor is first to find an accommodating way to deal with this various contributions, to be able to compare and quantify the damage induced by this defects in the silicon crystal. It can be achieved using the Non Ionizing Energy Loss (NIEL) hypothesis [84]: all the defects, whatever their particles types or energy, can be scaled/normalized on a common scale. The NIEL fluence is expressed in MeVmb or in the equivalent of neutrons of 1 MeV. The Figure 3.7 represents the NIEL cross section for neutrons, pions, electrons and protons over an energy range ranging from 100 eV to 10 GeV.

### 3.4.2 Macroscopic impact of radiation damages in silicon

The defects created in the bulk by radiation alters the structure of the Silicon and also the macroscopic behavior of the sensor. The macroscopic impact of radiation damage in silicon is of three types: increase of the leakage current, change in the operational bias voltage and

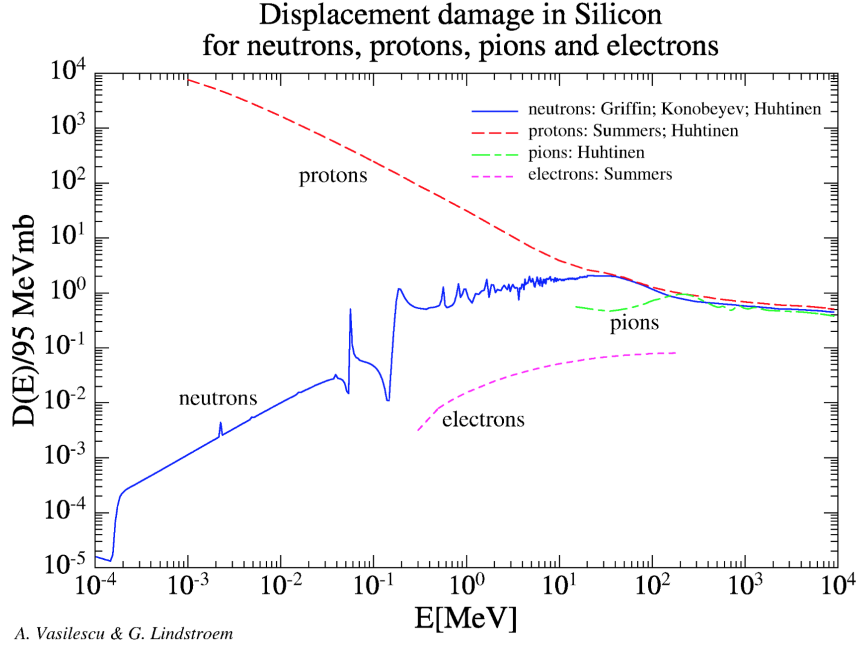


Figure 3.7 – Displacement damage in Silicon for different particles as a function of their energy [84].

decrease of the charge collection efficiency due to the charge trapping phenomenon. These three effects and their intensity depends of the amount of fluence the sensor has been exposed to, but also on the temperature and on time due to the annealing phenomena, which will be described in the next paragraph.

### Annealing

The thermal history of the sensor has to be taken into account as point defects can move at room temperature: they can annihilate with an associated vacancy/interstitial site, or combine with other defects (creating di-vacancy). At high temperature, a dissociation phenomenon, the decomposition of a multiple defect in its subparts (e.g di-vacancy decomposed into two vacancies) can also happen [85]. The evolution of defect concentration with temperature is called annealing. The beneficial annealing consist of a decrease of the effective doping concentration after stopping the exposure to particle fluence. Such phenomenon is considerably slowed down at low temperature (around or below 0°C) and is then insignificant during operational phases when the sensor is cooled down to -10°C or less. Nevertheless, the interesting property of beneficial annealing can be exploited after operational phases (for example during winter shutdowns in ATLAS) to diminish the effective concentration of defects. A standard beneficial annealing procedure consist in heating the sensor at 60°C during 80 minutes [85]. For longer time scale, the opposite trend, namely reverse annealing is observed: the effective doping concentration increases.

### 3.4.2.1 Leakage current

The increase of leakage current  $I_{leak}$  is a characteristic effect of radiation damage. It is more emphasized by close to middle gap defects and have for consequences to increase the noise and as it heats more the sensor, it increases the power consumption, hence the need to cool down the sensor to reduce the leakage current.

The leakage current increase  $\Delta I$  is dependent of the fluence  $\Phi$ , the temperature and the time (via annealing processes):

$$\Delta I(\Phi, T, t) = I(\Phi, T, t) - I_0 = \alpha(t, T) \mathcal{V}_{dep} \Phi \quad (3.12)$$

with  $\mathcal{V}_{dep}$  the depleted volume,  $\alpha(t, T)$  the current related damage rate which typical value after an annealing of 80 minutes at 60°C is  $\alpha \sim 4 \times 10^{-17} A/cm$  [85] [79]. As stated, one way to mitigate the leakage current increase is to keep the sensor cold.

### 3.4.2.2 Change in operational depletion voltage - Effective doping concentration

As already indicated in the microscopic defects overview, the defects can be charged and consequently can alter the space charge distribution and deform the electric field inside the sensor.

The depletion voltage  $V_{dep}$  is highly dependent of the fluence:

$$V_{dep} = \frac{q|Neff(\Phi)|d^2}{2\epsilon\epsilon_0} \quad (3.13)$$

where  $|Neff(\Phi)|$  is the doping concentration which depends on the fluence,  $d$  is the thickness of the sensor,  $\epsilon$  and  $\epsilon_0$  the permittivity of silicon and the vacuum.

In case of n-type bulk, the exposure to fluence of the order of  $10^{13} - 10^{14} \text{ n}_{eq}/cm^2$  [85] leads to a type inversion of the n-type bulk into a p-type bulk and to a steady increase of the full depletion voltage after type inversion. This is presented in Figure 3.8. The ATLAS IBL underwent type inversion in 2015: before inversion, depletion grows from the backside towards the pixel implant; after inversion, the depletion grows from the pixel implant to the backside. If the bulk is of negative space charge, the fluence exposure will be accompanied by an increase in the depletion voltage.

### 3.4.2.3 Charge trapping

Due to the presence of defects in the bulk resulting in the creation of new states into the band gap, electrons or holes can be trapped in trapping defect centers. As a result a loss of charge collection efficiency with the fluence is observed. The trapping time  $\tau_{trap}$

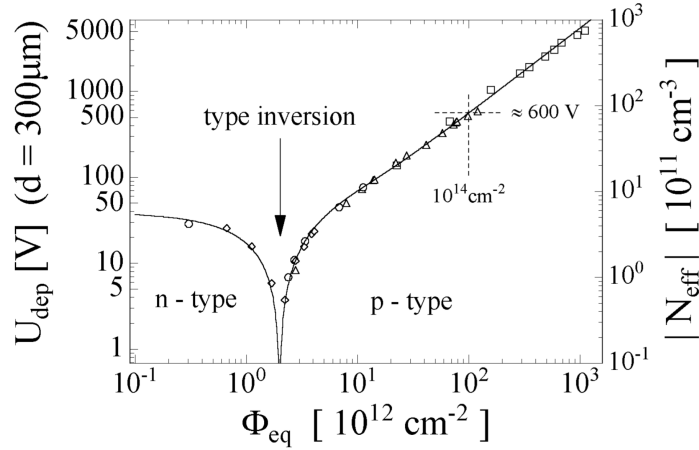


Figure 3.8 – Type inversion of a n-type bulk into a p-type bulk [85]

is the typical time after which a generated charge carriers can be trapped in a trapping center. It is inversely proportional to the fluence ( $\Phi$ ):  $\tau_{trap} = \beta\Phi^{-1}$ , with  $\beta$  the trapping constant which value is higher for holes ( $\beta_h = 5$  to  $8 \times 10^{-16} \text{ cm}^2/\text{ns}$ ) compared to electrons ( $\beta_e = 4$  to  $6 \times 10^{-16} \text{ cm}^2/\text{ns}$ ). The trapping constant  $\beta$  also has an annealing dependency, as described in [86].

#### 3.4.2.4 Conclusions on radiation damage in silicon

The noticeable impact of radiation damage on silicon sensor implies that it is of crucial importance to understand and incorporate radiation damage in the event simulation chain of current HEP experiment. The LHC experiment (ATLAS, CMS and LHCb[87]; see [88]) are currently trying to implement radiation damage in their Monte Carlo simulation to model the phenomenon. The Chapter 4 will describe the ongoing effort in the ATLAS collaboration.

## Conclusions

In this Chapter, the silicon pixel detectors technology used in the current ATLAS ID and foreseen for the ATLAS ITk have been described as well as the underlying physics processes associated. Among those, the radiation damage impact on sensors has been discussed. In the next chapter, the implementation of radiation damage in the ATLAS simulation chain will be documented. Chapter 6 and 7 will present in details planar pixel sensors production designed to be part of the ATLAS ITk at HL-LHC.



## Chapter 4

# ATLAS radiation damage digitizer

### Contents

---

<b>4.1</b>	<b>Modeling radiation damage</b>	<b>60</b>
4.1.1	Determination of the fluence	61
4.1.2	Electric fields maps	61
4.1.3	Diffusion study: Cluster size dependency on temperature and bias voltage: testbeam results	68
4.1.4	Charge chunking and trapping	69
4.1.5	Ramo potential and Induced Charge	70
<b>4.2</b>	<b>Validation of the model and perspectives</b>	<b>71</b>
4.2.1	Validation of the standalone framework	71
4.2.2	Validation of the Athena framework	72
4.2.3	Cluster properties	72
4.2.4	Charge collection efficiency	78
4.2.5	Tracking properties	80
<b>4.3</b>	<b>Conclusions and perspectives</b>	<b>85</b>

---

In this chapter the ATLAS radiation damage digitizer effort [89, 90] will be documented. The digitization step of the ATLAS Monte Carlo (MC) simulation consists in transforming energy deposition from simulated charged particles in the detector into digital signals recorded by the detector front-end and sent to the detector readout system. In what follows, the modifications to include the radiation induced effects, in particular the signal loss, to the current ATLAS digitizer will be presented.

In a first part, a brief overview and description of the radiation damage digitizer workflow will be given. The next sections will contain the results of the various studies in which I was involved concerning the digitizer: validation of the radiation damage digitizer in the ATLAS software framework, production of electric field TCAD maps and systematics variations study and study of the charge sharing over a wide range of bias voltage and temperatures.

Another study based on the evolution of the charge collection efficiency will be presented in Chapter 7 as it relies on ITk testbeam data.

## 4.1 Modeling radiation damage

Modeling radiation damage in pixel sensors, partially published in [90], requires various inputs and steps which are going to be described in the following and are schematized in Figure 4.1.

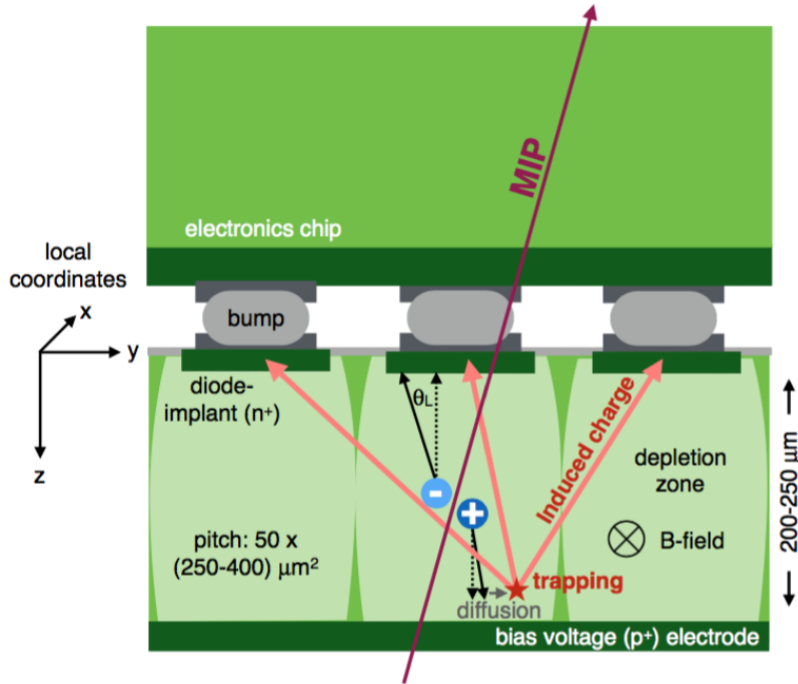


Figure 4.1 – Schematic diagram of the radiation damage digitizer physics processes (from [89]). A planar pixel sensor (either IBL planar or B-Layer, Layer1 or Layer 2 planar pixel sensor) bump-bonded to its electronics read-out chip is presented. A crossing MIP creates electron hole pairs along its paths which are moving according to various contributions including drift along the electric field lines, deflection by the Lorentz angle caused by the magnetic field, thermal diffusion and charge trapping implied by radiation damaged induced states in the silicon bulk. Eventually, the remaining induced charge is digitized by the electronics and converted into Time-over-Threshold (ToT).

Prior to the digitization it is necessary to collect information on the detector geometry and the fluence to which the detector was exposed. Then the input to the digitizer is an energy deposition in the sensor corresponding to the crossing of a charged particle (*e.g.* a Minimum Ionizing Particle, MIP, from GEANT4 [66]). Another important input is the electric field map expected in such sensors after irradiation: the electrical field is predicted using Technology Computed Aided Design (TCAD) simulation, while the Hamburg model [85] is used to account for annealing.



Charges then undergo the various dynamical components: drift, diffusion and deflection by the magnetic field according to the Lorentz angle ( $\theta_L$ ). The diffusion is not yet a part of the radiation damage digitizer, but some studies are ongoing to understand better its behavior at high voltage, it will be presented in Section 4.1.3. The charge can also be trapped if the sensor was exposed to some fluence.

Another ingredient in the digitization is the chunking of charges as it is computationally too heavy to drift each electron and hole. Finally, the induced charge including the component from the trapped chunks is evaluated using a Ramo weighting potential, including neighboring pixels. The charge is then converted into Time-over-Threshold [78] and clusters are formed by grouping neighboring pixels.

#### 4.1.1 Determination of the fluence

The fluence is determined from the integrated luminosity. The FLUKA framework [91, 92, 93], together with Pythia 8 [94, 95, 96] based simulations, is used to estimate the conversion factor between integrated luminosity and the fluence. The fluence systematic uncertainties are evaluated by comparing the leakage current extracted from the Hamburg model prediction and the real leakage current which is precisely measured. This procedure results in a 15% uncertainty on the fluence.

#### 4.1.2 Electric fields maps

One of the main input of the digitizer is the electric field map in the sensor, which strongly depends on the fluence and on the operational bias voltage. In this section the simulated electric field maps of IBL planar sensor at fluences from 0 to  $5 \times 10^{14}$   $\text{n}_{\text{eq}}/\text{cm}^2$  are documented.

The radiation-induced states in the silicon band gap alter the electric field in the bulk. Therefore it is necessary to produce look-up tables of the electric field both for ATLAS planar and 3D sensors under various fluence and bias voltages conditions. Those simulations are done using the TCAD software Silvaco [97] for planar sensors and Synopsis [98] for 3D sensors. Due to geometrical symmetries of the pixel cells it is possible to simulate only a part of it. Radiation damage TCAD models have always been developed targeting a specific bulk-type. The use of a model intended for n-bulk on a simulated p-bulk structure leads to incorrect results. The reason is that shallow dopants are not removed/inactivated in TCAD simulation so the traps concentration is adjusted to reproduce the measured data, which is clearly different for two irradiated sensors that differ only in the bulk doping type. Since IBL and Pixel planar sensors are built on n-bulk and IBL 3D on p-bulk, the TCAD radiation damage models used for the two have to be different.

The charge collection mechanism is different for planar and 3D sensors, so that two different setups are implemented which are going to be discussed in what follows.

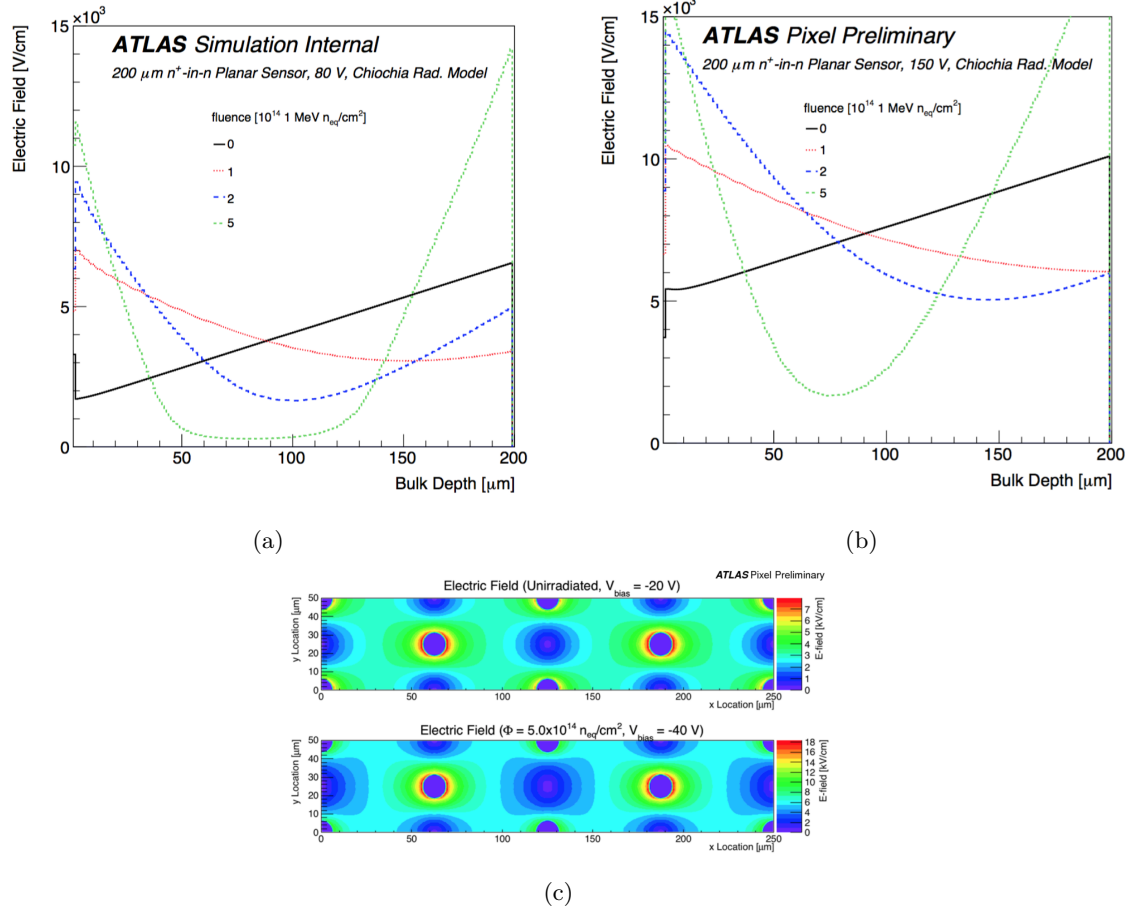


Figure 4.2 – Electrical field in planar sensors (a) at 80 V, (b) at 150 V and 3D pixel sensors (c). For 3D sensor, the top plot is the electrical field before irradiation at 20 V and the bottom plot after receiving a fluence of  $5 \times 10^{14}$   $n_{\text{eq}}/\text{cm}^2$  at 40 V. For planar pixel sensors, 4 fluence configurations are investigated: un-irradiated (black line), irradiated at  $1 \times 10^{14}$   $n_{\text{eq}}/\text{cm}^2$  (red),  $2 \times 10^{14}$   $n_{\text{eq}}/\text{cm}^2$  (blue),  $5 \times 10^{14}$   $n_{\text{eq}}/\text{cm}^2$  (green). From [89].

**3D sensors:** Unlike planar pixel sensors, electrons and holes in 3D sensors drift laterally and not through the bulk depth. Radiation damage effects for the 3D sensor are implemented in the Perugia [99] model with the Synopsys [98] TCAD package. Just 1/8 of the sensor is simulated to take advantage of the symmetry within the pixel. In the Perugia model there are two acceptors and one donor defects states, which activation energies are respectively  $E_c - 0.42$  eV,  $E_c - 0.46$  eV, and  $E_v + 0.36$  eV (with  $E_c$  the energy of conduction band and  $E_v$  the energy of respectively the valence band). The field distribution in the XY plane is presented in the Figure 4.2 (c) for one pixel cell of an un-irradiated sensor (top) and irradiated at a fluence of  $5 \times 10^{14}$  n<sub>eq</sub>/cm<sup>2</sup> at the bottom. The n<sup>+</sup> and p<sup>+</sup> implants are regions of no field due to their large doping.

**Planar sensors:** The model used to describe the electric field in planar sensor is the Chiochia model [100] which contains two defect states: one acceptor trap and one donor trap with activation energies set to respectively  $E_c - 0.52$  eV and  $E_v + 0.48$  eV. Other parameter values of importance for this model, such as the capture cross section for acceptors and donors for holes and electrons, and the donor and acceptor concentration are based on the Chiochia model ones [100] and are tabulated in Table 4.1.

In details, the parameters of this model are:

- Acceptor/Donor electrons/holes capture cross sections refers in the following respectively by  $\sigma_e^A$ ,  $\sigma_h^A$ ,  $\sigma_e^D$ ,  $\sigma_h^D$  which units are  $\text{cm}^2$ .
- Acceptor/Donor effective concentration (respectively  $N_T^A$  and  $N_T^D$ , which units are  $\text{cm}^{-3}$ ).
- Acceptor/Donor trap energy ( $E_T^A$  and  $E_T^D$ ).

Figure 4.2 (a) shows a field profile of one IBL planar pixel sensor at 80 V simulated at four different fluences. When the sensor is un-irradiated, the field is quasi linear: the depletion grows from the back side (where one can find the maximum value of the field) toward the pixel implant. After type inversion, the field maximum is on the opposite side of the sensor. With increasing fluence, there is a minimum in the electric field in the center of the sensor. For a fluence of  $5 \times 10^{14}$  n<sub>eq</sub>/cm<sup>2</sup> at 80 V (under-depletion regime), this minimum is broad and occupies nearly a third of the sensor.

As no uncertainties are given in the Chiochia model, we decided to add a 10% uncertainty on the effective concentration ( $N_T^A$  and  $N_T^D$ ) and the capture cross sections ( $\sigma_e^A$ ,  $\sigma_h^A$ ,  $\sigma_e^D$ ,  $\sigma_h^D$ ). An uncertainty on the trap energy of 0.4% is set corresponding to 10% of the thermal energy  $kT$ . This value is compatible with the IBL temperature variations: the IBL have changed frequently of operational temperature, from  $-15^\circ\text{C}$  to  $20^\circ\text{C}$ , as the simulations were performed for a temperature of  $-10^\circ\text{C}$ , the variation in thermal energy (simulation) is compatible with the variation of temperature (data). The Table 4.1, compiles the various values used, as well as the magnitude of parameters variation.

Table 4.1 – Summary of the Chiochia model parameters (from [100]) and relative uncertainties

<b>Fluence</b> ( $10^{14} \text{ n}_{\text{eq}}/\text{cm}^2$ )	$E_T^A$ (eV) $\pm 0.4\%$	$E_T^D$ (eV) $\pm 0.4\%$	$N_A$ ( $10^{14} \text{ cm}^{-3}$ ) $\pm 10\%$	$N_D$ ( $10^{14} \text{ cm}^{-3}$ ) $\pm 10\%$	$\sigma_e^{A,D} \ \& \ \sigma_h^D$ ( $10^{-15} \text{ cm}^2$ ) $\pm 10\%$	$\sigma_h^A$ ( $10^{-15} \text{ cm}^2$ ) $\pm 10\%$
<b>1</b>	$E_C - 0.52 \text{ eV}$	$E_V + 0.48 \text{ eV}$	3.6	5	6.60	1.65
<b>2</b>			6.8	10		
<b>5</b>			14	34		

In the following, I will present simulations at  $2 \times 10^{14} \text{ n}_{\text{eq}}/\text{cm}^2$  for a bias voltage of 80 V and 150 V. Electric field maps have been computed to emulate the conditions in terms of bias voltage (up to 400 V) and fluence (up to  $8.1 \times 10^{14} \text{ n}_{\text{eq}}/\text{cm}^2$ ) of the four planar pixel layers for various Run2 conditions milestones (up to the predictions for the end of 2018). The various results of the digitizer over the Run2 range of fluence and bias voltage are presented in the next section.

The Figure 4.3 presents the electric field maps and its variation for a fluence of  $2 \times 10^{14} \text{ n}_{\text{eq}}/\text{cm}^2$ . It can be seen that the electric field is highly sensitive to variations in the defect energy, especially to the variations in the acceptor energy ((a) and (b)), the electric field value at the surface of the sensor varies between 7000 V/cm to 14000 V/cm at 80 V (a) and between 12000 V/cm and 20000 V/cm at 150 V (b). The variation in donor energy is less important than the one for acceptor but is still significant: at 80 V and at the surface of the sensor, the electric field varies from 8000 to 12500 V/cm.

The Figure 4.4 presents the electric field in the sensor depth with various variation in the acceptor/donor capture cross sections for electrons/holes. As for the energy, a variation on the acceptor capture cross section seems to have a bigger impact than a variation of the donor cross section. Globally, for both bias voltages, the impact of the variations on the capture cross section is lower than for the energy variations. The variation for holes/electrons is comparable.

The Figure 4.5 presents the electric field in the sensor depth with various variation in the acceptor/donor concentrations. As for the energy and the capture cross sections, a variation on the acceptor concentrations have a bigger impact than a variation on the donor concentration. The variation impact is globally slightly bigger than the variations on capture cross sections and lower than the impact of trap energy variations.

In conclusion, one can say that:

- the electric field is highly sensitive to the variations in the trap energy, moderately sensitive to the defect concentration variation and slightly sensitive to the variation in capture cross sections.

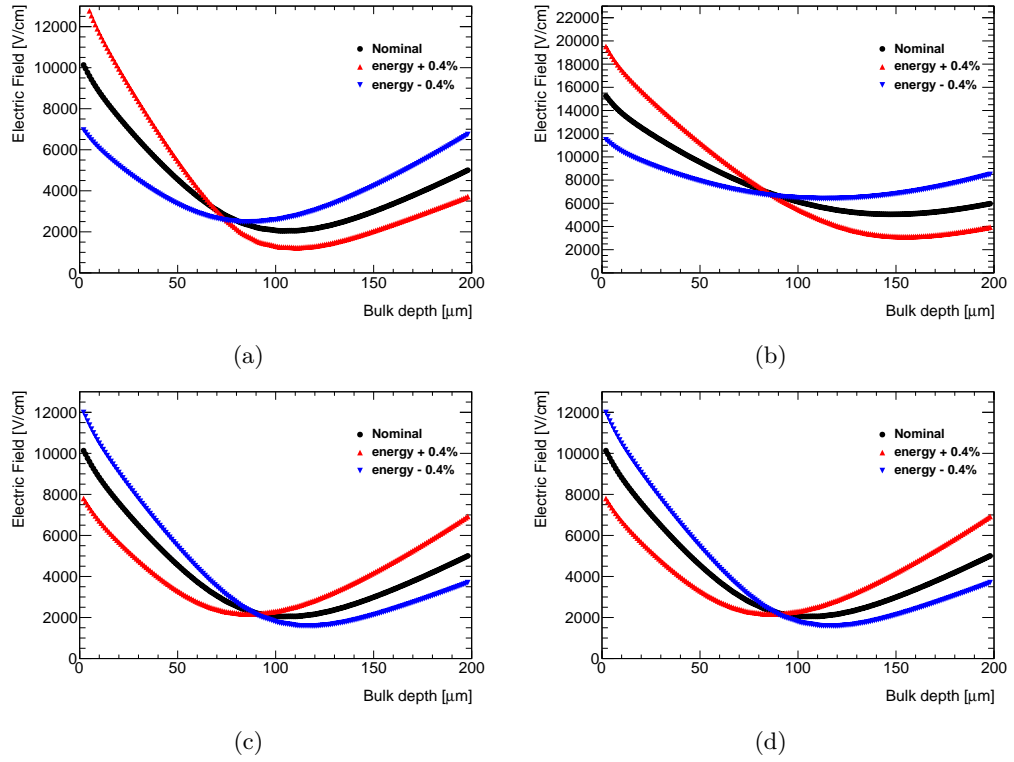


Figure 4.3 – TCAD Electric field maps vs sensor bulk depth. A variation of the defect energy by  $\pm 0.4\%$  is presented for a fluence of  $\Phi = 2 \times 10^{14} \text{ n}_{\text{eq}}/\text{cm}^2$ . Plots a and b (respectively c and d) shows the evolution of the acceptor (donor) energy. The bias voltage is either 80 V (a and c) or 150 V (b and d).

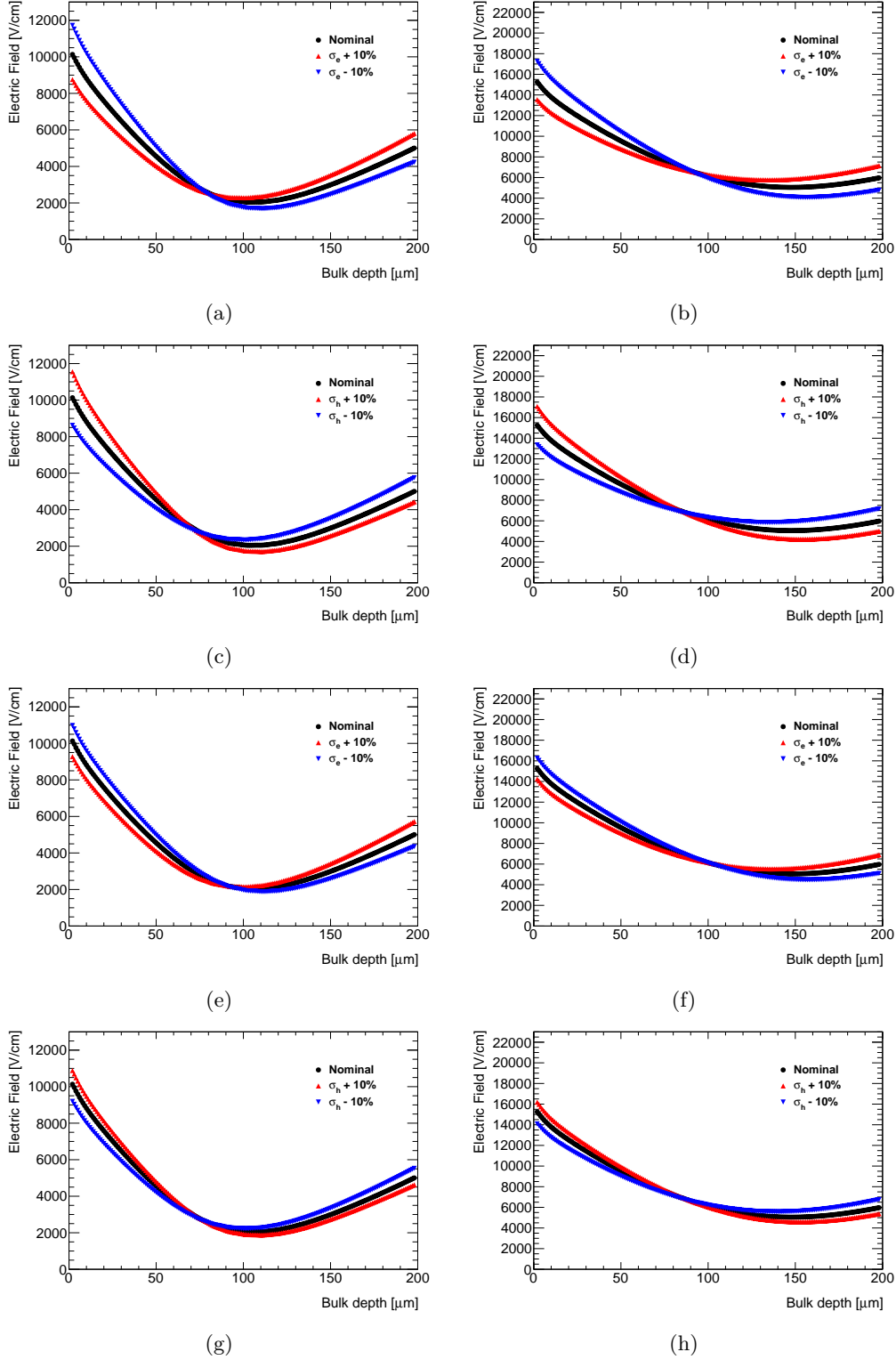


Figure 4.4 – TCAD Electric field maps vs sensor bulk depth. A variation of the electron and hole capture cross sections  $\sigma_{e,h}$  by  $\pm 10\%$  is presented for a fluence of  $\Phi = 2 \times 10^{14} \text{ n}_{\text{eq}}/\text{cm}^2$ . Plots a, b, c, and d (respectively e, f, g and h) show the evolution of the acceptor (donor) capture cross sections. The capture cross sections for electrons (respectively holes) are presented in Figure a, b, e and f (respectively c, d, g and h). The bias voltage is either 80 V (a, c, e and g) or 150 V (b, d, f and h).

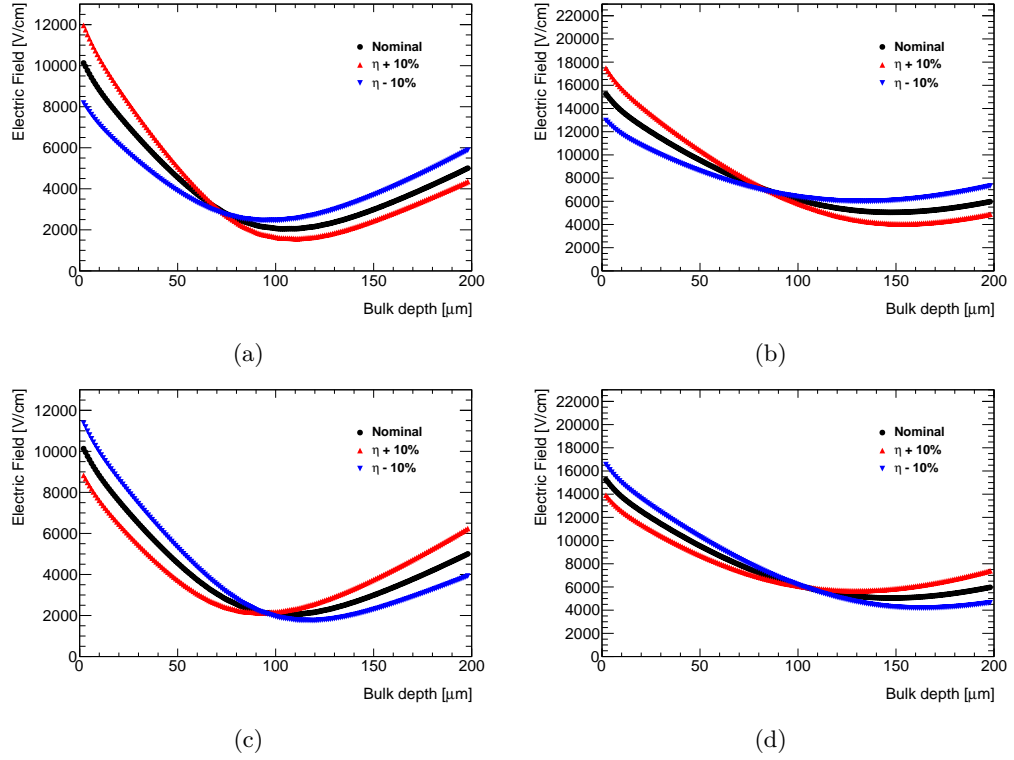


Figure 4.5 – TCAD Electric field maps vs sensor bulk depth. A variation of the acceptor/donor concentration by  $\pm 10\%$  is presented for a fluence of  $\Phi = 2 \times 10^{14} \text{ neq/cm}^2$ . Plots a and b (respectively c and d) show the evolution of the acceptor(donor) concentrations. The bias voltage is either 80 V (a and c) or 150 V (b and d).

- a variation on the acceptor observables results in a larger variation than for donor ones. It can be explained by the fact that acceptor is closer to intrinsic energy level than donor one (see Table 4.1).

#### 4.1.3 Diffusion study: Cluster size dependency on temperature and bias voltage: testbeam results

In this section, the evolution of the cluster size as a function of the voltage for several temperatures will be studied. A testbeam was carried out in the CERN North Area with a 120 GeV/c pions beam, orthogonal to the tested sensor. The purpose of this testbeam was to have a better description of diffusion, especially its dependency on bias voltage and temperature. The amount of data was not sufficient to conclude on the diffusion behavior but this testbeam resulted in an interesting study on the cluster size dependency on temperatures and bias voltage. A 200  $\mu\text{m}$  un-irradiated n-in-p sensor was tested at five different temperatures ( $-20^\circ\text{C}$ ,  $-10^\circ\text{C}$ ,  $0^\circ\text{C}$ ,  $10^\circ\text{C}$ ,  $20^\circ\text{C}$ ) and 12 different voltages (between 20 V and 450 V which was close to the breakdown voltage). The sensor depletion voltage was 60 V.

The Figure 4.6 presents the mean cluster size vs the bias voltage. Cluster refers to the group of pixels which have jointly been triggered by the passage of a particle through the sensor, the cluster size refers to the number of pixels involved. The fact that several pixels can trigger for one events is due to the charge sharing phenomenon. At 20 V, 60 V, 200 V and 450 V, a pixel charge sharing map (presenting the probability that adjacent pixels have triggered with respect to the hit position) is added. The pixel charge sharing map presents the cluster size in various part of a pixel, results from all the pixels are superimposed in one map. It illustrates the charge sharing between two pixels: if the crossing of the particle with the sensor happens close to the border of the pixel, the probability of charge sharing with neighboring pixel increases, as well as the mean cluster size.

From Figure 4.6, over the investigated temperature range, the cluster size variation is small (maximum variation in cluster size of 4% between  $-20^\circ\text{C}$  and  $20^\circ\text{C}$ ). *A contrario*, the voltage dependency is really clear. The mean cluster size increases from 1.35 to 1.62 between 20 V and 60 V which is the depletion voltage. Before the depletion, the depleted volume does not reach the bottom of the sensor and the signal is small. At the depletion voltage, the mean cluster size is maximum. Going to the over depletion regime, the electrical field is more intense and then the charge carrier drift faster, diffusion spread is smaller and then the mean cluster size decreases.

A comparison with simulations (in preparation) could lead to a better understanding and implementation of the diffusion inside a sensor and its evolution over a wide range of bias voltages and temperatures.



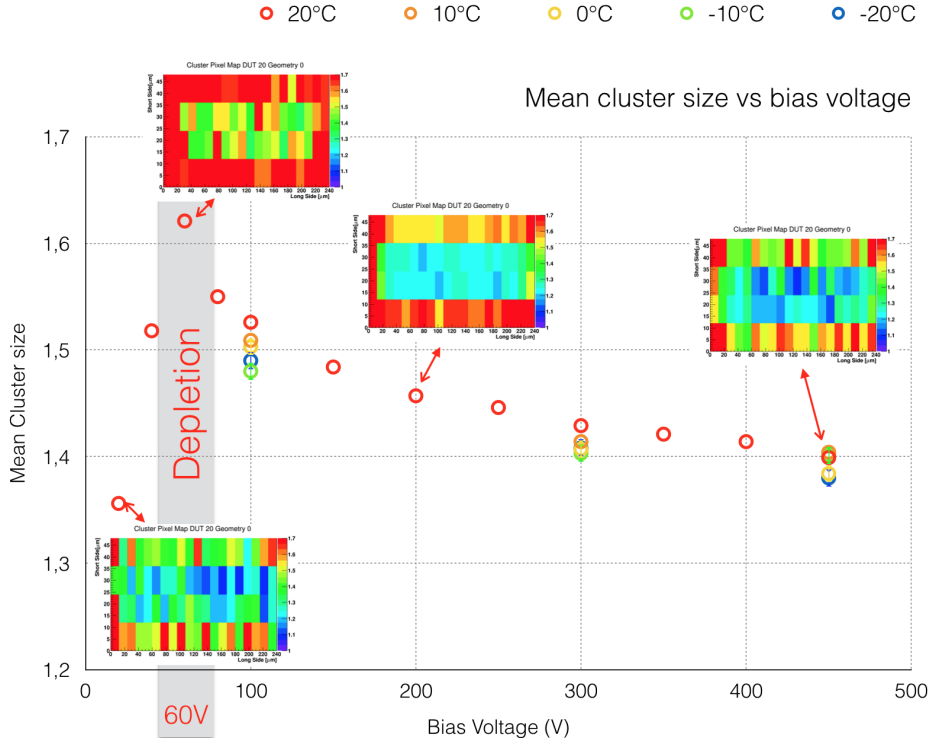


Figure 4.6 – Summary plot for radiation damage testbeam

#### 4.1.4 Charge chunking and trapping

In the pixel sensor, approximately 80 electron-hole pairs are generated per micron from the passage of a charged particle. The digitization of so many charge carriers is computationally too heavy, so charge carriers are clustered in chunks. Even though the mean cluster charge is similar if one considers charge chunks or single free charge carriers, the fluctuations in the induced charge can be over-estimated. Therefore the fluctuations have to be unsmeared: the mean collected charge  $Q$  is also computed and the charge  $Q$  is replaced by  $Q \rightarrow \langle Q \rangle + \frac{1}{\sqrt{n}}(Q - \langle Q \rangle)$  has the correct fluctuation size,  $n$  being the number of fundamental charges represented by one chunk. Figure 4.7 shows the distribution of charge collection versus time-to-electrode and illustrates the effect of the unsmeared. The time-to-electrode is the time between the generation of a charge carrier and its collection by the electrode. For planar sensors, as the electric field is nearly independent of  $x$  and  $y$ , the time-to-electrode value is obtained by the one dimensional integral:  $t = \int_{z_{initial}}^{z_{final}} \frac{dz}{r\mu(E)E}$ , where  $z_{initial}$  is the generation position,  $z_{final}$  the location of the electrode,  $r$  the Hall scattering factor with  $r \simeq 1$ ,  $E$  the electric field and  $\mu(E)$  the mobility (whose value is different for holes and electrons). The trapping time is the characteristic time a charge carrier will travel before it is trapped, it has different values for holes and electrons (see Section 3.4.2.3). In the digitizer, if the time-to-electrode is longer than the trapping time, the charge chunk is declared trapped. The left plot of Figure 4.7 is for 10 chunks, the middle one for 100 and the right one for 1000. The blue and green contributions are respectively collected and induced charge, before the corrections; the red and pink contributions are collected and induced charge after the

unsmearing. The effect of unsmearing is really striking in the left and middle plots, where the distribution is much broader before the corrections.

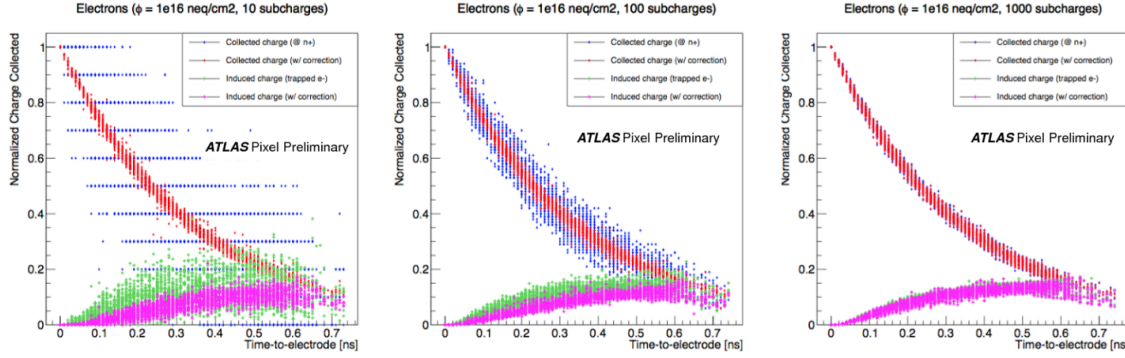


Figure 4.7 – Charge chunking unsmearing. This figure shows the normalized charge collected vs time to electrode. The red and blue curve are the collected charge respectively with/without unsmearing. The pink and green curve are the induced charge by trapped carriers respectively with/without unsmearing. The three plots are considering different numbers of sub-charges (chunks): the left plot shows results for 10 chunks, the middle one for 100 chunks and the right one for 1000 chunks.

#### 4.1.5 Ramo potential and Induced Charge

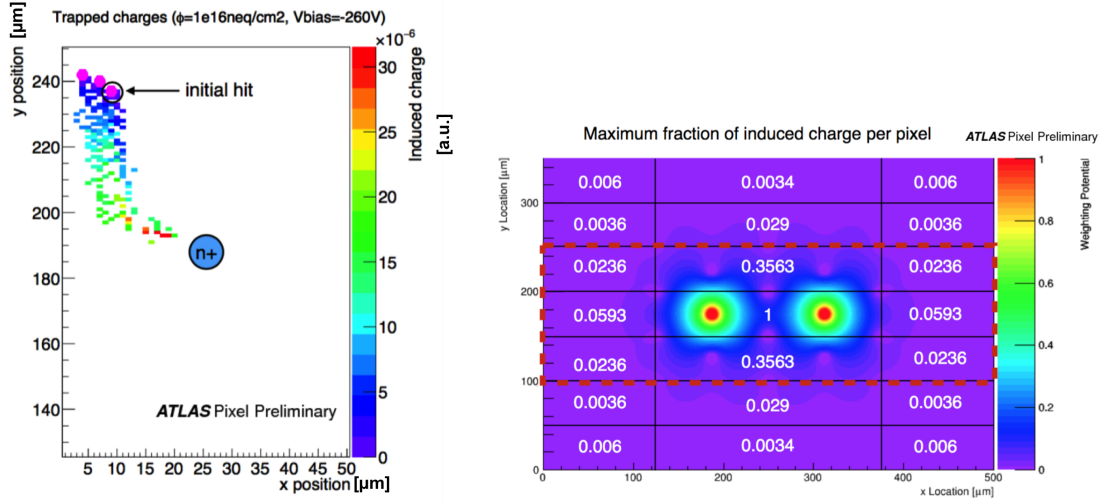


Figure 4.8 – Trapping effect on induced charge in a 3D sensor exposed at a fluence of  $1 \times 10^{16} \text{ neq/cm}^2$  and biased at 260 V. The left plot shows the induced charge at trap location for three electrons created in the upper half part. The right plot is a 2D map in the XY plane of the weighting potential for two simulated 3D columns.

Even if charges are trapped, they still induce a signal which can be evaluated using the Ramo potential [77]. The left part of Figure 4.8 shows this effect: three electrons are created in the up left corner and then drift following electric field lines. At some point they are trapped

and induce a charge as shown in the Figure 4.8. The right part of Figure 4.8 shows the Ramo potential value in the XY plane for two simulated 3D electrodes.

## 4.2 Validation of the model and perspectives

### 4.2.1 Validation of the standalone framework

The accuracy of the radiation damage model can be determined by comparing the charge collection efficiency between collision data and simulated data from our model. Figure 4.9 shows a comparison of the charge collection efficiency between IBL data collected during 2015 and 2016, with a bias Voltage of 80 V, 150 V and 350 V and simulated datasets, based on the new digitizer, implemented in the AllPix [101] framework.

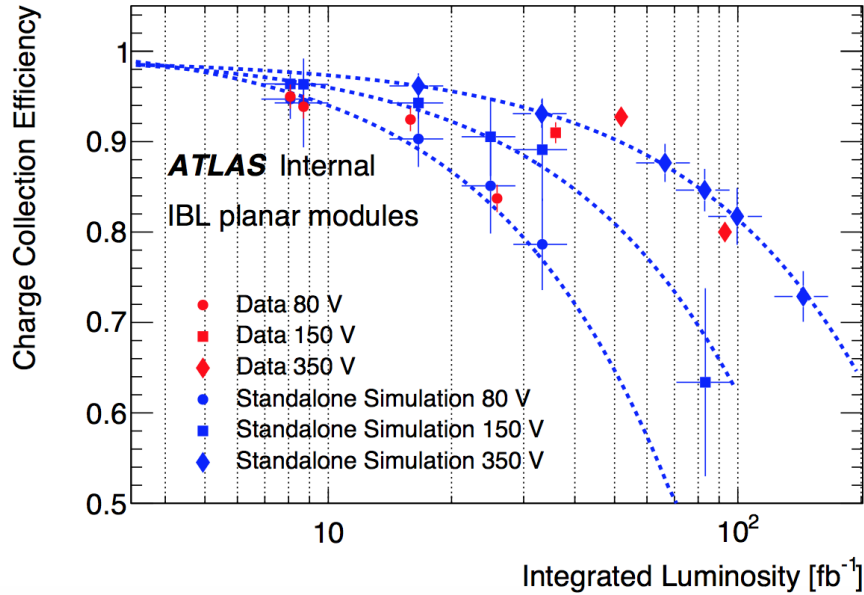


Figure 4.9 – Charge collection efficiency comparison between data and simulation in Allpix standalone simulation [101]). The red dots represent data during the Run2.

The fraction of collected charge is defined here as the ratio of the most probable value (MPV) of the charge collected by an irradiated device and the MPV of the charge collected by un-irradiated over-depleted devices. The level of agreement between data and simulation is satisfactory. The uncertainties reported in Figure 4.9 account for the following effects:

- uncertainty of 3% on the luminosity for the data (horizontal error bars);
- uncertainty of 15% on the luminosity for the simulated data due to the fluence to luminosity conversion (horizontal error bars);

- vertical error bars due to the systematics uncertainties on radiation model parameters such as energy of defects, concentration and capture cross section and trapping constant;
- vertical error bars in data due to the drift in the tuning of the modules: during operation, a drift in threshold and ToT with integrated luminosity have been noticed;

#### 4.2.2 Validation of the Athena framework

The charge collection efficiency presented in Figure 4.9 was obtained from a standalone framework [101]. The radiation damage digitizer needs to be part of the Athena framework [102] to be used in ATLAS MC samples production. An important part of the radiation damage digitizer effort has been to implement it in the Athena framework. I participated to the validation of the Athena implementation by studying its impact for several benchmarks scenarios on cluster properties and by comparing it to data. Once it has been validated on collision data, the digitizer can also be used to make predictions.

In the upcoming section, cluster and tracking properties evolution for various Run2 benchmarks conditions in terms of fluence and bias voltages will be presented. The seven benchmarks correspond to different configurations reproducing the fluence and bias voltage properties at milestones of the Run2 data taking period for the four pixel layers. Such benchmarks are described in the following Table 4.2: The bias voltages ranges from 80 V to 400 V and the fluences up to  $8.1 \times 10^{14} \text{ n}_{\text{eq}}/\text{cm}^2$ . In the table the various benchmarks are also translated in terms of accumulated fluence for the Run2. Benchmark 0 corresponds to no radiation damage for all layers. Benchmark1 corresponds to the beginning of Run2 (B-Layer, Layer 1 and 2 already had accumulated fluence from Run1). Benchmark 2 corresponds to mid 2016 Run2 conditions, after  $15 \text{ fb}^{-1}$  accumulated. Benchmarks 3/4 correspond to the end of 2016 run before/after change in operational bias voltages for B-Layer and Layer 1. Benchmark 5 corresponds to the end of 2017 Run2 ( $75 \text{ fb}^{-1}$ ). Benchmark 6 presents the extrapolated values of fluence for the end of 2018.

Two kind of samples have been used: simulated  $Z \rightarrow \mu\mu$  and  $VH \rightarrow b\bar{b}$  samples, reconstructed tracks (mostly low  $p_T$  pions) were considered with a  $p_T$  higher than 1 GeV for the cluster studies and higher than 20 GeV for the tracking study (in order to mitigate multiple scattering). The track selection criteria was tight, meaning than at least a minimum of 9 hits (11 if  $|\eta| > 1.65$ ) on the silicon layers of the ID are required and the maximum number of holes on tracks in the ID is set to two (0 pixel holes). For all studies, the two most central  $\eta$  modules were considered for the IBL and the most central  $\eta$  module for the other layers.

#### 4.2.3 Cluster properties

In this section, cluster size and cluster charge variations over the various benchmarks considered for the four pixel layers will be discussed. As the accumulated fluence varies with

Table 4.2 – Table of Run2 Benchmarks. Seven benchmarks are considered. One can find in the table the fluence and bias voltages for all layers and the corresponding Run2 luminosity.

Benchmarks	0		1		2		3		4		5		6	
Luminosity (Run2)	$0fb^{-1}$		$0fb^{-1}$		$15fb^{-1}$		$30fb^{-1}$ end 2016		$30fb^{-1}$ end 2016		$75fb^{-1}$ end 2017		$130fb^{-1}$ end 2018	
$\Phi$ ( $10^{14}$ n <sub>eq</sub> /cm <sup>2</sup> ) V (V)	$\Phi$	V	$\Phi$	V	$\Phi$	V	$\Phi$	V	$\Phi$	V	$\Phi$	V	$\Phi$	V
IBL	0	80	0	80	1	80	2	80	2	150	5	350	8.7	400
BLayer	0	150	0.7	150	1.2	150	1.7	150	1.7	350	3.1	350	4.6	400
Layer 1	0	150	0.3	150	0.5	150	0.7	150	0.7	250	1.3	250	2.1	250
Layer 2	0	150	0.2	150	0.3	150	0.4	150	0.4	150	0.8	150	1.3	150

the position of the considered modules *i.e* along the stave, only results for the most central modules of each layers will be presented.

### Cluster sizes

To understand the evolution of cluster sizes, one has to notice that the pixel layers have different characteristics which can explain their respective clusters sizes with respect to one another. These relevant characteristics are compiled in Table 4.3:

Table 4.3 – Table of characteristics of the actual pixel barrel sensors. Tilt angle refers to the tilt angle of the module with respect to the radial direction, it is chosen to compensate the Lorentz angle and to optimize the number of 2 pixel clusters which lead to an increase in the spatial resolution. Mechanical and space constraints have also influenced the value of the tilt angle. For IBL 3D sensors, the tilt reduces the impact on hit-efficiency of the insensitivity of the columns.

	IBL	B-Layer	Layer1	Layer2
Pitch ( $\mu\text{m} \times \mu\text{m}$ )	$50 \times 250$	$50 \times 400$	$50 \times 400$	$50 \times 400$
Thickness ( $\mu\text{m}$ )	200	250	250	250
Radial distance (mm)	32	50.5	80.5	122.5
Tilt angle ( $^\circ$ )	14	20	20	20

The Figure 4.10 presents the cluster size in the  $z$  direction for the most central  $\eta$  modules of the four pixel layers. The cluster size in  $z$  globally decreases with the radial distance of the layer, which is linked to the smaller solid angle covered by modules of the same length with the distance. For IBL, the bigger cluster size in  $z$  can also be explained by its smaller pitch (250  $\mu\text{m}$ ) compared to the other layers (400  $\mu\text{m}$ ). The thickness is also different for IBL (200  $\mu\text{m}$ ) than for the other layers (250  $\mu\text{m}$ ). For the two outermost layers, the cluster size in  $z$  gives rather similar values for all benchmarks:  $1.28 \pm 0.02$  for Layer 1 and  $1.23 \pm 0.02$

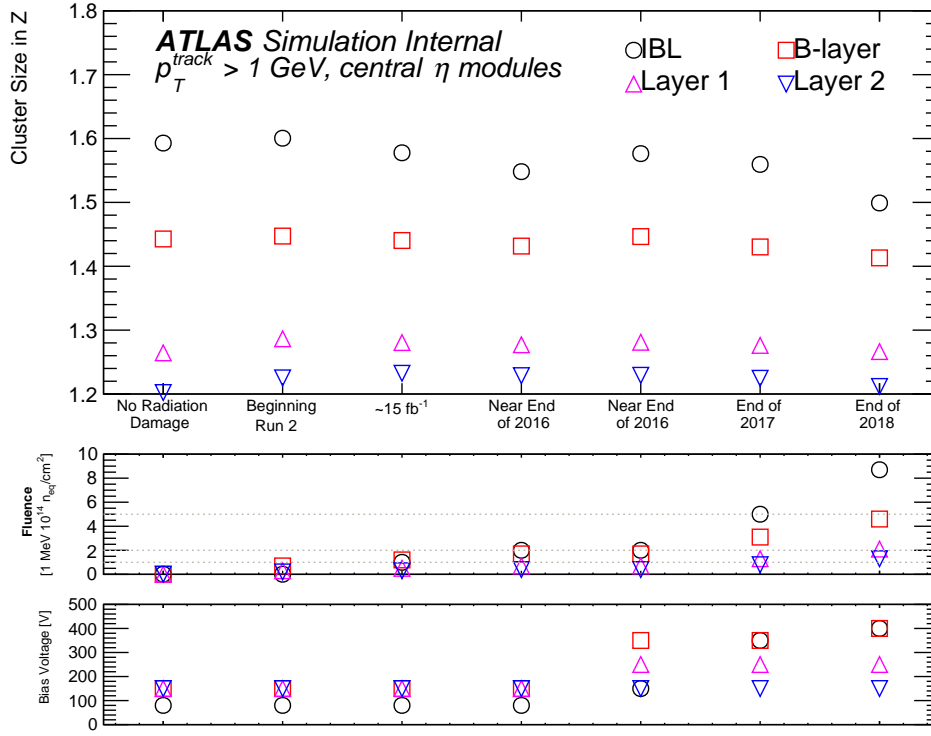


Figure 4.10 – Distribution of the mean cluster size in the  $z$  direction for the four ID pixel layers and the seven Run2 benchmarks considered.  $Z \rightarrow \mu\mu$  samples are considered. The evolution in bias voltage and fluence are reported on the two bottom plots.

for Layer 2. For the B-Layer and the IBL, the impact of fluence and bias voltage variations on the cluster size in  $z$  is more important which can be explained by the higher fluence dose integrated. By the end of 2018, the IBL cluster size in  $z$  is expected to reach 1.5 (compared to 1.6 at the beginning of Run2). Another factor which can explain the higher variations of the IBL cluster size in  $z$  is its smaller pitch (250  $\mu\text{m}$ ). Globally the cluster size in  $z$  seems rather independent of the fluence and bias voltages variations at these levels of irradiation.

The Figure 4.11 presents the cluster size in the  $\phi$  direction. By comparison with the cluster size in  $z$ , it is clear that this observable is more sensitive to the received fluence and operational bias voltage. Between the beginning of Run2 and the end of 2016, the cluster size in  $\phi$  is slightly decreasing for all four layers. After the increase in voltage for BLayer and Layer 1, a significant increase in the cluster size (from 1.60 to 1.85 for BLayer) can be observed. In case of the BLayer, it is explained by the deeper depletion of the sensors (before the bias change it was under-depleted, being biased at 150V whereas the depletion voltage was estimated around 160V <sup>1</sup>). For both BLayer and Layer1 the cluster size increase benefits from a faster charge collection (less charge trapping). The cluster size in  $\phi$  is higher in the B-Layer than in the IBL. It can be explained by the larger thickness of the B-Layer resulting in larger diffusion and by the fact that the B-Layer (20°) is more tilted than the IBL (14°). Between the end of 2017 and the end of 2018, the cluster size in  $\phi$  increases for the B-Layer, Layer1 and Layer2 by more than 20 % whereas the increase for IBL is just around 10%.

<sup>1</sup>MPI Private communication

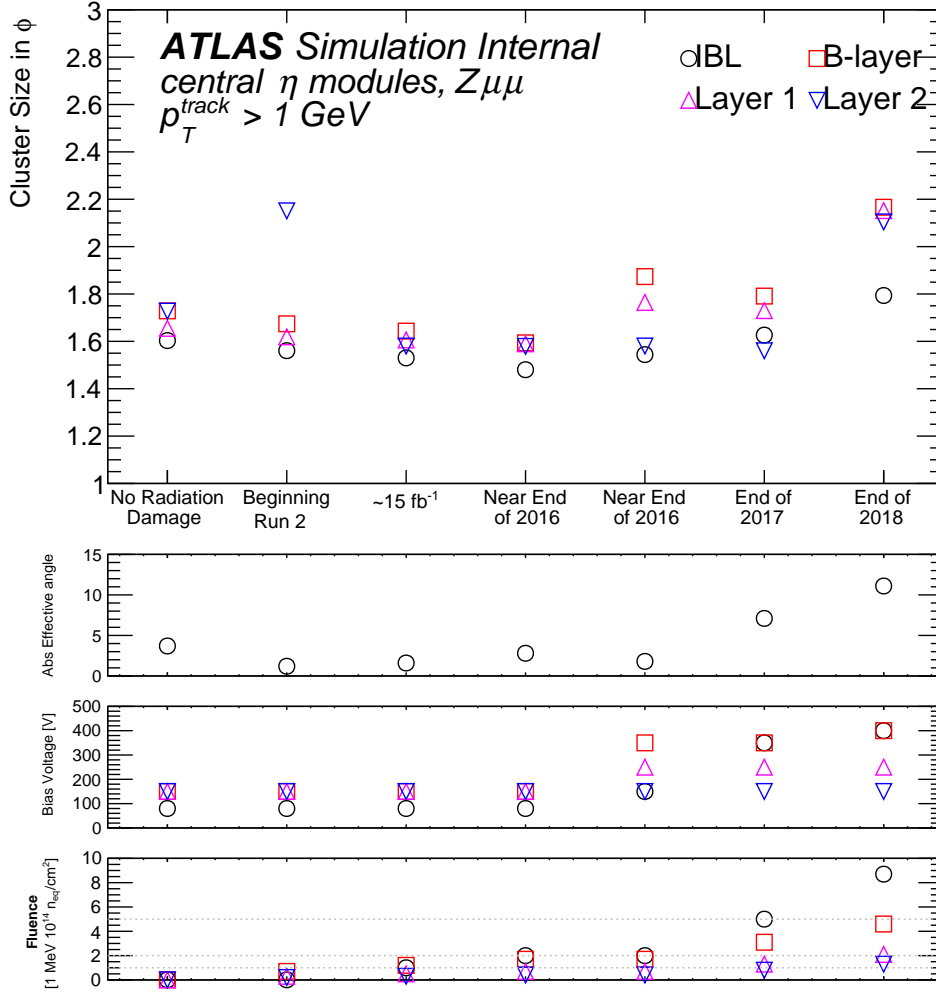


Figure 4.11 – Distribution of the mean cluster size in the  $\phi$  direction for the four ID pixel layers and the seven Run2 benchmarks considered. The evolution in IBL effective angle (absolute difference between the tilt angle and the Lorentz angle), bias voltage and fluence are reported on the three bottom plots.

As presented in Figure 4.6, the total mean cluster size of an un-irradiated planar pixel sensor reaches a maximum when its bias voltage reaches the depletion voltage. It slowly decreases afterwards in the over-depletion regime. One explanation for the high increase in cluster  $\phi$  at the end of 2018 can be that the operational bias voltage is closer to the depletion voltage for the considered fluences than what it was at the end of 2017. The evolution of the Lorentz angle with fluence between the end of 2017 and the end of 2018, can also explain this trend: the IBL effective angle (absolute difference between the IBL tilt angle and the Lorentz angle) increases from 7.1 to 11.1 degrees, which involves an increase in the cluster size in the  $\phi$  direction.

For the second Layer, the jump in cluster size at the beginning of Run2 is not understood at the moment.

The total ( $\phi$  and  $z$ ) cluster size is presented in Figure 4.12. Between the end of 2017 and the predictions for the end of 2018, the total cluster size increases drastically for the three outermost layers. The increase of the effective angle can explain such trend, as the effective angle increases by 55 % between the end of 2017 and the predictions for the end of 2018, which implies an increase in the cluster size. As explained in the previous paragraph, another factor could be that before the end of 2017, the modules are operated in an over-depleted mode. With the increasing fluence, the effective depletion voltage increases, the operational bias voltage remaining the same, the cluster size is supposed to increase, as shown in Figure 4.6.

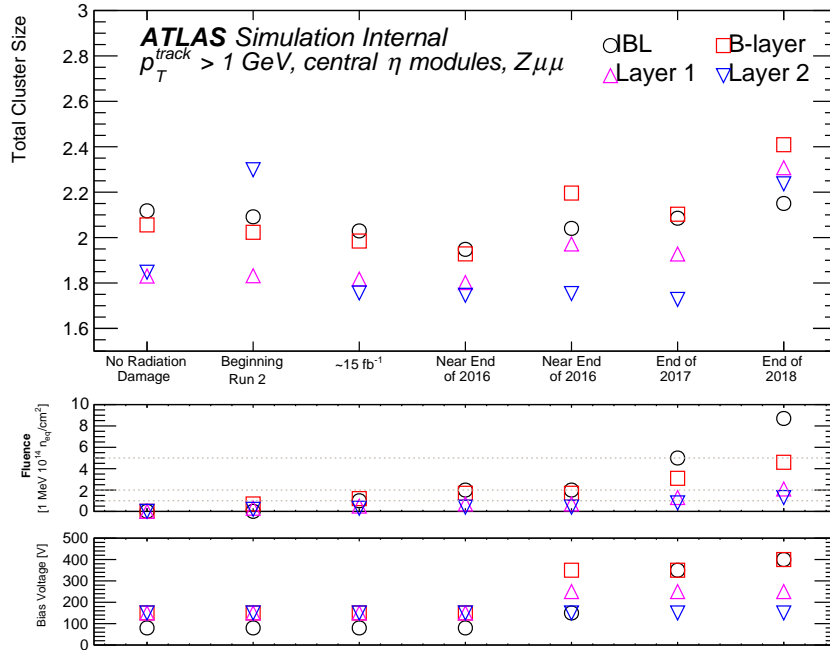


Figure 4.12 – Distribution of the mean total cluster size for the four ID pixel layers and the seven Run2 benchmarks considered. The evolution in bias voltage and fluence are reported on the two bottom plots.



### Cluster charge

The Figure 4.13 presents the evolution of the cluster charge distribution in the IBL for the seven benchmarks considered. With increasing integrated fluence, the distribution is shifted towards lower values as the charge trapping phenomenon is higher with increasing fluence. One can also notice a small discrepancy between the distribution at the Benchmark 0 (no radiation damage) and the Benchmark 1 (beginning of Run2) which can be explained by a different modeling of the mobility between the two benchmarks; the mean cluster charge distribution being rather similar between the two Benchmarks, this small discrepancy does not seem significant. The increase in bias voltage between benchmark 3 (150V) and 4 (350V) for the same fluence results as expected in an increase of the mean cluster charge, as the collection time decreases (less probability of charge trapping).

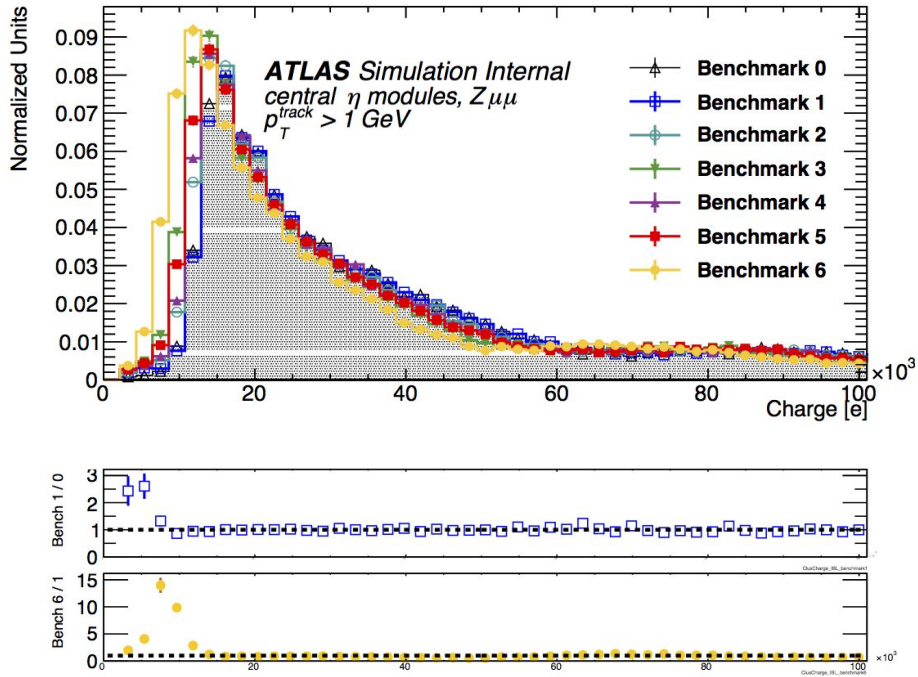


Figure 4.13 – IBL Cluster Charge distribution reported for the seven Run2 benchmarks considered. The top ratio plot (blue markers) presents the ratio of the beginning of Run2 benchmark over the "no radiation damage" benchmark (benchmark 0). The bottom ratio plot (yellow markers) presents the ratio of the end of 2018 benchmark over the beginning of Run2 benchmark.

The Figure 4.14 presents the mean cluster charge for the four layers and the seven benchmarks considered. The cluster charge collected is higher for the three outermost layers, which are thicker than the IBL.

At the beginning of Run2, as B-Layer, Layer1 and Layer2 has already been exposed to some radiation during the Run1, the mean cluster charge is slightly diminished (from 32500e to 31500e for B-Layer). The fluence dependency of the mean cluster charge is important and it is especially visible for the IBL and the B-Layer which are the closest layers to the interaction point.

Between the beginning of Run2 and the end of 2018 (predictions), the mean cluster charge of the IBL will be reduced by 6500 electrons, and for the B-Layer by 6000 electrons. The bias voltage increase allow to mitigate the charge trapping by increasing the depletion zone and the drift velocity of the charge carriers. For example, going from 150 V to 350 V for the IBL between 2016 and 2017 has allowed to keep roughly the same collected charge (23000 electrons) with a fluence increase of  $3 \times 10^{14} \text{ n}_{\text{eq}}/\text{cm}^2$ .

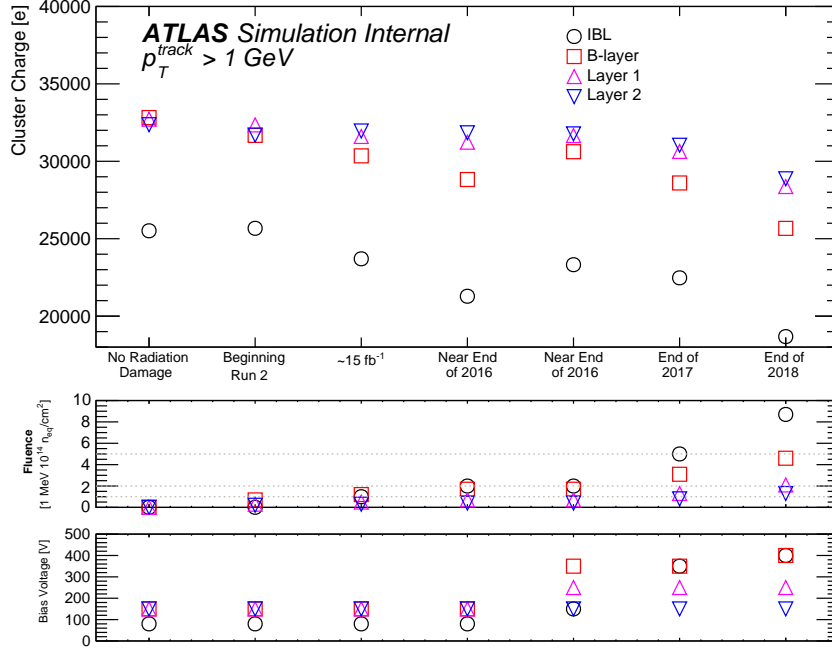


Figure 4.14 – Distribution of the mean cluster charge for the four ID pixel layers and the seven Run2 benchmarks considered. The evolution in bias voltage and fluence are reported on the two bottom plots.

#### 4.2.4 Charge collection efficiency

The Charge collection efficiency has been obtained by looking at the cluster charge distribution of the most central modules of the four pixel layers for the various benchmarks. In Figure 4.15 an estimation of the charge collection efficiency (ratio of the mean cluster charge) is shown for all four layers and for the seven benchmarks. Charge collection efficiency for IBL data is also reported on Figure 4.15: it is obtained by doing the ratio of the collected charge (obtained from cluster ToT) and the expected charge before irradiation (obtained from cluster ToT of cosmics or very first runs). The variations in the charge collection efficiency follows the increase in bias voltage and fluence both for data and MC. At the beginning of Run2, the three outermost layers have already lost 2 to 3 % of charge collection efficiency from Run1 exposition to radiation.

Between the beginning of Run2 and the end of 2016, the slope of the decrease in efficiency is proportional to the accumulated fluence evolution: the IBL loses charges more quickly than the B-Layer which itself loses charge at a higher rate than Layer 1 and 2. The simulation of

Layer 2 gives puzzling results in the Benchmark1 (Beginning of Run2), its charge collection efficiency is supposed to be higher than Layer1 which is closer to the beam pipe. This puzzling results can be put in regard of the Cluster sizes jumps for the same layers at the same benchmarks.

By the end of 2018, the simulated charge collection efficiency of the respective layers central modules is predicted to reach the following values:  $\simeq 89\%$  for Layer 2,  $\simeq 86\%$  for Layer 1,  $\simeq 78\%$  for B-Layer and  $\simeq 73\%$  for IBL.

The data to MC agreement is quite good even if the simulation seems to slightly over-perform the data especially at the end of 2016 and 2017. At the moment, only statistical uncertainties are shown, systematics uncertainties of radiation model parameters (energy of defects, concentration, capture cross section and trapping constant) are not yet implemented in the Athena digitizer framework. The slight discrepancy between MC and data can also be explained by the fact that the module temperatures, threshold and tuning configuration variations are not implemented in the digitizer at the moment.

The Figure 4.16 presents the charge collection efficiency obtained with simulated  $VH \rightarrow b\bar{b}$  samples and compared to Run2 IBL data (black): it is similar to the charge collection efficiency plot obtained with simulated samples of  $Z \rightarrow \mu\mu$  (Figure 4.15).

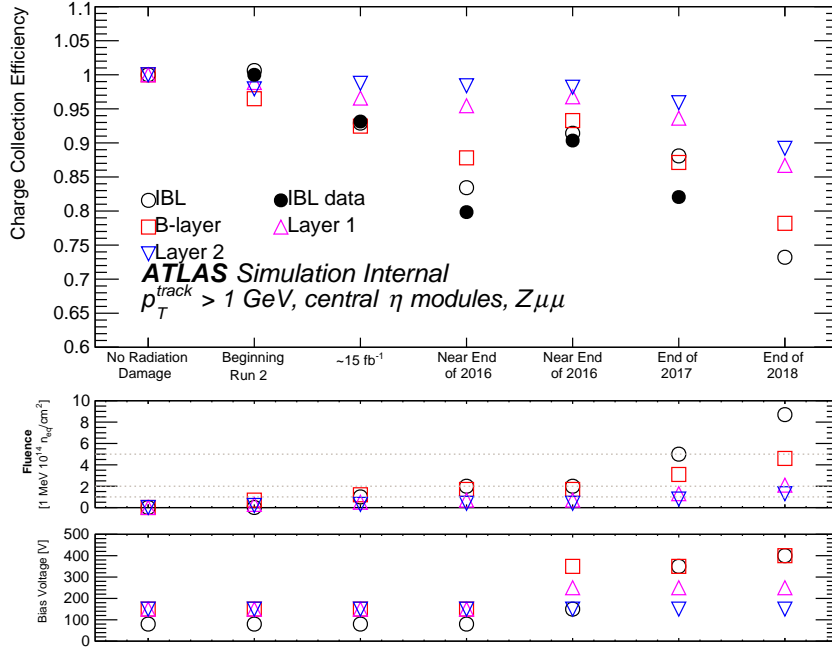


Figure 4.15 – Charge collection efficiency for the four ID pixel layers central  $\eta$  modules and the seven Run2 benchmarks considered. The evolution in bias voltage and fluence are plotted on the two bottom plots. IBL data are also presented

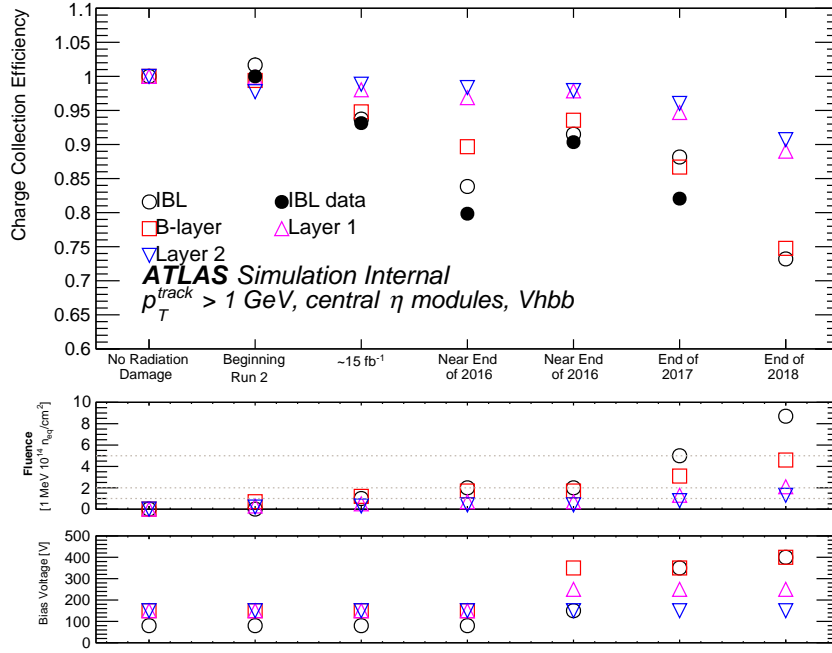


Figure 4.16 – Charge collection efficiency for the four ID pixel layers using  $VH \rightarrow b\bar{b}$  samples. Central  $\eta$  modules and the seven Run2 benchmarks are considered. The evolution in bias voltage and fluence are plotted on the two bottom plots. IBL data are also presented

#### 4.2.5 Tracking properties

In this section, tracking quantities will be studied: the residuals distributions and their resolutions as well as the tracks fake rate. Only the central modules of each pixel layers are considered.

The Figure 4.17 presents the  $p_T$  and  $\eta$  distribution of the reconstructed tracks of both samples. It can be noticed that the  $p_T$  is quite low:  $Z \rightarrow \mu\mu$  samples, if well fitted to explore pixel performance, are not the optimal choice to study the tracking properties due to its relatively low energy particles, prone to be deviated via multiple scattering.  $VH \rightarrow b\bar{b}$  samples are also used and its  $p_T$  spectrum is also displayed in the Figure 4.17.

#### Residuals

In Figures 4.18 and 4.20, the unbiased residuals RMS in X (short pixel side direction, equivalent to  $\phi$  direction) and Y (long pixel side direction, equivalent to  $z$  direction) are considered. Unbiased means that the hit on the layer is not included in the tracking process. The position of the hit in the sensor is obtained as follows: if only one pixel has fired, the hit position is assumed to be the center of the pixel; if two or more pixels have fired, the hit position is obtained by charge weighted method (charge interpolation technique as described in [103]). The track selection criteria for those tracks is  $p_T > 20$  GeV, which mitigates the impact of multiple scattering.

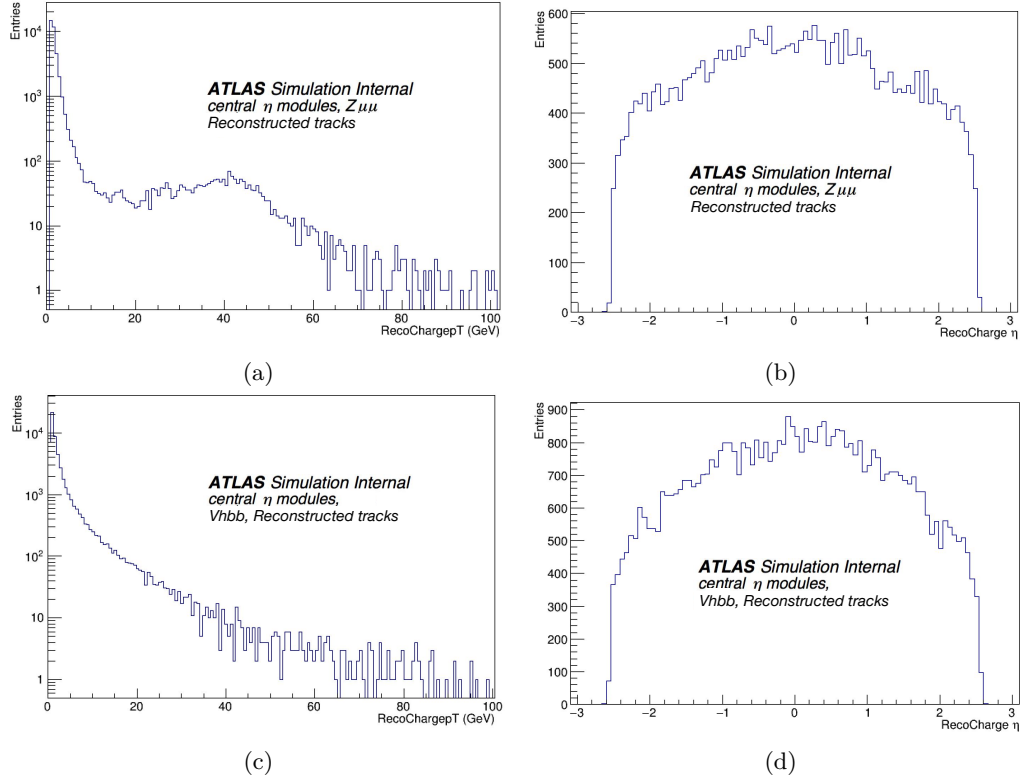


Figure 4.17 – Distribution of the reconstructed tracks  $p_T$  (a and c) and over the  $\eta$  spectrum (b and d).  $Z \rightarrow \mu\mu$  samples (a and b) and  $VH \rightarrow b\bar{b}$  (c and d) samples are considered.

If one considers tracks with a looser track selection criteria such as  $p_T > 1$  GeV, the RMS of the residuals is much larger than the digital resolution ( $14 \mu\text{m}$ ): for example the RMS of the unbiased residuals in X for the IBL at the beginning of Run2 is expected to be of the order of  $10 \mu\text{m}$  (thanks to clusters of 2 pixels which improve the spatial resolution) and observed at more than  $35 \mu\text{m}$ . It can be explained by the fact that at low  $p_T$  the multiple scattering is the dominant effect.

The Figure 4.18 presents the unbiased resolution in X. The cluster size in  $\phi$  is also shown as well as the IBL effective angle variations, the bias voltages and fluences variations. The hierarchy in terms of unbiased residuals RMS in X can be explained if one considers that due to the tracking process, Layer2 tracks are very unconstrained which does not give a reliable resolution determination.

The fluence increase results in higher residuals RMS and hence poorer spatial resolution: for example, between the end of 2017 and the end of 2018, the unbiased residuals resolution in X of IBL, Blayer and Layer 1 have been respectively degraded by 15%, 45% and 25 %, even if the bias voltages have been increased by 50V for both IBL and Blayer in the meantime. Part of this variation could come from the uncertainties arising from the effect of remanent multiple scattering, which is not entirely negligible for a  $p_T$  of the order of 20 GeV.

The increase in bias voltage (at fixed fluence) reduces the unbiased residuals RMS in X, if one consider for example the comparison between the end of 2016 and the end of 2017 for

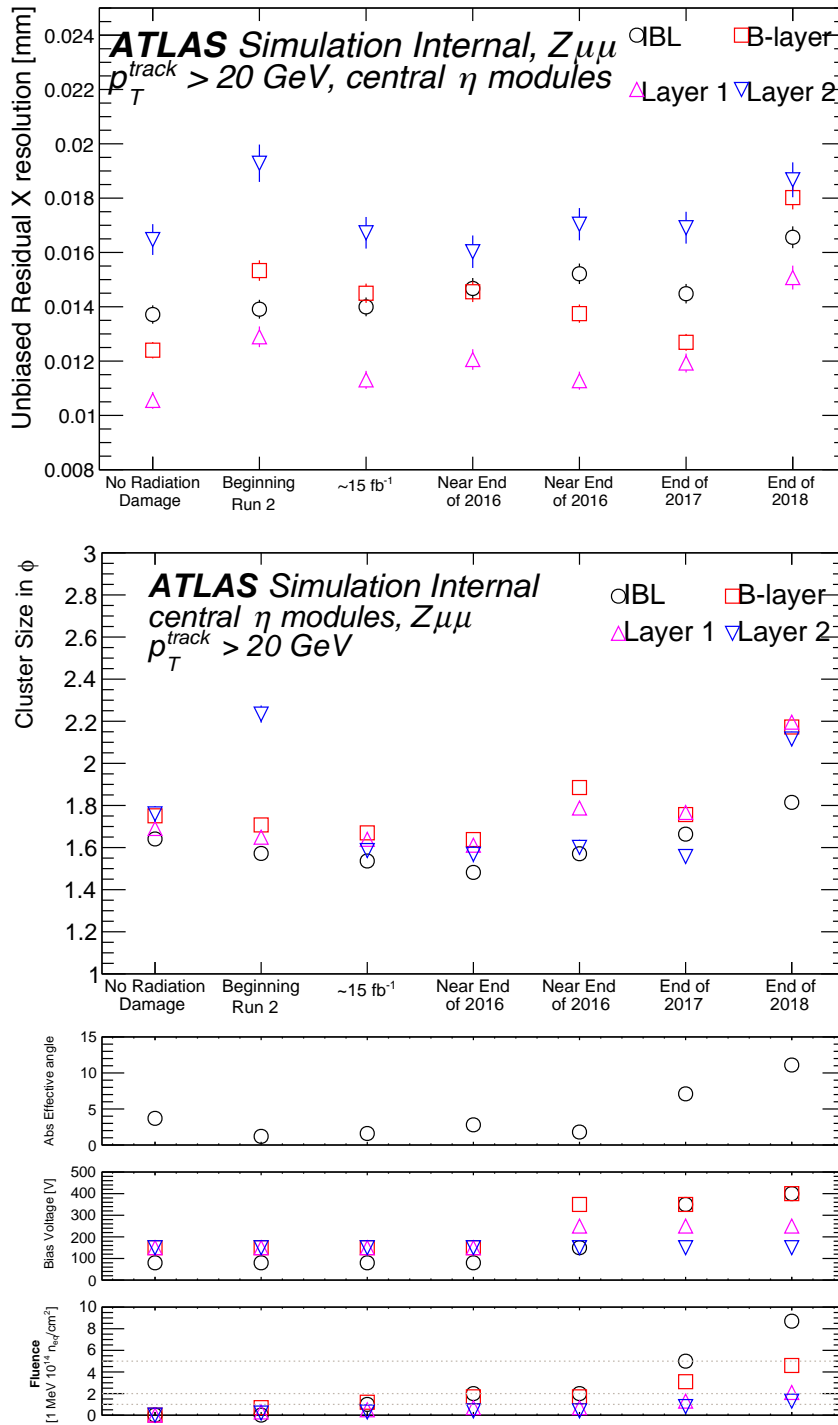


Figure 4.18 – Distribution of the unbiased residuals RMS in the short pixel direction for the four ID pixel layers and the seven Run2 benchmarks considered. The evolution in cluster size in  $\phi$ , effective angle for the IBL, bias voltage and fluence are plotted in the bottom plots. The following tracks selection criteria is considered:  $p_T > 20 \text{ GeV}$ .

IBL and B-Layer, even if the fluence have been more than doubled, the unbiased residuals RMS for BLayer slightly decreases from 14.5 to 12.5  $\mu\text{m}$  thanks to the increase of the bias voltage from 150 V to 350 V.

The variation in cluster size in  $\phi$  seems also correlated to the variation in the unbiased residual resolution in X: the unbiased resolution degrades when the cluster size in  $\phi$  decreases between the first benchmark and the fourth one, it is especially visible for the IBL, which cluster size in  $\phi$  decreases from 1.6 to 1.5 whereas the spatial resolution degrades from less than 14  $\mu\text{m}$  to 14.6  $\mu\text{m}$ .

To conclude on the variation of the unbiased residual resolution in X, it seems to be sensitive to fluence increase and slightly sensitive to variations in bias voltage and effective angle. To definitely quantify the impact of radiation and bias voltage on this observables, higher  $p_T$  samples with higher statistics are required to disentangle the multiple scattering effect from the real radiation and operational bias voltage variation impact.

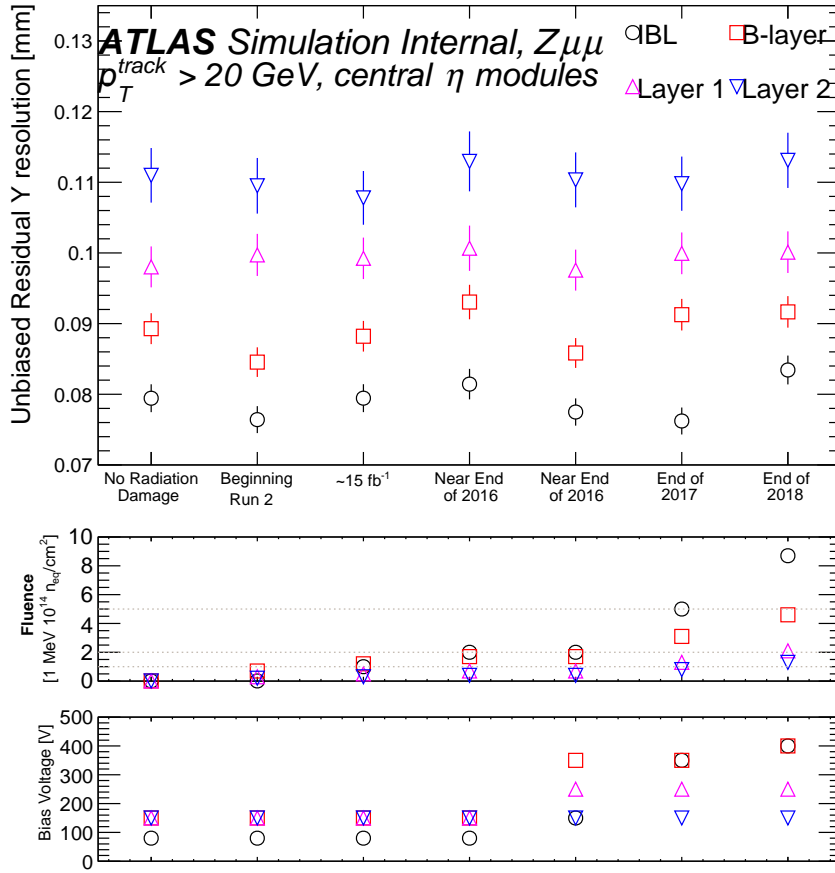


Figure 4.19

Figure 4.20 – Distribution of the unbiased residuals RMS in the long pixel direction for the four ID pixel layers and the seven Run2 benchmarks considered. The evolution in bias voltage and fluence are plotted in the two bottom plots. The following tracks selection criteria is considered:  $p_T > 20$  GeV.

For the residuals in Y, shown in Figure 4.20, the hierarchy between the layers is expected, IBL Unbiased residuals RMS is smaller than other layer RMS as the IBL pitch in Y is smaller.

Residuals in Y are less sensitive to the increase in bias voltage, as even after the increase in bias voltage from 150 V to 350 V for the IBL, the unbiased residuals stays at 75  $\mu\text{m}$ .

By the end of 2018, if one consider the unbiased residuals in X and Y, the spatial resolution for the IBL would be degraded by approximately 6% in the long pixel direction and approximately 20% in the short pixel direction.

### Fake rate

The fake rate is the fraction of reconstructed tracks which are not matched with truth tracks over the number of reconstructed tracks. The Figure 4.21 presents the fake rate obtained for simulated  $Z \rightarrow \mu\mu$  (black circles) and  $VH \rightarrow b\bar{b}$  (red squares) samples. The track selection criteria is set to Tight which means that a minimum of 9 hits (11 if  $|\eta| > 1.65$ ) in the silicon part of the tracker is required, hits in all pixel layers are required. The number of fake tracks is not statistically significant (5 tracks). Concerning  $VH \rightarrow b\bar{b}$  samples, the fake rate is higher and the number of fake tracks is significantly increased (more than 120). Looking at the evolution between the end of 2016 and the predictions for the end of 2018, it can be noticed that the fake rate is slightly increased with the fluence (0.18% to 0.2%) which could be linked to the observed degradation of spatial resolution. To conclude on the impact of radiation damage on fake rate, higher statistical samples are required, as well as  $t\bar{t}$  samples, which are the classical samples used for tracking studies.

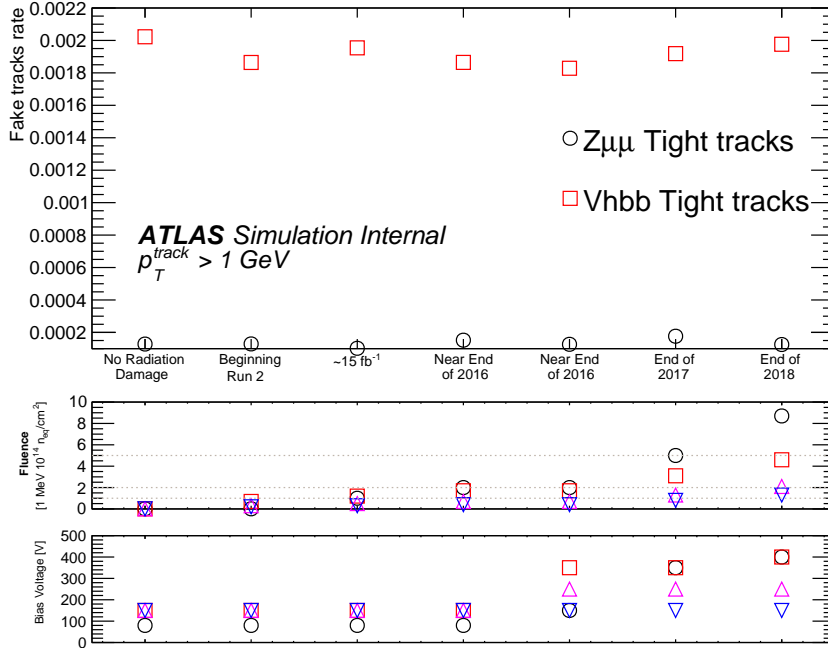


Figure 4.21 – Tracks fake rate for the seven Run2 benchmarks considered. The evolution in bias voltage and fluence are reported in the two bottom plots.



## Conclusions

The study of simulated  $Z \rightarrow \mu\mu$  and  $VH \rightarrow b\bar{b}$  samples has shown the impact of the radiation damage on the cluster properties, especially on the collected charge, with a significant loss of charge of the order of 10 to 16 % for all pixel layers between the beginning of their lifetime to the end of 2018 (predictions). The impact of radiation on track residuals and track fake rate have also been investigated for both type of samples: the residuals distribution as well as the fake rate for  $Z \rightarrow \mu\mu$  samples seems to evolve slightly with the bias voltage and the fluence. This result is compatible with data, the ATLAS tracking group being unaware of tracking performance deterioration with time. This is possible thanks to the excellent signal-to-threshold ratio of the ATLAS pixel detector, along with robust tracking algorithms. Nevertheless, the prediction for the end of 2018 and using a  $p_T$  cut of 20 GeV/c shows a visible degradation in the spatial resolution in the short pixel side (15 % for IBL); it will be compared to data as soon as available. To investigate further the radiation impact on tracking quantities (such as the track reconstruction efficiency and impact based parameters resolutions) and b-tagging quantities, higher statistical samples with higher  $p_T$  are required, as well as  $t\bar{t}$  samples.

## 4.3 Conclusions and perspectives

A radiation damage digitizer, which is an essential piece of the MC simulation machinery to correctly account for the aging of the silicon pixel detector, has been developed and is expected to be soon a part of the ATLAS MC chain. By providing a better match between MC and data, it aims to create good prediction towards the next data taking period (Run 3) but also to make important design decisions for the upgraded ATLAS detector that must survive the harsh HL-LHC radiation environment (see next chapter).

I participated to the development of the digitizer by three contributions. Firstly, I produced electric field maps used by the digitizer as look up tables. I also analyzed testbeam data whose purpose were to investigate the evolution of diffusion at high temperature and high bias voltage as well as the charge collection efficiency at ITk-like fluences (presented in Chapter 7). Eventually, I was in charge of analyzing the cluster and track properties and their variations for different conditions of fluence and operational bias voltage at several steps of the digitizer development.

The radiation damage modeling has been validated by looking at charge collection efficiency which was studied by comparing simulated and Run 2 data: a reasonable agreement between the simulation and the data have been observed. The validation of the radiation damage modeling has allowed us to use the digitizer as an investigation and prediction tool.  $Z \rightarrow \mu\mu$  and  $VH \rightarrow b\bar{b}$  samples have been used to investigate the impact of radiation damage on cluster and track properties. It has been shown that the variation in fluence and operational bias voltages have a significant impact on cluster charges and sizes and hence on charge collection efficiency. The residuals distributions are also sensitive to this variations, their RMS which give an estimation of the spatial resolution generally increases with the fluence and decreases with higher operational bias voltage. The fake rate has also been

studied and for  $VH \rightarrow b\bar{b}$  samples it seems that the accumulated fluence tends to slightly increase the numbers of fake tracks (gain of 0.02% between the beginning and the end of Run2).

To investigate and conclude on tracking properties, high statistics  $t\bar{t}$  samples with higher  $p_T$  spectrum and consequently less impact of multiple scattering are currently being produced. High statistics  $VH \rightarrow b\bar{b}$  samples are also under production and will be used to estimate the impact of radiation on higher level observables such as b-tagging variables or the Higgs invariant mass.

## Chapter 5

# ATLAS during the High Luminosity LHC

### Contents

---

<b>5.1</b>	<b>The High Luminosity LHC . . . . .</b>	<b>87</b>
<b>5.2</b>	<b>ATLAS HL-LHC upgrade . . . . .</b>	<b>88</b>
<b>5.3</b>	<b>ATLAS Inner Tracker (ITk) . . . . .</b>	<b>89</b>
5.3.1	ITk pixels . . . . .	91
5.3.1.1	Inclined layout . . . . .	92
5.3.1.2	Sensors design . . . . .	92
5.3.1.3	ITk Electronics & Mechanics . . . . .	94
5.3.2	ITk Performance . . . . .	95
5.3.2.1	Tracking and Vertexing . . . . .	96
5.3.2.2	Flavour tagging . . . . .	97
5.3.2.3	Particle identification . . . . .	97
5.3.3	Physics perspectives at HL-LHC . . . . .	97
5.3.3.1	Higgs studies . . . . .	98
5.3.3.2	Supersymmetry & exotics . . . . .	99

---

The CERN plans to transform the LHC into a High Luminosity machine, the HL-LHC. In this chapter the upgrade of ATLAS and of its Inner Tracker (ITk) to cope with the challenging conditions of the HL-LHC will be developed.

## 5.1 The High Luminosity LHC

The first proton-proton collisions at the High Luminosity LHC (HL-LHC [104]) are scheduled for 2026. The HL-LHC ultimate goal in terms of instantaneous luminosity is to reach  $\mathcal{L} \simeq$

$7.5 \times 10^{34} \text{ cm}^{-2}\text{s}^{-1}$  which corresponds to approximately 200 inelastic proton proton collisions per bunch crossing at  $\sqrt{s} = 14 \text{ TeV}$ . By the end of the HL-LHC data taking period ( $\simeq 2039$ ), the integrated luminosity will reach  $4000 \text{ fb}^{-1}$  as shown in Figure 5.1. The HL-LHC's construction will start in early 2019, two dedicated periods, the Long Shutdown 2 (LS2: 2019 - 2020) and the Long Shutdown 3 (LS3: 2024 - 2026) are scheduled to perform the upgrades of both the LHC and its experiments. In this chapter, the ATLAS upgrade and more specially the ATLAS Inner Tracker (ITk [105, 106, 107]) upgrade will be discussed.

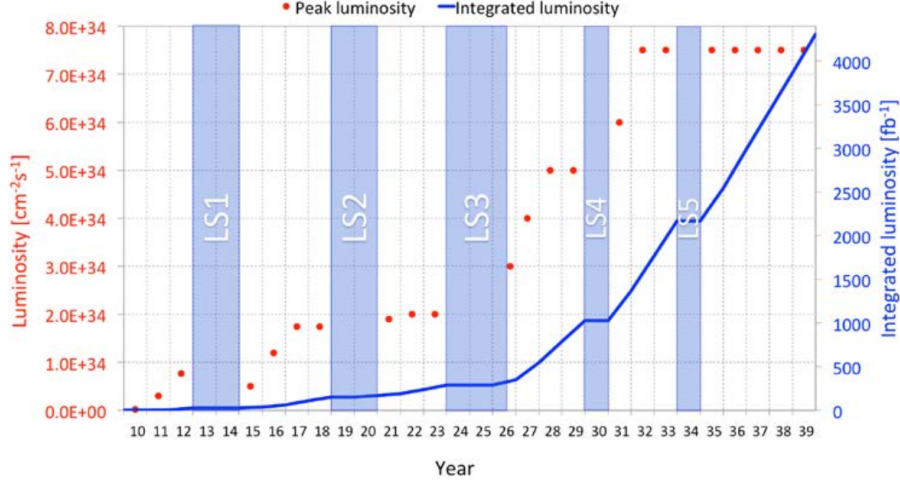


Figure 5.1 – HL-LHC planned instantaneous peak luminosity (red dots) and integrated luminosity (blue line) [108]

## 5.2 ATLAS HL-LHC upgrade

The dataset collected by ATLAS at the end of the HL-LHC data taking period will be 10 times larger with respect to the one collected during the LHC phase (2010-2023). In terms of physics, this massive amount of data will allow more precise measurements of SM processes and precise measurements of the Higgs mass and couplings to particles (especially with the second generations of fermions). The measurements of the trilinear Higgs self coupling is also being considered. The search of new physics signals will continue thanks to enlarged data sets, extending the physics reach in terms of mass and precision for couplings.

During the data taking period of the HL-LHC [108] the ATLAS detector will have to take data in extreme conditions with:

- an instantaneous peak luminosity of the order of  $\mathcal{L} \simeq 7.5 \times 10^{34} \text{ cm}^{-2}\text{s}^{-1}$ , a five to seven-fold increase with respect of today;
- an average of 200 inelastic proton proton collisions per bunch crossing;

- an accumulated luminosity of  $4000 \text{ fb}^{-1}$  by the end of 2039, which means that the innermost tracker layer will be exposed to a fluence of  $2 \times 10^{16} \text{ n}_{\text{eq}}/\text{cm}^2$  (4-6 times the IBL fluence at the end of LHC Run3).

To cope with such conditions, ATLAS needs to be upgraded to continue its investigation of the high energy physics spectrum. In terms of performance, this upgrade should allow ATLAS to compete with or even exceed the actual physics performance of the current detector.

The ATLAS Inner detector (ID) will be replaced by an all silicon new tracker, the ITk (Inner Tracker) made of pixels in its inner part and of strips in its outer part. The all-silicon option was decided because of the need of highly radiation-hard materials and for data rates and occupancy considerations (TRT occupancy would reach 100 % at HL-LHC).

The other detectors (the calorimeters and the muon spectrometer) will also undergo some upgrades [109]. The Liquid Argon calorimeter and the hadronic calorimeter's electronics will be upgraded to cope with the high radiation level: the entire LAr calorimeter readout chain will be upgraded and the hadronic calorimeter will undergo an upgrade of its readout electronics and associated mechanics.

A new detector, the High Granularity Timing Detector (HGTD [110]) will be added. It will be placed at high  $\eta$  ( $2.4 < |\eta| < 4$ ) and its goal will be to add timing information on forward tracks. The high timing resolution ( $30 \text{ ps}$ ) will help to disentangle pile-up tracks which origin collision points (primary vertices) are spatially close but separated in time.

In the following section, a description of the ITk will be given. The performance and physics prospects expected for which ITk will be the crucial detector will also be discussed.

### 5.3 ATLAS Inner Tracker (ITk)

The ITk will have to ensure a good tracking efficiency and to identify charged particles with high efficiency and purity in a high pile-up environment, with a large  $\eta$  coverage (up to  $|\eta| = 4$  with respect to 2.5 of the ID). From the high rate environment emerge two technological challenges:

- The need for a finer granularity to allow a precision tracking and ease the disentanglement of neighboring tracks. The development of an adequate front end chip, the RD53 chip [111] is also required.
- Radiation hard detectors: both the sensors and the chip will have to cope with high fluences (see Figure 5.2 and Table 5.1). Fluences up to  $2 \times 10^{16} \text{ n}_{\text{eq}}/\text{cm}^2$  are expected. 3D silicon pixel sensors and thin planar silicon sensor technologies are excellent candidates, thanks to their good performance in highly radiative environment, as anticipated in Chapter 3.

The actual foreseen ITk layout (see Figure 5.4) will comprise two sub-detectors: a strip detector and a pixel detector.

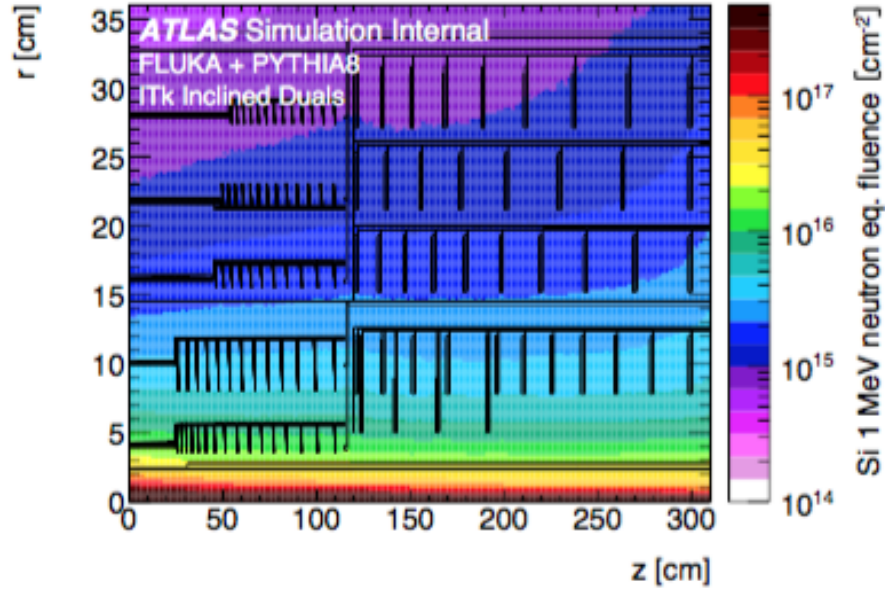


Figure 5.2 – Fluence simulation in an ITk pixel section [107].

Table 5.1 – Maximum accumulated fluences expected at the end of lifetime of the five pixel layers. Layer 0 and 1 will be replaced after  $2000 \text{ fb}^{-1}$  whereas Layers 2 to 4 will remain until the end of the HL-LHC period ( $4000 \text{ fb}^{-1}$ ). From [107].

	Maximum Fluence $\Phi$ expected ( $10^{15} \text{ n}_{\text{eq}}/\text{cm}^2$ )		
	Flat barrel	Inclined barrel	End-caps
Layer 0	13.1	12.3	6.8
Layer 1	2.7	3.5	3.8
Layer 2 - 4	2.8	3.0	3.8

The pixel detector will be divided in a barrel and two end-caps. It will extend up to  $|\eta| = 4$  and will contain 5 successive layers (up to a radius of 345 mm). The first two barrel layers, the closest to the beam-pipe, will be replaceable independently from the rest of the detector; they are expected to be exchanged after having integrated half of the expected luminosity. The barrel geometry will be more complex than the current geometry: a flat barrel will be followed by an inclined barrel whose modules will be tilted. The pixel barrels will be complemented by a end cap ring system, with sensors perpendicular to the beam axis.

The strip detector [106] will have four barrel layers and 6 end-caps petals disks on each end. It will cover an  $\eta$  region up to  $|\eta| > 2.7$ . In terms of tracking performance, the inclined layout will provide at least 13 hits per tracks up to  $|\eta| > 2.6$  and 9 hits per track beyond that.

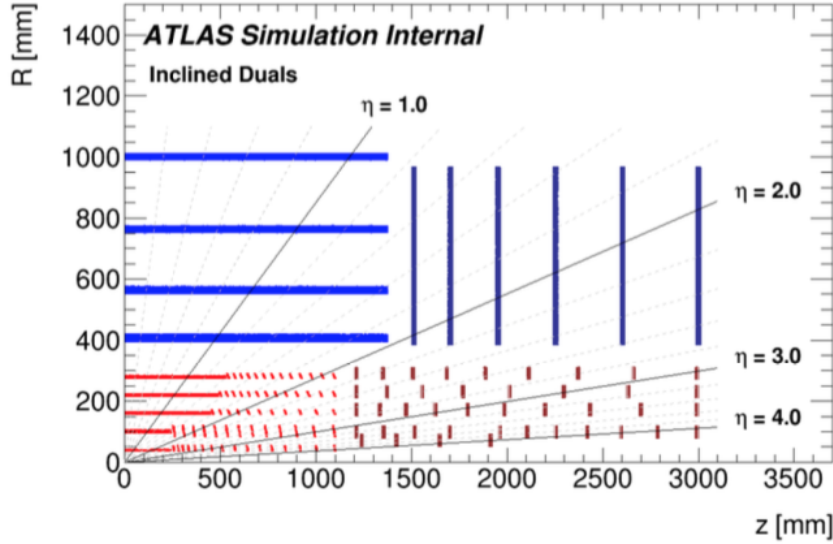


Figure 5.3 – ITk inclined layout scheme [107]

Figure 5.4 – The red part represents the ITk pixel detector, the blue one represents the ITk strips detector.

In the following, the ITk pixels sub-detector will be described.

### 5.3.1 ITk pixels

As they possess a bi-dimensional fine granularity and a good radiation damage resistance, pixel sensors, both planar and 3D, are at the core of the ITk design. The inclined pixel layout will be described in the following.

### 5.3.1.1 Inclined layout

To increase the efficiency at high  $\eta$ , an innovative layout design, *i.e* the inclined layout, has been proposed. After a flat barrel ( $|z| < 240$  mm), similar to the one used in the current pixel detector, an inclined barrel covering the region between  $240 \text{ mm} < |z| < 1100$  mm will be installed. This inclined barrel is composed of tilted sensors. The tilt angle is chosen such as an incoming particle will cross quasi perpendicularly the sensor. The advantage of such design is that the particle crosses a reduced quantity of sensor material even if it crosses one extra pixel layer compared to Run2 layout as presented in Figure 5.5, which increases the tracking resolution. The inner end-cap system will be located between  $1100 \text{ mm} < |z| < 3000$  mm. The radii of all ITk pixel part are described in Table 5.2.

Table 5.2 – ITk layers radius

	Layers:	L0	L1	L2	L3	L4
Radius (mm)	<b>Flat barrel</b>	39	99	160	220	279
	<b>Inclined barrel</b>	36	80	155	215	274
	<b>End-caps Rings</b>	50	78	152	212	271

The ITk pixel will feature inclined single modules (one read out chip for one sensor) in its first barrel layer inclined part, dual modules (two read out chips for one sensor) for its outer inclined-part barrel layers and for the flat first barrel layer part, and quad modules (Four read out chips for one sensor) for the rest of the layers. The instrumented pixel surface will reach  $12.74 \text{ m}^2$  and the numbers of electronic channels will be of the order of five billions.

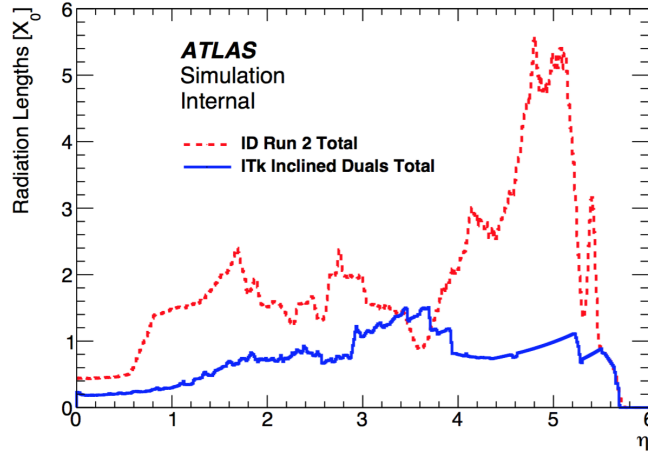


Figure 5.5 – Material budget comparison between Run2 in red and ITk layout in blue.[107]

### 5.3.1.2 Sensors design

The granularity of the ITk pixels is increased by a factor five compared to the IBL pixels. Two options are considered, either a pixel pitch of  $50 \mu\text{m} \times 50 \mu\text{m}$  or  $25 \mu\text{m} \times 100 \mu\text{m}$ .



The first two layers will be made of 3D sensors and planar pixel sensors. The outermost layers will be composed of planar pixel sensors and possibly of CMOS sensors for the last layer. The sensor design is driven by ITk requirements, especially in terms of hit efficiency which is set to 97 % after the integrated dose and fluences expected at the end of detector lifetime in order to maintain good tracking performance. The power dissipation and limitation in terms of leakage current and depletion voltage are other important criteria. Several production designs from various foundries (Advacam [112], CNM [113], FBK [114], Sintef [115] and VTT [116]) are actually tested in laboratories and during testbeam campaigns (more in Chapter 7).

### Planar pixel sensors design and performance

The n-on-p planar pixel technology is the preferred option for the ITk layers except the first one. The n-on-p technology is simpler than the previously used n-on-n technology (used in IBL) as it requires a single-sided processed wafer (n-on-n sensors are instead double-sided, which is a more complex process). This technology is also more radiation hard as it will not undergo type inversion, as the bulk is p-doped (see Chapter 3).

The Layer 1 will be replaced after  $2000 \text{ fb}^{-1}$  after having received a fluence of  $3.8 \times 10^{15} n_{eq}/cm^2$  and a corresponding dose of 3.2 MGy. For the outer part of the ITk, the maximum fluence will be  $3.0 \times 10^{15} n_{eq}/cm^2$  in the barrel and  $3.8 \times 10^{15} n_{eq}/cm^2$  in the end-cap, which corresponds to a maximal dose of 3.2 MGy after an integrated luminosity of  $4000 \text{ fb}^{-1}$ .

To maximize the geometrical acceptance of the detector, active edge technology has been investigated on planar pixel sensors. Edges etched via Deep Reactive Ion Etching (DRIE) allow to extend the depletion in the area between the last pixel and the physical edge of the sensor. Active edge sensors produced by FBK and Advacam have been irradiated and tested on beam and have demonstrated good hit-efficiency performance in the edge area, as it will be presented extensively in Chapter 7.

### 3D pixel sensors design

The 3D sensors are the baseline option for the innermost layer (Layer 0) of the ITk. 3D sensors are intrinsically radiation hard, as the columns are oriented perpendicularly to the sensor surface, hence the drift occurs laterally on a smaller distance compared to planar pixel sensors. During testbeam, heavily irradiated 3D sensors have shown excellent hit-efficiency performance, exceeding the 97 % hit efficiency when biased at a relatively low bias voltage (less than 200 V), as presented in [80]. This low operational bias voltage implies a reduced power dissipation of  $10 \text{ mW}/cm^2$ , compared to the planar pixel sensors ( $25 \text{ mW}/cm^2$ ).

The ITk innermost pixel layer (Layer 0) will be replaced after  $2000 \text{ fb}^{-1}$  which corresponds to a fluence of  $1.31 \times 10^{16} n_{eq}/cm^2$  and a dose of 7.2 MGy.

## CMOS pixel sensors design

Standard High resistivity CMOS technology are also an option for the ITk outermost layer. They are an industrial mature technology, whose cost is reduced compare to 3D and planar pixel sensors. As CMOS sensors are monolithic sensors, there is no need of bump-bonding and flip chipping sensors (which are delicate and costly operations). The drawback of such technology is its lower resistance to radiation, it has just been tested up to a fluence of about  $1 \times 10^{15} \text{ n}_{\text{eq}}/\text{cm}^2$  [107].

### 5.3.1.3 ITk Electronics & Mechanics

#### Electronics

A new readout chip, RD53 [111] is currently being developed jointly by ATLAS and CMS in the RD53 collaboration framework. The new readout-chip is based on a 65 nm CMOS technology. The pixel pitch will be  $50 \times 50 \mu\text{m}^2$ . Each readout-chip will have  $400 \times 192$  pixels. The tolerance of the actual chip prototype has been tested up to 500 MRad, it is expected to survive higher doses and tests are currently in progress. The chip is also designed to cope with Single Events Upsets (SEU), which are caused by ionization in the chip and results in an unexpected bit-flip of a digital register. To cope with SEU, some redundancy mechanisms are implemented. A first prototype, the RD53A chip [111] have been produced and is currently being tested.

#### Mechanics

The ITk pixel mechanics [107] is optimized to allow the instrumentation at high  $\eta$  and to keep the material budget at minimum. The two innermost layers are on a different structure compared to the three outermost layers as they have to be removable independently of the rest of the detector. The ITk pixel structure (presented in Figure 5.6) is divided in several parts, also represented in Figure 5.6:

- Inner pixel system: It is divided in inner flat barrel (1), barrel rings (2) and inner end-cap rings (3). The inner pixel system is encapsulated in the Inner Support Tube (IST) which span over 6 meters in length. It hosts the 2 first barrel layers (L0 and L1) of pixels, both the flat and inclined area. L0 and L1 support structures are made of truss constructions. The inner layer design structure has to be compatible with the fact that it will be removed at mid term ( $2000 \text{ fb}^{-1}$ ), due to sensor aging from fluence.
- Outer pixel barrel structure: L2 and L3 barrel layers share a common 2 m long double sided processed stave called longeron. The longeron consists of a hollow shell, the various services such as cables will run inside it. Both flat (4) and tilted (5) barrel sensors are on the same longeron. L4 support consists in a single-sided processed longeron.

- Outer pixel end caps (6): it consists in a clam-shell structure, two 2 m long half cylinder structures with 3 sets of concentric half-cylinders. Each half cylinder supports a dozen of half-rings which will host the modules, with different positions for each layers.

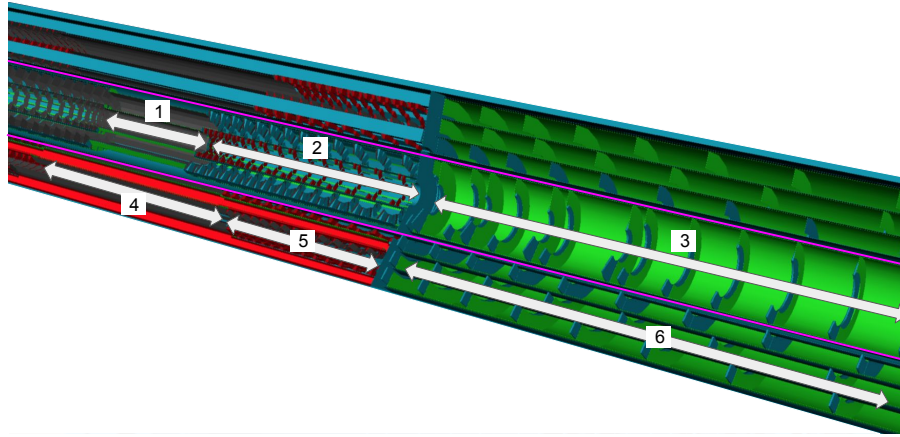


Figure 5.6 – ITk pixel layout simulation from [107]. The ITk pixel layout is divided in several parts. Parts 1 (flat barrel), 2 (inclined barrel rings) and 3 (end-caps rings) and their symmetrics are the Inner pixel system. It is limited by the Inner Support Tube (IST), represented in magenta on the Figure. Part 4 and 5 form the Outer pixel barrel: L2 and L3 are on the same double sided longeron, whereas L4 is on a single sided longeron. Part 6 is the outer pixel end-caps.

## Cooling

Concerning the cooling of modules [107]: each module, either inclined or flat, would be supported by a pyrolytic graphite plate used as a heat spreader and bonded to a cooling block (two geometries for inclined or flat section) made of a highly conductive material such as aluminium-carbon fibre or graphite. Each cooling block would be connected to titanium based cooling pipes in which will circulate some cool  $CO_2$ .

### 5.3.2 ITk Performance

In this part, the expected performance of the ITk detector are presented. The upgraded detector performance will be compared to the Run2 performance. On a first section, the focus will be on the tracking and vertexing performance. Then the expected performance of b-tagging will be described. The expected performance is estimated from simulation of events in the HL-LHC conditions, using Monte Carlo events based on a Geant4 simulation [66]. The average pile-up  $\langle \mu \rangle$  was set to 200.

### 5.3.2.1 Tracking and Vertexing

The track reconstruction efficiency and the fake rate for a  $t\bar{t}$  sample are presented in Figure 5.7. The ITk track reconstruction efficiency performs better than the Run2. Concerning the fake rate the ITk outperforms the Run2 ID by at least a factor 10 over the common  $\eta$  range and is also highly performing at high  $\eta$ .

This good tracking performance is due to three factors:

- the silicon hits requirement is higher for the ITk compare to Run 2, the track pattern recognition requires 9 hits;
- the pixel granularity is increased;
- the level arm is enlarged due to the addition of a fifth pixel layer.

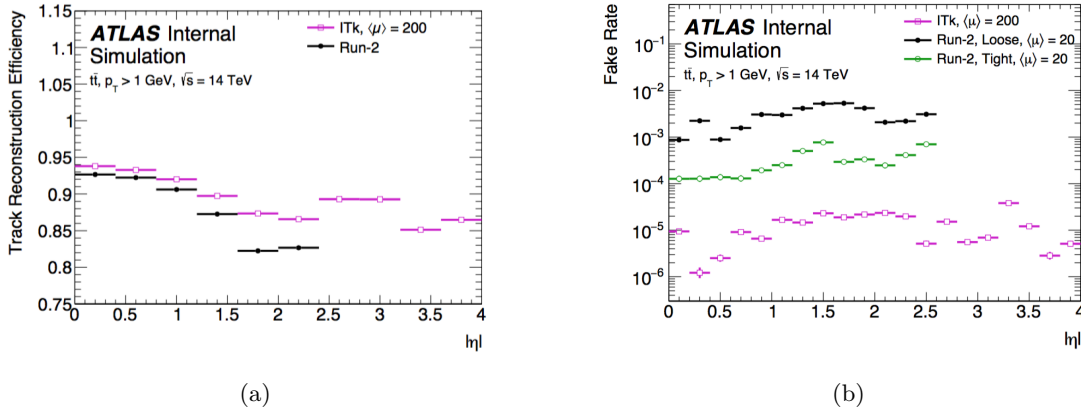


Figure 5.7 – ITk Track efficiency and fake rate compare to Run2 for  $t\bar{t}$  samples. From [107].

The track parameter resolutions have been estimated using single muons with a  $p_T > 100$  GeV/c [107]:

- $\sigma(d_0)$  is of the order of 7  $\mu\text{m}$  for the 50  $\mu\text{m} \times 50 \mu\text{m}$  option for  $\eta < 2.5$  which is comparable to the Run 2 resolution.  $\sigma(d_0)$  is significantly better (globally twice better over the full  $\eta$  range) with the 25  $\mu\text{m} \times 100 \mu\text{m}$  option. At large  $\eta$  the resolution is still good which is a bonus for b-tagging and pile-up jet rejection.
- $\sigma(z_0)$  is significantly better for ITk compared to the Run2 over the all  $p_T$  spectrum thanks to a decreased pixel pitch in the z direction.  $\sigma(z_0)$  is of the order of 10 to 30  $\mu\text{m}$  for the 50  $\mu\text{m} \times 50 \mu\text{m}$  scenario and 1 to 2.5 times worst for the 25  $\mu\text{m} \times 100 \mu\text{m}$ .
- The momentum resolution is twice better than the one obtained during Run2. The 25  $\mu\text{m} \times 100 \mu\text{m}$  performs better, especially in the forward region.

### 5.3.2.2 Flavour tagging

The flavor tagging at ITk will be helped by the addition of a fifth layer and by the increase in the geometrical acceptance. The addition of the HGTD could also help to increase the performance of low level taggers. An optimization of the current low level taggers algorithm is ongoing and will be described in details in Chapter 8. The Figure 5.8 presents the c-jet and light-jet rejection efficiency vs b-jet efficiency. The used samples consisted in  $t\bar{t}$  samples with an average pile-up of 200 and  $\sqrt{s}=14$  TeV. In the central  $\eta$  region, the ITk outperforms the Run2 performance.

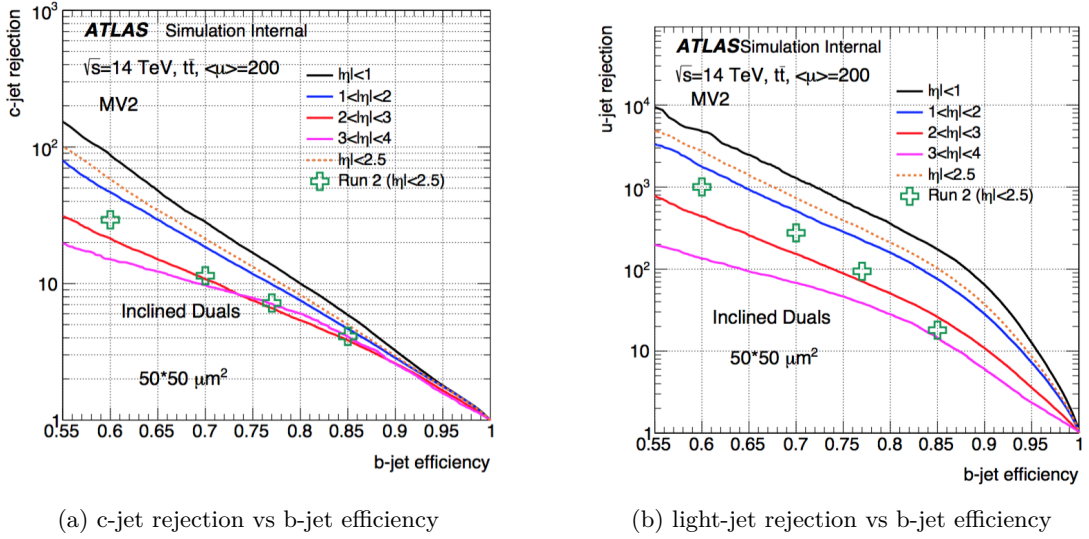


Figure 5.8 – Comparison of c-jet and light-jet rejection vs b-jet efficiency between Run2 and ITk [107].

### 5.3.2.3 Particle identification

The photon reconstruction efficiency and its resolution are extremely important for all physics channels exploiting the photon signature such as  $H \rightarrow \gamma\gamma$ . Photon can interact with the material and convert into an  $e^+e^-$  pair. As shown in Figure 5.9 a, the fraction of converted photons decreased for ITK compare to Run2 as the material budget is reduced in the ITk layout. Furthermore, as shown in Figure 5.9 b, the conversion identification efficiency is greater with the ITk layout compared to the Run2 layout.

Some other studies have been performed on  $E_T^{miss}$ , pile up jet tagging, electron, muon and taus identification are discussed in greater details in the ITk pixels TDR [107].

## 5.3.3 Physics perspectives at HL-LHC

The large dataset which will be collected by the end of the HL-LHC is expected to allow major breakthrough in different physics areas which are going to be documented in the next

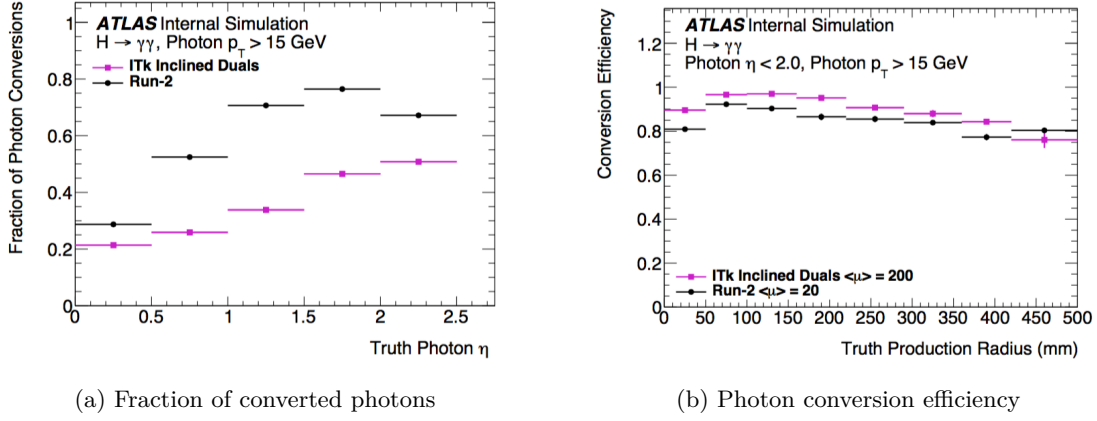


Figure 5.9 – Comparison of converted photons fractions between Run2 and ITk. Photon conversion identification efficiency for ITk [107].

section. Firstly, an increase of the precision measurements is foreseen, especially couplings of the Higgs bosons to massive particles. This large dataset will allow to start to investigate the Higgs trilinear self couplings. Last but not least, the luminosity increase will extend the reach of the LHC in terms of masses and couplings of Beyond the Standard Model scenarios. In what follow a brief overview of some of the physics cases relevant for the HL-LHC phase will be given.

### 5.3.3.1 Higgs studies

#### Precision measurements

Thanks to the good momentum resolution and improvement in b-tagging, pile-up jet tagging, photon and  $\tau$  identification, the sensitivity and accuracy for several Higgs decays will increase at HL-LHC. The mass resolution will also be improved compared to Run2. Concerning the Higgs production with muons in the final states (either  $h \rightarrow ZZ \rightarrow 4l$  or  $h \rightarrow \mu\mu$ ), the good momentum resolution provided by ITk and its large  $\eta$  coverage (as well as an upgraded muon spectrometer) allow a reduction of the width invariant mass as shown on Figure 5.10. The width of the reconstructed Higgs boson mass distribution is determined via Gaussian fits to the mass peak [107]. It is shown as a function of the rapidity of the muon with the largest  $|\eta|$  value.

#### Higgs trilinear coupling

The improvement of tracking, b-tagging performance, tagging of pile-up jets,  $\tau$  and photon identification and the enlarged dataset that will be collected during the HL-LHC lifetime will give a first estimation of the Higgs trilinear coupling. As shown in the Figure 5.11 from [117] the highest branching ratios involve b-quarks, which show the importance of an optimized b-tagging (cf Chapter 8). As previously described, ITk b-tagging performance are better than the one obtained in Run2, hence the access to the trilinear couplings could be possible

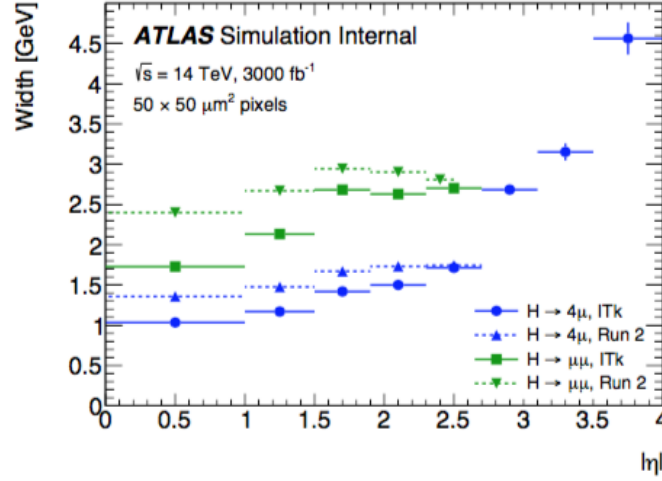


Figure 5.10 – Width of  $h \rightarrow ZZ \rightarrow 4\mu$  and  $h \rightarrow \mu\mu$  invariant mass for ITk layout (plain markers) and Run2 (dashed markers) [107].

thanks to the ITk (the best channel,  $hh \rightarrow \gamma\gamma b\bar{b}$  is expected to reach  $1.5\sigma$  after  $3000\text{ fb}^{-1}$  [107]).

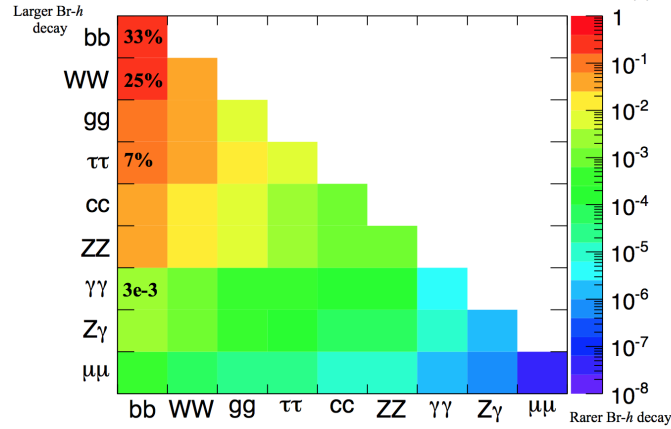


Figure 5.11 – HH branching ratios coupling [117]

### 5.3.3.2 Supersymmetry & exotics

The increased luminosity and the development of performance especially in dense environment is a critical aspect for BSM searches. BSM particles of several theories (e.g leptophobic  $Z'$  [107]) decay primarily in a  $t\bar{t}$  pair. Due to the high mass of the BSM particles, the  $t\bar{t}$  pair will be highly boosted and the produced jets will be extremely collimated. To detect such events, the improvement of b-tagging and of tracking in dense environments permitted by the use of the ITk layout is of the uttermost importance.

## Conclusions

In this Chapter, the importance of an upgrade of the Inner tracker of the ATLAS experiment to cope with the challenging conditions of the HL-LHC has been discussed: thanks to the new tracker, performance are expected to reach or even outperform the current Run2 performance, which enlarges the spectrum of physics prospects. The pixel sensors are at the core of the ITk and their radiation hardness is of crucial importance to deal with the high data rate of the HL-LHC. In the two next chapters, pixel sensor productions for ITk will be discussed (Chapter [6](#)) and their performance in beam will be investigated (Chapter [7](#)).



## Chapter 6

# Silicon pixel sensors for ATLAS ITk

### Contents

---

<b>6.1</b>	<b>FBK-LPNHE Productions . . . . .</b>	<b>101</b>
6.1.1	Production 1: Active edge sensors . . . . .	105
6.1.2	Production 2: Thin sensors . . . . .	107
6.1.3	Irradiation of the second production . . . . .	108
6.1.4	Production 3: Thin and Active edge sensors . . . . .	112
6.1.5	RD53A compatible sensors . . . . .	115
<b>6.2</b>	<b>Pixel module tuning . . . . .</b>	<b>116</b>

---

In this chapter the characteristics of pixel sensors produced by LPNHE, FBK<sup>1</sup> and INFN<sup>2</sup> and aimed at the ATLAS ITk will be presented. Their performance on beam will be discussed in the next chapter.

## 6.1 FBK-LPNHE Productions

To cope with the harsh environment foreseen at the high luminosity conditions of HL-LHC, the ATLAS pixel detector has to be upgraded to be fully efficient with a good granularity, a maximized geometrical acceptance and an high read out rate, as presented in the previous Chapter.

LPNHE, FBK and INFN are involved in the development of thin and edgeless planar pixel sensors whose goal is to be fully efficient after having received an ITk-like fluence.

---

<sup>1</sup>FBK-CMM (Trento, Italy): <http://cmm.fbk.eu/>

<sup>2</sup>INFN: [home.infn.it/en/](http://home.infn.it/en/)

Thinning down the sensor allows to mitigate the charge trapping effect caused by radiation. A passivation layer (BCB), has also been added on top of sensors (in Productions 2 and 3) before irradiation: this passivation layer allows to avoid discharge between the chip and the sensor when the latest is biased at High Voltage, the sensor can then be biased at higher voltage which increases the overall charge collection efficiency and hit efficiency.

Edgeless sensors consist in sensors in which the insensitive area at their borders is minimized thanks to the active edge technology. As explained in 3.3.1, thanks to an ion etched trench at the edge of the sensor, the sensor lateral depletion can be extended up to a few micrometers from the edge [81]. Results from testbeam of un-irradiated and irradiated sensors of Productions 1 and 3 will be presented in the next chapter.

Two biasing options have been tested: a standard punch through option for Production 2 sensors and a temporary metal option for Productions 1 and 3. Both biasing processes have been described in 3.3.1, the temporary metal is expected to get rid of the inefficiencies observed on the punch through structures. Results on biasing options will be presented at the end of the next Chapter.

Three productions of n-on-p planar pixel sensors have been designed, produced and tested on beams. The sensors of the three productions were bump-bonded to FE-I4B [46] readout chips at IZM Berlin<sup>3</sup>. Each pixel sensor is composed of 336 rows  $\times$  80 columns of rectangular pixels cells whose dimensions are 50  $\mu\text{m}$   $\times$  250  $\mu\text{m}$ . The three productions characteristics are summarized in Table 6.1.

The thickness of the sensors varies among the productions: the first production (LPNHE5 and LPNHE7 modules) consisted in 200  $\mu\text{m}$  thick sensors, whereas the second (W30 and W80 modules) and third one (M1.4 module) consist in thinner sensors of a thickness of 130  $\mu\text{m}$  or 100  $\mu\text{m}$ . The first production was intended as a first step toward edgeless radiation-hard pixel modules; to be radiation hard, thinner sensor wafers such as the one of the second and third pixels production are needed, to better cope with the high fluences expected at the HL-LHC [107].

The first and third productions are active edge sensors (standard active edge for the first one, staggered active edge for the third one). The active edge technology allows to reduce the insensitive area at the border of the sensor thanks to an ion etched trench which avoids the crystal damage produced by the standard mechanical dicing process [118]. Further details on the active edge can be found in Section 3.3.1 and in the sections dedicated to the first and third productions.

A section of the sensor is presented in Figure 6.1. On top of the p-type bulk (of various thicknesses from a production to an other), one can find a n+ type implantation. The implant width is of the order of 30  $\mu\text{m}$  in the short pixel direction and of 230  $\mu\text{m}$  in the long pixel direction, as shown in Figure 6.2. For the three productions, a uniform layer of p-doped silicon (p-spray) has been used to ensure the inter pixel isolation. In addition, at the virtual

---

<sup>3</sup>Fraunhofer-Institut für Zuverlässigkeit und Mikrointegration IZM - Gustav-Meyer-Allee 25, 13355 Berlin, Germany

Table 6.1 – Characteristics of the three production sensors tested on beam. GR refers to Guard Rings. The biasing system refers to the biasing process used to polarize the sensor before bump-bonding. TM stands for Temporary Metal and PT for Punch-Through. The 2 pixel to trench distances given for M1.4 sensor from the third production refers to the innermost and outermost edge fences.

	Production 1		Production 2		Production 3
Module names	LPNHE 5	LPNHE7	W30	W80	M1.4
Thickness (μm)	200	200	100	130	130
Active edge	Yes, classic trench		No		Yes, staggered trench
Number of GR	0	2	5	2	0
Trench distance (μm)	100		-		37 and 52
P-spray	Yes				
P-stop	Yes	No	No		Yes
Biasing system	TM		PT		TM
Irradiation limit ( n <sub>eq</sub> /cm <sup>2</sup> )	Unirradiated		1.4 × 10 <sup>16</sup>		2.7 × 10 <sup>15</sup>
Depletion Voltage (V)	For Unirradiated sensors: 20 V				

pixel limit between two implants, a thin strip implant of highly p-doped silicon (called p-stop) can be found for productions 1 and 3; it is presented as the green rectangle surrounding the pixel cell in Figure 6.2. On top of the implant one can find a layer of thermally grown oxide. Several apertures on the oxide are performed to put on contact the n+ implant and the layer of aluminum (electrode) on top. The electrode pattern can be seen in brown in Figure 6.2, its width is of the order of  $35 \mu\text{m}$  in the short pixel direction and of  $240 \mu\text{m}$  in the long pixel direction. On top of the alumina, a passivation layer is deposited, it consists of silicon oxide and nitride, its goal is to ensure chemical and mechanical resistance of the sensor. An aperture in the passivation layer (represented by the circles in 6.2) allow the electrode to be in contact with the metallic bumps. The readout-chip is then connected on top of the sensor through bump bonding.

From the Figure 6.2, one can notice the different biasing techniques used to bias the sensor before bump-bonding: productions 1 and 3 use temporary metal line (dashed blue strips on top of the bump bonding aperture) whereas the production 2 uses punch through. From this Figure, the shape of the implant can also be compared between the three productions: the implant of the third one is more squared in the corners, which reduces the distance between the implant and the virtual corner of the pixel.

In this chapter the three production designs will be presented, as well as their behaviors in terms of leakage current and power dissipation after irradiation.

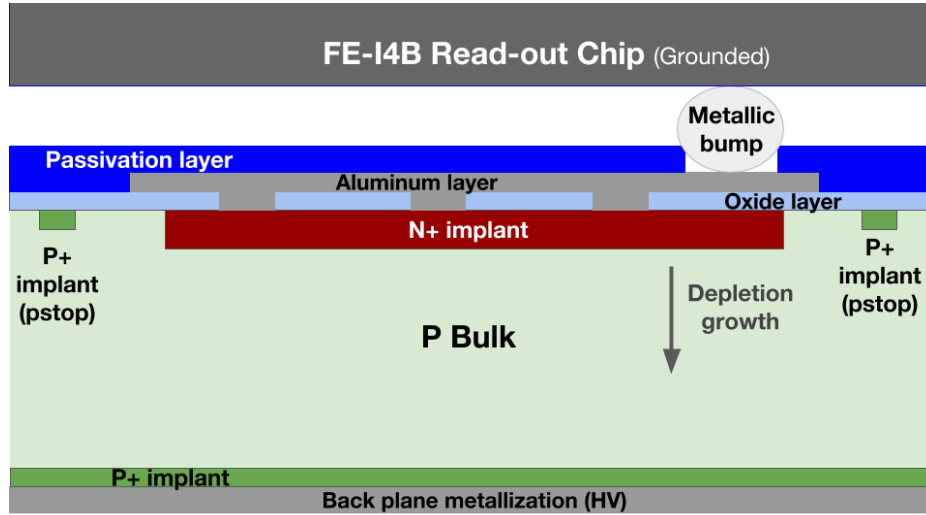


Figure 6.1 – Section of a pixel sensor, not to scale.

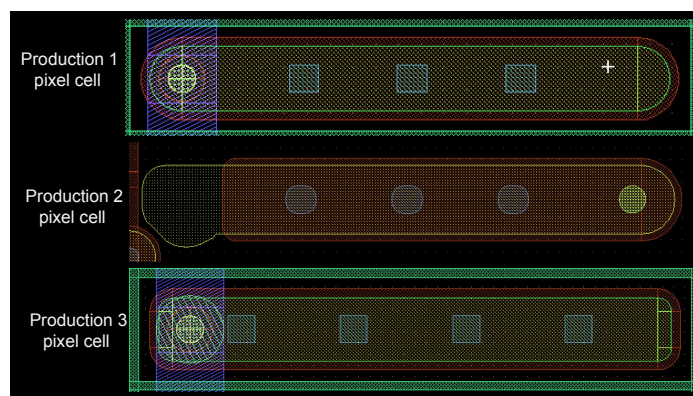


Figure 6.2 – Details of the pixel cell for the three LPNHE/FBK productions.

### 6.1.1 Production 1: Active edge sensors

The first ITk sensor production [119] that has been designed and produced by LPNHE and FBK foundry featured 200  $\mu\text{m}$  thick n-on-p pixel sensors whose boundaries are delimited by an active edge. Two detector module prototypes, have been tested with beams at CERN and DESY. Their performance will be detailed in the next chapter. The active edge is one of the possible choices to realize edgeless detectors, *i.e.* detectors with no (or very limited) insensitive area at the edge. Figure 6.3 features a scheme of the trench and a SEM photo of a trench. Along the sensor border a trench is dug by deep reactive ion etching (DRIE), reaching through the whole thickness of the substrate (hence a support wafer is required). The trench is then doped with boron and filled with polysilicon. The cut realized through DRIE produces an edge region much less damaged than the one resulting from a standard diamond-saw cut. This leads to less generation centers and implies lower leakage current generated at the border. Moreover, the edge doping prevents the depletion region from reaching the physical trench walls, hence carriers created at the edge do not experience an electric field, are not effectively separated and just recombine, without contributing significantly to the device leakage current. Three sensors of this first production were bump-bonded at IZM. Their

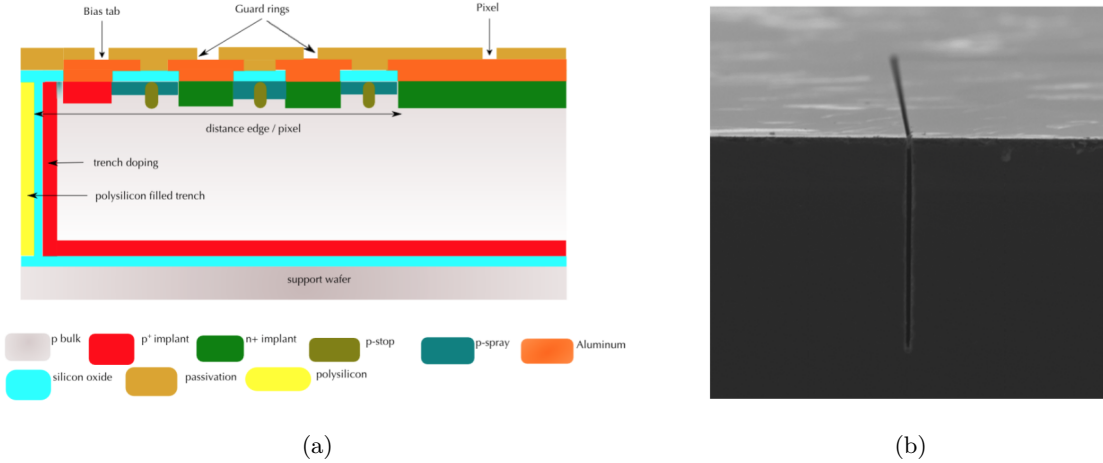


Figure 6.3 – (a) Scheme of a depth cut of the edge area of an active edge sensor from the first production, the bias tab is only on one edge of the device. (b) SEM picture of a test trench structure. From [119].

pixel to trench distance was 100  $\mu\text{m}$ , they differ by the number of guard rings (GRs) surrounding the active area, ranging from zero to two. In Figure 6.4 a detail of the sensor edge can be seen for all the three samples.

This sensor production was also equipped with a temporary metal grid [120] shorting the pixels of one column before bump-bonding. This temporary metal was used at wafer level for checking the sensor current; it was further removed from the tested detectors. The temporary metal line can be seen in the pictures in Figure 6.4. LPNHE5 has no GRs, LPNHE4 has one GR and LPNHE7 has two GRs. All sensors include a uniform p-spray implant on the pixel side to provide enough insulation among them. LPNHE4 and LPNHE5 sensors have,

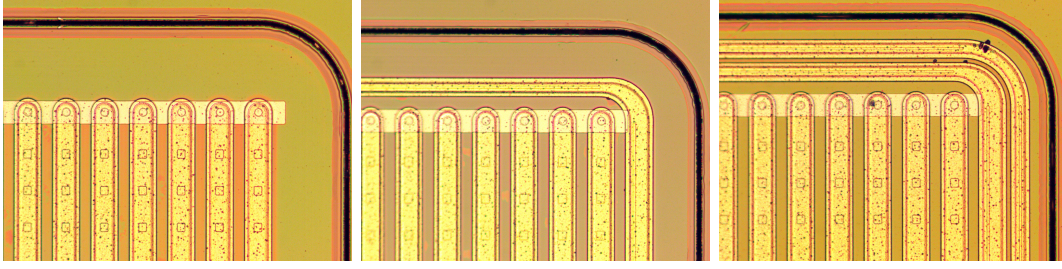


Figure 6.4 – Microscope picture of corners of the three bump-bonded sensors of the first production: LPNHE5 (left), LPNHE4 (middle) and LPNHE7 (right). The black line at the top and on the right is the trench. The shortest distance from the pixels to the trench is  $100\text{ }\mu\text{m}$  for all the three sensors. For LPNHE4 there is one GR surrounding the pixel matrix; for LPNHE7 there are two GRs.

in addition, p-stops implants that surround the implants of pixels and GRs, as shown in Figure 6.5. The main characteristics of the devices are summarized in Table 6.2.

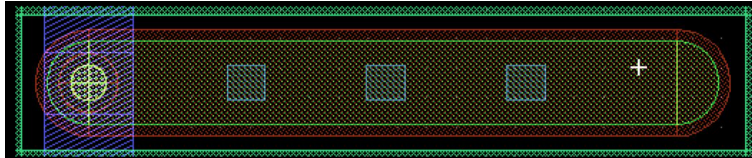


Figure 6.5 – Details of a pixel of the first production

Table 6.2 – Tested devices characteristics.

Name	Number of GRs	p-stop implant
LPNHE5	0	yes
LPNHE4	1	yes
LPNHE7	2	no

The performance of un-irradiated LPNHE5 and LPNHE7 devices are detailed in the next chapter. The LPNHE4 module was used in an irradiation experiment before the beam tests. Laboratory measurements after irradiation showed that, due to the lack of electrical insulation layer between the sensor and the FEI4-B readout chip, it could not be biased up to full depletion. Hence there will not be results for irradiated detectors from this pixel sensor production.

During all measurements the innermost GR, if present, was kept at ground voltage by the FEI4B readout chip; the second GR, when present, was left floating. The depletion voltage for all three devices was about 20 V.

The effect of GRs on the breakdown voltage can be seen in Figure 6.6, where the current-voltage curves of test structures featuring FEI4-like pixels and different number of GRs are reported; the distance between the last pixels and the doped trench is  $100\text{ }\mu\text{m}$ . These test structures come from the same wafer of the sensors tested on beam. The breakdown voltage increases by more than 70% (from 70 to 120 V) by adding a second, floating GR.



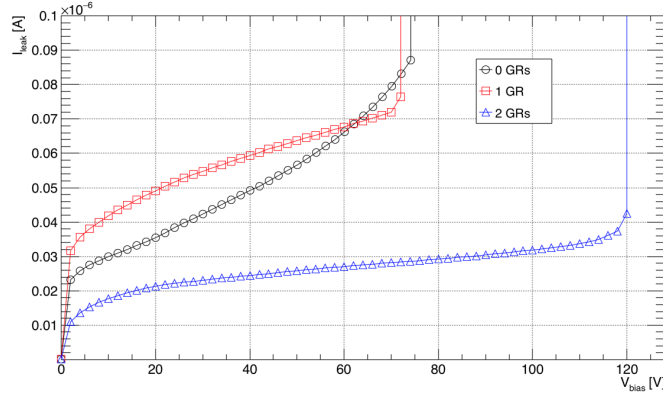


Figure 6.6 – Current-Voltage curves for test structures featuring different number of GRs. The innermost GR, if present, was kept at ground voltage. The shortest distance from the pixels to the trench is 100  $\mu\text{m}$ . The measurement for the test structure with 2 GRs was taken at a lower temperature with respect to the other two samples.

### 6.1.2 Production 2: Thin sensors

The second pixel production consists of thin  $n-on-p$  planar pixel sensors (100  $\mu\text{m}$  and 130  $\mu\text{m}$  thick sensors), realized at FBK on high resistivity 6 inches wafers (as a reminder, the previous one was produced on 4-inches wafers) within the framework of the INFN Phase-2 program [121]. Such thin sensors are more suitable in hard radiation environment as they are less sensitive to charge trapping. Si-Si Direct Wafer Bonded (DWB) wafers were chosen to fabricate pixel detectors; Si-Si DWB are obtained bonding together two different wafers: a high-resistivity (HR) Float Zone sensor wafer and a low-resistivity (LR) Czochralski handle wafer. The FZ wafer is thinned to the desired thickness value, so as to obtain a wafer with a thin active layer plus a relatively thick mechanical support layer. P-type wafers of two different active depths (100 and 130  $\mu\text{m}$ ) with 500  $\mu\text{m}$  thick handle wafer were used. The wafer layout included compatible single and double FE-I4 chip [46] modules, with pixel pitch of  $50 \times 250 \mu\text{m}^2$ . In Figure 6.7 a picture of one wafer from this production.

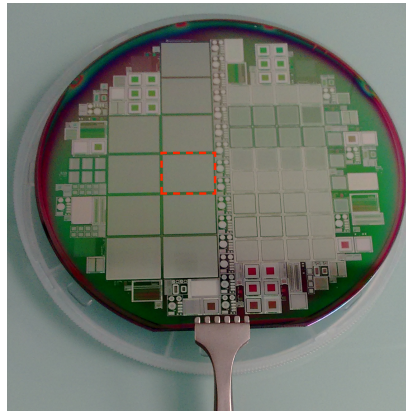


Figure 6.7 – Wafer from the  $n-on-p$  planar technology production [121] whose layout was mainly based on ATLAS FE-I4 and CMS PSI46 [122] designs. The red rectangle encircles one pixel sensors compatible with the FE-I4 readout chip.

Two sensors of this production were bump-bonded and tested on beams: *W80* and *W30*. This production was not equipped with active edges, the two tested sensors edge to pixel distances were 450  $\mu\text{m}$ . The two sensors differed by their thicknesses 130 (100)  $\mu\text{m}$  for W80 (W30) and by their number of guard rings, 5 and 2 respectively. In both detector assemblies the 500  $\mu\text{m}$  thick handle wafer was not thinned. A BenzoCycloButene (BCB) passivation layer was deposited on sensors for spark protection between the chip, kept at ground, and the sensor edges, at high voltage.

This second production is not equipped with temporary metal as the first one but with traditional punch through biasing system, which can be seen in the pixel detail scheme of Figure 6.8.

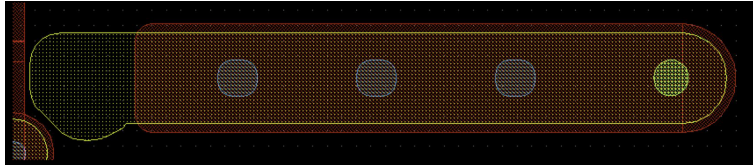


Figure 6.8 – Pixel details of the second production. At the bottom left, part of the bias dot and metal bias line can be seen.

### 6.1.3 Irradiation of the second production

W80 and W30 sensors were irradiated up to a cumulative fluence of  $1 \times 10^{16} \text{ n}_{\text{eq}}/\text{cm}^2$  at CERN IRRAD<sup>4</sup> facility with a beam of 24 GeV/c protons. The irradiation was staged in two steps, a first irradiation of  $\simeq 3 \times 10^{15} \text{ n}_{\text{eq}}/\text{cm}^2$ , followed by a second one few months later of  $\simeq 7 \times 10^{15} \text{ n}_{\text{eq}}/\text{cm}^2$ ; in Table 6.3 the detail of the irradiation program of W80 and W30 is described.

Table 6.3 – Irradiation program for the two FE-I4 pixel modules *W80* and *W30*.

Module name (thickness [ $\mu\text{m}$ ], # of GRs)	Beam spot size (FWHM - [ $\text{mm}^2$ ])	Fluence $\phi$ [ $10^{15} \text{ n}_{\text{eq}}/\text{cm}^2$ ]	Cumulative fluence $\Phi$ [ $10^{15} \text{ n}_{\text{eq}}/\text{cm}^2$ ]
W80 (130, 2)	$20 \times 20$	3	same
W30 (100, 5)	$12 \times 12$	4	same
W80 (130, 2)	$20 \times 20$	7	10
W30 (100, 5)	$20 \times 20$	7	11

Several beam position monitors (BPMs), which register the beam intensity during the irradiation along the horizontal and vertical direction orthogonal to the beam, allow to reconstruct the beam profile, which is presented in Figure 6.9. The irradiation beam profile for W80 was gaussian with a FWHM of 20 mm. The accuracy in the position determination is of the order of 2 mm, which include the different sources of misalignment. The two projections have been fitted with a gaussian to determine the center position and the beam widths.

<sup>4</sup><http://ps-irrad.web.cern.ch/>



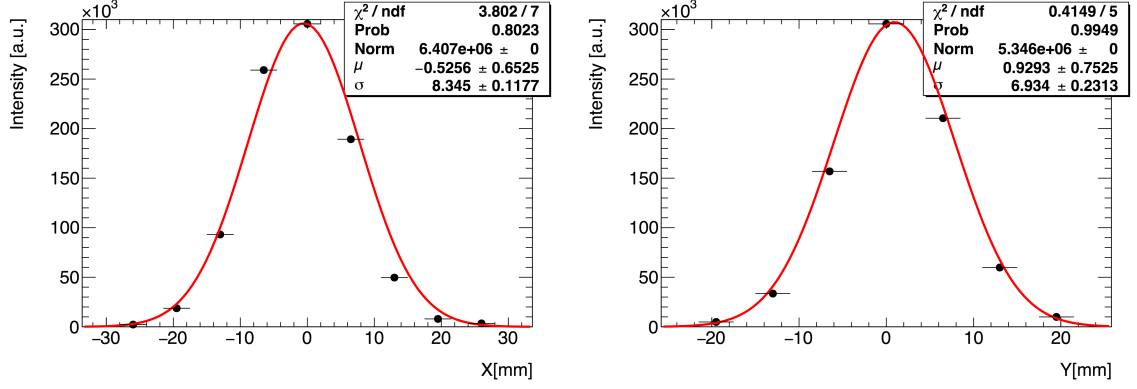


Figure 6.9 – Projections of the proton beam profile used at CERN IRRAD to irradiate the W80 module. Left: horizontal direction; right: vertical direction. A gaussian fit is superimposed. The (0,0) position correspond to the nominal beam center.

It can be seen that the center vertical position is not compatible with  $y = 0$ ; this has been confirmed by the IRRAD facility managers.

The Figure 6.10 presents the beam profile intensity after the first irradiation (Left plot) and after the second irradiation (Right plot). After the second irradiation, the peak fluence is  $1.4 \times 10^{16}$  n<sub>eq</sub>/cm<sup>2</sup> and the average fluence across the sensor is  $1 \times 10^{16}$  n<sub>eq</sub>/cm<sup>2</sup>. At the detector periphery the fluence is as low as  $\Phi = 3.5 \times 10^{15}$  n<sub>eq</sub>/cm<sup>2</sup>.

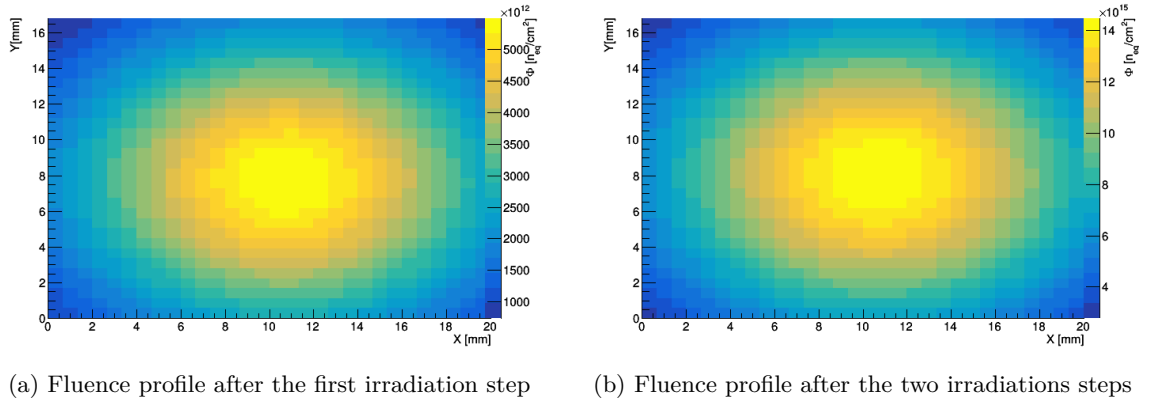


Figure 6.10 – Fluence profile for W80 module after the the first (Left plot) and second irradiation step (Right plot). The area reported corresponds to the surface of the pixel module.

The dosimetry information made possible to estimate the total delivered proton fluence, transformed then into n<sub>eq</sub>/cm<sup>2</sup> using an hardness factor of  $\kappa = 0.59$ , with an uncertainty of about 10%.

Thanks to the high segmentation of the detector modules it was then possible to probe several fluences over a large range of values with just one pixel detector.

In the two upcoming paragraphs, the leakage current and power dissipation of W80 sensor will be reported. The measurements of the leakage current and the sensor power dissipation were performed with the electronic chip powered on.

### Leakage current

The leakage current  $I_{leak}$  of W80 module was measured after each irradiation steps at low temperature. Its evolution as a function of the bias voltage is presented in Figure 6.11.

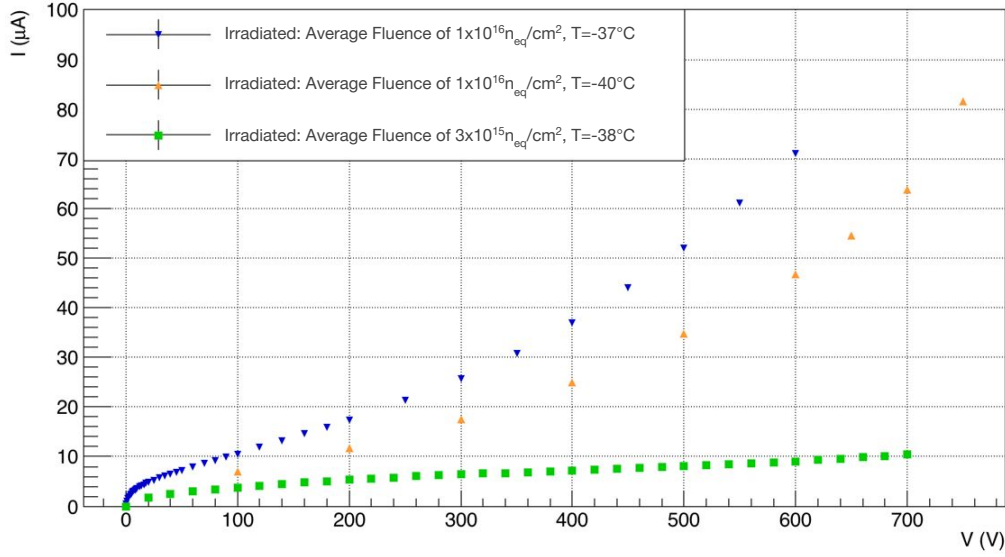


Figure 6.11 – Current-Voltage curves of W80 sensor after a fluence of  $3 \times 10^{15} \text{ n}_{eq}/\text{cm}^2$  (green markers) and after an cumulative fluence of  $1 \times 10^{16} \text{ n}_{eq}/\text{cm}^2$  (blue and yellow markers). The temperature is indicated in the legend.

The leakage current ( $I$ ) is known to increase linearly with the fluence ( $\Phi$ ):  $\Delta I = \alpha V \Phi$ , where  $\alpha \sim 4 \times 10^{-17} \text{ A/cm}$  and  $V$  is the volume of the sensor [85]. The defects in the bulk act as emission center of electrons and holes and this leads to increase of the leakage current in the sensor. By comparing the two fluences  $3 \times 10^{15} \text{ n}_{eq}/\text{cm}^2$  and  $1 \times 10^{16} \text{ n}_{eq}/\text{cm}^2$  at  $-38^\circ\text{C}$  it is clear from the plateau of the curves that radiations induce an increase of the leakage current: at 600 V,  $I_{leak}(\Phi = 3 \times 10^{15} \text{ n}_{eq}/\text{cm}^2) \simeq 9 \mu\text{A}$  and  $I_{leak}(\Phi = 1 \times 10^{16} \text{ n}_{eq}/\text{cm}^2) \simeq 71 \mu\text{A}$ .

Due to the variation of the intrinsic charge density with temperature, the leakage current dependency on temperature is large, as shown from the comparison of the two IV curves at a fluence of  $1 \times 10^{16} \text{ n}_{eq}/\text{cm}^2$  at  $-40^\circ\text{C}$  and at  $-37^\circ\text{C}$ . At 600 V, the leakage current at  $-40^\circ\text{C}$  is  $47 \mu\text{A}$ , it ramps up to  $71 \mu\text{A}$  at  $-37^\circ\text{C}$ . Part of the increase could also be due to the self-heating of the pixel module.

W80 sensor has spent several weeks in an environment where the temperature was not controlled; especially just after the irradiation phases for deactivating purpose in the CERN Irradiation facility. The  $\alpha$  value is then expected to have decreased due to this prolonged

stay at room temperature [85]. The values of  $\alpha$  can be found in Table 6.4, using two hypothesis concerning the activation energy of silicon sensors after irradiation,  $E_{eff} = 1.12 \text{ eV}$  from recent studies (see [123, 124]) and  $E_{eff} = 1.21 \text{ eV}$  which is the commonly accepted value (see [125]). All the  $\alpha$  values found from the two hypothesis are of the correct order of magnitude  $O(10^{-17} \text{ A/cm})$ . The  $\alpha$  values at  $\Phi = 3 \times 10^{15} \text{ n}_{eq}/\text{cm}^2$  are close to the reference value ( $4 \times 10^{-17} \text{ A/cm}$ , see section 3.4.2.1), whereas those values are increased at  $\Phi = 1 \times 10^{16} \text{ n}_{eq}/\text{cm}^2$ . This discrepancy can be related to the annealing phenomenon which was not monitored.

Table 6.4 –  $\alpha$  values for W80 sensors for two fluences and different temperatures. The uncertainty on the values is obtained by increasing or decreasing the temperature by  $1^\circ\text{C}$ .

	$\alpha$ ( $10^{-17} \text{ A/cm}$ )	
	$E_{eff} = 1.12 \text{ eV}$	$E_{eff} = 1.21 \text{ eV}$
$\Phi = 3 \times 10^{15} \text{ n}_{eq}/\text{cm}^2, \quad T = -38^\circ\text{C}$	$2.6 \pm 0.4$	$4.0 \pm 0.6$
$\Phi = 1 \times 10^{16} \text{ n}_{eq}/\text{cm}^2, \quad T = -40^\circ\text{C}$	$5.2 \pm 0.7$	$8.2 \pm 1.2$
$\Phi = 1 \times 10^{16} \text{ n}_{eq}/\text{cm}^2, \quad T = -37^\circ\text{C}$	$5.3 \pm 0.7$	$8.2 \pm 1.2$

### Power dissipation of irradiated pixel detectors

An other interesting observable which is linked to the leakage current is the power dissipation of irradiated pixel sensors. ITk specifications [107] impose some restrictions on the power dissipation at the end of the detector life time. The power dissipation of the sensor is expressed here as the product of the leakage current and of the bias voltage. In the Figure 6.12, the power dissipation of the sensor per  $\text{cm}^2$  is presented for data taken at  $-40^\circ\text{C}$ . At  $3 \times 10^{15} \text{ n}_{eq}/\text{cm}^2$ , the power dissipation for a bias voltage of  $600 \text{ V}$  is of the order of  $1.5 \text{ mW}/\text{cm}^2$ . For the same bias voltage but irradiated up to  $1 \times 10^{16} \text{ n}_{eq}/\text{cm}^2$  it reaches  $10 \text{ mW}/\text{cm}^2$ . The leakage current doubles every  $7^\circ\text{C}$ , which means that at the temperature operating point of the ITk ( $-25^\circ\text{C}$ ), the power dissipation of the sensor of the second production would be of the order of  $6 \text{ mW}/\text{cm}^2$  when irradiated at  $3 \times 10^{15} \text{ n}_{eq}/\text{cm}^2$  (which is lower than the ITk requirement for sensor exposed at a fluence of  $2 \times 10^{15} \text{ n}_{eq}/\text{cm}^2$  [107]) and at about  $40 \text{ mW}/\text{cm}^2$  when irradiated up to  $1 \times 10^{16} \text{ n}_{eq}/\text{cm}^2$ , which is of the same order ( $25\text{-}45 \text{ mW}/\text{cm}^2$ ) as  $100 \mu\text{m}$  thick ITk pixel sensors from VTT as presented in [126].

By comparison, the power dissipation of 3D pixel sensors [80] exposed to a fluence of  $1 \times 10^{16} \text{ n}_{eq}/\text{cm}^2$  have been recently estimated to be of the order of  $8 \text{ to } 10 \text{ mW}/\text{cm}^2$  at  $-25^\circ\text{C}$ , close to four times less than what we estimated for W80 sensor.

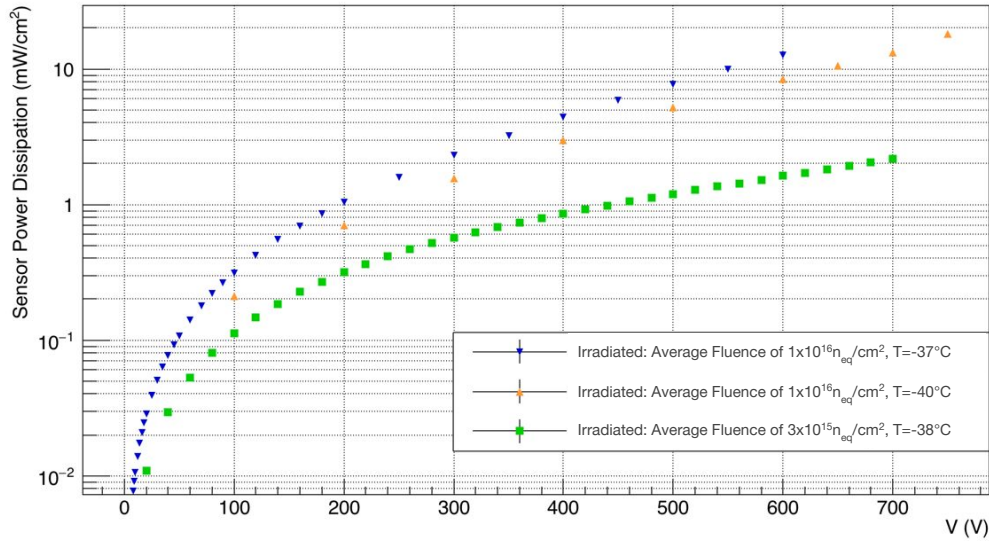


Figure 6.12 – Sensor power dissipation curves of W80 sensor after a fluence of  $3 \times 10^{15} \text{ n}_{\text{eq}}/\text{cm}^2$  (green markers) and after a fluence of  $1.1 \times 10^{16} \text{ n}_{\text{eq}}/\text{cm}^2$  (blue, yellow and red markers). The green, blue and yellow markers gives results obtained at  $\simeq -40^\circ\text{C}$ .

#### 6.1.4 Production 3: Thin and Active edge sensors

The last production [127] combines the two technologies previously presented as it features active edge sensors on thin substrates. Two bulk thicknesses are considered: 100  $\mu\text{m}$  and 130  $\mu\text{m}$  as the silicon substrates were the same as the second production. The distance between the trench and the last pixel has been reduced down to 50  $\mu\text{m}$ , while the number of guard rings was at maximum 1.

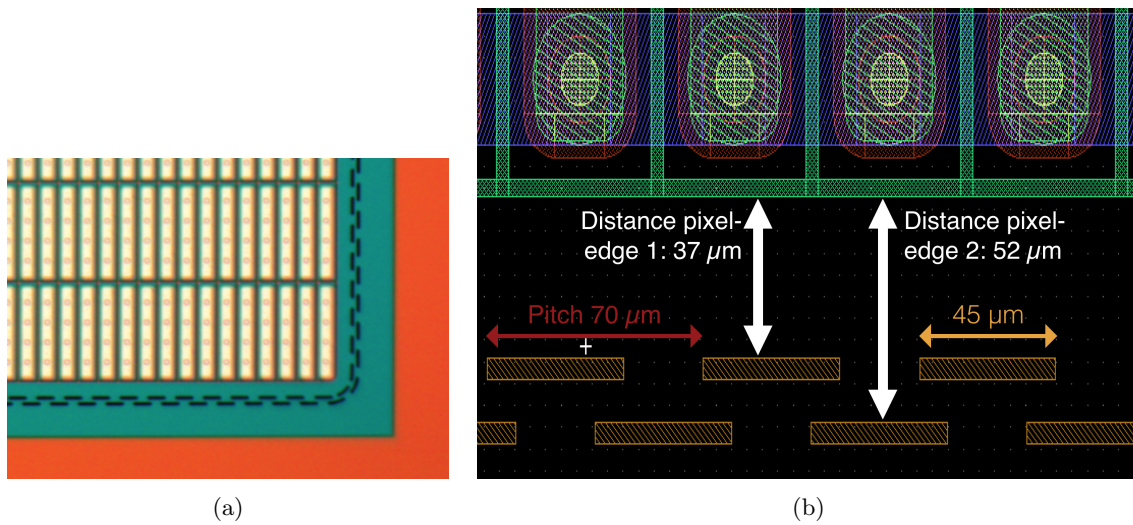


Figure 6.13 – Details of the third production staggered edge. The Figure (a) presents a large view of one of the corner of M1.4 sensor. In Figure (b) the pixel to edge distances, the edge pitch and the segments dimensions are reported.

The design of the active edge is different than the one used in the first production as it consists of a staggered trench whose dimensions are documented in Figure 6.13. It is composed of two fences of edge segments surrounding the active area of the sensor. The first edge fence starts at 37  $\mu\text{m}$  from the last pixel limit and the second one starts at 52  $\mu\text{m}$ . The segments, which pass through the whole sensor thickness, have a pitch of 70  $\mu\text{m}$  and a length of 45  $\mu\text{m}$ . The dicing lane is 350  $\mu\text{m}$  away from the outermost trench fence; as a first test of this new edge design, a conservative distance for the distance between the last fence and the dicing line has been adopted. For future productions, this distance will be reduced. One of the advantages of this new edge design is that in principle the sensor wafer does not require a support wafer.

Concerning the pixel design, the implant is wider with respect to the first two productions, and the corners are more squared than the previous productions as indicated in Figure 6.14. A temporary metal line, similar to the one used in the first production, was deposited to bias the sensor before bump-bonding and removed after the electrical test phase.

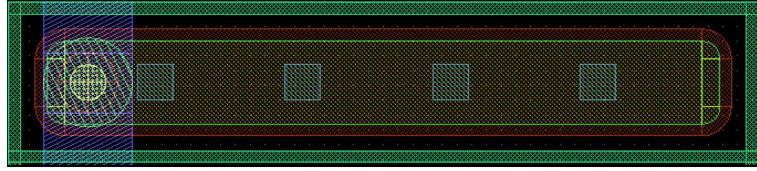


Figure 6.14 – Pixel scheme of the third production.

One sensor of this production, named M1.4, was tested on beam before and after irradiation. M1.4 is 130  $\mu\text{m}$  thick, its pixel to trench distance is  $\simeq 50$   $\mu\text{m}$  (37  $\mu\text{m}$  for the innermost fence and 52  $\mu\text{m}$  for the outermost) and it does not possess guard rings. M1.4 was uniformly irradiated at KIT [128] with 23 MeV protons to reach a fluence of  $2.7 \times 10^{15}$   $\text{n}_{\text{eq}}/\text{cm}^2$ , with an uncertainty of 10 % on the fluence. The irradiation happened in a cooled box at a temperature of -30  $^{\circ}\text{C}$ . Afterwards the sensor was kept in a freezer to prevent annealing.

The irradiated sensor shows an early breakdown around 90 V as presented in Figure 6.15. The value of  $\alpha$  was also evaluated for M1.4 at 90 V: for the hypothesis of  $E_{\text{eff}} = 1.12$  eV,  $\alpha$  is found to be equal to  $0.94 \pm 0.10 \times 10^{17}$  A/cm; for the hypothesis of  $E_{\text{eff}} = 1.21$  eV,  $\alpha = 1.46 \pm 0.2 \times 10^{17}$  A/cm, where the uncertainties are due to the current scaling with temperatures and temperatures uncertainties ( $\pm 1^{\circ}\text{C}$ ). This low value of  $\alpha$  compared to the reference value of  $4 \times 10^{17}$  A/cm could indicate that the sensor is not entirely depleted which is expected due to the observed early breakdown.

### Power dissipation after irradiation

In the Figure 6.16, the power dissipation per  $\text{cm}^2$  of the M1.4 sensor is presented for data taken at -40  $^{\circ}\text{C}$ . At a fluence of  $2.7 \times 10^{15}$   $\text{n}_{\text{eq}}/\text{cm}^2$ , the power dissipation for a bias voltage of 90 V (for which we were able to collect good data during testbeam as presented in next Chapter) is less than 0.1  $\text{mW}/\text{cm}^2$ . After 90 V, the breakdown regime develops. At 110 V,



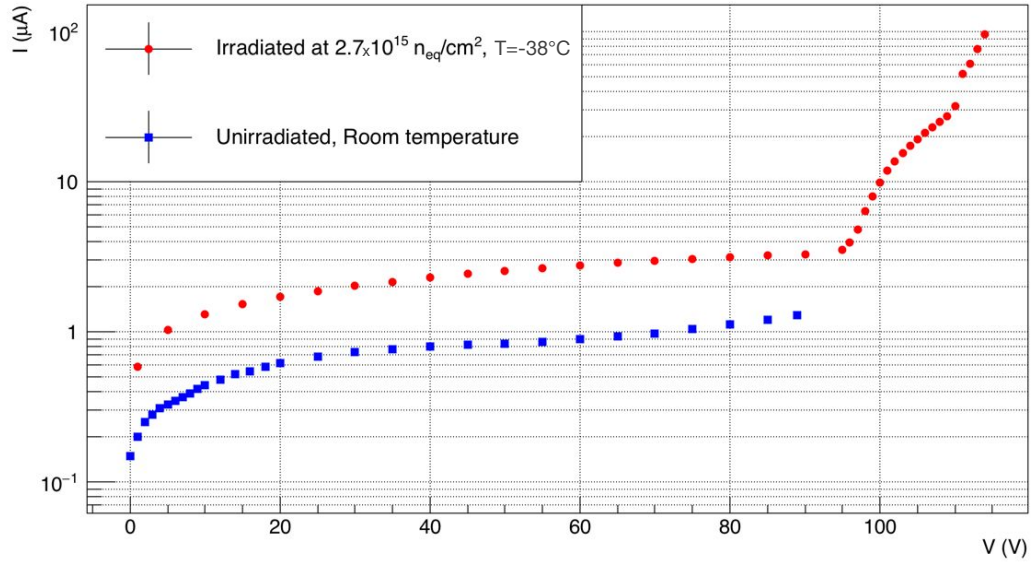


Figure 6.15 – Current-Voltage curves of M1.4 before and after irradiation.

the power dissipation is 10 times what it is at 90 V. At the operating point of the ITk ( $-25^{\circ}\text{C}$ ), the power dissipation of the sensor of the third production would be of the order of  $0.4 \text{ mW}/\text{cm}^2$  when irradiated at  $2.7 \times 10^{15} \text{ n}_{\text{eq}}/\text{cm}^2$ , which is approximately one order of magnitude below W80 results at the same fluence. It can be explained because of the low operational bias point of M1.4 implied by its early breakdown.

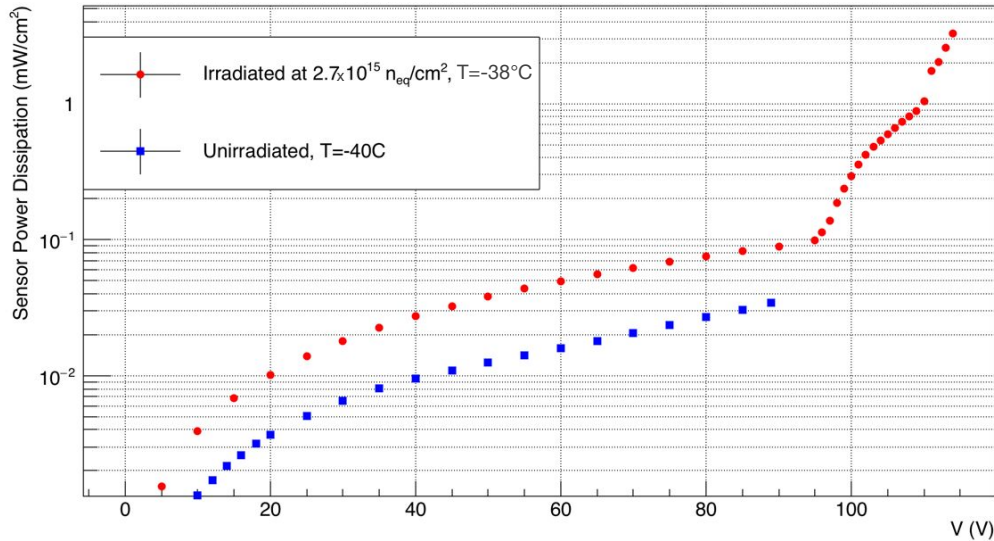


Figure 6.16 – Sensor Power dissipation curve of M1.4 before and after irradiation.

### 6.1.5 RD53A compatible sensors

RD53A [111] compatible sensors were included in the third LPNHE production. Sensors from seven wafers containing for a total of 49 RD53-compatible sensors, have been already processed and some were flip-chipped at IZM. On each wafer, there are seven RD53 compatible sensors, including five  $50\text{ }\mu\text{m} \times 50\text{ }\mu\text{m}$  pitch pixels and two  $25\text{ }\mu\text{m} \times 100\text{ }\mu\text{m}$ . Both SiSi (Silicon-on-Silicon) and SOI (Silicon-on-Insulator) wafers technologies were investigated. SOI and SiSi are two different techniques to join the sensors and the handle wafer. For SOI, an oxide layer is grown on top of the handle wafer and then the handle wafer is joined to the back of the sensor. For SiSi, two silicon wafers, a low resistivity handle wafer and a high resistivity sensor wafer are bonded together, without any oxide between them. The thickness of the sensors was either 100 or 130  $\mu\text{m}$ . For the  $50\text{ }\mu\text{m} \times 50\text{ }\mu\text{m}$  pitch sensors, both punch through and temporary metal have been used; for the  $25\text{ }\mu\text{m} \times 100\text{ }\mu\text{m}$  option, the biasing before bump bonding is just performed via punch through.

The Figure 6.17 presents I-V measurements performed at FBK. Two pitches options and two wafer flavors (SiSi or SOI) were investigated. Before bump-bonding, most of the sensors were having a breakdown voltage around 100 V, for a depletion voltage of about 20 V, which is very promising.

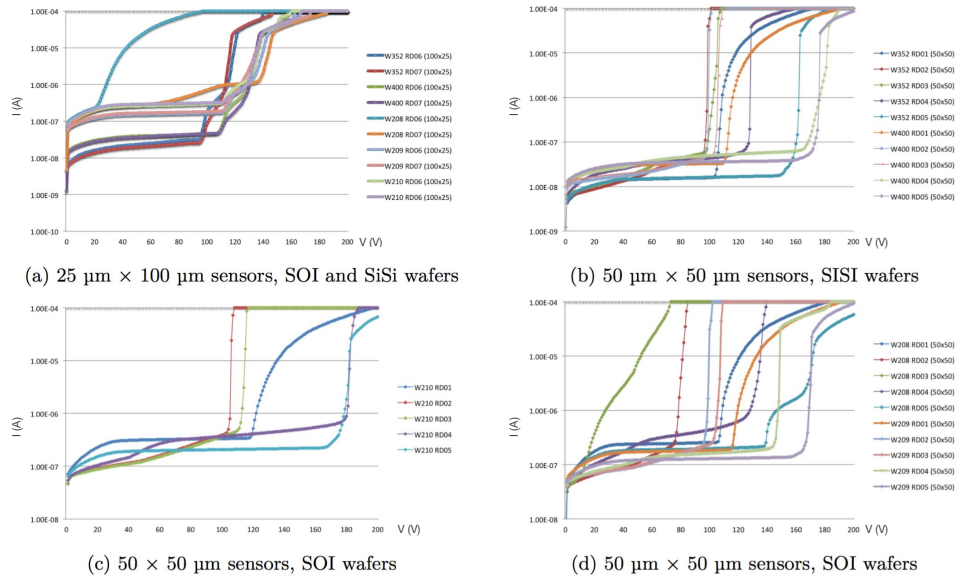


Figure 6.17 – I-V curves of RD53A compatible sensors. Two pixel pitch options are considered:  $25\text{ }\mu\text{m} \times 100\text{ }\mu\text{m}$  (a) and  $50\text{ }\mu\text{m} \times 50\text{ }\mu\text{m}$  (b, c, d). Two wafer technologies are considered: SiSi (a and b) and SOI (a, c and d). The bias range goes from 0 to 200V and the current scale (which is logarithmic) goes from  $10^{-10}$  to  $10^{-4}$  A. The legend compiles the various wafer names.

## 6.2 Pixel module tuning

Prior to the data taking, the FEI4-chip have to be carefully tuned. One has to choose a threshold and a gain between charge and Time-over-Threshold (ToT). The signal implied by the passage of a MIP inside the sensor is digitized into a 4 bit ToT. Before starting the ToT counter, a threshold is applied to the discriminator output of each pixel.

The goal of the tuning is to ensure a uniform value of threshold and ToT gain over the entire chip. Both threshold tuning and ToT tuning are divided in two steps: a global tuning sets a global value and a local tuning which adjusts the individual response of each pixels to reach the target value.

### Threshold tuning

The threshold is chosen to maximize the signal efficiency while minimizing the electronics noise. For the thin sensors of the second and third productions, a set of thresholds ranging from 700e to 1200e were investigated. Once a global tuning of the threshold is achieved, a local adjustment of the threshold in each pixel is performed using the 5 bits TDAC register. The local tuning reduces the threshold dispersion to less than 300 electrons. By modifying the feedback current, it mitigates the fluctuations in threshold values observed pixel by pixel.

### ToT tuning

Once a threshold is selected, a ToT to charge tuning has to be performed: a dedicated ToT value will account for an amount of charge induced in the electrodes. Usually this calibration is tuned to match the ToT Most Probable Value (MPV) and the expected signal of a MIP in the sensor. For example, in 130  $\mu\text{m}$  thick sensors, a MIP is expected to produce about  $130 \times 80 = 10400$  electrons. For such sensor, an adequate tuning before irradiation would be 6 ToT corresponding to 8000 electrons: the ToT peak would then be displayed in the middle (7) of the ToT range (1 to 14), which minimizes the risk of overflow.

The first preamplifier transforms the charge in analog ToT. The slope of the curve can be tuned using appropriate feedback tuning (regulation of feedback current) using the 4 bit FDAC register. The comparator produces digital signal with ToT=0 for signal if under threshold, ranging on a 4 bit register (ToT) otherwise.

### Hit Discrimination logic

To correct for timewalk effects, before applying the charge to ToT calibration, a modification of the ToT value has to be performed. The ToT value obtained in the data represents the ToT code and not the True ToT value. As explained in [129], the FEI4 chip possesses in addition to the 4 ToT bit register, an additional register, named Hit Disc Config (HitDiscCnfg), which allows recording low ToT hits whose rising slope is too small to be accounted in the correct bunch crossing. Due to this timewalk effect one small ToT hit could be registered in the next bunch crossing as illustrated in Figure 6.18.



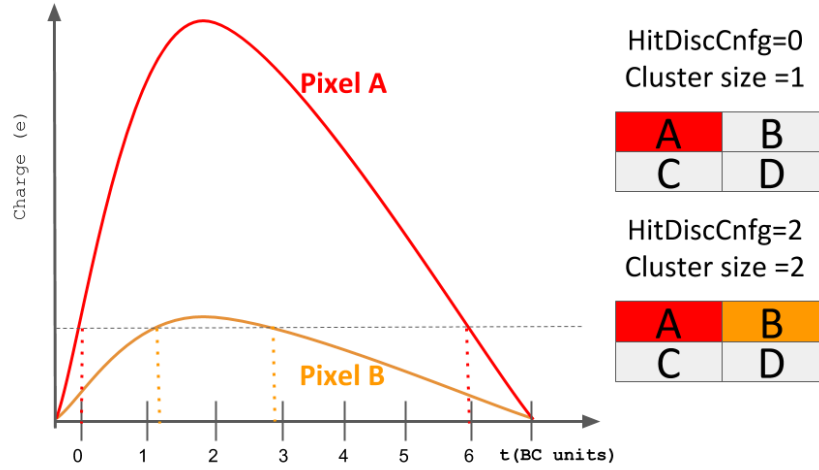


Figure 6.18 – ToT scheme with HitDiscCnfg discussion

When HitDiscCnfg is set to 2, the ToT code of a small hit (ToT of 1 or 2) neighboring a big hit and in the next bunch crossing compare to the big hits is recorded and the big hit and the small hit are associated to form a cluster of 2 pixels. The ToT code value is decreased by 3 ToT units compared to the True ToT value (see [129], Table 7). When HitDiscCnfg is set to 0, small hits in the next bunch crossing are not copied and the ToT code value is decreased by 1 ToT unit compared to the True ToT value.

### Charge to ToT calibration

The charge to ToT relation is not linear. To estimate which charge value corresponds to which ToT values, a charge to ToT calibration scan has to be performed. The FEI4 chip produces a range of signal amplitudes using the voltage injector  $V_{cal}$ . For each injected charge signal, an equivalent ToT signal is registered. The response of each pixels can be different especially after irradiation of the chip. Once this scan has been performed, one can extract 3 parameters describing a second order polynomial function which gives the correspondence between the charge and the ToT. Such calibrations curves are presented in Figure 7.18 in the next chapter.

## Conclusions

The three LPNHE planar pixel sensor production designs have been presented. They were designed to be part of the ITk, their performance in terms of sensor power dissipation and leakage current make them perfect candidates for the four outermost ITk pixel layers. In the next chapter, the performance on beam of the three productions will be discussed.



# Chapter 7

## Performance on beam of pixel detectors

### Contents

---

<b>7.1</b>	<b>Data taking at Testbeam . . . . .</b>	<b>120</b>
<b>7.2</b>	<b>Observables . . . . .</b>	<b>122</b>
7.2.1	Charge collection efficiency . . . . .	122
7.2.2	Hit efficiency . . . . .	123
7.2.3	Hit residuals and spatial resolution . . . . .	125
<b>7.3</b>	<b>Performance of un-irradiated sensors of the first production . .</b>	<b>128</b>
<b>7.4</b>	<b>Performance of irradiated thin sensors . . . . .</b>	<b>129</b>
7.4.1	Irradiation fluence peak constraint . . . . .	129
7.4.2	Charge collection efficiency of W80 . . . . .	133
7.4.2.1	ToT distributions . . . . .	133
7.4.2.2	Charge collection efficiency . . . . .	139
7.4.3	Global hit efficiency . . . . .	142
7.4.4	Conclusion on thin and irradiated sensors . . . . .	145
<b>7.5</b>	<b>Active edge performance . . . . .</b>	<b>145</b>
7.5.1	Standard active edge performance . . . . .	146
7.5.1.1	Comparison with TCAD simulations . . . . .	147
7.5.1.2	Lateral depletion in the edge region . . . . .	148
7.5.2	Staggered active edge performance . . . . .	149
7.5.2.1	Comparison with TCAD simulations . . . . .	150
7.5.3	Conclusions on Active edges sensors . . . . .	154
<b>7.6</b>	<b>Biasing structure and implant design . . . . .</b>	<b>157</b>
<b>7.7</b>	<b>Conclusions on the pixel R&amp;D for ITk . . . . .</b>	<b>158</b>

---

The main work carried during my PhD was to determine the performance of planar pixel detectors for ITk from the joined LPNHE-FBK production. Testing the sensors at different steps of irradiation, with different tunings and temperatures, involved my participation to 11 testbeams campaigns, both at DESY and at CERN from 2016 to 2018. For most testbeams, I was in charge of planning the data taking, tuning the sensors, taking data and analyzing the data.

In this chapter, the performance of detectors from the three productions are described. A first introductory section will describe the testbeam data taking phase and the various observables considered. Then the performance of un-irradiated and irradiated thin sensors of the second production will be given. The following section will focus on the active edge sensors and their performance in terms of edge hit efficiency. Afterwards, the next section will summarize the performance of two biasing methods at various steps of irradiation. Eventually conclusions on the three tested production will be drawn.

## 7.1 Data taking at Testbeam

The results presented in this chapter are based on data taken at the DESY (Deutsches Elektronen-Synchrotron) beam test facility<sup>1</sup> and at the CERN North Area experimental area<sup>2</sup>. At both testbeam facilities EUDET telescopes [130] were used. Data were collected during several testbeam campaigns both at CERN SPS with 120 GeV/c pions and at DESY with 3 - 5 GeV/c electrons/positrons. Due to the multiple scattering implied by the low energy of the electron beam, the spatial resolution at DESY was worse compared to the one at CERN-SPS. Both testbeam areas and the tracks telescope will be described in the following.

### CERN SPS beam

The 120 GeV/c momentum positive pions beam used to test our sensor at CERN [131] is originated from the SPS 400 GeV/c primary beam which is extracted onto three primary targets. Two super cycles of a few tens of seconds spills are provided to the four beam lines of the North area, the particle rate was approximately of 400 to 500  $Hz$ . The beam availability is subject to variations, and depends on the stability of LHC and SPS accelerators and experiments.

### DESY beam

The beam provided by DESY [132] consisted in a quasi continuous flow of 3 to 6 GeV/c momentum electrons. The particle rate was approximately of  $1kHz/cm^2$  for 5 GeV/c momentum electrons. The beam is originated from the DESY II electron synchrotron, the

---

<sup>1</sup><http://testbeam.desy.de/>

<sup>2</sup><http://sba.web.cern.ch/sba/>

testbeam line is a parasitic user of the PETRA III injector (see Figure 7.1). Three carbon fiber targets generate bremsstrahlung photons from electrons or positrons coming from DESY II. Those photons are then converted via a target in electrons and positrons which energy (up to 6 GeV) can be selected using a dipole magnet and a collimator. High energy electron beam results in low rate, a compromise between sufficient rate and an acceptable energy is obtained by selecting 4 GeV electrons. At these energies, the multiple scattering [133] is the spatial resolution dominant effect, as discussed in Section 7.2.3. The measured spatial resolution (see Section 7.2.3) is consequently worse at DESY than at CERN-SPS.

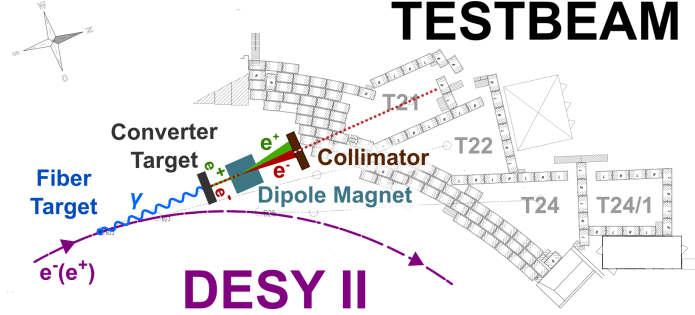


Figure 7.1 – Scheme of DESY beam production for testbeam

### EUDET telescope

At both laboratories the data were recorded using a copy of the EUDET/AIDA telescope [130]. This generation of beam telescopes consists of six detection planes equipped with the Mimosa26 [134] monolithic active pixel sensors, with a fine pitch of  $18.4\ \mu\text{m}$  by  $18.4\ \mu\text{m}$ . A reference plane with a similar chip flavor as the tested sensors is also used to ensure the temporal coincidence because the timing acquisition of the mimosa planes is of the order of  $200\ \mu\text{s}$  which is long compared to the FE-I4 chip one (readout clock of  $25\ \text{ns}$ ). The data read out was triggered by the coincidence of plastic scintillators, whose area were of about  $1\ \text{cm}^2$ . The data from the DUTs (Devices Under Test) were recorded using two different Data Acquisition (DAQ) systems: the Reconfigurable Cluster Element (RCE) [135] system and the UsbPix [136] system. The typical averaged <sup>3</sup> trigger rate was in the range of 250-1000 Hz, depending on the beam conditions and on the DAQ system used for the DUTs.

The DUTs were located between the two arms of the telescope (each arm having three detection planes). To screen the DUTs from the light, they were operated inside a cooling box, capable of maintaining the DUT temperature constant.

### Reconstruction

The track reconstruction for testbeam data consists of a set of algorithms, implemented in the EU Telescope framework [137], to process raw data into tracks. After the data taking, as first step a noisy pixels data bank is created both for telescope planes and DUTs, looking at pixels which fired at a frequency higher than a certain threshold (typically more than

<sup>3</sup>Averaged over a supercycle at CERN

0.5% within the selected number of events per cycle); at later stages, signals from the pixels appearing in the data bank are discarded. Next comes the clustering step: in each plane neighboring pixels firing in the same bunch crossing are grouped together to form clusters. For each cluster, hit coordinates are computed in the global frame and a first alignment of the telescope planes and the DUTs is performed. The final alignment, based on the Millipede algorithm [138], is then performed to align each DUT plane independently from other DUT planes. Eventually, tracks are reconstructed using a Kalman-filter based algorithm and a  $\chi^2$  fit is performed to obtain the best possible track parameters with hits on each plane. At the end of the process a ROOT [67] file is created containing basic observables ready to be analyzed in the data analysis framework, TBmon2 software [139]. TBmon2 allows studying the quantities discussed below.

## 7.2 Observables

To assess the sensor performance some observables are of particular interest. In this section, two observables will be described thoroughly: the charge collection efficiency and the hit efficiency. The spatial resolution of the sensor is also important and it will be described at the end of the section.

### 7.2.1 Charge collection efficiency

The charge collection efficiency is defined as the ratio of the collected charge versus the expected charge. Here we study the charge collection efficiency of irradiated sensors compared to un-irradiated ones.

The charge collection efficiency of W80 sensor was estimated over the ITk fluence range and a fit was performed on the data to extract the trapping constants  $\beta$ . The Hecht equation [140] describes the charge collection efficiency (CCE) of an idealized 1D silicon pad:

$$CCE = \frac{Q}{Q_0} = \left( \frac{d_e + d_h}{w} \right) - \left( \frac{d_e}{w} \right)^2 \left( 1 - \exp \left( -\frac{w}{d_e} \right) \right) - \left( \frac{d_h}{w} \right)^2 \left( 1 - \exp \left( -\frac{w}{d_h} \right) \right) \quad (7.1)$$

where the subscript e and h refers to electrons and holes contributions,  $Q$  is the charge collected by the electrodes after irradiation,  $Q_0$  is the charge collected before irradiation,  $d_{e,h} = v_{e,h} \tau_{e,h}$  is the collecting distance which is the product of the carrier velocity  $v_{e,h}$  (which is assumed to be saturated) and of the trapping time  $\tau_{e,h}$ . The trapping time depends on a constant  $\beta_{e,h}$  and on the fluence  $\Phi$  such as  $\tau_{e,h} = (\beta_{e,h} \Phi)^{-1}$ ;  $w$  is the thickness of the sensor.

The following describes the various steps leading to Equation 7.1:

The rate of charge created by the passage of a MIP per unit length in silicon is  $R \simeq 80e/\mu\text{m}$ ; hence  $Q_0 = Rw$ .

To express the charge appearing on the electrode of an irradiated sensor, one has to take into account the trapping effect. It is modeled through an exponential attenuation with time

of the drifting carriers:

$$q_{e,h}(t) = q_{e,h}(0) \exp\left(-\frac{t}{\tau_{e,h}}\right) \quad (7.2)$$

where  $q_{e,h}$  is the charge on the electrode at time  $t$ .

The corresponding instantaneous current  $i(t)$  from electrons and holes is equal to:

$$i_{e,h}(t) = q_{e,h}(0) \frac{v_{e,h}}{d_{e,h}} \exp\left(-\frac{t}{\tau_{e,h}}\right) \quad (7.3)$$

The charge appearing on the electrode is obtained by integrating  $i(t)$  over the thickness ( $w$ ) of the sensor and the collecting time

$$Q_{e,h} = \int_0^w dz \int_0^{z/v_e, w-z/v_h} dt R \frac{v_{e,h}}{w} \exp\left(-\frac{t}{\tau_{e,h}}\right) \quad (7.4)$$

$$Q_e = Q_0 \frac{d_e}{w} \left(1 - \frac{d_e}{w} \left(1 - \exp\left(-\frac{w}{d_e}\right)\right)\right) \quad (7.5)$$

$$Q_h = Q_0 \frac{d_h}{w} \left(1 - \frac{d_h}{w} \left(1 - \exp\left(-\frac{w}{d_h}\right)\right)\right) \quad (7.6)$$

By adding Equations 7.5 and 7.6 and dividing it by  $Q_0$ , one can find Equation 7.1.

The saturated velocities are assumed to be equal for holes and electrons and the values considered,  $v_{sat,e} = v_{sat,h} \simeq 1.06 \times 10^7 \text{ cm/s}$ , are the one used in Silvaco simulations [141] for Silicon at 235 °K. For the tested sensor (W80 of the second production), the depth was 130µm. The only free parameters left in the fit are the  $\beta$  constants, which will be extracted over the ITk fluence range in the Section 7.4.2.2.

### 7.2.2 Hit efficiency

#### Global Hit efficiency

The global hit efficiency is defined as the fraction of reconstructed tracks crossing a sensor that have an associated hit in that sensor. In case of hybrid pixel detectors, a bad bump bonding can degrade severely the efficiency of the sensor. The quoted efficiency is measured in a fiducial region, defined by the surface of the pixel module where each pixel cell is hit by at least 1 track. From Figure 7.2 it can be seen that the fiducial region, defined by the trigger scintillators area, was in general smaller than the surface of the detector.

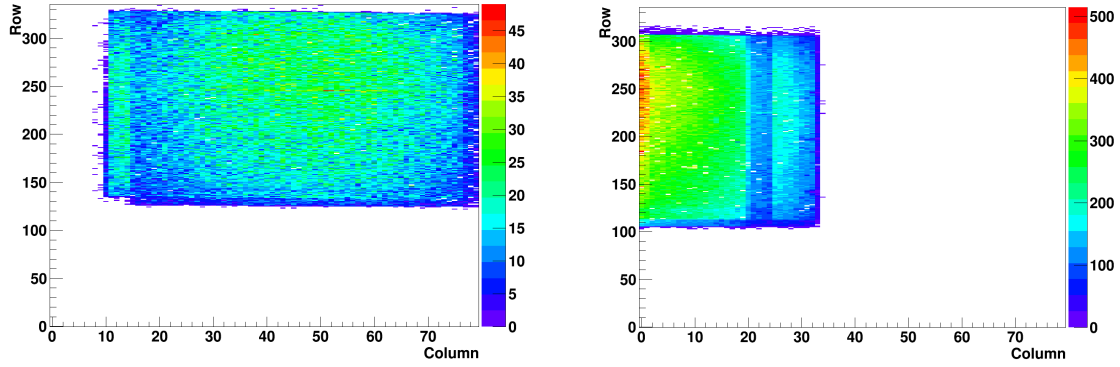


Figure 7.2 – Hit map of a tested sensor in beam. On the abscissa is the pixel column index, on the ordinate axis is the pixel row index. (Left) the beam is focused on the center of the sensor; (right) the beam is focused on the edge, which allows to perform edge efficiency scan. The area where hits are seen is a  $1\text{ cm}^2$  rectangle and correspond to the area of the trigger scintillator.

### In-pixel Hit efficiency

The in-pixel hit efficiency is obtained by superimposing the 2D maps of efficiency as a function of the local position in each pixel cell of the sensor. The granularity of this analysis is of the order of the total pointing resolution (sum of the telescope resolution and the multiple scattering). The in-pixel efficiency gives valuable information on the homogeneity of the charge collection, stressing the presence of low efficiency areas due, for instance, to permanent biasing structures. Two biasing structures for testing purposes, a permanent one (punch through) and a temporary one (temporary metal) were present in the tested sensors. The two techniques and their results in terms of in-pixel efficiency are investigated in Section 7.6. The shape and extension of the n+ implant can also alter the in-pixel efficiency, results will be discussed in the same section.

### Active edge Hit efficiency

To assess whether the active edge ensures a high hit efficiency in the area between the last pixels rows/columns and the doped trench, an efficiency measurement as a function of the track position in the edge area is performed, using data collected with the beam focused on the edge area; see for more details the Figure 7.2.

The lateral depletion can be investigated looking at the edge hit efficiency performance for several values of the bias voltage.

The active edge efficiency maps are compared with Silvaco TCAD [97] simulations of the edge area to investigate the impact of Guard Rings (GR), of the segmented trench or the lateral extension of the electrical field.



### 7.2.3 Hit residuals and spatial resolution

#### Spatial resolution and Multiple scattering

The digital spatial resolution of a planar pixel sensor readout in binary mode is obtained by dividing its pitch by  $\sqrt{12}$ . In addition, to obtain the intrinsic spatial resolution of a sensor, one has to consider the contribution from clusters, the pointing resolution of the telescope or of the detector and the multiple scattering contribution which is described in the following.

The passage of a charged particle through the sensor creates several thousands of electrons and holes (for a  $O(100\mu\text{m})$  sensor) which drift towards the electrode and can trigger several neighboring pixels. The group of pixels involved is called a cluster. To find the position of the hit in the cluster, a charge (in ATLAS reconstruction chain) or ToT (in testbeam) weighted method is used: a weight (its charge or ToT) is assigned to each pixel and the hit position is evaluated to be the barycenter.

When charged particles cross the sensor, they interact via Coulomb interaction with nuclei in the lattice and as they exchange momentum at each interaction, their trajectory in the sensor is deviated. The ensemble of these deflections is called Multiple Scattering (MS) [133]. The total deviation angle  $\theta$  distribution [68] follows more or less a Gaussian distribution and its RMS is given by :

$$\theta_{plane}^{rms} = \frac{13.6\text{MeV}}{\beta pc} z \sqrt{x} X_0 \left( 1 + 0.0038 \ln \left( \frac{x}{X_0} \right) \right) \quad (7.7)$$

where  $p$  is the particle momentum (MeV),  $\beta$  the velocity in units of  $c$ ,  $\frac{x}{X_0}$  is the thickness of the absorption medium in units of radiation length ( $X_0(\text{silicon}) = 21.82 \text{ g/cm}^3$  [68]).

The deviation between the entrance and the exit points in the transverse coordinate ( $x$ ) compared to the thickness ( $z$ ) of the sensor is given by  $x_{plane}^{rms} = \frac{1}{\sqrt{3}} z \theta_{plane}^{rms}$ . From this formula 7.7, it is clear that the MS shift increases for low momentum particles. To mitigate the multiple scattering effect, pixel sensors and read-out chips used in HEP are usually thinned down to reach a thickness of the order of few hundreds of micrometers.

#### Hit residuals

The hit unbiased residuals are defined as the difference between hit position in the DUT (Device Under Test) and the position of the intersection between the associated reconstructed track and the DUT. Unbiased refers to the fact that the DUT is not used in the tracking process. The study of the residual distribution gives valuable information on the sensor spatial resolution after accounting for the pointing resolution of the telescope, multiple scattering and charge sharing between neighboring pixels.

The multiple scattering at CERN SPS has a significantly smaller effect ( $\sim 4\mu\text{m}$ ) compared to the detector resolution as beam particles are high momentum pions of 120 GeV/c. The

spatial resolution is obtained from the RMS of the residual distribution for all clusters. The main components of the clusters residuals distribution are:

- The residual distribution of one-pixel clusters. This distribution is expected to be flat and to span over a width compatible with the pixel implant one (30  $\mu\text{m}$  in the short pixel side for the first production). However, since the pointing resolution of the telescope smear the edges of the flat distribution, the residuals can be fitted by a flat distribution convoluted with a Gaussian, whose width gives an estimation of the telescope pointing resolution, convoluted with the multiple scattering induced shift [72].
- The residual distribution for two-pixels clusters. The hit position is obtained by using a ToT weighted method, described in Section 7.2.3. The charge sharing occurs in an area between two pixels which is narrower than the pixel pitch, consequently the spatial resolution for a two-pixels cluster is better than for a one-pixel cluster. The distribution is fitted with 2 Gaussians: a narrow one which is the true residual distribution for two-pixels clusters and a broad outlier Gaussian which takes into account badly reconstructed hits. The RMS of the narrower Gaussian gives an estimation of the spatial resolution for two-pixels clusters. The area of the narrow Gaussian over the area of the sum of the two Gaussians is the fraction of correctly reconstructed two-pixels clusters.

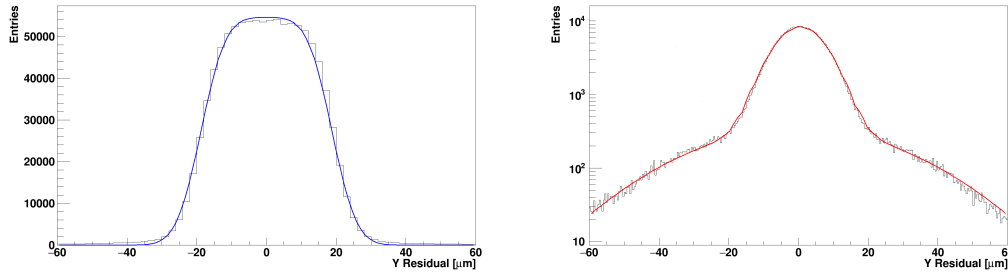


Figure 7.3 – Left: residual distribution for clusters of 1 pixel cell fitted with a box function convoluted with a Gaussian. Right: residual distribution in logarithmic scale of two pixels clusters, fitted with the sum of two Gaussians. Data were taken at CERN-SPS, hence the multiple scattering contribution is small (4  $\mu\text{m}$ ). The threshold was 1400 electrons, the ToT tuning was 7 ToT corresponding to 1400 electrons and the sensor was biased at 40V.

The two histograms in Figure 7.3 show respectively the residual distribution in the narrow pixel direction for one and two pixels clusters.

The RMS of the residuals for clusters of one pixel is of the order of 14  $\mu\text{m}$  which is compatible with the expected digital resolution. The distribution is fitted with a box function convoluted with a Gaussian; the pointing resolution of the telescope (convoluted with the multiple scattering effect due to the important number of sensors and the cooling box) which is obtained by looking at the RMS of the Gaussian, is of the order of 5  $\mu\text{m}$ .

The residuals distribution of clusters of two pixels (Figure 7.3 right) is fitted by a convolution

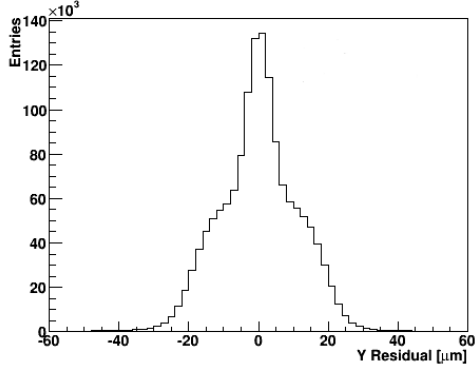


Figure 7.4 – Residual distribution of LPNHE7 for all clusters in the short pixel direction (50  $\mu\text{m}$  pitch). The RMS of the residual is about 11.5  $\mu\text{m}$ . Data were taken at CERN-SPS, hence the contribution from pointing resolution convoluted with the multiple scattering is small ( $\sim 5\mu\text{m}$ ). The threshold was 1400 electrons, the ToT tuning was 7 ToT corresponding to 1400 electrons and the sensor was biased at 40V.

of a narrow core Gaussian and a broad outlier Gaussian, the latter to account for badly reconstructed hits. From the fit, the percentage of correctly reconstructed hits is 86 % and the width of the charge sharing region, approximated here by the RMS of the core Gaussian, is of the order of 7  $\mu\text{m}$ . From those plots it is clear that maximizing the number of two-pixels clusters significantly improves the spatial resolution.

The RMS of the total cluster residuals reported in Figure 7.4 (data taken at CERN), is  $\sim 12 \mu\text{m}$ . Once the multiple scattering contribution and telescope resolution are subtracted (in quadrature), the spatial resolution in the short direction of the pixel can be evaluated to be of the order of 10  $\mu\text{m}$ . This resolution is better than the expected digital resolution for 50  $\mu\text{m}$  pitch sensors, i.e.  $50 \mu\text{m} / \sqrt{12} \simeq 14\mu\text{m}$  is due to the presence of clusters formed by two pixels. In Figure 7.4 the contributions of different cluster sizes is clearly visible.

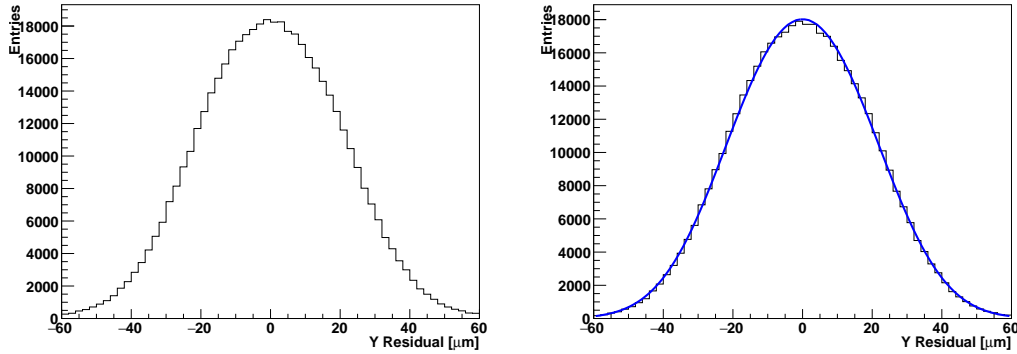


Figure 7.5 – Left: residual distribution for all cluster sizes in the short pixel direction (Y). Right: residual distribution for clusters of 1 pixel cell in Y direction fitted with a box function convoluted with a Gaussian. Data were taken at DESY, hence the multiple scattering contribution is important.

The spatial resolution at DESY, which is impacted by the multiple scattering as the beam consists of electrons with a momentum of 4 GeV/c can be extracted from the plots of Figure 7.5. The left plot is the residual distribution for all pixel clusters, it is clearly enlarged by comparison with the precedent CERN-SPS distribution on Figure 7.4. The spatial resolution evaluated from its RMS is 19.9  $\mu\text{m}$ . The middle plot shows the residual distribution of

1 pixel cluster which RMS is  $19.5\ \mu\text{m}$ . The superimposed fit is a box function, its RMS gives an indication of the pointing resolution of the telescope, which is impacted by the multiple scattering, ( $15\ \mu\text{m}$ ). The multiple scattering is the dominant effect in terms of spatial resolution.

### 7.3 Performance of un-irradiated sensors of the first production

The performance documented in this section are about the first LPNHE pixel production of active edge sensors [81]. The section focuses on the overall efficiency over the sensor, the performance in the edge area are detailed in Section 7.5. The sensors put on beam are two  $200\ \mu\text{m}$  thick sensors, LPNHE5 and LPNHE7 with respectively 0 and 2 GRs between the active edge and the last pixel (see Table 6.2). Both detectors were un-irradiated.

#### Global Hit Efficiency

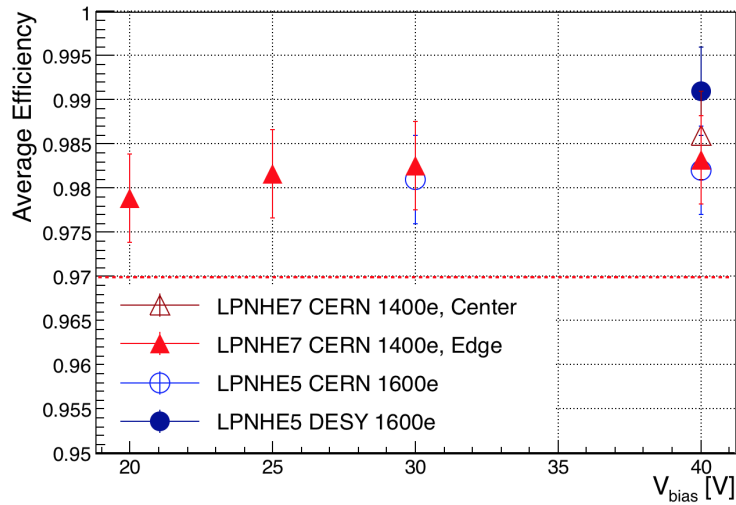


Figure 7.6 – Global hit efficiency for the 2 sensors (LPNHE7 and LPNHE5), for various bias points, threshold configurations (1600 or 1400 electrons) and beam tests (CERN or DESY). *Edge/Center* identifies data taken when the beam was focused at the detector periphery/center. The uncertainties are dominated by the systematics from the reconstruction software.

The hit efficiency has been investigated at CERN SPS and DESY with a set of two thresholds corresponding to an input charge of 1400 electrons or 1600 electrons and for various bias points. The global hit efficiency is higher than 97.5 % for both the LPNHE5 and LPNHE7 sensors, as shown in Figure 7.6. For LPNHE7 at the CERN SPS with a threshold of 1400 electrons, two beam configurations were investigated, one with the beam focused on the center of the sensor (open triangles), the other with the beam focused on the edge of the sensor (full triangles). The depletion voltage of un-irradiated sensor was of about 20 V (see

Table 6.1). Biasing the sensor above 25 V allows the sensors to reach a 98 % efficiency whatever the threshold.

## 7.4 Performance of irradiated thin sensors

Two thin sensors (W80 and W30) of the second production have been irradiated to high fluences, comparable to those expected at the HL-LHC. One of the goals for those irradiated thin sensors was to prove that at least a 97% hit efficiency in harsh radiation environment is maintained. To fulfill this requirement, the sensor has to be capable to reach a high bias voltage without triggering any discharge, hence the sensor is coated with a thin passivation layer (BCB). In the following, the charge collection efficiency and hit efficiency of the W80 sensor obtained from testbeam data are investigated. The performance of W30 are presented before irradiation, as results after irradiation are not in a mature enough state.

### 7.4.1 Irradiation fluence peak constraint

The irradiation history of W80, the sensor from the second production whose performance are presented in this section, has been documented in Section 6.1.3. From dosimetry results, the fluence beam profile (see Figure 6.10) can be modeled by 2D gaussians, with a 2 mm uncertainty on the position on both X and Y directions.

To further constraints the fluence peak position and reduce the uncertainties on this position, the average cluster ToT distribution across the sensor was used. As the charge trapping effect increases with the fluence, the collected charge and consequently the ToT are also reduced. Hence the position of the minimum of the average cluster ToT distribution is a valid approximation to constraint the fluence peak position. For this purpose, various configurations in terms of threshold, ToT configuration and bias voltages have been investigated (which are reported in Table 7.1).

Threshold (electrons)	850	850	850	1000	1000	1200
Corresponding ToT at $i \times 1000$ electrons	8 at 4	8 at 4	8 at 4	8 at 4	6 at 4	6 at 4
Bias Voltage (V)	600	500	400	600	600	600

Table 7.1 – Table of the various configurations investigated for W80 after having received the two irradiation doses. The ToT tuning describes the ToT value corresponding to a collected charge by the electrode. "i" corresponds to the target value of charge (in units of thousand of electrons)

The search of the fluence peak position has been performed with data taken at DESY where the beam profile was less collimated than what it was at CERN-SPS.

During this testbeam two ROI (Regions Of Interest) have been considered whose area were covered by the beam with a sufficient amount of statistics (the edges of the beam profiles where the statistics is too limited are not considered). The ROI covering the lower part of the sensor will be referred as "Down" position in the following; the other covering the upper-medium part of the sensor will be referred as "Up" position in the following. Both ROIs are presented in Figure 7.7

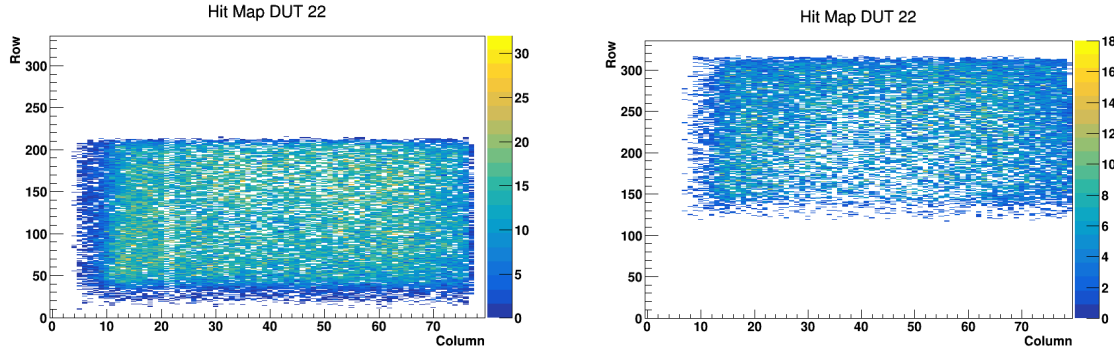


Figure 7.7 – Hit map of W80. The Down and Up ROI are visible respectively in the left/right plots.

Two profiles have been created, an horizontal profile which average all the average ToT values of each pixels along the vertical axis in the ROI and a vertical profile which average all the average ToT values of each pixels along the horizontal axis in the ROI.

To obtain the value of the peak fluence position, the average ToT profiles have been created for all the configurations from Table 7.1 and they are presented in Figure 7.8. Each distribution is fitted with a 2nd degree polynomial and the minimum of the distribution is extracted from the fit. The mean of the average ToT minimum position value, which corresponds to the fluence peak position is obtained by averaging the extracted values of all configurations. The fluence peak has been shifted by 1.2 mm in X and by 1 mm in Y, which are within the 2 mm uncertainty on the position indicated by the CERN irradiation facility.

The fluence horizontal and vertical profiles with and without the fluence peak correction are presented in the Figure 7.9.

The uncertainty on the fluence in the following plots is set to  $0.5 \times 10^{15} \text{ n}_{\text{eq}}/\text{cm}^2$ , which corresponds to the variation of the fluence at 2 mm of the peak value. It accounts for the uncertainty on the peak fluence and on the fluence profile modeling approximation.

The effect of the modification of the peak fluence is presented in Figure 7.10 which shows the average ToT vs fluence for 3 different bias voltages with (right plot) and without (left plot) fluence peak constraint. The constraint of the fluence peak (right plot) results in less dispersion in the average ToT values for the same fluence.

Even if the constraint on the fluence peak shows better results in terms of dispersion, some caveats have to be mentioned. The average ToT distribution is highly sensitive to the chosen Threshold and ToT value, as well as to the bias voltage. As several tunings have been inves-

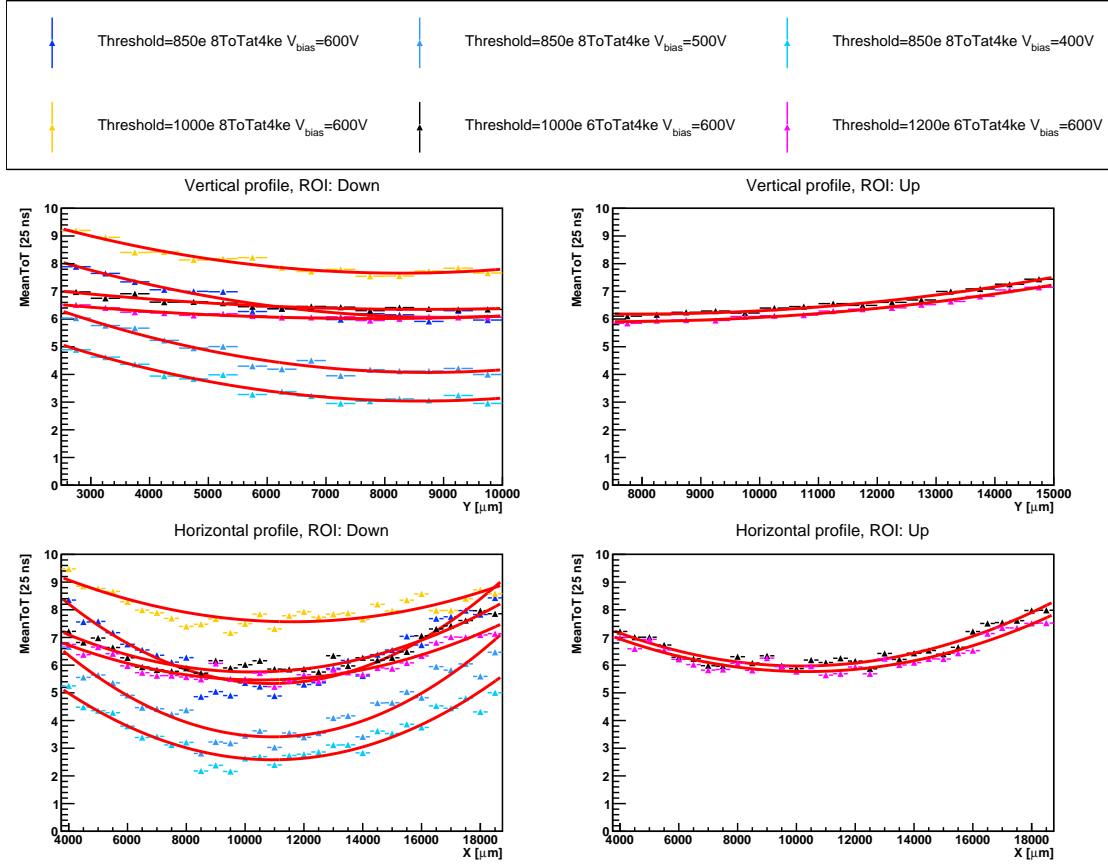


Figure 7.8 – Average ToT profiles for the two ROI. The threshold, ToT tuning and bias voltage are indicated in the legend box. All distribution are fitted with a polynomials of degree two (red lines).

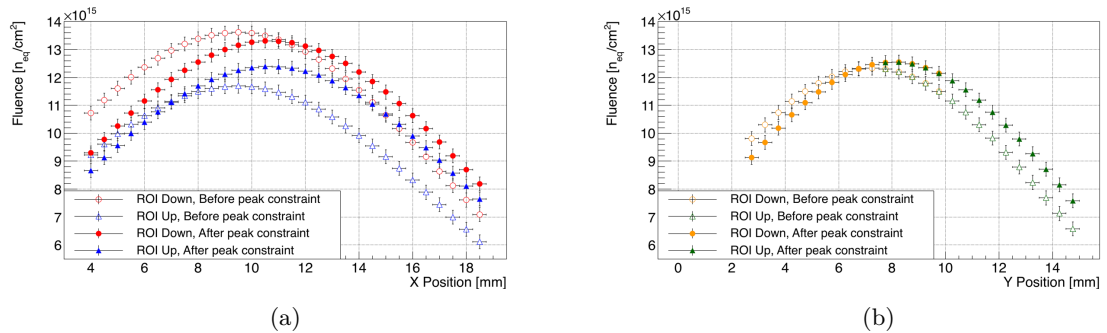


Figure 7.9 – Horizontal (a) and vertical (b) fluence profiles with and without fluence peak constraint. The blue/red and green/yellow points represent data taken in the Up/Down ROI.

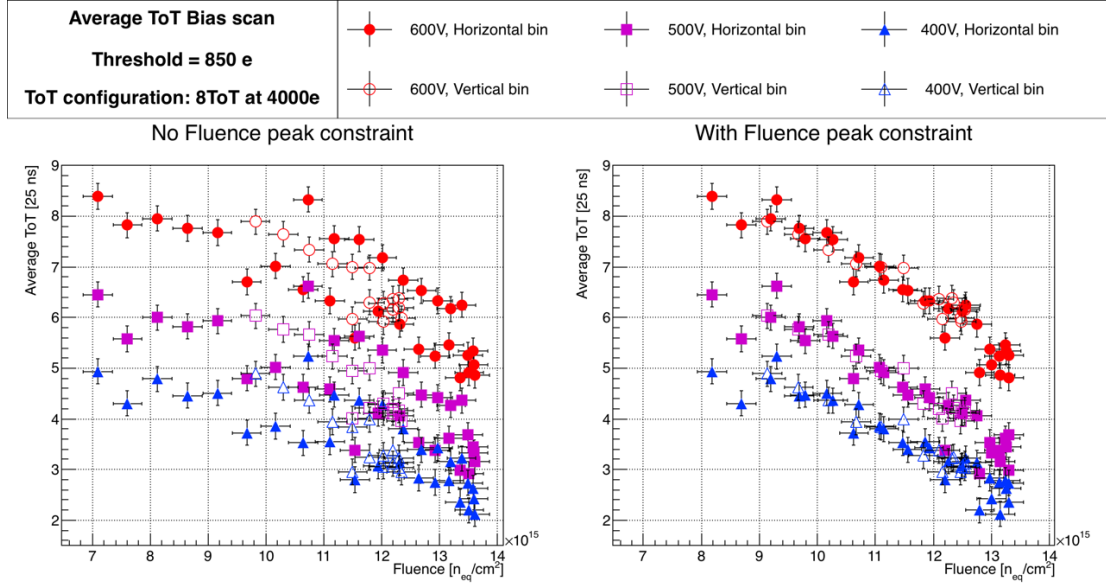


Figure 7.10 – average ToT distribution vs fluence for three different bias voltages. The left/right plot is without/with fluence peak constraint. The horizontal/vertical bin label in the legend means that the fluence and average ToT have been extracted from an horizontal/vertical profile of the Down ROI.

tigated and gives consistent results with respect to one another, the peak fluence position is assumed rather independent of the tuning. Another caveat is the non uniformity of threshold observed in the FEI4 chip. This has an impact on the average ToT as presented in the Figure 7.11 which shows the average ToT distribution on the un-irradiated reference DUT used in the testbeam where the previous data were extracted.

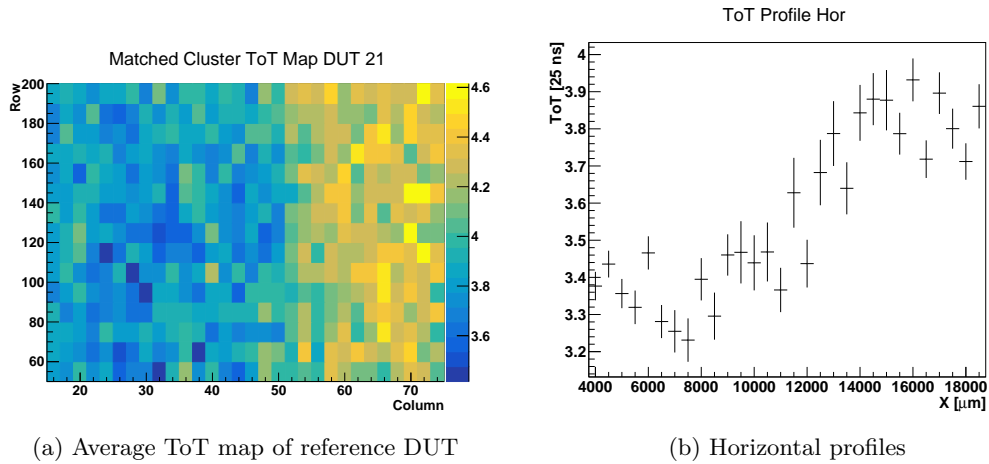


Figure 7.11 – Cluster ToT map (a) and ToT horizontal profiles for the reference DUT (un-irradiated).

A variation on the average ToT can be seen across the sensor even if this sensor was un-irradiated. The drift in ToT is of the order of 0.5 ToT. The difference in ToT occurs mainly horizontally. This ToT drift can be explained by a drift in the threshold already seen by



other users of FEI4 modules<sup>4</sup>. To take into account this effect, which is difficult to quantify from one chip to another, a conservative systematic uncertainty was added on the ToT value of 0.5 ToT.

### 7.4.2 Charge collection efficiency of W80

The charge collection efficiency is defined as the ratio of charge collected by the sensor after a certain dose of irradiation compared to the charge collected by the same sensor before irradiation. To access this quantity, a preliminary step is to look at the ToT which is how the charge is digitized in the module. The first part of this section will investigate the ToT distributions, then the results of charge to ToT calibration realized at CERN-SPS and DESY using the STControl framework [130] will be used to access the charge quantity.

#### 7.4.2.1 ToT distributions

In this section, the ToT distributions of the irradiated W80 130  $\mu\text{m}$  thick sensor will be evaluated for different fluences, threshold and bias voltages. Those comparisons are developed at the ToT level and not at the charge level because we did not have charge to ToT calibration with a threshold of 850 electrons and a ToT gain of 8ToT at 4000 electrons or with a threshold of 1200e and a ToT gain of 6ToT at 4000 electrons.

In this section, either the ToT Most Probable Value or the average ToT were considered. When the statistics was sufficient and the ToT fit (Landau convoluted with Gaussian, see Section 3.2.1) was good enough, the extracted MPV was considered. Otherwise the average ToT is considered.

#### ToT Code and True ToT

As explained in Section 6.2, the ToT value obtained at the output of the reconstruction is not the True ToT but the ToT code. If one wants to retrieve the True ToT, the HitDiscCnfg parameters has to be considered: the True ToT value is then equal to the ToT code value +  $1 + \text{HitDiscCnfg}$ .

In the following, three tuning configurations will be considered:

- Un-irradiated W30 sensor: HitDiscCnfg was set to 2, the threshold was 1200 electrons and the ToT was tuned at 6 ToT corresponding to 6000e.
- Irradiated W80 sensor (average of  $3 \times 10^{15} \text{ n}_{\text{eq}}/\text{cm}^2$ ): HitDiscCnfg was set to 0, the threshold was 1200 electrons and the ToT was tuned at 6 ToT corresponding to 6000e.
- Irradiated W80 sensor (average of  $1 \times 10^{16} \text{ n}_{\text{eq}}/\text{cm}^2$ ): HitDiscCnfg was set to 0, the threshold was 1000 electrons and the ToT was tuned at 6 ToT corresponding to 4000e.

---

<sup>4</sup>MPG ATLAS group, private communication

The Cluster ToT distributions for the three configurations considered are plotted in Figure 7.12. The Figure illustrates how to calculate the True average ToT value (indicated in the caption) which is equal to the average ToT code value + 1 + HitDiscCnfg value as explained in Section 6.2.

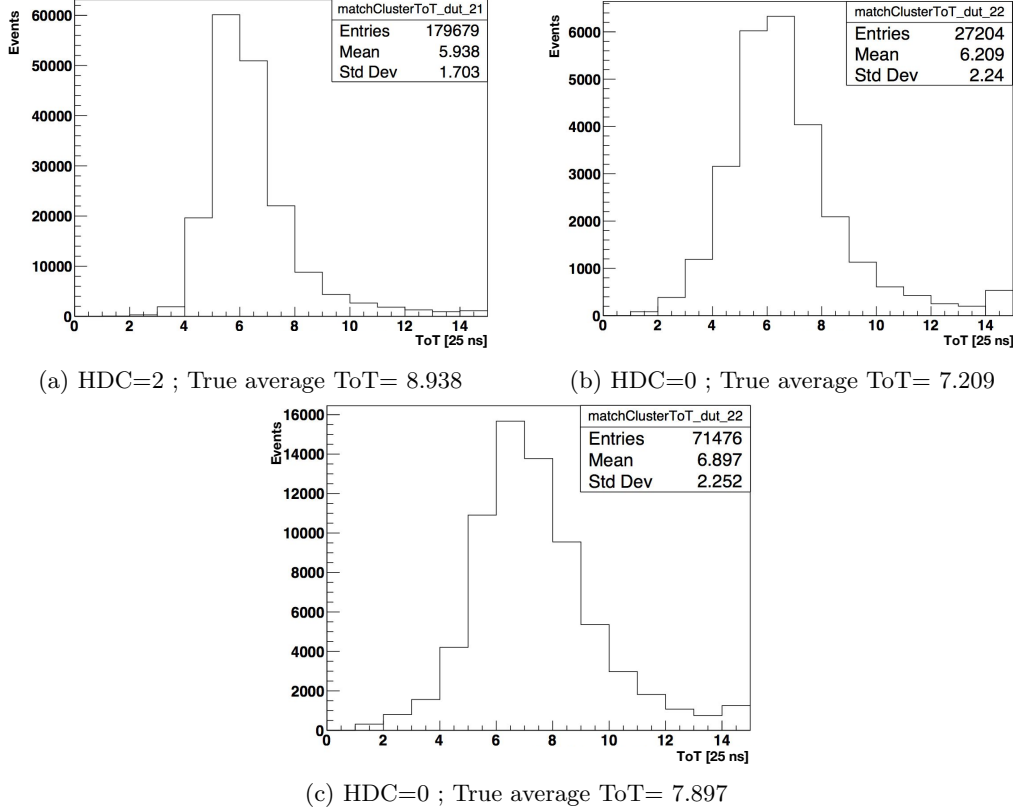


Figure 7.12 – ToT distribution for thin sensors with 3 different irradiations and configurations: (a) W30 before irradiation, threshold of 1200e, ToT gain of 6ToT for 6000 electrons; (b) W80 irradiated at  $3 \times 10^{15}$  n<sub>eq</sub>/cm<sup>2</sup>, threshold of 1200e, ToT gain of 6ToT for 6000 electrons; (c) W80 irradiated at  $1 \times 10^{16}$  n<sub>eq</sub>/cm<sup>2</sup>, threshold of 1000e, ToT gain of 6ToT for 4000 electrons. The Mean true ToT value are reported below each plot. HDC refers to the HitDiscConfig register.

In the following paragraphs, the average true ToT (not the ToT Code) will always be plotted.

### ToT distribution vs Fluence

As shown on Figure 7.13 [142] which presents the ToT distribution for the W30 un-irradiated sensor and W80 irradiated sensor at  $3 \times 10^{15}$  n<sub>eq</sub>/cm<sup>2</sup>, the irradiation of the sensor shifts the ToT distribution towards lower values as some charges are trapped in the bulk due to new states introduced in the energy band gap by radiation damage. As W30 (100 μm) is thinner than W80 (130 μm), the charge loss is even more drastic than the one observed: the collected charge for W80 un-irradiated sensor would have been higher than the one from un-irradiated W30 sensor (which is thinner).

The configurations for both sensors were the following: threshold at 1000 electrons and 6 ToT for 6000 electrons before and after the first step of irradiation; the un-irradiated sensor was

biased at 150 V and the irradiated one at 600 V.

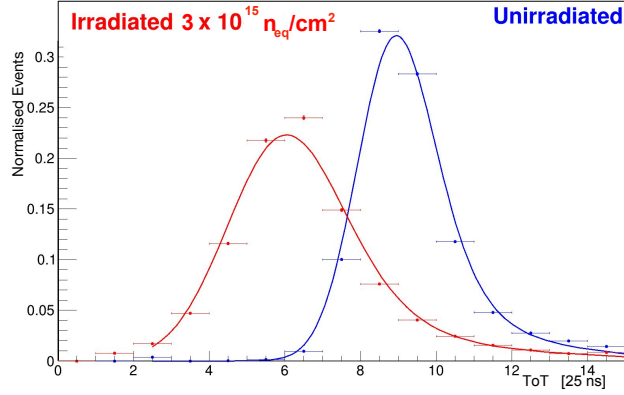


Figure 7.13 – ToT distribution for thin un-irradiated sensor (blue) biased at 150 V and for thin irradiated at  $3 \times 10^{15} \text{ n}_{\text{eq}}/\text{cm}^2$  sensors biased at 600 V (red). The fit consists in a Landau convoluted with a Gaussian.

The irradiation at  $3 \times 10^{15} \text{ n}_{\text{eq}}/\text{cm}^2$  of 130  $\mu\text{m}$  thick sensor reduces the signal by at least 3 ToT units, the charge Most Probable Value (MPV) before irradiation is about 9 ToT (for the 100  $\mu\text{m}$  thick sensor) and after is close to 6 ToT, so a reduction of more than 30% in the charge collection efficiency is expected. As the charge to ToT conversion is not linear, it is non trivial to extract the charge value of the MPV for the un-irradiated sensor. For the sensor irradiated at  $3 \times 10^{15} \text{ n}_{\text{eq}}/\text{cm}^2$ , the MPV of the ToT distribution is really close to the calibration value (6000 electrons for 6 ToT) so the amount of induced charge is of the order of 6000 electrons.

In the following, the ToT distribution will be studied on a finer fluence granularity and on a wider fluence range, using data originated from three different testbeams with three different configurations introduced in the previous paragraph 7.4.2.1.

For the irradiated sensors, only DESY data are used because of the larger coverage of the beam; this had allowed us to investigate a wider range of fluences, with more statistics as DESY's beam is quasi continuous.

The Figure 7.14 presents the average True ToT values over the full range of fluences studied with 3 different tunings. The red and black datasets have the same tuning (threshold of 1200 electrons and the ToT was tuned at 6 ToT for 6000e). As expected the average ToT decreases with the fluence. The blue data sets correspond to the sensor highly irradiated, it was tuned at a lower threshold compare to the 2 previous datasets (1000 electrons as a threshold instead of 1200) and the ToT to charge tuning is also different (6 ToT for 4000e).

### ToT distribution vs Bias voltage

The Figure 7.15 [142] shows the ToT distribution of W80 irradiated with an average fluence of  $1 \times 10^{16} \text{ n}_{\text{eq}}/\text{cm}^2$  for 5 different bias voltages, from 400 V to 600 V with steps of 50 V.

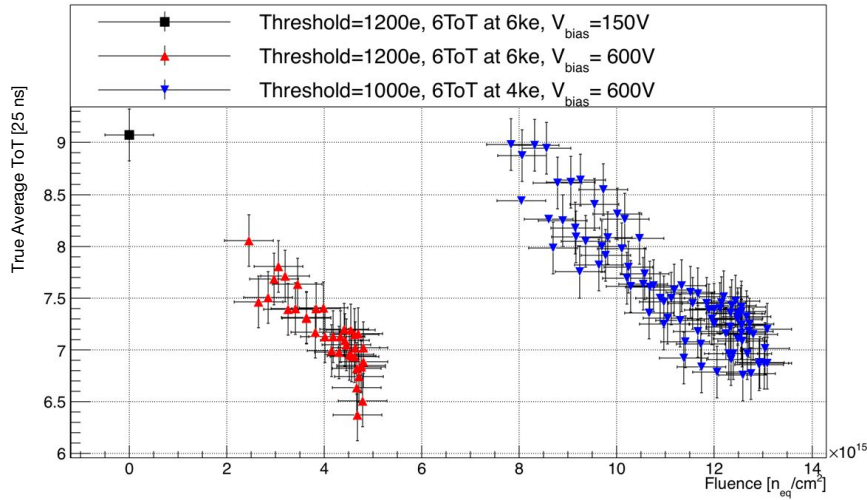


Figure 7.14 – Average ToT vs Fluence for two sets of tuning: Threshold = 1200 electrons, 6ToT at 6000 electrons (150V un-irradiated and 600V irradiated) and Threshold = 1 000 electrons, 6ToT at 4000 electrons (600V)

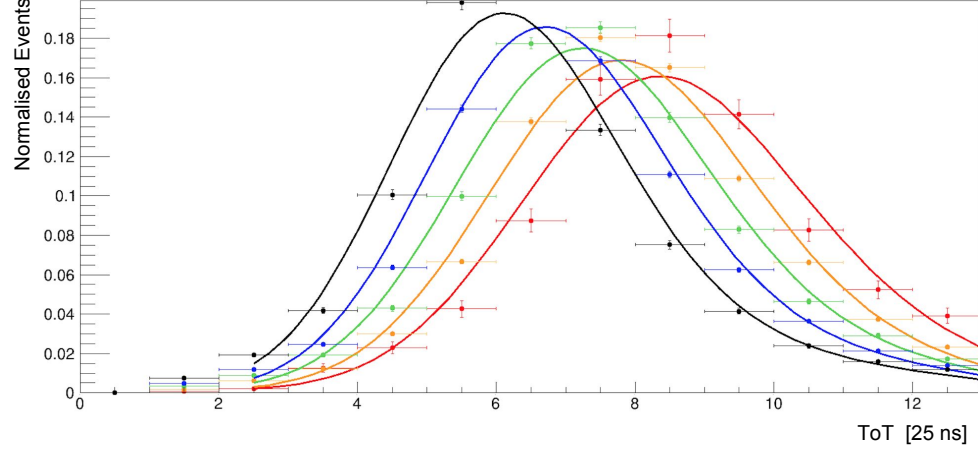
Data were taken at CERN and the level of beam collimation did not allow us to do the detailed fluence analysis proposed for data taken at DESY. Hence the fluence is averaged over the illuminated area. The tested configurations had a threshold of 850 electrons and the ToT to charge calibration was 8 ToT for 4000 electrons. All the distributions were fitted with a Landau convoluted with a Gaussian allowing the determination of the Most Probable Value (MPV). At 400 V the MPV is 73% of the one at 600 V.

The Figure 7.16 presents the average ToT distribution for a set of three bias voltages (400 V, 500 V, 600 V); data were taken at DESY with a threshold of 850e and a ToT gain of 8 ToT for 4000 electrons. At  $9 \times 10^{15} \text{ n}_{\text{eq}}/\text{cm}^2$  and 600 V, the average ToT value is of the order of 8ToT, at 500 V it decreases by 2 ToT units and loses another ToT unit at 400 V. At  $1.3 \times 10^{16} \text{ n}_{\text{eq}}/\text{cm}^2$  the trend is similar, at 600 V, the average ToT value is of the order of 5.5ToT, at 500 V it decreases by 2 ToT units moving to 3.5 ToT and loses another ToT unit at 400 V. An interesting feature of this plot is the linear dependency of the average ToT over the studied fluence range, it seems to be the case for the three investigated bias voltages. Both contributions from the averaging over columns and rows (respectively open and full symbols) present similar results, which is an indication of the goodness of the fluence peak constraint and fluence distribution modeling.

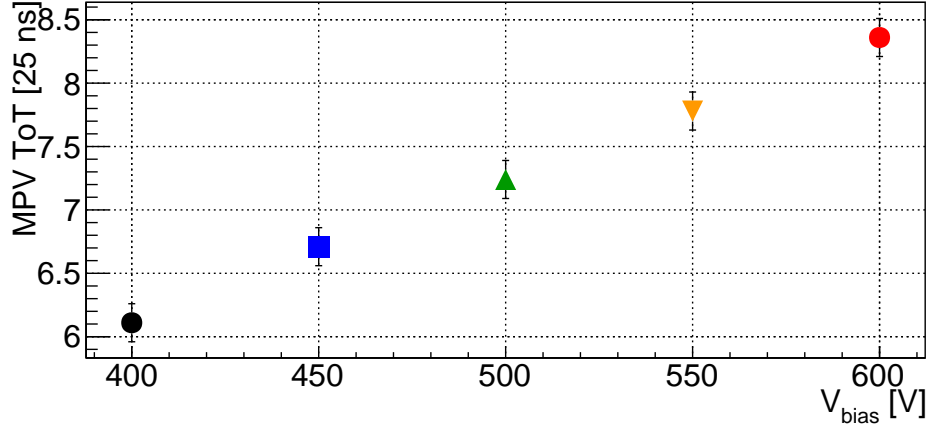
### ToT distribution vs Threshold

The Figure 7.17 presents the average ToT distribution for a set of two thresholds (1200e and 1000e). Both curves were taken with the same ToT tuning (6 ToT corresponding to 4000 electrons) and with the same bias voltage (600V).

Moving from 1000 electrons to 1200 electrons globally decreases the ToT by a ToT unit, over the tested fluence range. The average ToT is decreasing with the fluence for all threshold



(a)



(b)

Figure 7.15 – ToT distribution (a) for W80 thin sensor irradiated at  $1 \times 10^{16} \text{ n}_{\text{eq}}/\text{cm}^2$ . Five bias voltages between 400 V and 600V were considered (black 400 V, blue 450 V, green 500 V, orange 550 V, red 600 V), the threshold was set to 850 electrons. All the distribution are fitted by a gaussian convoluted with a landau and the MPV of the ToT distribution is extracted and reported in the bottom plot, uncertainties on the MPV are obtained by changing the fit range.

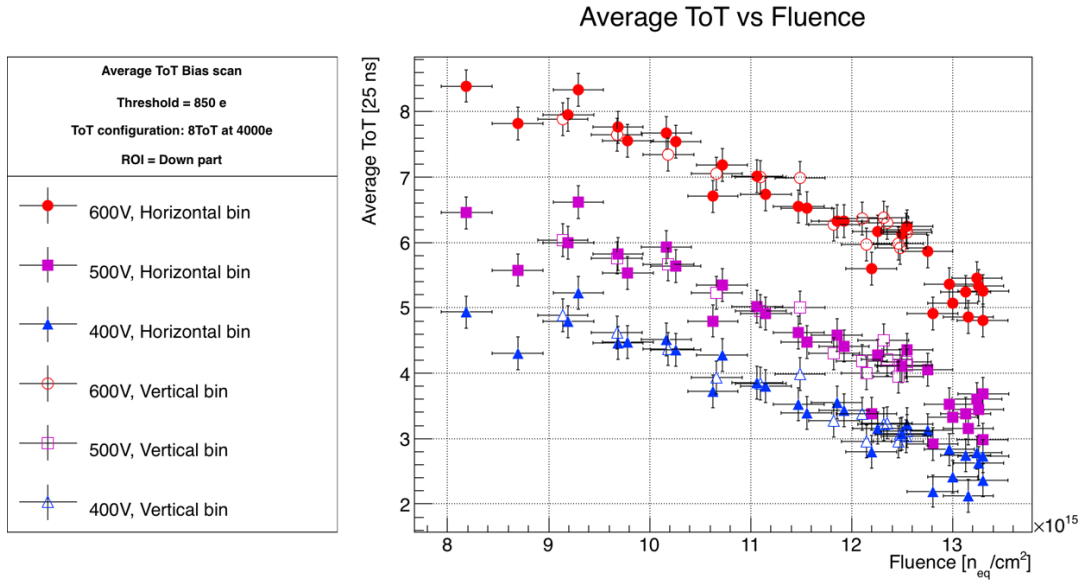


Figure 7.16 – Average ToT distribution vs fluence for 3 different bias voltages. The horizontal/vertical bin label in the legend means that the fluence and average ToT have been extracted from an horizontal/vertical profile of the region of interest.

tunings. Both data obtained from horizontal and vertical profiles are plotted and seems coherent among themselves, meaning that no significant deviation is observed especially in the Horizontal profiles which could be caused by the already mentioned horizontal FE-I4 threshold drift.

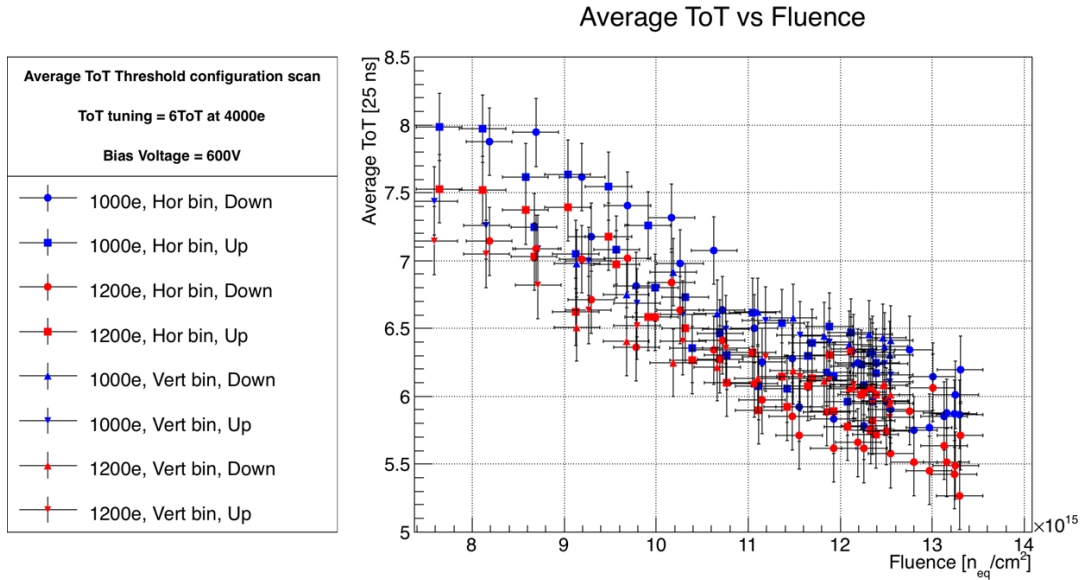


Figure 7.17 – average ToT distribution vs fluence for 2 different threshold tunings. The horizontal/vertical bin label in the legend means that the fluence and average ToT have been extracted from an horizontal/vertical profile of the region of interest (Down or Up).

### 7.4.2.2 Charge collection efficiency

#### Charge to ToT calibration

As explained in section 6.2, the charge to ToT relation is not linear. To precisely estimate the charge to ToT conversion, a charge to ToT calibration scan has to be performed using STControl [143]. The Figure 7.18 shows several Charge to ToT calibration curves for three tunings, with different threshold (1200e, 1000e and 1500e), different ToT to charge tuning (6ToT for 4000e and 6ToT for 6000e). The temperature of the sensors during the scans was around  $-39^{\circ}\text{C}$ . As expected, for a similar ToT tuning, a higher threshold implies a lower collected charge, as small signals are lost. It can be seen that the target value of the ToT to charge conversion is respected by all curves.

Various charge to ToT calibration scans have been performed, and the variability between two calibration curves is used as a systematics uncertainty on the charge value. For the configuration with a threshold of 1000e and a ToT gain of 6ToT for 4000e, three calibrations curves are plotted (in black, red and magenta). They are all contained in a conservative safety margin of 500 electrons around the black curves. In the following the uncertainty on the charge arising from the uncertainty of charge to ToT calibration is then set to 500 electrons.

The uncertainty on the fluence arises from the modeling of the fluence profile and on the uncertainty on the peak position. It is set to  $0.5 \times 10^{15} \text{ n}_{\text{eq}}/\text{cm}^2$  which corresponds to the variation of fluences at 2 mm from the fluence peak.

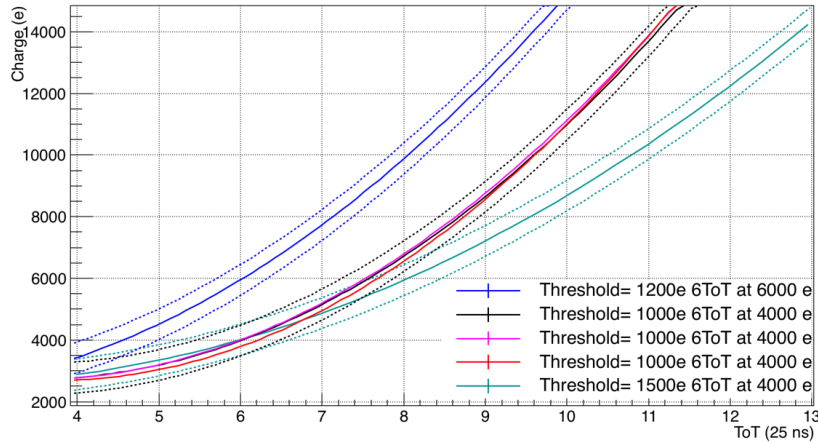


Figure 7.18 – Charge to ToT calibration curves for three sets of tuning and threshold. Curves in black, red and magenta are obtained for the same tuning values (threshold of 1000 electrons and ToT calibration of 6 ToT corresponding to 4000 electrons). Dashed lines represents a  $\pm 500\text{e}$  uncertainty.



### Cluster charge distribution

The collected charge for the irradiated W80 module and for the un-irradiated W30 module is plotted in 7.19. This plot compiles results from 3 testbeams where the W30 sensor was tested un-irradiated, biased at 150 V and with a threshold of 1200e and a ToT configuration of 6ToT corresponding to 6000 electrons (black square on the plot), and W80 sensor was tested irradiated un-homogeneously at  $3 \times 10^{15} \text{ n}_{\text{eq}}/\text{cm}^2$  (red triangles) and irradiated un-homogeneously at  $1 \times 10^{16} \text{ n}_{\text{eq}}/\text{cm}^2$ . Before irradiation, the average collected charge is 12500 electrons which is quite close to what is expected for a 100  $\mu\text{m}$  thick sensor. The decrease with fluence of collected charge is steeper at lower fluences (red markers) than at higher fluences (blue markers). This is probably due to a threshold tuning of poorer quality of the former with respect to the latter.

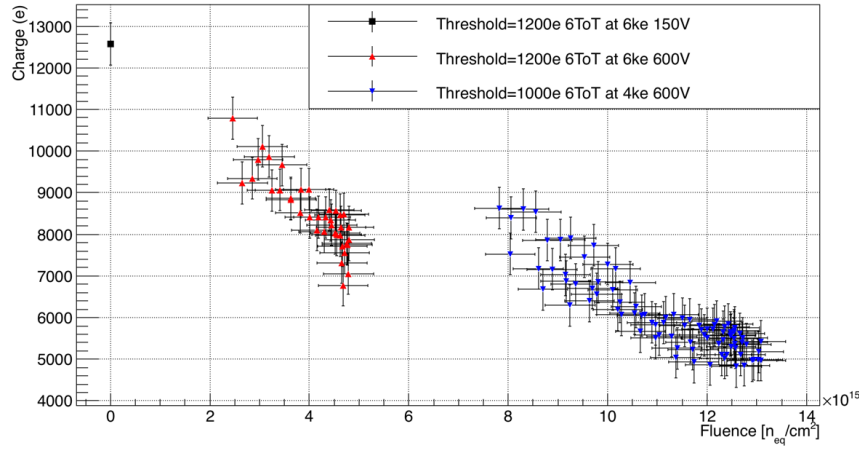


Figure 7.19 – Collected charge vs Fluence for two sets of tuning: Threshold=1200e, 6ToT at 6ke (150V, un-irradiated and 600V, irradiated) and Threshold=1000e, 6ToT at 4ke, 600V.

### Charge collection efficiency

From Figure 7.19, the charge collection efficiency was derived. The charge value at a fluence  $\Phi = 0$  was obtained from W30 sensor whose thickness was 100  $\mu\text{m}$ . For the other fluence, the charge reported in Figure 7.19 was obtained from W80 sensor, whose thickness was 130  $\mu\text{m}$ . Consequently, to evaluate the charge collection efficiency, a scale factor of 1.3 was applied to the charge value obtained at  $\Phi = 0$  to emulate the charge value which would have been obtained for the un-irradiated W80 sensor. The Figure 7.20 shows the Charge collection efficiency of W80 over a typical ITk like fluence range. The distribution is fitted with the Hecht function described in section 7.2.1. From those fits one can extract the effective  $\beta$  values, which in a first approximation was set equal for holes and electrons. For the intermediate fluence dataset (red triangles)  $\beta_e = \beta_h = 5.5 \pm 0.2 \times 10^{-16} \text{ cm}^2/\text{ns}$ ; for the higher fluence dataset (blue triangles)  $\beta_e = \beta_h = 3.6 \pm 0.1 \times 10^{-16} \text{ cm}^2/\text{ns}$ . The two values are of the same order of magnitude, their differences can come from the different tuning



configurations, from a different annealing time or from the various approximations used (such as  $\beta_e = \beta_h$ ).

As reported in [86],  $\beta$  evolves with the temperature, the annealing, the type of silicon material and the irradiation particles. W80 was irradiated in 2 times with high energy protons. It has annealed during an unmonitored amount of time (order of several weeks). For such temperatures and an irradiation by protons (up to a fluence of  $1 \times 10^{14} \text{ n}_{\text{eq}}/\text{cm}^2$ ), the values of  $\beta$  at  $-40^\circ\text{C}$  are found in [86] to be of the order of  $\beta_e = 6.6 \pm 0.3 \times 10^{-16} \text{ cm}^2/\text{ns}$  and  $\beta_h = 10.1 \pm 0.3 \times 10^{-16} \text{ cm}^2/\text{ns}$ .

Values from W80 modules are of the same order but significantly lower. This can be explained by the fact that data from [86] describe sensors just up to  $1 \times 10^{14} \text{ n}_{\text{eq}}/\text{cm}^2$  and our range of fluence extend over 2 more orders of magnitude. The non uniform irradiation of the sensor as well as its unmonitored annealing times can also explain this discrepancy.

The mono-dimensional hypothesis for the sensor geometry from the Hecht formula does not take into account the real geometry of the sensor. Hence the obtained  $\beta$  values can be considered as lower limits for the true  $\beta$  values of the sensor.

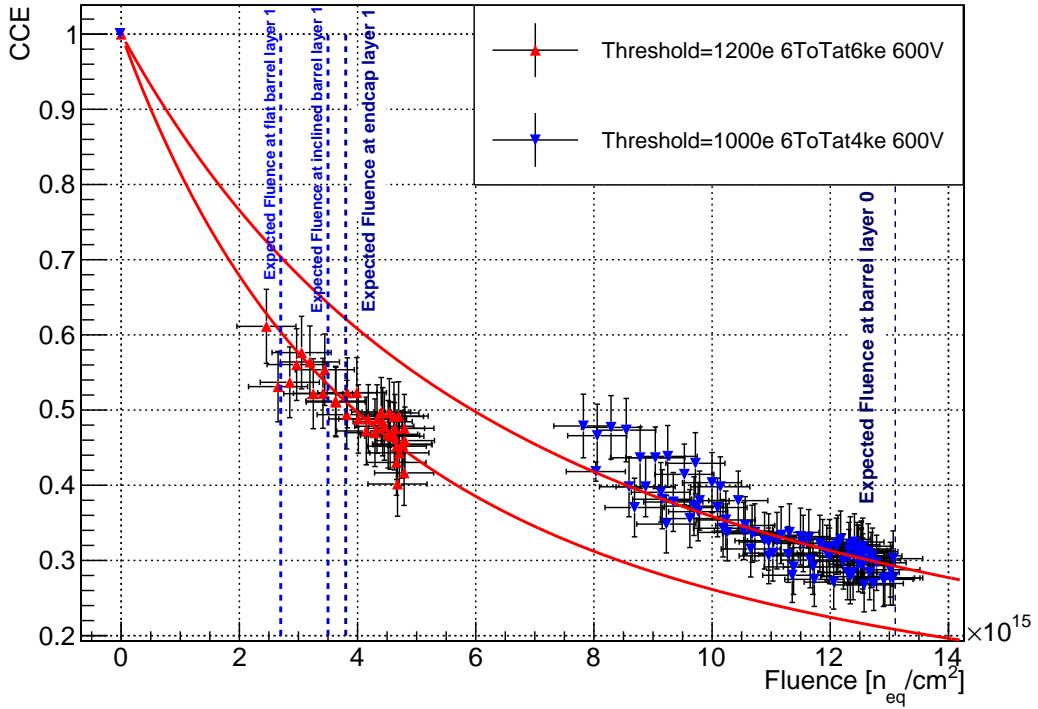


Figure 7.20 – Charge collection efficiency extrapolation for two sets of tuning: Threshold=1200e, 6ToT at 6000e and Threshold=1000e, 6ToT at 4000e. Expected end-of-lifetime fluences for ITk are also indicated.

The 4 vertical blue dotted lines symbolize the limit fluence expected at the end of lifetime of 4 different layers of ITk [107]. From left to right one can find:

- The fluence expected ( $2.7 \times 10^{15}$  n<sub>eq</sub>/cm<sup>2</sup>) at the layer 1 (second layer from the beam pipe) in the central flat part.
- The fluence expected ( $3.5 \times 10^{15}$  n<sub>eq</sub>/cm<sup>2</sup>) at the layer 1 in the inclined part.
- The fluence expected ( $3.8 \times 10^{15}$  n<sub>eq</sub>/cm<sup>2</sup>) at the layer 1 in the endcap part
- The fluence expected ( $13.1 \times 10^{15}$  n<sub>eq</sub>/cm<sup>2</sup>) at the layer 0 (closest layer from the beam pipe) in the flat barrel part.

Table 7.2 – Charge collection efficiency for 2 tunings over the ITk fluence range

	Fluence ( $10^{15}$ n <sub>eq</sub> /cm <sup>2</sup> )			
	<b>2.7</b>	<b>3.5</b>	<b>3.8</b>	<b>13.1</b>
Thr=1200e, 6ToT at 6000e, CCE =	<b>61%</b>	<b>53%</b>	<b>51%</b>	<b>21%</b>
Thr=1000e, 6ToT at 4000e, CCE =	<b>71%</b>	<b>64%</b>	<b>62%</b>	<b>29%</b>

The Table 7.2 compiles the values of the intersections of the 2 fits with the 4 fluence lines. The intersection of the Hecht fit with the fluence lines, indicates that the charge collection efficiency drops by approximately 5% over the all fluence range when the threshold is increased from 1000 electrons to 1200 electrons. For the 1000 electrons threshold and the three fluences corresponding to the accumulated dose at layer 1, the charge collection efficiency is higher than 60%. At  $1.3 \times 10^{16}$  n<sub>eq</sub>/cm<sup>2</sup>, the fluence expected at Layer 0 in the flat section after 2000 fb<sup>-1</sup>, the charge collection efficiency is lower than 30%.

The Figure 7.21 compares the charge collection efficiency of IBL modules and the standalone simulation from Chapter 4 and our charge collection efficiency estimation for the ITk. The use of thinner sensors (130 μm) and high voltage allows to have similar charge collection efficiency but with an order of magnitude more in terms of fluence compared to IBL modules. Those data will also be used to investigate the modeling of radiation damage at high fluence in the perspectives of providing an accurate radiation damage digitizer for ITk, on the same basis as the one developed for the Run2 (see Chapter 4).

### 7.4.3 Global hit efficiency

By exploiting CERN SPS data, we were able to retrieve the global hit efficiency. As shown in the figure 7.22, the efficiency of the thin sensors is really close to the 97% ATLAS ITk requirement. At  $3 \times 10^{15}$  n<sub>eq</sub>/cm<sup>2</sup> and 600 V, the efficiency reaches 97%. At  $1 \times 10^{16}$  n<sub>eq</sub>/cm<sup>2</sup> and 600 V, the efficiency is  $96.3 \pm 0.5\%$ , quite close to the 97% ATLAS ITk requirement. At  $3 \times 10^{15}$  n<sub>eq</sub>/cm<sup>2</sup>, the hit efficiency seems to saturate around 96.5% between 400V and 500V.

As it was previously done for the charge collection efficiency analysis, to obtain a better approximation of the performance in terms of efficiency with respect to the fluence, the hit efficiency had also been evaluated using DESY data and are reported in Figure 7.23.

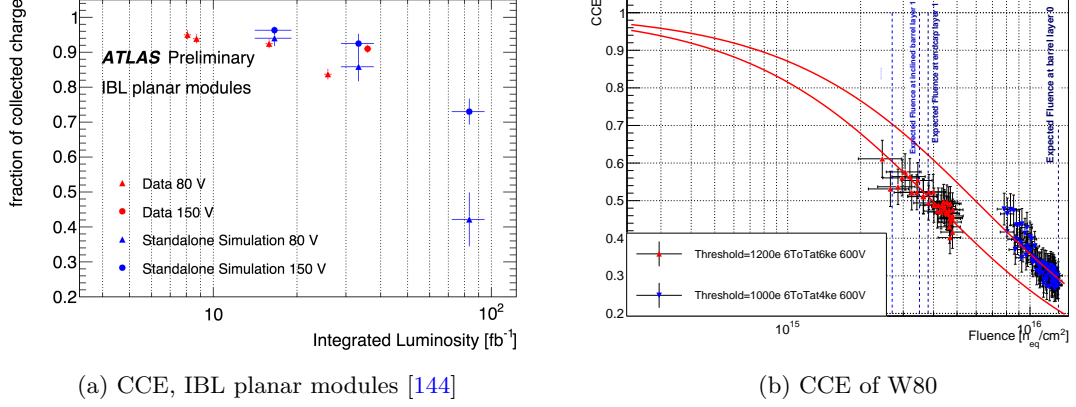


Figure 7.21 – (a) CCE expected at the end of Run2 with current IBL sensors, compared to (b) charge collected efficiency obtained for 2 sets of fluence at the end of ITK lifetime for the second layer (red), and for the first layer (blue) at mid luminosity course, if production2-like sensors were considered. The lines are the result of a fit with Hecht formula.

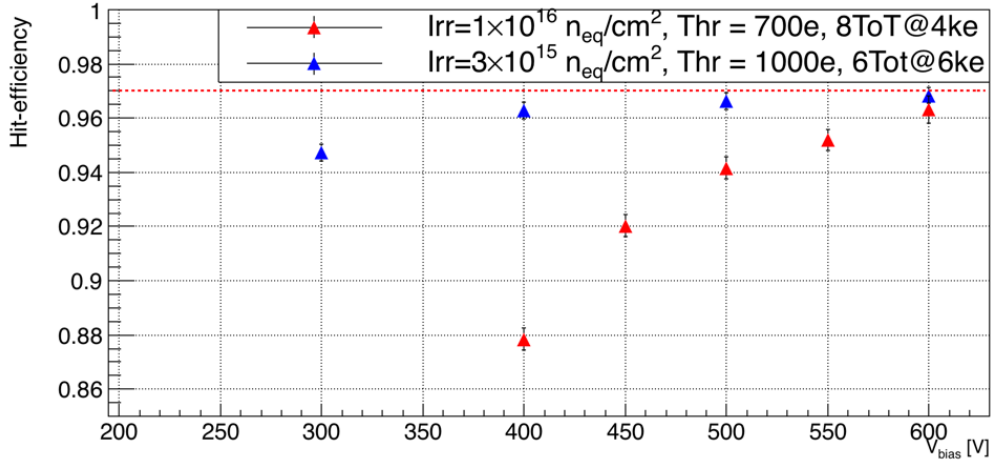


Figure 7.22 – Hit efficiency for thin irradiated sensors. The red triangles are for sensor irradiated at an average fluence of  $1 \times 10^{16} \text{ n}_{\text{eq}}/\text{cm}^2$  and the blue ones at an average fluence of  $3 \times 10^{15} \text{ n}_{\text{eq}}/\text{cm}^2$ . Threshold and gain are indicated in the upper box.

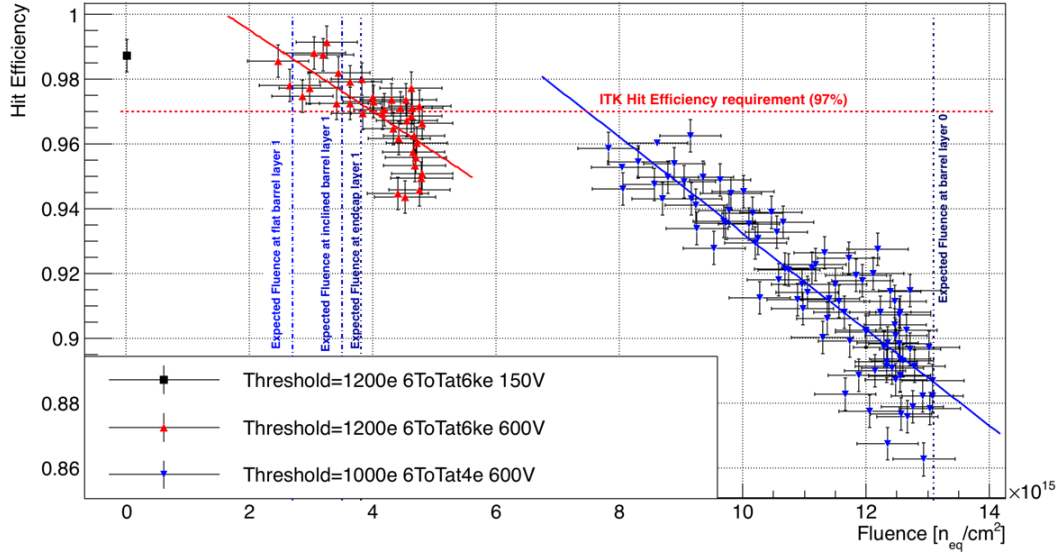


Figure 7.23 – Hit efficiency for thin irradiated sensors. The blue triangles are for sensor irradiated at  $1 \times 10^{16}$   $n_{eq}/cm^2$  and the red ones at  $3 \times 10^{15}$   $n_{eq}/cm^2$ . The black square represents data for a thin un irradiated sensor. Threshold and gain are indicated in the box.

The two datasets were fitted with a straight line. The horizontal uncertainty bars account for the uncertainty on the fluence peak position and on the modeling of the irradiation profiles, as explained in Section 6.1.3. The vertical error bars are the combination of the systematic uncertainties arising from the selection criteria variations (0.4%) and from the statistical fluctuations (0.25%). For the statistical part, for all fluence points at least 5000 tracks were considered, hence the statistical (binomial) error is less than 0.25%. The horizontal red dotted line represents the hit efficiency requirements expected by ITK (97%). The 4 vertical blue dotted lines symbolize the limit fluence expected at the end of lifetime of 4 different layers of ITk. From left to right one can find:

- The fluence expected ( $2.7 \times 10^{15}$   $n_{eq}/cm^2$ ) at the layer 1 (second layer from the beam pipe) in the central flat part.
- The fluence expected ( $3.5 \times 10^{15}$   $n_{eq}/cm^2$ ) at the layer 1 in the inclined part.
- The fluence expected ( $3.8 \times 10^{15}$   $n_{eq}/cm^2$ ) at the layer 1 in the endcap part
- The fluence expected ( $13.1 \times 10^{15}$   $n_{eq}/cm^2$ ) at the layer 0 (closest layer from the beam pipe) in the flat barrel part.

The Table 7.3 presents the expected efficiency for the various fluences, obtained from the crossing point of the fit and the fluence lines. The efficiency obtained for the various part of layer 1 are all beyond the 97% requirement. A lower threshold and a better tuning could certainly help to reach higher values in terms of efficiency. For example, the prediction from the 1000 electrons threshold data, assuming a linear dependency shows that the crossing between the ITk requirement line and the extrapolated values happen around  $7 \times 10^{15}$   $n_{eq}/cm^2$ .

For higher fluences, such as the one expected at end of the lifetime of Layer 0, the efficiency drops below 97 %: the tested sensor is clearly not suited for the ITk innermost layer.

Table 7.3 – Table of extrapolated efficiency for ITk benchmarks fluences.

Fluence ( $10^{15}$ n <sub>eq</sub> /cm <sup>2</sup> )	2.7	3.5	3.8	7.45	13.1
Threshold (electrons)	1200	1200	1200	1000	1000
ToT tuning (ToT corresponding to electrons)	6at6	6at6	6at6	6at4	6at4
<b>Extrapolated Hit Efficiency</b> (% $\pm$ 0.5%)	<b>98.6</b>	<b>97.6</b>	<b>97.2</b>	<b>97.0</b>	<b>88.6</b>

#### 7.4.4 Conclusion on thin and irradiated sensors

Thin sensors (130  $\mu\text{m}$  thick) have been tested on beams and their performance in terms of charge collection efficiency and hit efficiency have been evaluated. Up to  $3.8 \times 10^{15}$  n<sub>eq</sub>/cm<sup>2</sup>, the hit efficiency is higher than ITk requirement, the charge collection efficiency is similar to what is now achieved at the end of Run2 but with an order of magnitude more in terms of fluences. The power dissipation at this fluence is extrapolated to be 6 mW at  $-25^\circ\text{C}$ . For the fluence expected at Layer0, the hit efficiency of such sensor would be around 88 %, with a charge collection efficiency inferior to 40% and a power dissipation greater than 40 mW/cm<sup>2</sup>. By comparison, 3D pixel sensors [80] exposed to a fluence of  $1 \times 10^{16}$  n<sub>eq</sub>/cm<sup>2</sup> have been recently tested and they exceed the ATLAS ITk hit efficiency requirement (97%) with a power dissipation of the order of 8 to 10 mW/cm<sup>2</sup> at  $-25^\circ\text{C}$ .

In conclusion it seems that thin sensors from this production are suited to be part of the ITk intermediate layers. The use of an adequate tuning (lower threshold and adequate Charge to ToT tuning) is important and could help to gain in hit efficiency. It is uneasy to reach an acceptable low threshold with the actual chip, while it will be more easily achievable using the RD53 chip [111], which should also ensure higher uniformity of performance over the pixel matrix

## 7.5 Active edge performance

The development of sensors with a reduced dead area is necessary to ensure an optimal geometrical acceptance of the ITk. Active edge sensors have a reduced dead area at their borders thanks to their chemical etched edges and their reduced numbers of guard rings. The first production of sensor (sensors LPNHE5 and LPNHE7 in the following) have standard active edge at 100  $\mu\text{m}$  from the edge of the last pixel. The option with 0 and 2 Guard Rings (GR) was investigated.

The module M1.4 from the third LPNHE production have also active edge, but a different version: the edge is not continued but staggered. Such design allows in principle to bypass

the use of a support wafer. The pixel to trench distance of M1.4 is 50  $\mu\text{m}$  and it possesses no guard rings (see Table 6.1).

### 7.5.1 Standard active edge performance

The hit efficiency at the detector edge for both LPNHE5 and LPNHE7 is presented in Figure 7.24 (from [81]). LPNHE5 and LPNHE7 were measured at DESY and at CERN respectively; the threshold was set to 1600 (1400) e for LPNHE5 (LPNHE7), while the bias voltage was 40 V for both detectors.

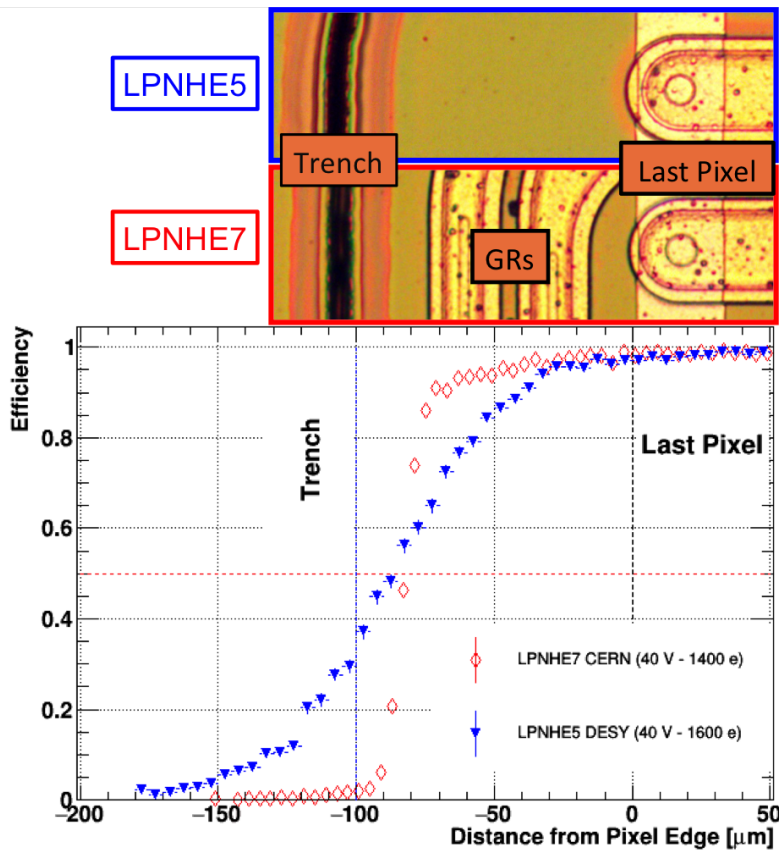


Figure 7.24 – Edge efficiency profiles for LPNHE5 (no GRs - full markers) and LPNHE7 (2 GRs - open markers). Laboratory where the data were taken, device bias voltage and threshold are indicated too. The horizontal dashed line marks the 50%-point efficiency. The device photograph on top helps in visualizing which physical area of the pixel is related to the efficiency profile.

Thanks to the active edge technology both detectors are efficient even in the un-instrumented area: for both LPNHE5 and LPNHE7 the efficiency is higher than 50% up to about 90  $\mu\text{m}$  away from the last pixel, that is only 10  $\mu\text{m}$  from the cut edge. This performance meets the specifications of ATLAS ITk pixel modules [106] in terms of distance from the active region to the cut edge.

As a reminder, LPNHE7 has 2 GRs, one connected to ground laying between 13  $\mu\text{m}$  and 50  $\mu\text{m}$  from the last pixel, one floating between 55  $\mu\text{m}$  and 80  $\mu\text{m}$ ; LPNHE5 has no GRs. The behavior of the 2 samples is rather similar in the first 30  $\mu\text{m}$ , where the efficiency is basically flat. Then the efficiency drops faster for LPNHE5, while for LPNHE7 the efficiency is a plateau between 0 and -50  $\mu\text{m}$  then it smoothly decreases to reach 90 % at -80  $\mu\text{m}$ , before sharply dropping to 0.

Even if data taking conditions were different and clearly sub-optimal for LPNHE5 (higher threshold, multiple scattering, ...), the detector is still quite efficient in the edge area. In particular, it is to be noted that the slope of the hit efficiency curve is consistent with the smearing in the telescope tracking resolution due to the multiple scattering. Nevertheless, further tests on active edge sensors without GRs are necessary (see Section 7.5.2).

For LPNHE7, the good performance in terms of efficiency in the edge area indicates that the presence of GRs does not degrade the hit efficiency, even in the area of the innermost connected GR.

### 7.5.1.1 Comparison with TCAD simulations

To better understand the efficiency in the GRs region, two dimensional numerical simulations (for details see [119]) were run; the edge area of sensors with 0 and 2 GRs and a 100  $\mu\text{m}$  distance between the last pixel and the doped trench were studied. The results are shown in Figure 7.25 for a simulated bias voltage value of 40 V.

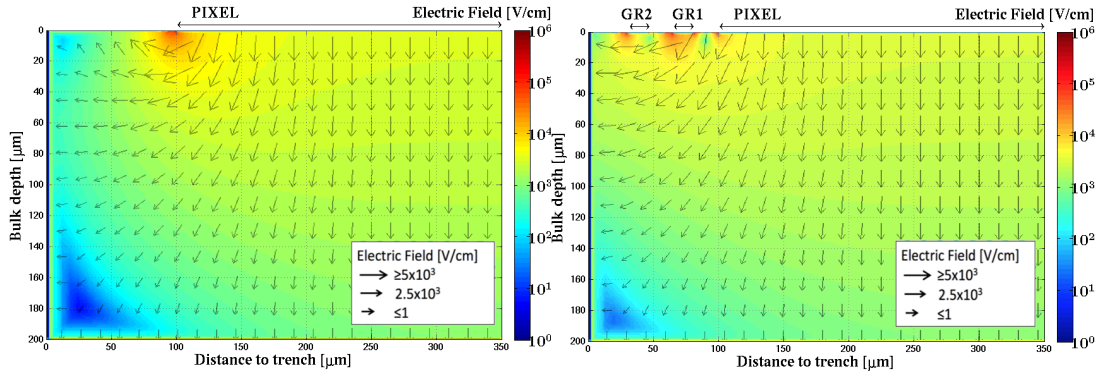


Figure 7.25 – Numerical simulation of the electric field. Left: 0 GRs; right: 2 GRs. The simulated bias voltage value was 40 V.

From Figure 7.25 it can be seen that the GRs do not deeply influence the electric field lines. The charge carriers, following the electric field lines, are collected by the last pixels if they are electrons or by the trench or backside if they are holes. This seems to be the case from the simulation results, except for electrons generated within a small depth below the GRs. This picture is consistent with the efficiency results shown in Figure 7.24.

From Figure 7.25 it can also be seen that the depleted area is slightly larger for the sensors with 2 GRs and extends till the sensor edge: the GRs are contributing to the depletion of the sensor bulk. The simulated electric field magnitude in Figure 7.25 shows a weak electric



field region in the bottom left corner; this is due to the presence of two close equipotential planes, the doped trench and the sensor backside. Carriers generated here drift so slowly that they do not produce a signal during the latency of the read-out electronics, and the efficiency drops.

In summary, based on the above results, supported by numerical simulations, it can be stated that GRs do not preclude the possibility to have edgeless detectors; their presences make possible at the same time high hit efficiency at the detector edge, by extending laterally the depletion region, and high breakdown voltage (as shown in Figure 6.6).

### 7.5.1.2 Lateral depletion in the edge region

In order to further investigate the lateral depletion of the LPNHE7 sensor in the un-instrumented area between the last pixel and the trench, the hit efficiency was measured as a function of the track distance (predicted by the telescope) from the sensor last pixel edge for several values of the bias voltage, as shown in Figure 7.26.

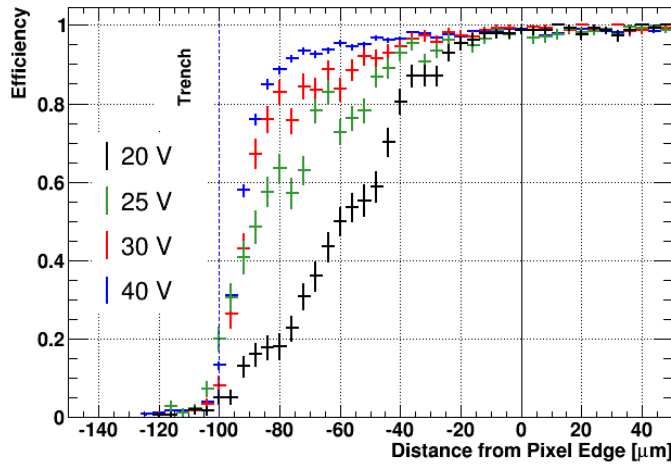


Figure 7.26 – Comparison of edge efficiency profile of LPNHE7 for several bias voltages

The edge efficiency is highest at 40 V, where the lateral depletion is such that the efficiency exceeds 50% up to a distance of 90  $\mu\text{m}$  from the pixel edge. At 20 V, the lateral depletion is clearly not completed as the 50% efficiency point is reached at 60  $\mu\text{m}$ . The 30 V efficiency profile is quite close to the 40 V curve, although the high efficiency ( $>95\%$ ) in the region between 50  $\mu\text{m}$  and 70  $\mu\text{m}$  is possible only at the 40 V. A few events yield non zero efficiency up to 20  $\mu\text{m}$  beyond the edge. This is consistent with the spatial resolution of the hits formed by one pixel cell.



### 7.5.2 Staggered active edge performance

One sensor of the third production, M1.4 has been irradiated uniformly at KIT [128] with low energy protons to reach a fluence of  $2.7 \times 10^{15} \text{ n}_{\text{eq}}/\text{cm}^2$ . After irradiation, the sensor suffered from an early breakdown when biased around 90-95 V at  $-40^\circ\text{C}$  as presented in Figure 6.16. The Figure 7.27 compare the efficiency performance close to the edge area of the M1.4 sensor before and after irradiation. Even in early breakdown regime, the efficiency performance of the irradiated sensor in the edge area is comparable to what was reached before irradiation. For a threshold of 1000 electrons and a ToT tuning of 6 ToT for 4000 electrons, the efficiency is higher than 50% up to 44  $\mu\text{m}$  from the last pixel. The data reported in this Figure were taken at DESY testbeam and they are consequently affected by the multiple scattering.

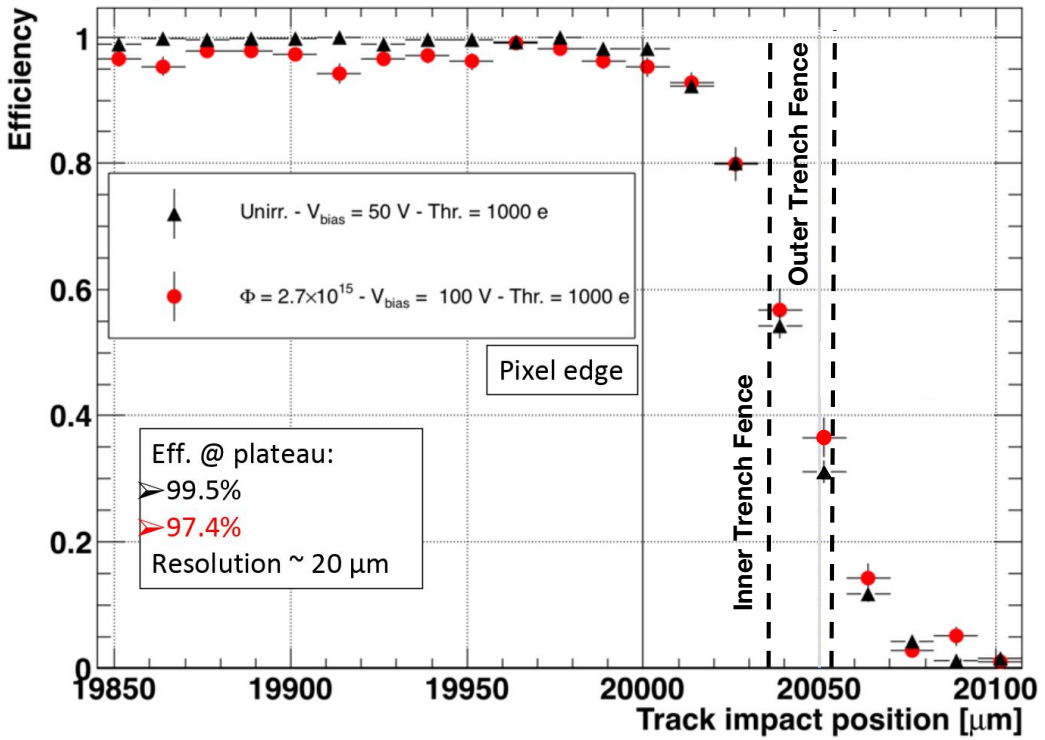


Figure 7.27 – Comparison of edge efficiency profile before and after irradiation of one sensor of the third production (M1.4). Data were taken at DESY

The data presented in Figures 7.28 shows performance of the irradiated M1.4 sensor ( $2.7 \times 10^{15} \text{ n}_{\text{eq}}/\text{cm}^2$ ) with data taken at CERN-SPS testbeam with different tunings and bias voltages. Other tunings and three bias voltages (90, 100, 110 V) have been tested on beam:

- Threshold: 1000 electrons, 8 ToT for 4000 electrons. The three bias points give rather similar results, the efficiency reaches 50% at 44  $\mu\text{m}$  from the last pixel except for the configuration at 110V which seems to be 2  $\mu\text{m}$  lower. This value is obtained by performing a fit with an error function in the edge region. The efficiency at the plateau is close to 99 %.

- Threshold: 1200 electrons, 6 ToT corresponding to 6000 electrons. The three bias points gives similar results, the efficiency reaches 50% at 44  $\mu\text{m}$  from the last pixel. This value is obtained by performing a fit with an error function in the edge region. The efficiency at the plateau is about 99.5 %.

The six tested configurations gives rather similar results in terms of efficiency at the edge. The events shown after the second edge (at 52 $\mu\text{m}$ ) are not physical, they appear to be after the edge because of the spatial resolution of the sensor which is of the order of 14  $\mu\text{m}$  as presented in the section 7.2.3.

The edge structure of the third production has a pitch of 70  $\mu\text{m}$ , as presented in Section 6.1.4. The Figure 7.29, shows the efficiency in the area between the last column pixels and the staggered trench. The trench pitch being 70  $\mu\text{m}$ , this figure is an efficiency map whose Y dimension is folded to obtain a superposition of all 2 pitches (140  $\mu\text{m}$ ) cell. This folding allow to investigate the behavior of the efficiency in the various part of the trench with sufficient statistics. One can see that the efficiency extend further in the area where there is the second edge fence but not the first one, with an efficiency higher than 50 % up to 50  $\mu\text{m}$  from the last pixel limit whereas when the innermost trench segment is present, the 50% efficiency point is reached around 35  $\mu\text{m}$  from the last pixel limit.

The edge efficiency profiles of Figure 7.30 intersects respectively the first fence (a) between  $Y=56\text{ }\mu\text{m}$  and  $Y=70\text{ }\mu\text{m}$  and the second fence (b) between  $Y=28\text{ }\mu\text{m}$  and  $Y=42\text{ }\mu\text{m}$ .

From those profiles it is clear that the lateral depletion extends further in the second case. The 50% efficiency point is at approximately 47  $\mu\text{m}$  in the second case and 37  $\mu\text{m}$  in the first case. In the first case, the drop of efficiency is sharper than the second case and the efficiency reaches 20% around 43  $\mu\text{m}$  whereas in the second case, this limit is reached at 55  $\mu\text{m}$ .

### 7.5.2.1 Comparison with TCAD simulations

In order to understand in detail the lateral depletion of edgeless sensors and the observed efficiency behavior in the two cases previously considered, numerical TCAD simulation (using Silvaco [97]) have been used and will be compared in the following to the testbeam results of the previous section. TCAD simulation shows only un-irradiated sensor.

The simulated 3D structure represented in Figure 7.31 features the detector edge edge and half pixels in the long (250  $\mu\text{m}$ ) pixel directions. As the edge pitch (70  $\mu\text{m}$ ) differs from the pixel pitch, 2 edge pitches are simulated in the Y direction, which corresponds to 2 short pixel pitch and 4/5 of a third one. The structure was 200  $\mu\text{m}$  wide (X), 140  $\mu\text{m}$  (Y) high and 132  $\mu\text{m}$  (Z) deep. A detailed description of the simulation, including details on the doping and on the physical models used can be found in appendix A.

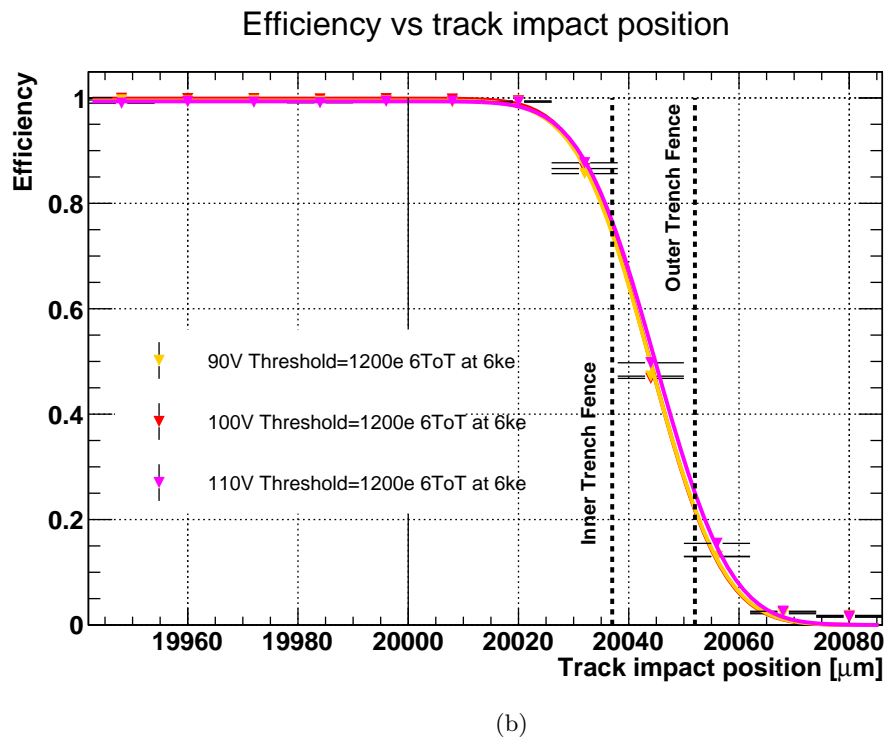
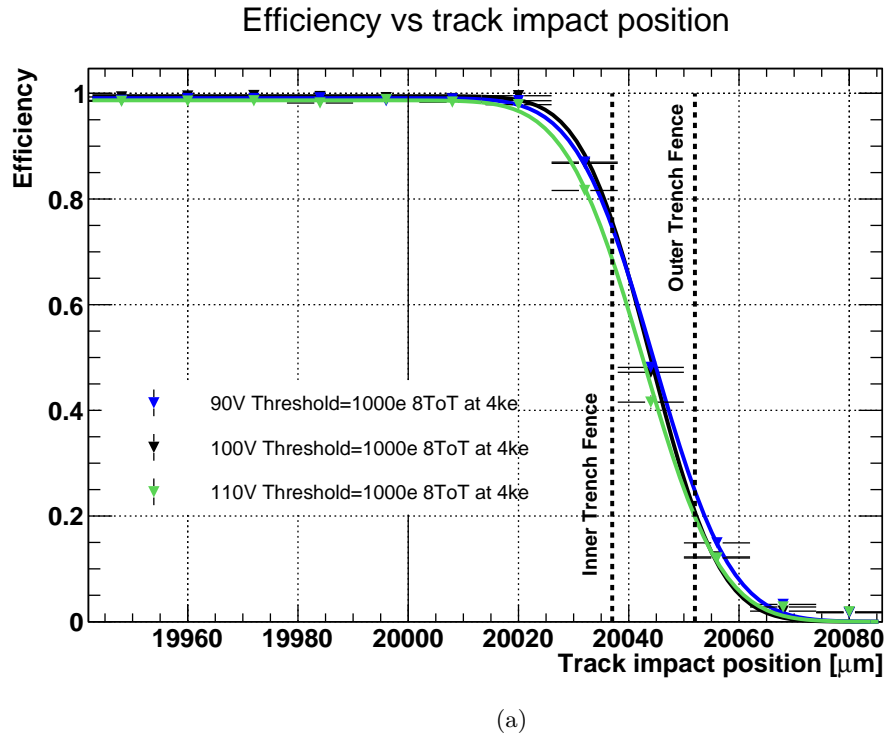


Figure 7.28 – Comparison of edge efficiency profile of irradiated M14 for three bias voltages (90 V, 100 V and 110 V). The two black dashed lines represents the 2 edge fences, the thin dark line at 20000  $\mu\text{m}$  represents the virtual limit of the last pixel. (a) presents results for a threshold of 1000 electrons and a ToT gain of 8 ToT for 4000 e; (b) presents results for a threshold of 1200 electrons and a ToT gain of 6 ToT for 6000 e

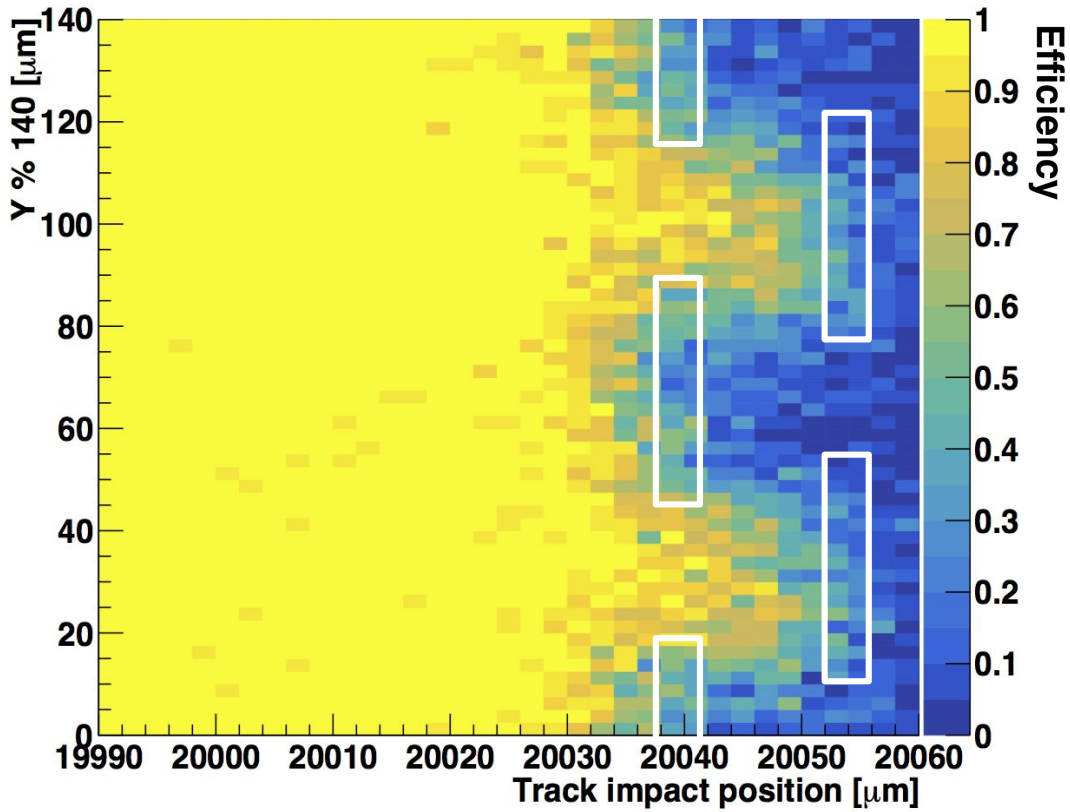


Figure 7.29 – Two dimensional edge efficiency profile for M1.4 at 40 V after irradiation (data taken at CERN-SPS). The white rectangles correspond to trench segments.

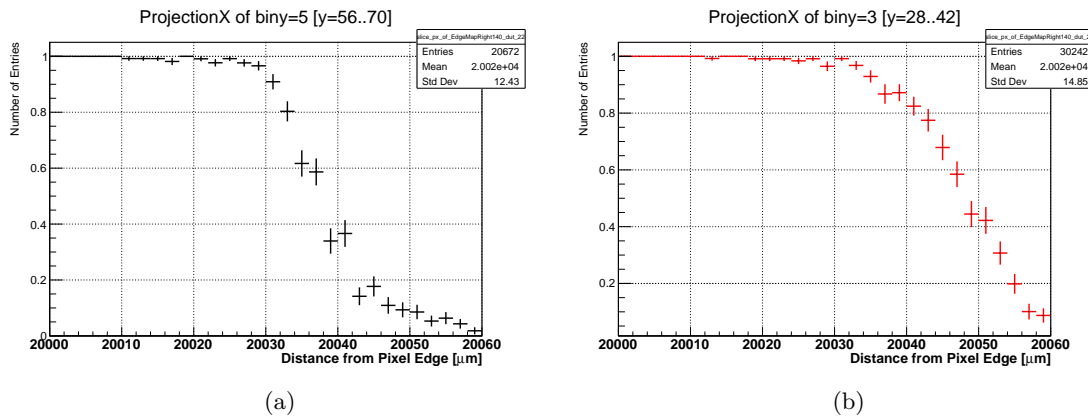


Figure 7.30 – Edge efficiency profiles intersecting respectively the first fence of edge (a) and the second one (b).

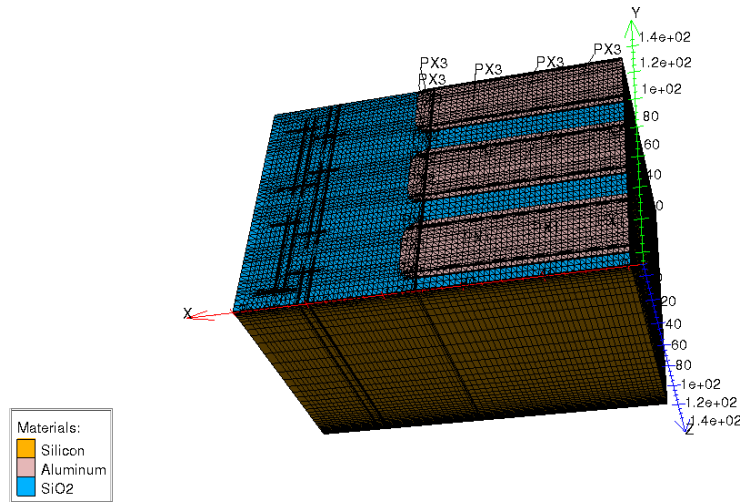


Figure 7.31 – Graphical representation of the simulated 3D structure. The visible part of the mesh grid is superimposed.

### TCAD Simulation results

The Figure 7.32 is the result of a 3D simulation which represents the electric field inside the sensor depleted at 50 V in the vicinity of the edge. The electric field scale is logarithmic. From this figure, it can be seen that in the bottom corner, close to the edge, the electric field is really weak. It indicates that, as seen for the previous production, the lateral depletion is limited by this weak electric field spot.

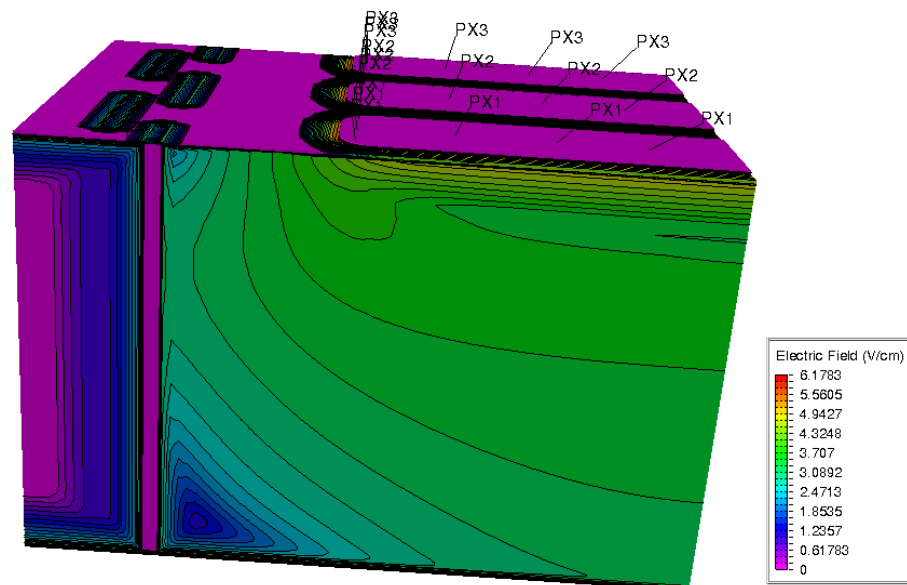


Figure 7.32 – Simulation in 3D of the electric field in the edge area for 50V (un-irradiated sensor). The pink color correspond to a null electric field. One can notice that the electric field is 0 in the trench.

From the 3D simulation, slices for fixed depths in the bulk were extracted. The Figure 7.33 shows the electric field and holes concentration in the edge area. In the horizontal direction, the scale goes from the middle of edge pixels to 75  $\mu\text{m}$  after the virtual pixel limit. This range is sufficient to intersect the two edge fences. The simulations were obtained for three different depths: at 10  $\mu\text{m}$ , 65  $\mu\text{m}$  and 120  $\mu\text{m}$  from the surface. It can be seen that the electric field magnitude decreases with the depth, as well as in the X direction in the edge area. In the top plots (10 $\mu\text{m}$  below the surface), the pixel implant impact on the electric field is clearly visible. The electric field seems to extend at least to the innermost fence.

From the hole concentration plot (Figure 7.33 b), it is shown that the hole concentration varies up to the innermost fence and also between two segments of the innermost fence. The Figure 7.33 d is rather similar to the Figure 7.33 b, but its electric field counterpart, the Figure 7.33c, is rather different than Figure 7.33a.

Figure 7.33 e and f shows that the electric field is close to 0 in the edge area at a depth of 120  $\mu\text{m}$ . This absence of electric field has to be compared with the testbeam results in terms of efficiency: the depletion being incomplete in the depth of the edge area, it is normal that charge created at this depth are not collected by the electrode, and it can explain the experienced drop in efficiency. From Figure 7.33 it can also be seen that the electric field beyond the trenches is, as expected, negligible compared to the one below the pixels.

To have a better insight into the electric field behavior in the edge area and explain the edge efficiency profiles obtained for M1.4 in Figure 7.30, two horizontal sections of the electric field simulations have been plotted in Figure 7.34.

Both sections of the simulation (Figure 7.34) go from the virtual limit of the pixel to 60  $\mu\text{m}$  from the pixel limit. The first section, corresponding to the black squared markers, intersects the innermost edge fence which starts at 37  $\mu\text{m}$  and ends at 42  $\mu\text{m}$ . Close to the beginning of the edge, the electric field start to rise as the trench is highly doped with respect to the bulk (high-low junction). Then it sharply drops to reach 0 in all the edge thickness. After the edge, the remaining electrical field is negligible even if it increases a bit in the vicinity of the second edge fence. The second section, corresponding to the red triangle markers, intersects only the outermost edge fence which start at 52  $\mu\text{m}$  and end at 57  $\mu\text{m}$ . The electric field smoothly decreases up to  $\simeq 48 \mu\text{m}$  where it stats to rise sharply due to the proximity of the outermost edge fence. The 3 plots correspond to three different depths: the left-top one is at 10  $\mu\text{m}$  below the surface, the right-top one is 65  $\mu\text{m}$  below the surface (middle of the sensor) and the bottom one is at 120  $\mu\text{m}$  below the surface (close to the back plane).

### 7.5.3 Conclusions on Active edges sensors

Two active edges designs have been investigated and compared to TCAD simulations. The first production consisted in a 200  $\mu\text{m}$  thin n-on-p silicon sensor with a continuous trench and a 100  $\mu\text{m}$  pixel to trench distance. It was tested un-irradiated on beam and shows an efficiency higher than 80 % up to 75  $\mu\text{m}$  from the last pixel virtual limit. The addition of Guard Rings (GRs) impact has also been studied using TCAD simulations. It has been

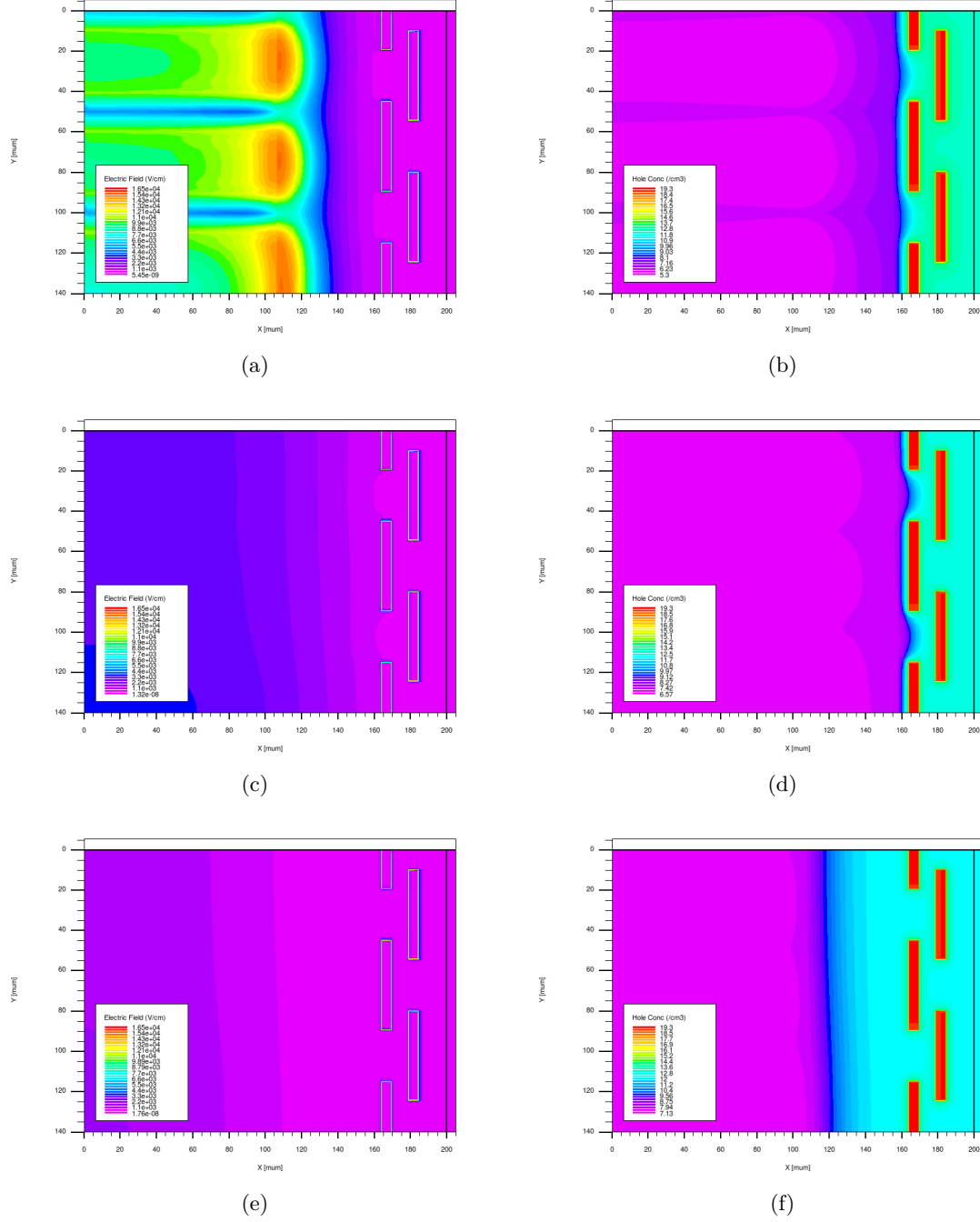


Figure 7.33 – Numerical simulation of the electric field (a, c and e) and of the Holes concentration (b, d and f). The a, b/c, d/e, f plots represent respectively the electric field or hole concentration at a depth of 10/65/120  $\mu\text{m}$  under the surface of the sensor. This simulation was obtained for a bias voltage of 50 V.

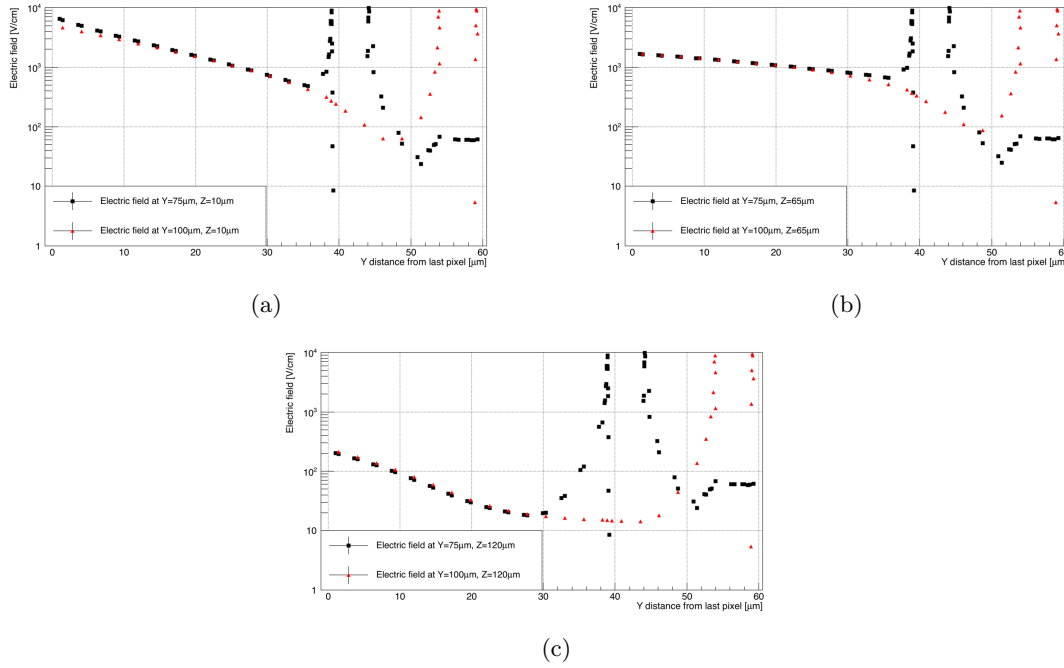


Figure 7.34 – Numerical simulation of the electric field for different trenches in Y. The black curves intersects the innermost staggered trench whereas the red one intersects the outermost ring of trench. The left/right/bottom plots represents the electric field at a depth of 10/65/120  $\mu\text{m}$  under the surface of the sensor.

noticed that the addition of GRs between the edge and the last pixel does not lead to a decrease of the efficiency: the charge is not collected by the GRs apart from a few  $\mu\text{m}$  below them. It seem that the addition of the GRs participates to the bulk depletion in this edge zone, so it is beneficial.

The other production features 130  $\mu\text{m}$  thin n-on-p silicon sensor with a staggered trench: two segmented edge fences surround the active area of the sensor, the innermost at 37  $\mu\text{m}$  from the pixel limit, the outermost at 52  $\mu\text{m}$  from the pixel limit. This sensor was tested un-irradiated and irradiated at  $2.7 \times 10^{15} \text{ n}_{\text{eq}}/\text{cm}^2$ . After the irradiation, the sensor suffers from an early breakdown. Nevertheless, the performance in terms of edge efficiency of the irradiated sensor when depleted at 100 V were similar to the one of the un irradiated sensor, for the range of tested tunings. The efficiency in the edge area is globally higher than 80 % up to 25  $\mu\text{m}$  from the last pixel, the 50% efficiency point being reached at 44  $\mu\text{m}$  from the last pixel. The efficiency expand further in the edge area when the charge does not intersect the innermost pixel trench: the 50% efficiency point is in this case at approximately 47  $\mu\text{m}$  from the last pixel. In the other case, when it intersects the innermost fence, the 50% efficiency point is reached around 37  $\mu\text{m}$ .

Additional irradiated sensors with guard rings will be tested, as well as continuous trench irradiated modules. To minimize the risk of early breakdown, some new active edge sensors designs are under study for which the end of the chip stops close to the virtual limit of the last pixel column, such as the distance between the active edge (at high voltage) and the



physical edge of the chip (at ground) increases, which would minimize the risk of discharges and early breakdown.

## 7.6 Biasing structure and implant design

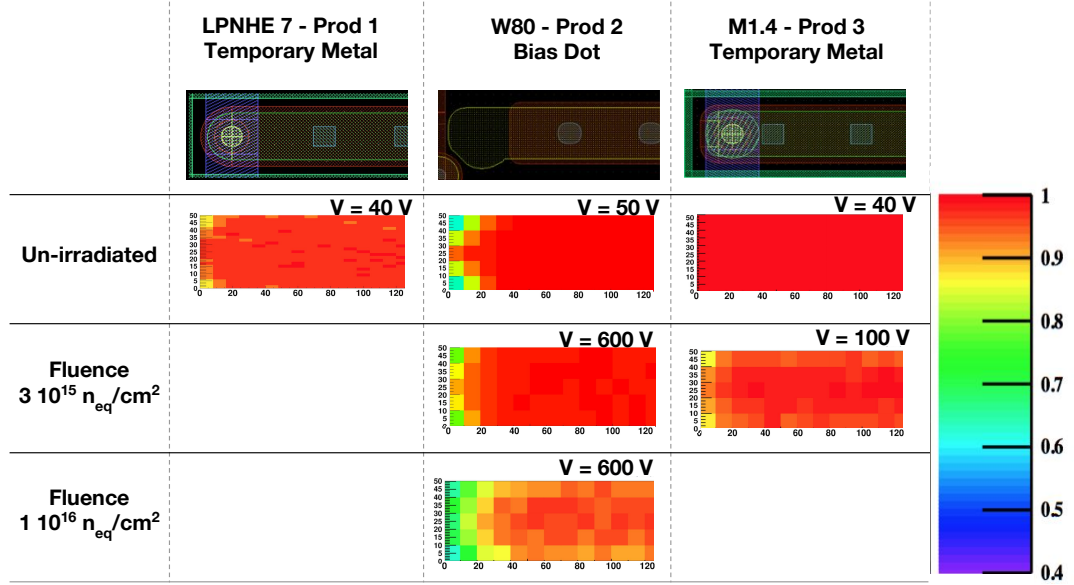


Figure 7.35 – In pixel efficiency presented in a half pixel cell for the three sensors. Results are presented for 3 different fluences when available. A scheme of the pixel is presented in the top part of the figure.

The Figure 7.35 shows the in-pixel efficiency which is a 2D map of the efficiency in all pixel folded in 1 pixel cell. It is presented for three different fluences; un-irradiated on top, irradiated at  $3 \times 10^{15} \text{ n}_{\text{eq}}/\text{cm}^2$  in the middle and at  $1 \times 10^{16} \text{ n}_{\text{eq}}/\text{cm}^2$  in the bottom. The efficiency scale from 40% to 100%. As observed in Figure 7.35 the in-pixel efficiency for un-irradiated sensors with a temporary metal is very homogeneous. This high homogeneity demonstrates the interest of using a temporary metal to bias the sensors for electrical tests before bump-bonding instead of adding a permanent structure such as punch-through bias dots. A tiny drop of efficiency can be observed at the pixel corner, where it decreases to 95%. This is due to the charge sharing occurring between three or four neighboring pixels. In those clusters, the charge induced in one of the pixels could be under threshold and then not taken into account, which biases the hit reconstruction and hence the hit efficiency.

From Figure 7.35 it can be seen that the punch through structure clearly degrades the performance at the corner of sensor cell. Also the cluster size distribution is shifted to lower value due to the loss of the charge collection efficiency. By comparison between the un-irradiated in pixel efficiency between LPNHE7 and M1.4, the efficiency in the edge seems to be higher for M1.4 which could be explained by the use of a wider implant, it can also be due to the fact that this in pixel efficiency scan was taken at DESY where the spatial resolution is less than what it is at CERN.

After an irradiation of  $3 \times 10^{15} \text{ n}_{\text{eq}}/\text{cm}^2$ , the use of temporary metal (M1.4 sensor) results in better efficiency in the pixel corners, it reaches 87% for M1.4 and 70 % for W80 for the same order of fluence.

To investigate further this effect, a sensor with the temporary metal solution will be irradiated and tested on beam to be compared with the results from W80 at  $1 \times 10^{16} \text{ n}_{\text{eq}}/\text{cm}^2$ .

## 7.7 Conclusions on the pixel R&D for ITk

The three LPNHE planar pixel sensor productions have been successfully tested on beams both un-irradiated and irradiated. The design choices have allowed to test different biasing solutions, different thicknesses and different edge designs.

The active edge sensors have demonstrated good efficiency results in the edge area: the efficiency is higher than 80% up to 25  $\mu\text{m}$  from the edge, even after irradiation at  $2.7 \times 10^{15} \text{ n}_{\text{eq}}/\text{cm}^2$  and being in an early breakdown regime. The use of TCAD simulation has demonstrated that the use of guard rings in this area does not impact negatively the hit efficiency. The edge pitch structure of the third production has also been investigated using TCAD simulations. The lateral depletion have been studied and a remaining zone of low electric field in the bottom/edge area explained the fact that the efficiency drops before reaching the edge of the sensor. Additional tests are required to assess the active edge reliability on large scale detectors, especially tests on sensors with Guard Rings.

Concerning thin sensors irradiated over the all ITk fluence range, it has been shown that 130  $\mu\text{m}$  FBK-LPNHE thick sensors passivated with BCB meets the ITk requirement in terms of hit efficiency (higher than 97%) and power dissipation for the intermediate layers of ITk (up to  $3.8 \times 10^{15} \text{ n}_{\text{eq}}/\text{cm}^2$ ). When irradiated to the expected fluence at the end of lifetime of the innermost layer, the hit efficiency reaches 89%. The charge collection efficiency has been determined over the all fluence range and fitted with a function describing the charge collection efficiency of an idealized 1D diode. The charge collection efficiency values will be used in the framework of the ATLAS Radiation damage digitizer group, to investigate the modeling of the radiation damage of pixel sensors at ITk fluences.

Eventually, two biasing solutions have been investigated and the temporary metal solution appears to give better results in terms of in-pixel efficiency before irradiation and after an irradiation of  $3 \times 10^{15} \text{ n}_{\text{eq}}/\text{cm}^2$ . The temporary metal solution is superior to the punch-through solution, even after irradiation.

Based on the current study, thin sensors with the temporary metal biasing option seem a good option for ITk as they present sufficient performance in terms of power dissipation and hit-efficiency. To conclude on whether to use or not active edge sensors, additional tests of irradiated sensors (with Guard Rings) are required, especially to investigate the early breakdown phenomenon. Subsequent studies on RD53a bump bonded modules un-irradiated and after irradiation are actually ongoing.

The final ITk decision concerning the choice of biasing options as well as whether to use active edges or not will be taken at the end of the market survey (fourth trimester of 2018).

## Chapter 8

# B-tagging upgrade for ITk

### Contents

---

<b>8.1</b>	<b>B-tagging</b>	<b>160</b>
8.1.1	Introduction	160
8.1.2	B-tagging algorithms	161
8.1.2.1	Impact parameters based algorithms	161
8.1.2.2	Jet Fitter tagging algorithm	162
8.1.2.3	Secondary vertices algorithms	162
8.1.2.4	Multivariate techniques	163
<b>8.2</b>	<b>B-tagging optimization for ATLAS ITk</b>	<b>163</b>
8.2.1	Layouts comparison	164
8.2.2	SV1 optimization	166
8.2.2.1	Material rejection and vertex cleaning	166
8.2.2.2	SiHits and $p_T$ scans performance	170
8.2.2.3	Conclusions on SV1 optimization	176
8.2.3	B-tagging extrapolation for high $p_T$ jets	176
<b>8.3</b>	<b>Conclusions</b>	<b>178</b>

---

B-hadrons production at LHC is substantial and one of the main challenges of the ATLAS analysis chain is to be able to identify those b-hadrons and their decay products. The identification of jets from b-quarks or b-jets is called b-tagging [63].

During the HL-LHC phase, with the increase in luminosity, the dominant source of uncertainties will become the systematics for many analysis. As the b-tagging uncertainties enter the calculus of systematics, the optimization of b-tagging performance can have a decisive impact on physics searches involving b-hadrons decays, such as the search of the Higgs trilinear self coupling with at least two b quarks in the final state (which is highly favored as shown in Figure 5.11).

In this chapter the b-tagging algorithm upgrade in view of the HL-LHC will be presented. The first section will describe the b-tagging algorithms, the following section will discuss the optimization of b-tagging algorithms for ITK, with a special emphasis on the work I have done in the framework of the ATLAS b-tagging optimization group: layout comparison, optimization of the SV1 tagger and b-tagging extrapolation in high  $p_T$  regime.

## 8.1 B-tagging

### 8.1.1 Introduction

The identification of jets from the decay of b-hadrons or b-jets is called b-tagging. The b-tagging exploits the fact that b-hadrons are relatively long lived hadrons and decay few hundreds of micrometers away from their primary vertex. The b-hadron decay, which is schematized in Figure 8.1, is characterized by:

- the large b-hadron mass;
- the presence of a secondary vertex: b-hadrons are heavy and mainly decay via the electroweak channel, the dominant decay channel being  $b \rightarrow cW$  with W decaying semi-leptonically ( $W \rightarrow l\nu$ ) or hadronically ( $W \rightarrow qq$ , q being u, d, c, or s). The lifetime of b-hadrons is large which results in the presence of a secondary vertex, which is displaced from the primary vertex by a few hundreds of micrometers ( $c\tau = 500\mu\text{m}$  for  $B^+, B^0, B_S$ ).
- tracks with large impact parameters values: the impact parameters  $d_0$  and  $z_0 \sin(\theta)$  are enlarged compare to the one from tracks from a primary vertex, this is caused by the long life time of b-hadrons.

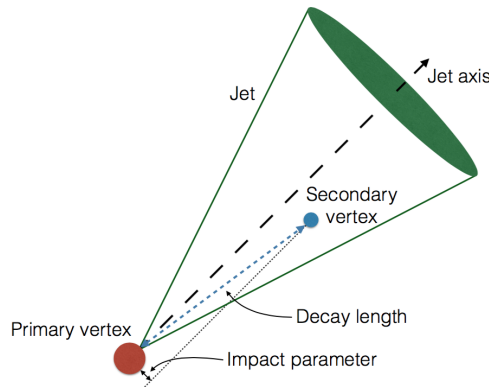


Figure 8.1 – B-hadron decay, salient features. From [145].

The b-jets have to be discriminated from jets originated from the decay of c-hadrons (c-jets) and jets originated from light-flavour hadron decays (u, d, s or gluons). Consequently, to define b-tagging performance, several observables are used:

- the b-tagging efficiency which is defined as the fraction of true b-jets that are tagged as b-jets by a tagging algorithm;
- the c-jet and light jet mis-tag rate are the fraction of c-jet and light-jets which are falsely tagged as b-jets. The c and light jet rejection is the inverse of the mis-tag rate.

The light and c mis-tag rate are evaluated for a fixed b-jet efficiency point referred as b-tagging efficiency working points. A typical working point for ATLAS is 70%; it will be used throughout the various studies presented in the next sections

### 8.1.2 B-tagging algorithms

In the following, three type of b-tagging algorithms are described: impact parameters based algorithms (IP3D), secondary vertex based algorithm (SV1) and a tagger relying on the topology of the b-hadron decay (JetFitter). These algorithms can be combined using multivariate techniques which will be briefly introduced later. As I worked intensively on the upgrade of SV1, impact-based algorithms and topological ones will be presented briefly first and then more space will be devoted to secondary vertex taggers.

#### 8.1.2.1 Impact parameters based algorithms

The impact parameter based algorithms [146] exploit the large impact parameters ( $d_0$  and  $z_0 \sin(\theta)$ ) of tracks generated from b-hadron decays. There are several impact parameters based algorithms:

- IPxD taggers: this family of taggers relies on a log likelihood ratio (LLR) to discriminate b-jets and Light-flavor jets. The IP3D tagger[146] which is the most common IPxD tagger makes use of the transverse impact parameter significance  $d_0/\sigma(d_0)$  and of the longitudinal impact parameter significance  $z_0 \sin(\theta)/\sigma(z_0 \sin(\theta))$  after a track selection steps. IP3D uses exclusive track categories based on track's hit pattern (number of hits, location of hits, shared hits ...). For each track categories is associated a b and Light-flavor jet Probability density function, which have been determined in a Monte Carlo  $t\bar{t}$  simulation sample and are obtained via reference histograms. After this track categorization step, three LLR discriminant functions separating b-jets from light-jets, b-jets from c-jets and light-jets from c-jets are computed over all tracks of a given jet.
- RNN tagger [147]: This new tagger relies on a recursive neural network. It uses the same track categorization and impact parameters significances than IP3D but in addition exploits the fraction of transverse momentum carried by the track relative to the jet  $p_T^{frac}$  and the angular distance between the track and the jet axis  $\Delta R(track, jet)$ . No optimization for HL-LHC have been performed on RNN tagger at the moment.

### 8.1.2.2 Jet Fitter tagging algorithm

The JetFitter tagging algorithm [148, 146] is a decay chain multi vertex algorithm. It aims to reconstruct the full b-hadron decay chain (by exploiting the topology of the decay of a b-hadron in association with a W in a c-hadron). For this purpose, a Kalman filter is used to find a straight line on which lies the primary vertex, the secondary b-hadron vertex and the tertiary c-hadron vertex.

### 8.1.2.3 Secondary vertices algorithms

The b-tagging using secondary vertices [149] occurs in two steps. First, secondary vertices (SV) are listed using the Secondary Vertex Finder (SVF) algorithm. Hence the secondary vertex b-tagging algorithm (SV1) take the list of SV and classifies them in SV from b-jets, c-jets or light-jets. These two algorithms are detailed in the following section.

#### Secondary Vertex Finder (SVF) algorithms

The SVF algorithm method to find Secondary Vertices is the following: a pool of two-track vertices is formed and then spatially close two-track vertices are merged into multi tracks vertices. This approach is less CPU consuming than a method which would try to find directly multi tracks secondary vertices. The workflow of the SVF algorithm consists in:

- **Tracks selection inside a jet and track selection criteria:** Only tracks inside a jet cone of  $\Delta R < 0.4$  are considered. Some hit requirement are also used in terms of number of pixel hits, SCT hits, shared pixel hits... A cut on the  $\chi^2/ndf (< 3)$  is also imposed on tracks. To mitigate the impact of pile-up and reduce the number of fake vertices tracks with a low  $d_0/\sigma_{d_0} (< 2)$  and a high  $z_0/\sigma_{z_0} (> 6)$  are discarded [146].
- **Formation of all possible two track vertices:** Among the pool of tracks retained in the previous step, all two track vertices are listed.
- **Selection on the two track vertex:** The first applied criteria requires the 2-tracks vertex to be significantly displaced from the primary vertex. The invariant mass of the 2-tracks vertex should also be less than 6 GeV as b-hadrons masses are usually less than 6 GeV. A vertex cleaning operation is also performed to disentangle true secondary vertices from long lived particles ( $K_s$  or  $\Lambda$ ) decay vertices, photon conversion vertex and vertices from hadronic interaction with matter. Tracks from long lived particles are identified by looking at their invariance mass spectrum. Vertices candidates in the mass peak window are refitted and if their impact parameter is small, their tracks are considered as bad tracks and are discarded from the pull of tracks. For photon conversion SV vertices with a mass smaller than 40 MeV are discarded. To ensure the cleaning of additional vertices from hadronic interactions a comparison between the radius of the SV and of the radius of the pixel layers and beam pipe is performed. SV which are too close to material layers are discarded. All the tracks which pass the detailed 2-track vertex selection are then added in a new list of tracks

- **Iterative procedure to merge the two track vertices into a multi tracks vertex:** an iterative procedure fits the vertex until reaching an acceptable  $\chi^2$ . If the obtained vertex contains just two tracks, an additional cleaning step is performed. If several secondary vertices are found inside a jet, the vertex with the highest multiplicity is considered.

### Secondary Vertex-tagging algorithm (SV1)

The SV1 tagger uses the output of SVF finder algorithms; SV1 calculates the ratio of the multivariate b-jet vertex probability density function to the light-jet probability density function. The likelihood ratio is used as a discriminant variable between b-jets and c and light-jets.

The probability density function are constructed using:

- the invariant mass of all particles in the secondary vertex;
- the energy fraction which is the ratio of the sum of energies of tracks in the SV to the energy of all tracks in the jet;
- the number of two-track vertices after cleaning steps;
- $\Delta R$  between the direction of the Secondary Vertex - Primary vertex and the jet direction.

#### 8.1.2.4 Multivariate techniques

Two kind of multivariate techniques [150] are used to combine the output of the low level taggers (IP3D, SV1 and JetFitter) to discriminate b-jets from Light-flavour jets or c-jets. The MV1 algorithm which was used during Run1 is based on neural network. The MV2cx0 algorithms are the new options which are currently used in Run2. MV2 algorithms are based on a boosted decision tree which combines 24 input variables from SV1, IP3D and JetFitter. Mv2cx0 algorithms perform better than MV1 one and are simpler [150]. MV2cx0 exists in three versions, MV2c00, MV2c10 and MV2c20. Those are optimized with MC enriched in c-jets (0,10 and 20 referring to the percentage of c-jets added in the MC).

## 8.2 B-tagging optimization for ATLAS ITk

The optimization of b-tagging for the ATLAS ITk is an important step in view of the HL-LHC phase, as it enters in a large number of analysis. As reported in the ITk pixel TDR [107], the Higgs Self-Coupling Measurement using both  $hh \rightarrow b\bar{b}b\bar{b}$  and  $hh \rightarrow b\bar{b}\gamma\gamma$  channels will benefits from the optimization of b-tagging. The sensitivity to the Higgs trilinear coupling can be improved using the ITk b-tagging with an increase of at most 20% [107].

The optimization study uses two types of MC samples to ensure an optimal  $p_T$  and  $\eta$  coverage:

- $t\bar{t}$  events with an average of 200 pile-up events were used.  $t\bar{t}$  samples cover the low and medium part of the  $p_T$  spectrum, with  $p_T$  up to 400 GeV.  $t\bar{t}$  samples are ideal to test b-tagging due to the high ( $\simeq 1$ ) decay probability of top into b-quarks.
- $Z'$  samples with mass ranging from 500 GeV to 5 TeV are used to investigate the high  $p_T$  region.

As presented in Chapter 5 the IP3D tagger has already been optimized for ITk [107]. The IP3D optimization consisted in updating the track categories to match the complex ITK geometry. It resulted in better performance in terms of c jet rejection (doubled compared to Run2) and light jet rejection (tripled compared to Run2) vs b-jet efficiency as was shown in Figure 5.8.

In the following three studies that I worked on in the ATLAS b-tagging optimization group framework are discussed. First the b-tagging performance for two ITk layout considered in 2017 are presented. Then the actual effort on the optimization of the SV1 tagger will be discussed. Eventually results on b-tagging performance and extrapolation at high  $p_T$  will be presented.

### 8.2.1 Layouts comparison

In this section the comparison between two ITk layout options (considered in 2017 and shown in Figure 8.2) will be presented. The two layout options were: the inclined layout (blue in Figures 8.3 and 8.4) which is close to the actual layout used in the ITk pixel TDR [107]; the extended layout (red in Figure 8.3 and 8.4), which does not feature inclined sensor and is closer to the actual ID, with more layers.

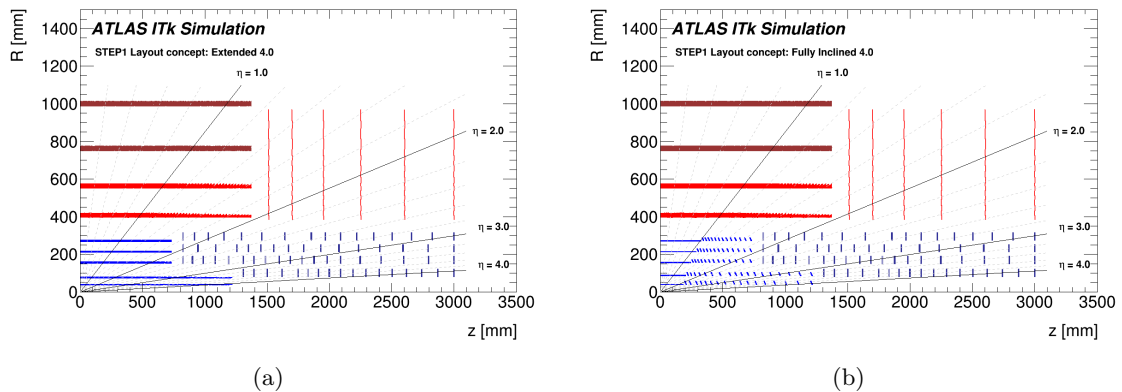


Figure 8.2 – Extended (a) and Inclined (b) layouts.

The Figure 8.3 represents the light jet mis-tag rate for the MV2c20 tagger vs  $\eta$  and  $p_T$  of the jet. From this Figure, it is clear that the inclined layout results in better performance in



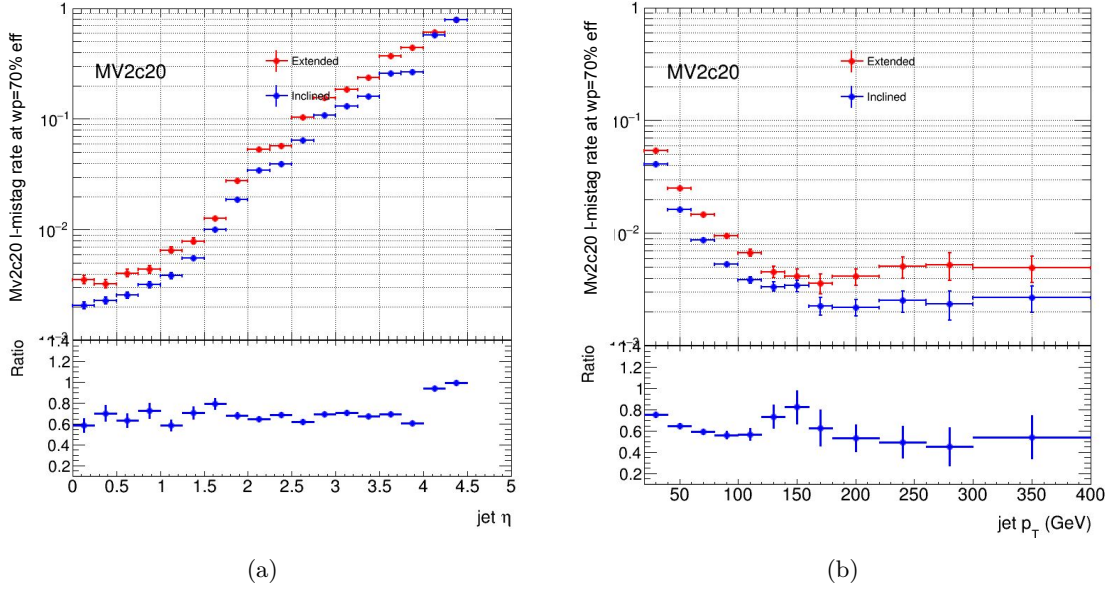


Figure 8.3 – Comparison of the light mis-tag rate vs  $\eta$  (a) and vs  $p_T$  (b) for two layout options. The MV2c20 tagger is here considered. At the bottom the ratio of inclined over extended is presented.

terms of light jet mis-tag rate as it is globally 60 % to 80% less for the inclined version over the all  $p_T$  range and up to  $|\eta| = 4$ .

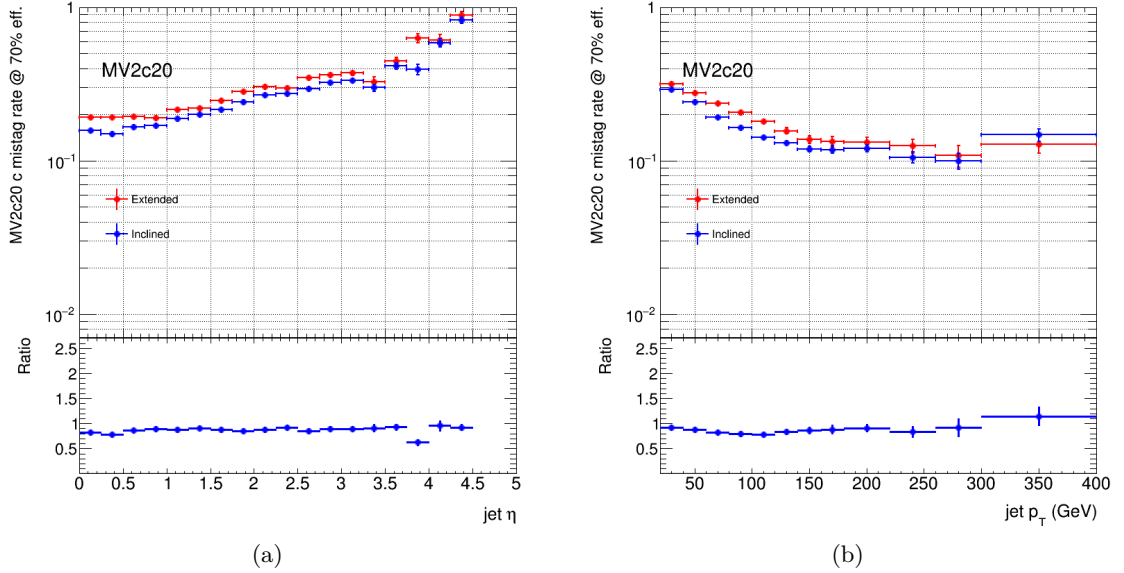


Figure 8.4 – Comparison of the c-jet mis-tag rate vs  $\eta$  (a) and vs  $p_T$  (b) for two layout options. The MV2c20 tagger is here considered. At the bottom the ratio of inclined over extended is presented.

The Figure 8.4 represents the c jet mis-tag rate for the MV2c20 tagger vs  $\eta$  and  $p_T$  of the jet: the inclined layout performs better in terms of c-jets rejection, as the c-jet mis-tag rate for the inclined layout is globally 80 to 90 % of the extended layout one. At high  $p_T$ , the hierarchy is not obvious due to the low statistics. At high  $\eta$ , there is more active layers

crossed by a charged particle in the inclined layout compared to the extended layout, which enhance the tracking performance and may explain the higher gap in light and c jets mis-tag rate between extended and inclined layouts around  $\eta = 3.5$ . The inclined layout was eventually retained for the ITk pixel detector.

### 8.2.2 SV1 optimization

The SV1 optimization was carried on  $t\bar{t}$  sample at a center-of-mass of  $\sqrt{s} = 14$  TeV proton-proton collisions, at the high pile-up conditions  $\langle \mu \rangle = 200$ . The inclined layout described in the ITk pixel TDR was simulated using Geant4 (see dedicated Chapter on simulations in ITk Pixel TDR [107]).

The Tables 8.1 & 8.2 compile all the different cuts applied during each steps of the algorithm: at the track selection step and at the two-track vertices steps. Three options were tested in terms of Silicon hit cuts (7,9,11) as well as three options in terms of lower limits in  $p_T$  (700, 900 and 1100 MeV).

Table 8.1 – Tracks selection criteria

Cut on $\chi^2/ndof$	3
$\Delta R(jet)$ Cone around the jet for track selection	0.4
Cut on number of Silicon hits	7, 9, 11
Cut on number of Pixel hits	4
Cut on number of SCT hits	3 up to $\eta = 2.6$ , 0 afterwards
Cut on number of Shared hits	1
Cut on track $p_T$ (MeV)	700, 900, 1100
Cut on $z_0$ (mm)	25
Cut on $z_0$ error (mm)	5
Cut on $d_0$ (mm)	5
Cut on $d_0$ error (mm)	1

#### 8.2.2.1 Material rejection and vertex cleaning

The first step was the optimization of the secondary vertex finder algorithms and the modification of the code to take into account the new geometry of the ITk, as the actual tagging algorithms are based on ATLAS Run2 geometry. As already stated b-hadron decay is not the only process that gives a displaced vertex. The following processes can produce a displaced vertex too:

- random crossing of two tracks in the volume where b-hadrons are supposed to decay;

Table 8.2 – Two-tracks vertices candidates selection criteria

Cut on $\chi^2/ndof$ of fitted two tracks	10
Cut on 3D significance between PV and SV	4.5
Cut on 3D significance between PV and considered track	2
Sum of the 3D significances of the two tracks	2
Secondary vertex mass	$< 6$ GeV
Material rejection	Yes
Vertex cleaning	Yes

- hadronic interactions with the detector materials or beam pipe or services;
- photon conversion;
- $\Lambda$  or  $K^0$  decays.

Consequently the first step is to discard those secondary vertices (SV) from the two-tracks vertices candidates pool. To discard two-tracks vertices from photon conversion or  $\Lambda$  or  $K^0$  decay, a vertex cleaning procedure is applied, similar to the one used during the Run2. To disentangle two-tracks vertices originated from the interaction with the detector material, the material rejection algorithm was updated to take into account the ITk geometry, the cuts used are reported in Table 8.3. Vertices that were too close to detector layers were rejected. For the inclined and end-caps ring, the geometry being complicated, a first approach have been to use huge and conservative safety margins to encapsulate all the modules. In a further iteration customized cuts will be used to match all modules and services of the ITk pixel detector.

Table 8.3 – Material cleaning: Safety margins around ITk layers. Both layers radius and safety margins are reported.

	Layers:	L0	L1	L2	L3	L4
<b>Flat barrel</b>	Radius (mm)	39	99	160	220	279
	Safety Margin (mm)	2.5	5	5	5	5
<b>Inclined barrel</b>	Radius (mm)	36	80	155	215	274
	Safety Margin (mm)	10	20	10	10	10
<b>End-caps Rings</b>	Radius (mm)	50	78	152	212	271
	Safety Margin (mm)	20	20	20	20	20

The Figure 8.5 presents the distribution of two-track vertices (n2t) with and without material rejection and vertex cleaning. For both Light-flavour jets and b-jets, the cleaning results in a global decrease of the number of two-track vertices (n2t) candidates. This is specially true

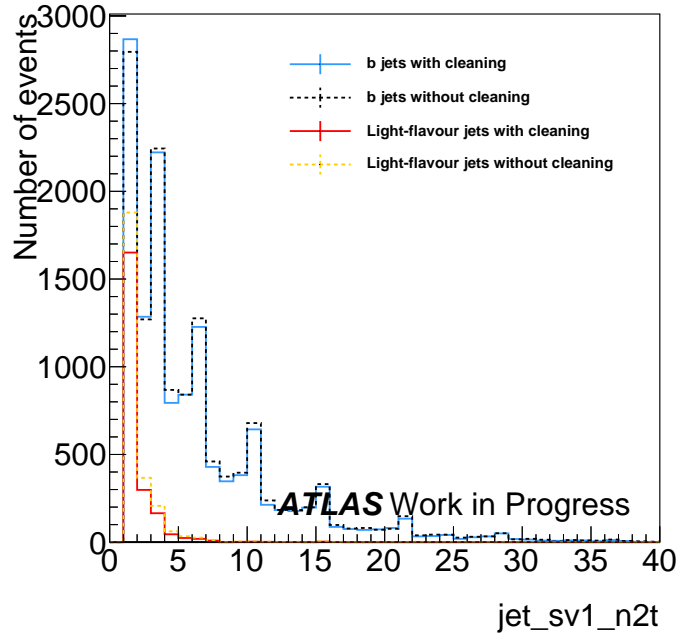


Figure 8.5 – Distribution of two-track vertices ( $n2t$ ) for b-jets and light flavour jets, with (plain lines) and without (dashed lines) the cleaning step

about  $n2t$  originated from light-flavour jets which are reduced by about 15 % after material cleaning and vertex rejection.

An other interesting observable to consider is the transverse distance between the secondary vertex and the primary vertex ( $L_{xy}$ ). It is plotted in Figure 8.6 both for Light-flavour jets (a) and b-jets (b). For the light flavour jets, without the cleaning procedure (in orange) some peaks are visible in the Figure 8.6 a, they correspond to the interaction with the beampipe (around 25 mm), the first layer flat section (peak at 39 mm), end-caps section (peak around 50 mm). Once the material rejection procedure is applied (red), those peaks disappear. A safety margin around the layers is defined to take into account poor transverse spatial resolution. This safety margin varies for the various part of ITk: 2.5 mm in the flat section, up to 20 mm in the end-caps section to account for the inclined geometry.

As already shown for Run2 [149], close to the material rejection areas, few events remains, after the cleaning. As the coincidence with the secondary vertex and the layer position is the only way to distinguish true b-hadrons from hadronic interactions, true b-hadrons whose decay vertex is close to the material layers are discarded, which impact the b-jet reconstruction efficiency as shown on Figure 8.6 b. This effect could be mitigated by implementing a better description of the ITk in the inclined and end-caps region, and reducing the safety margins.

The Figure 8.7 features the light mis-tag rate of SV1 at a 70% working point, vs  $\eta$  of the jet and vs  $p_T$  of the jet. The black markers represent data without cleaning and red ones with cleaning. The use of material rejection and vertex cleaning decreases significantly the light

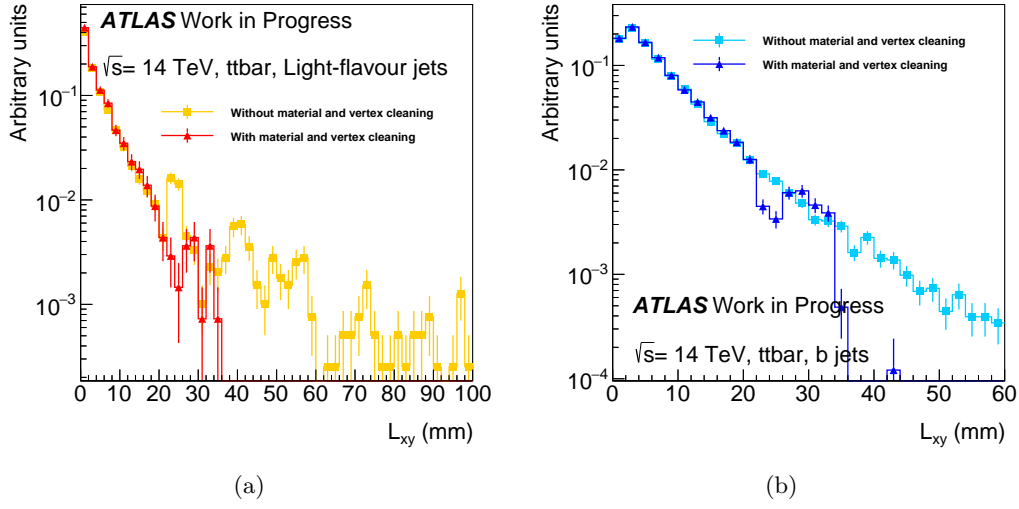


Figure 8.6 – Comparison of the transverse distance between the secondary vertex and the primary vertex associated with/without material rejection and vertex cleaning.

mis-tag rate, especially in the  $\eta$  region going from  $0.5 < |\eta| < 3.5$ . The light-jet mis-tag rate is also diminished by at least 20 % over the jet  $p_T$  spectrum.

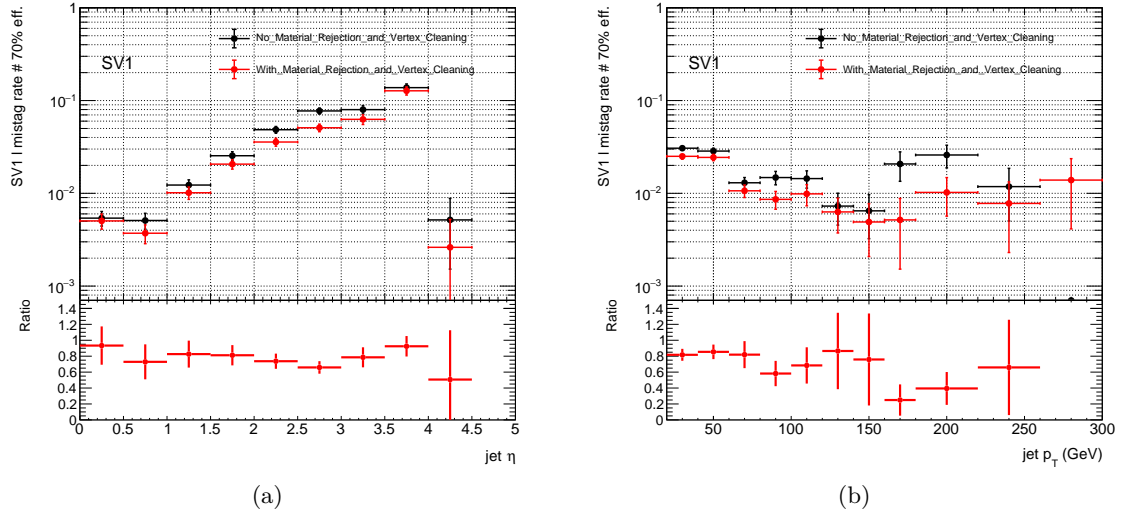


Figure 8.7 – Light mis-tag rate vs  $\eta$  (a) and  $p_T$  (b) with (red markers) and without (black markers) vertex cleaning and material rejection. At the bottom, the ratio of light mis-tag rate with over without material rejection and vertex cleaning is reported.

### 8.2.2.2 SiHits and $p_T$ scans performance

In order to optimize the track selection cuts, a scan over the Silicon Hits per tracks requirements (SiHitsCuts) and track  $p_T$  cuts ( $p_TCuts$ ) in (MeV) have been performed. In the following, 3 configurations are investigated:

- SiHitsCuts = 7 &  $p_TCuts$  = 700 MeV,
- SiHitsCuts = 9 &  $p_TCuts$  = 900 MeV,
- SiHitsCuts = 11 &  $p_TCuts$  = 1100 MeV

The selection criteria for the other variables are the ones expressed in Tables 8.1 & 8.2.

The Figure 8.8 presents the average of the input variables used by SV1 to discriminate b-jets, c-jets and light jets. Those plots are profiles which plot the mean value of the observable as a function of  $\eta$  and  $p_T$ . The various colors indicates the jets flavors (blue for b-jets, green for c-jets and red for light flavor jets). The various marker shapes indicate 3 different cut selections on tracks: on the number of Silicon hits per tracks (either 7, 9 or 11) and on the  $p_T$  track cut (either 700, 900 or 1100 MeV). The right plots shows the  $\eta$  dependency; the left plots shows the  $p_T$  dependency.

From the Figure 8.8 a and b, it can be seen that the SV mass is a powerful discriminant variable between b-jets and light/c-jets up to  $\eta = 3$ . Afterwards, the SV mass of b-jets drops. Concerning the  $p_T$  dependency, the light and c-jets SV mass distribution are rather flat (1 GeV) whereas the SV mass for b-jets starts at SVmass=1700 MeV and increases before  $p_T=50$  GeV/c to reach a plateau around SVmass = 2000 MeV. The three configurations investigated seems quite similar. Moving to more stringent cuts seems to decrease slightly the SV mass, as expected.

The Figure 8.8 c and d represents the number of two-track vertices in the selected jet respectively vs  $\eta$  and the  $p_T$  of the jet. As SV mass, it is a powerful discriminant between b-jets and c and light flavor jets. The light jets number of two-track vertices are quasi constant over the all  $\eta$  and  $p_T$  range. The c-jet distribution is also quite flat but the statistic is quite low for this contribution. The b-jet distribution is less constant. It is lower ( $\simeq 4$ ) at high  $\eta$  (after  $|\eta| = 3$ ). The discrepancy between the 3 configurations investigated is more important than what it was for SV mass. The third configuration gives lower values for the 3 components. Over the jet  $p_T$  spectrum, the c and light jets components are close to 2 whereas the b-jets component starts at 4 around 25 GeV to reach a plateau between 6 and 7 up to 300 GeV.

The Figure 8.8 e and f presents the energy fraction of the SV which is the ratio of the sum of energies of tracks in the SV to the energy of all tracks in the jet. Among the three variables it seems to be the one with the more  $\eta$  dependency. The discriminative power between b-jets and c-jets of this energy fraction ration is quite low. Going to stringent cuts in terms of

track selection seems to result in higher value of SV energy ratio, especially for light-jets, as expected.

Globally, the SV variables seems less discriminative at high  $\eta$ , which can be explained by the reduction in tagged b-hadrons secondary vertices in the end-caps due to the drastic material cleaning. The analysis could be refined by implementing a correct descriptions of the inclined and end-caps part and reducing the safety margins surrounding the material in the forward part.

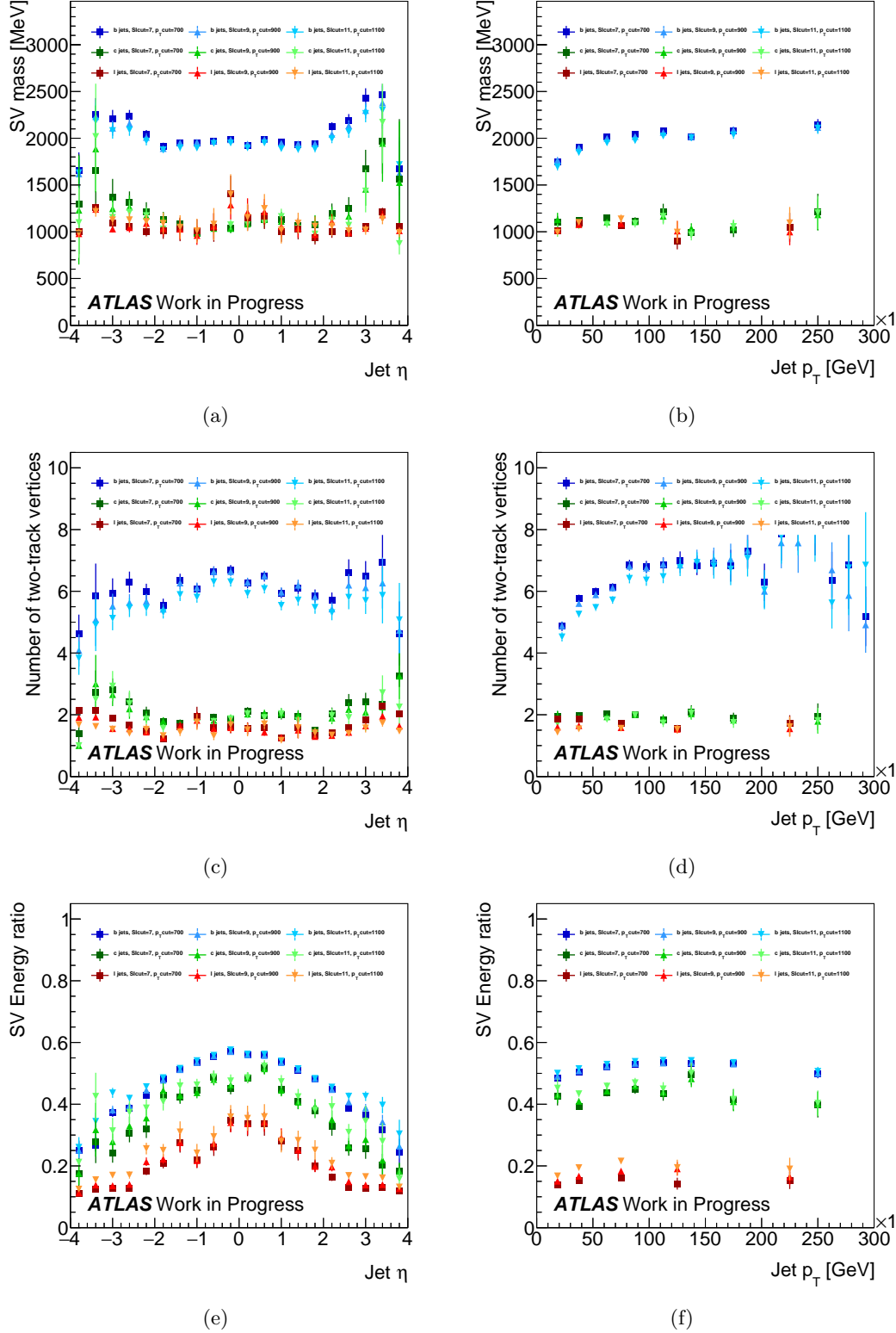


Figure 8.8 – Comparison of the secondary vertex mass distribution (a,b), number of two tracks vertices (c,d), energy fraction (e,f), vs  $\eta$  (a, c, e) or  $p_T$  (b, d, f). Three tracks selection criteria are considered: SiHitsCuts = 7 and  $p_T$ Cuts = 700 MeV; SiHitsCuts = 9 and  $p_T$ Cuts = 900 MeV; SiHitsCuts = 11 ;  $p_T$ Cuts = 1100 MeV



In the Figure 8.9, the number of two track vertex candidates ( $jet\_sv1\_n2t$ ) and the number of tracks associated with a vertex ( $jet\_sv1\_ntrkv$ ) are plotted. Those two plots illustrates the interest to increase the  $p_T$  Cuts and SiHitsCuts: the discriminating power is increased. Both Light-flavour jets and b-jets number of two-tracks vertices and the number of total tracks in a vertex distributions are shifted towards lower values, nevertheless the decreasing amplitude is higher for light-flavour jets. Increasing the cuts from (7,700) to (11,1100) decreases the mean number of two tracks vertices for light jets from 1.6 to 1.4.

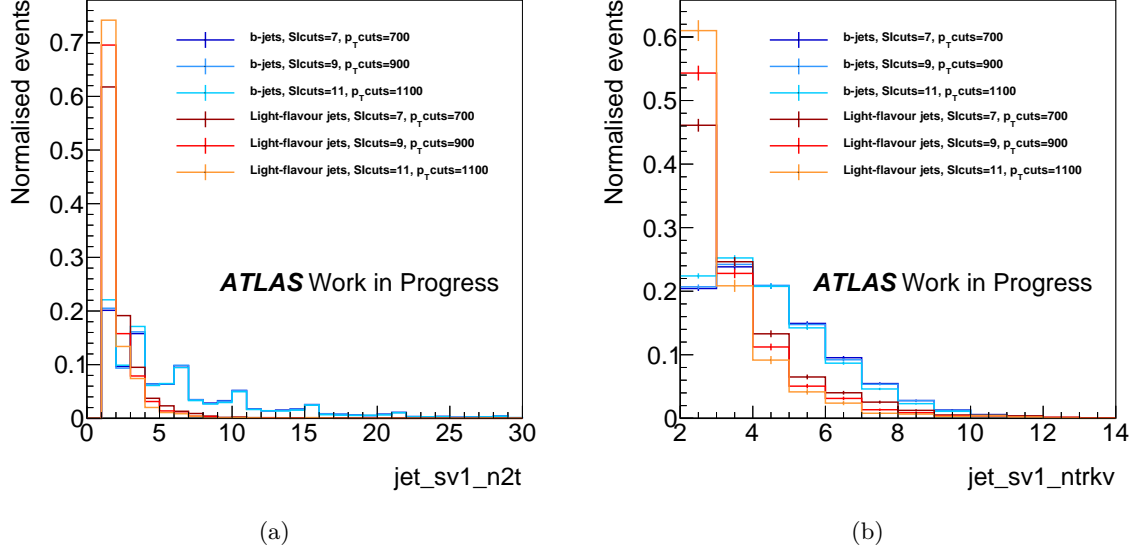


Figure 8.9 – Comparison of number of two tracks vertices candidates (a)/ number of tracks per secondary vertex (b) for various tracking cuts scenari ( SiHitsCuts = 7 and  $p_T$ Cuts = 700 MeV; SiHitsCuts = 9 and  $p_T$ Cuts = 900 MeV; SiHitsCuts = 11 ;  $p_T$ Cuts = 1100 MeV).

The secondary vertex reconstruction efficiency (fraction of b-jets which have a reconstructed SV vertex [149]) and fake rate (fraction of light-jets which have a fake reconstructed SV vertex [149]) are plotted in the Figure 8.10 as a function of the  $\eta$  of the jet.

Going to stringent cuts seems to decrease the SV reconstruction efficiency of c-jets even if the low statistics make it difficult to conclude. It seems also to degrade the SV reconstruction efficiency for b-jets at high  $\eta$  ( $|\eta| > 3$ ). The reconstruction efficiency of b-jets is more or less constant (75%) over the  $\eta$  region going from  $[-1.5; 1.5]$ . Afterwards it decreases to reach 50% for the more stringent cuts and 60 % for the base configuration. Nevertheless, the statistics in this zone is quite poor.

The most important effect can be seen at high  $\eta$  for the light-flavour jet fake rate: at  $|\eta| > 3$ , it is divided by more than 2.

The Figure 8.11 presents the light mis-tag rate vs  $\eta$  and  $p_T$  for the three configurations. The most stringent selection gives better results at medium and high  $\eta$  and along the all  $p_T$  range.

The light jet rejection vs b-tagging efficiency is presented in Figure 8.12. The best performance are obtained for a SiHitsCuts = 11 and  $p_T$ Cuts = 1100 MeV. Compared to the the

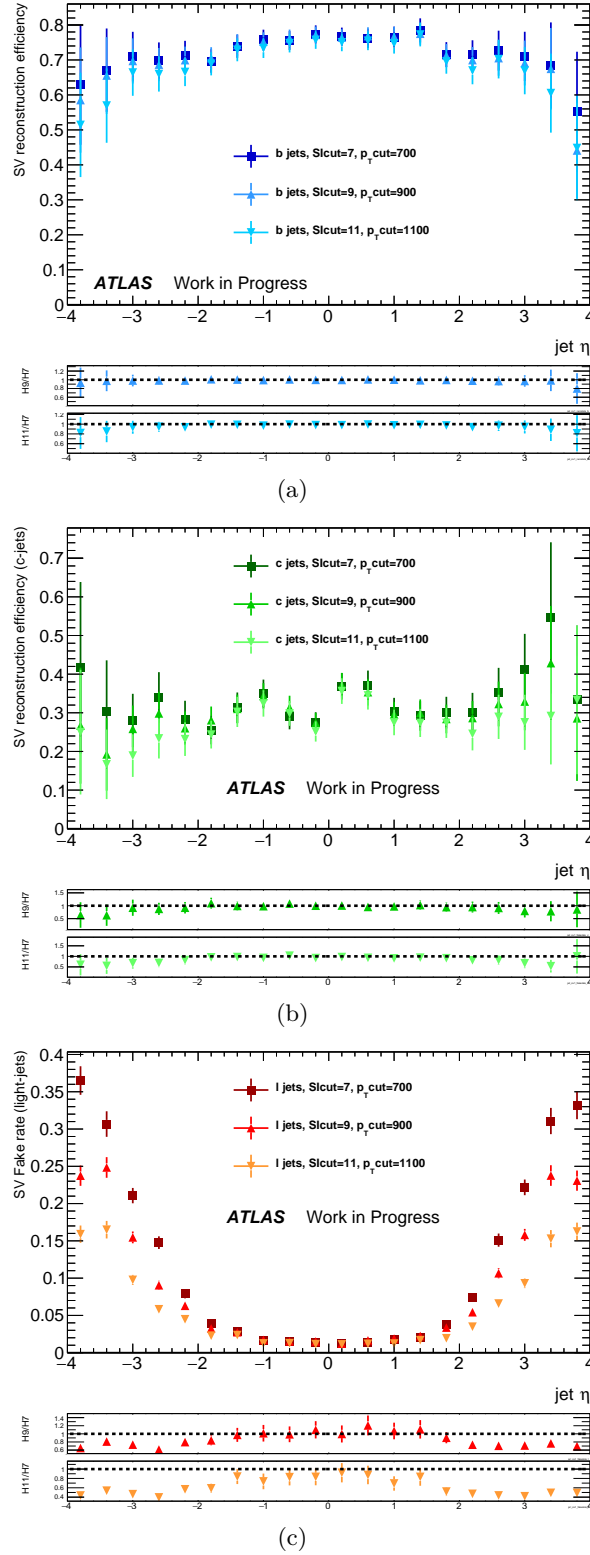


Figure 8.10 – Secondary vertex reconstruction rate for b-jets(a), c-jets (b) and light flavour jets (c). Three tracks selection criteria are considered: SiHitsCuts = 7 and  $p_T$ Cuts = 700 MeV; SiHitsCuts = 9 and  $p_T$ Cuts = 900 MeV; SiHitsCuts = 11 ;  $p_T$ Cuts = 1100 MeV. The top/bottom ratio plots represents respectively the ratio of the (9,900)/(11,1100) configurations with the (7,700) one.

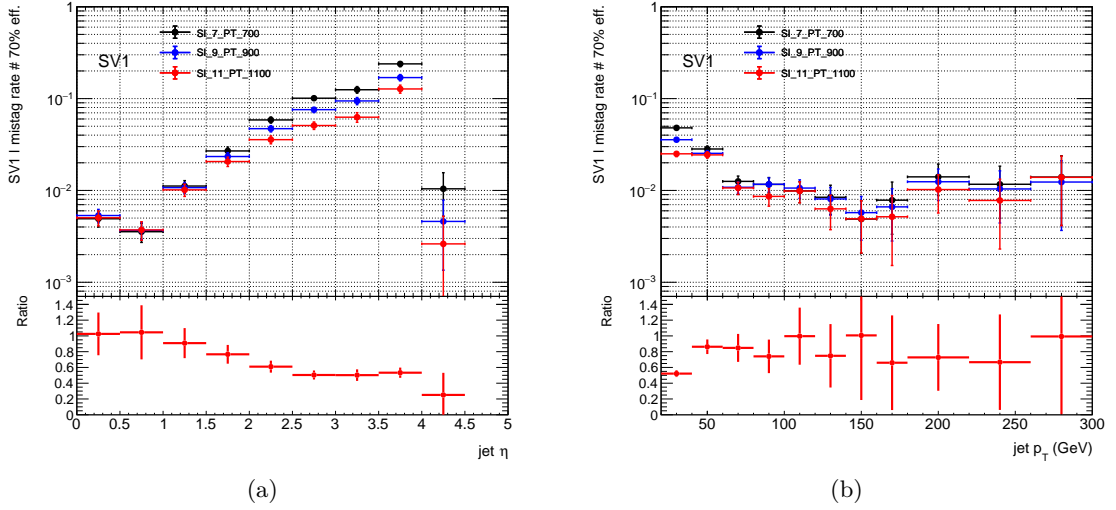


Figure 8.11 – Light mistag rate for various tracking cuts tested: SiHitsCuts = 7 and  $p_T$ Cuts = 700 MeV; SiHitsCuts = 9 and  $p_T$ Cuts = 900 MeV; SiHitsCuts = 11 and  $p_T$ Cuts = 1100 MeV. In the ratio plot, the red markers represents the ratio of the config (11,1100) with respect to the (7,700) configuration.

configuration 1 (SiHitsCuts = 7 and  $p_T$ Cuts = 700 MeV), the configuration 3 results in an increase of the Light-flavour jet rejection of roughly 30%. The curves stop around 70% as a 70% working point is considered.

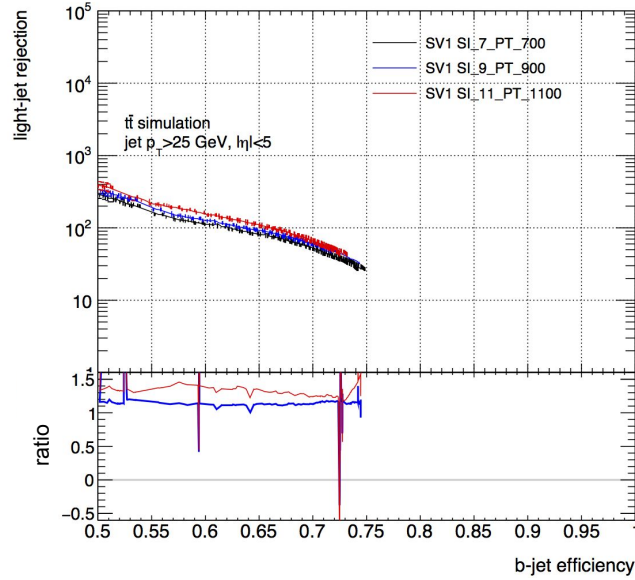


Figure 8.12 – Light jet rejection vs b-jet efficiency. Various cuts on  $p_T$  (PtCuts) and Silicon hits cuts (SiCuts, including the pixel hits and the SCT hits) have been investigated. The black/blue/red curves shows performance for the following couples of SiCuts and PtCuts: 7&700 , 9&900 and 11&1100. In the ratio plot, the blue/red curve represents the ratio of the config (11,1100)/(9,900) with respect to the (7,700) configuration.

### 8.2.2.3 Conclusions on SV1 optimization

SV1 is powerful in reducing the light jet contamination; with the most stringent configuration (SiHitsCuts = 11 &  $p_T Cuts = 1100$  MeV) this ability at high  $\eta$  more or less double compared to the first configuration (SiHitsCuts = 7 &  $p_T Cuts = 700$  MeV). This optimized configuration will be used, together with the optimized IP3D algorithms to study the b-tagging performance for physics analysis prospects at ITk.

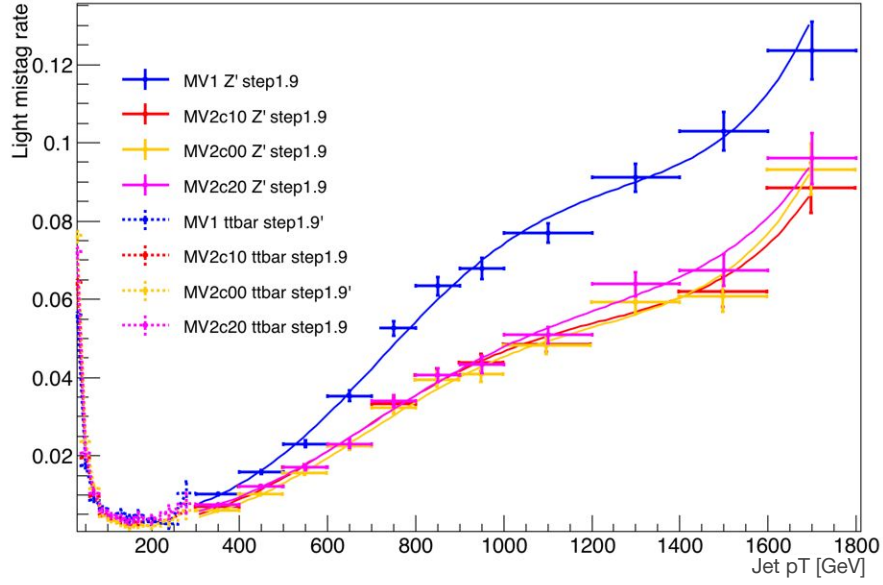
### 8.2.3 B-tagging extrapolation for high $p_T$ jets

B-tagging optimization at high  $p_T$  is crucial to tag very energetic b-hadrons, which are characterized by enhanced decay lengths and jet collimated in a narrow cone. To study b-tagging performance at high  $p_T$ , Monte Carlo  $Z'$  samples are used, as  $t\bar{t}$  samples only cover a  $p_T$  region going from 25GeV to 300GeV. The presented study has been done using an ITk layout proposition which was use prior to ITk pixel TDR iteration [107]. Eight  $Z'$  samples whose masses ranged from 1 TeV to 5 TeV have been studied.

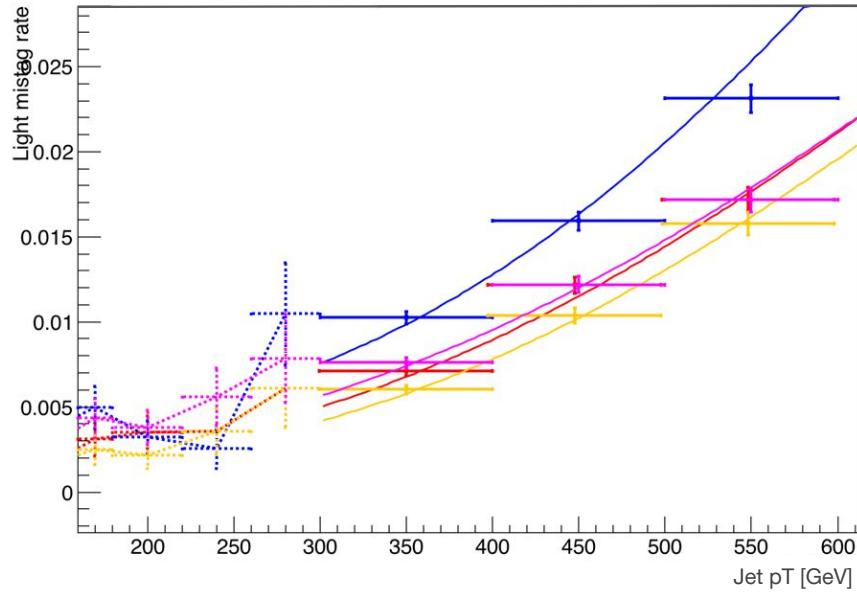
The performance at high  $p_T$  are extrapolated from a fit on the  $Z'$  performance, and will be used to emulate the performance at high  $p_T$ . An updated version of this performance should be derived with more statistics for the final ITk layout once the  $Z'$  MC samples will be available.

The first step is to ensure that b-tagging of  $Z'$  and  $t\bar{t}$  are not too dissimilar. It is done by looking at the continuity of the b-tagging performance at 300 GeV, which correspond to the end of the  $p_T$  spectrum for the  $t\bar{t}$  samples and at the beginning of the  $p_T$  range of the  $Z'$  samples.

The Figure 8.13 represents the light mis-tag rate vs the jet  $p_t$  for  $t\bar{t}$  samples (up to 300 GeV/c) and for several  $Z'$  samples with different masses ranging from 1 TeV to 5 TeV. The mis-tag rate are plotted for several MV taggers: MV1, MV2c0, MV2c10 and MV2c20. From this plot it is demonstrated that there is a good continuity in  $p_T$  at 300 GeV, which show that the use of  $Z'$  samples to extrapolate at high  $p_T$  is valid. The MV2 classifier presents better performance than the MV1 algorithm at high  $p_T$ . The best light mis-tag rate performance are obtained for MV2c00 and MV2c10. The second step is to fit the distribution of light and c mis-tag rate vs  $p_T$  with  $(Exp(a + bx + cx^2 + dx^3 + e\sqrt{x} + f\sqrt[3]{x} - 1))^{-1}$  and to extract the parameters. Two working points were considered, 70% and 85%. The high  $p_T$  performance for the MV2c10 tagger, for the working point of 70 % will be used by physics groups to prepare predictions involving high  $p_T$  object and b-tagging.



(a)



(b)

Figure 8.13 – Light-flavour jet mis-tag rate vs jet  $p_T$  for MV taggers for the intermediate ITK layout using  $Z'$  samples of masses ranging from 1 TeV to 5 TeV and  $t\bar{t}$  samples. (b) presents a zoom on the  $p_T$  region around 300 GeV.

### 8.3 Conclusions

The optimization of b-tagging algorithms is actually ongoing with the goal of obtaining better results of b-tagging in the harsh conditions of HL-LHC. The IP3D upgrade has been presented in the recent pixel TDR [107]. I worked on the optimization of the SV1 tagger. The use of updated material cleaning, vertex rejection and more stringent cuts in tracking requirements results in better light rejection vs b-jet efficiency performance:  $\simeq 30\%$  of improvement for more stringent cuts. In terms of light jet rejection over the all  $p_T$  region and  $\eta$  region (except for  $|\eta| < 0.5$ ) the use of updated material rejection and vertex cleaning results in  $\simeq 20\%$  of improvement. Parametrization of the performance of b-tagging at high  $p_T$  have also been prepared and will be used in physics analysis projections using highly boosted objects.

# Conclusions and Perspectives

After eight years of data-taking, the ATLAS experiment has produced a spectacular amount of physics results and advances especially in the Higgs sector. The Higgs boson has now been observed in five different decay channels including the recent  $h \rightarrow b\bar{b}$  channel [2]. These discoveries have been made possible by the combination of cutting edge statistical techniques and excellent detector performances. Among the detector, the Inner detector, has played a leading role in the recent discovery of  $h \rightarrow b\bar{b}$ . To push further the understanding of the detectors and especially the consequences of the exposition to radiation of the ATLAS Inner detector, a radiation damage digitizer has been elaborated in the two last years and I have participated at multiple levels to this effort. By providing a better match between MC and data, it aims to create good prediction towards the next data taking period (Run 3) but also to make important design decisions for the upgraded ATLAS detector that must survive the harsh HL-LHC radiation environment.

I participated to the development of the digitizer by producing electric field maps used by the digitizer as look up tables, by producing various validation plots at several steps of the digitizer development and by analyzing testbeam data whose purpose were to investigate the evolution of diffusion at high temperature and bias voltage and the charge collection efficiency at ITk-like fluences. The radiation damage modeling has been validated by looking at charge collection efficiency which was studied by comparing simulated and Run 2 data: a reasonable agreement between the simulation and the data have been observed. The validation of the radiation damage modeling has allow us to use the digitizer as an investigation and prediction tool.  $Z \rightarrow \mu\mu$  and  $VH \rightarrow b\bar{b}$  samples have been used to investigate the impact of radiation damage on cluster and track properties. It has been shown that the variation in fluence and operational bias voltages have a significant impact on cluster charges and sizes and hence on charge collection efficiency. The impact on tracking quantities seems less important. To further investigate and conclude on the impact of radiation damage on physics observables, high statistics  $t\bar{t}$  samples with higher  $p_T$  spectrum and consequently less impact of multiple scattering are currently being produced, as well as high statistics  $VH \rightarrow b\bar{b}$  samples which will be used to estimate the impact of radiation on higher level observables such as b-tagging variables or the Higgs invariant mass.

As the LHC will enter its High Luminosity phase (HL-LHC), the ATLAS detector and particularly its inner tracker will be upgraded. With the upgraded tracker, performance are expected to reach or even outperform the current Run2 performance, which enlarges the spectrum of physics prospects: for example, the sensitivity to the Higgs trilinear coupling

should be enhanced thanks to the upgrade Inner tracker. I have made significant contribution to the upgrade effort through the characterization of ITk pixel sensors candidates and through the optimization of b-tagging algorithms.

Pixel sensors are at the core of the ITk design and their radiation hardness are of crucial importance to deal with the high radiation fluence of the HL-LHC. ITk-like sensors designed by LPNHE have been successfully tested on beams both un-irradiated and irradiated. The active edge sensors have demonstrated good efficiency results in the edge area: the efficiency is higher than 80% up to 25  $\mu\text{m}$  from the edge, even after irradiation at  $2.7 \times 10^{15} \text{ n}_{\text{eq}}/\text{cm}^2$ . These performances have been supported by TCAD simulation. Concerning thin sensors irradiated over the all ITk fluence range, it has been shown that 130  $\mu\text{m}$  FBK-LPNHE thick sensors passivated with BCB meets the ITk requirement in terms of hit efficiency (higher than 97%) and power dissipation for the intermediate layers of ITk (up to  $3.8 \times 10^{15} \text{ n}_{\text{eq}}/\text{cm}^2$ ). When irradiated to the expected fluence at the end of lifetime of the innermost layer, the hit efficiency reaches 89%. The charge collection efficiency values will be used in the framework of the ATLAS radiation damage digitizer group, to investigate the modeling of the radiation damage of pixel sensors at ITk fluences.

Eventually, two biasing solutions have been investigated and the temporary metal solution have been found superior to the punch-through solution, even after irradiation. Technologies tested on LPNHE sensors production have demonstrated solid performance which qualified them as candidates for the four outermost layers of the ITk barrel pixel detector. Concerning the ITk planar pixel designs, decisions on the biasing options and whether to use active edge sensor should be taken by the end of the market survey (end of 2018). LPNHE active-edge sensors bonded to the new RD53A chip will soon be tested on beams and will undergo some fluence exposure to study with great accuracy foreseen ITk-like sensors.

The optimization of b-tagging algorithms is currently ongoing with the goal of obtaining better results of b-tagging in the harsh conditions of HL-LHC. I worked on the optimization of the SV1 tagger. The use of updated material cleaning, vertex rejection and more stringent cuts in tracking requirements results in better performances in terms of light-jet rejection vs b-jet efficiency performances:  $\simeq 30\%$  of improvement for more stringent cuts. Some parametrization of the performances of b-tagging at high  $p_T$  have also been performed and will be used in physics analysis projections using highly boosted objects. The optimization of other b-tagging algorithms such as JetFitter is currently being considered. Ultimately the optimization of b-tagging algorithms would increase the overall sensitivity of the ATLAS experiment to all channels with b quarks in their final states such as the Higgs trilinear coupling.

In conclusion, all my PhD has been devoted to the development of tracking detectors for the High-luminosity phase of ATLAS and to the performance assessment of important tools like accurate Monte Carlo simulations and b-tagging algorithms. This work will be important for fundamental analysis at HL-LHC.



# Appendices



## Appendix A

# Appendix: Simulation details

### Details of the simulation

A 3D structure of a part of the third production has been simulated; some of its features can be seen in Figure A.1. The simulated 3D structure feature the pixel edge and half pixels in the long (250  $\mu\text{m}$ ) pixel directions was simulated. As the edge pitch (70  $\mu\text{m}$ ) differs from the pixel pitch, 2 edge pitches are simulated in the Y direction, which corresponds to 2 short pixel pitch and 4/5 of a third one. The structure was 200  $\mu\text{m}$  wide (x), 140  $\mu\text{m}$  (y) high and 132  $\mu\text{m}$  (z) deep.

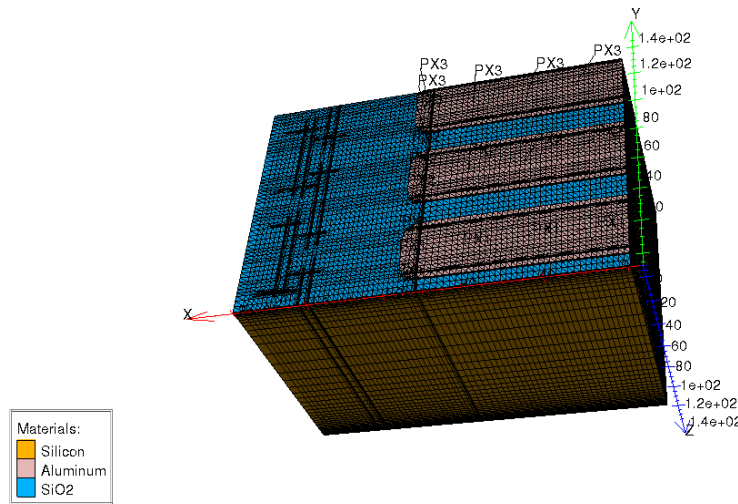


Figure A.1 – Graphical representation of the simulated 3D structure. The visible part of the mesh grid is superimposed.

An extra 5  $\mu\text{m}$  wide silicon-made region was added beyond the  $X=200 \mu\text{m}$  region to simulate the cut-region. The simulated silicon bulk thickness was 130  $\mu\text{m}$ ; the top surface was covered with a 0.8  $\mu\text{m}$  thick oxide. The silicon-silicon oxide interface was taken as the  $Z = 0 \mu\text{m}$  position. The backside was covered by a uniform aluminum deposition to realize the ohmic

contact. Pixel electrodes on the frontside, again in aluminum, were extending  $3\text{ }\mu\text{m}$  beyond the underneath n+ implant (the so-called metal overhang). Trenches were  $130\text{ }\mu\text{m}$  deep,  $10\text{ }\mu\text{m}$  wide and  $44\text{ }\mu\text{m}$  high, as in the real sensor. They were arranged in 2 lines along the X direction with a pitch of  $15\text{ }\mu\text{m}$ ; along the Y direction neighboring trenches were separated by  $26\text{ }\mu\text{m}$ .

In Figure A.2 a graphical representation of the doping regions of the structure; the Figure reports the doping concentrations in the  $X - Y$  plane at the  $Z=0.2\text{ }\mu\text{m}$  depth.

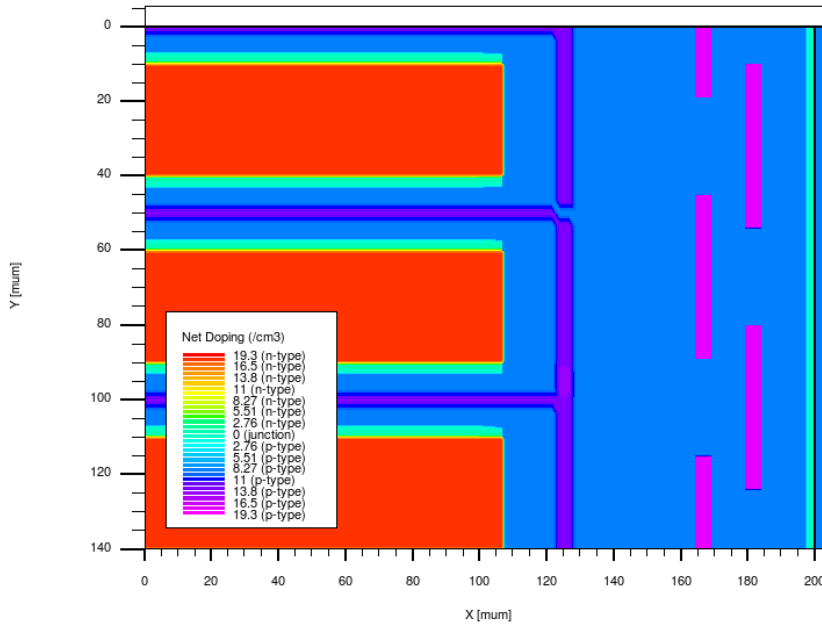


Figure A.2 – Graphical representation of the doping regions of the simulated 3D structure. The picture correspond to a region at depth  $Z=0.2\text{ }\mu\text{m}$

All non-uniform dopings were modeled using gaussian profiles. The doping concentration peak values and profiles were modeled based on information gotten from the FBK foundry.

The silicon bulk was uniformly Boron-doped with a concentration of  $1.5 \times 10^{12}/\text{cm}^3$ ; the cut-line had the same doping of the bulk. Pixels implants were realized with a Phosphorous doping having a peak concentration of  $2 \times 10^{19}/\text{cm}^3$ , decreasing to  $1 \times 10^{16}/\text{cm}^3$  over a distance of  $1\text{ }\mu\text{m}$ . Pixel implants isolation was assured by a combination of p-spray and p-stop. P-spray Boron-doping was uniform in the  $X - Y$  plane, with a peak concentration of  $5 \times 10^{16}/\text{cm}^3$  at  $Z=0\text{ }\mu\text{m}$  depth and reaching  $1 \times 10^{15}/\text{cm}^3$  over a distance of  $0.2\text{ }\mu\text{m}$ . P-stop doping was arranged as a Boron-doping grid around the pixel implants; the peak concentration was of  $2 \times 10^{17}/\text{cm}^3$  at  $Z=0\text{ }\mu\text{m}$  depth and reaching  $1 \times 10^{15}/\text{cm}^3$  over a distance of  $0.4\text{ }\mu\text{m}$ . Each trench was Boron doped with a peak concentration of  $2 \times 10^{19}/\text{cm}^3$ , decreasing to  $1 \times 10^{12}/\text{cm}^3$  over a distance of  $0.2\text{ }\mu\text{m}$ . The backside implant was realized with a Boron-doping uniform in the  $X - Y$  plane with a peak concentration of  $2 \times 10^{19}/\text{cm}^3$ , decreasing to

---

$1 \times 10^{15} / \text{cm}^3$  over a distance of  $1.5 \text{ } \mu\text{m}$ . In Figure A.2 the pixel, p-stop and trench dopings can be seen.

SILVACO TCAD uses a complete set of physical models for semiconductor device simulation. Among them, models for concentration dependent mobility, field dependent mobility, bandgap narrowing, concentration dependent lifetime, trap-assisted and Auger recombination were used. Oxide fixed charge density (with surface density  $Q_{ox} = 5 \times 10^{10} / \text{cm}^2$ ) and surface recombination velocity have been set according to measured IV and CV characteristics of diodes of the third production. the generation-recombination lifetime was set to a rather low value ( $10^{-7} \text{ s}$ ) for the sake of numerical convergence of the simulation; larger generation-recombination lifetime values, closer to reality, give numerical inaccurate simulation results, increasing the simulation time too, since the magnitude of the simulated leakage current is comparable with the numerical accuracy of the simulator. Since the goal of these simulations was to investigate the lateral extension of the depleted region, this choice of generation-recombination lifetime has negligible impact on the reliability of the simulations predictions.

The defects at the edge have been modeled with the  $5 \text{ } \mu\text{m}$  wide region in which the generation-recombination lifetime was set to a low value ( $10^{-12} \text{ s}$ ). If the trench doping were not effective, a large current would appear as soon as the electric field reaches the edge area.

All simulations were run at  $t = -15^\circ \text{ C}$ , the mid-point of the temperature range at which detectors were measured on beam ( $-40$  and  $+20^\circ \text{ C}$ ).



# Annexe B

## Résumé

L'expérience ATLAS a récemment mesuré les couplages du boson de Higgs avec la troisième génération de quarks : la désintégration du boson de Higgs en deux quarks  $b$  [1] ainsi que la production du boson de Higgs en deux quarks top [2].

D'ici 2026, le LHC sera amélioré en un collisionneur à plus haute luminosité instantanée : le HL-LHC (LHC à Haute Luminosité). Pour être capable de prendre des données dans ce cadre à haute luminosité, le détecteur ATLAS et plus particulièrement son trajectographe doivent être améliorés. L'amélioration du trajectographe d'ATLAS est axée autour de trois problématiques : la résistance des capteurs aux radiations ; l'augmentation de la granularité des pixels pour prendre en compte le haut taux de données ; l'augmentation de l'acceptance géométrique du détecteur à travers l'instrumentation à grand  $\eta$  et le développement de capteurs à bords fins ("Active edge").

Mon travail de thèse s'est articulé autour de trois sujets principaux englobant les problématiques d'amélioration du trajectographe d'ATLAS, d'amélioration des simulations monte Carlo d'ATLAS et d'amélioration de l'identification des jets issus de la désintégration de  $b$ -hadrons, ingrédient essentiel pour la recherche de bosons de Higgs se désintégrant en deux quarks  $b$ . Ce résumé abordera ces trois problématiques :

- Digitization des dommages liés aux rayonnements sur les capteurs en silicium du trajectographe de l'expérience ATLAS ;
- Recherche et développement autour de capteurs en silicium à pixels planaires pour l'amélioration du trajectographe d'ATLAS ;
- Amélioration des algorithmes d'étiquetage des jets issus de la désintégration des  $b$ -hadrons.

## Implémentation des dommages liés aux rayonnements dans les simulation Monte Carlo d'ATLAS

La digitisation est une étape des simulation Monte Carlo d'ATLAS. Elle consiste en la transformation des dépôts d'énergie obtenu lors du passage de particules chargées dans les détecteurs en un signal correspondant à la réponse du détecteur enregistrée par l'électronique de lecture du détecteur.

Les étapes précédant la digitisation des signaux sont la génération d'évènements et la simulation du détecteur. Il est important de prendre en compte la fluence à laquelle le détecteur a été exposé car une diminution d'efficacité de collection de charge est observée après irradiation (phénomène de piégeage de charges). La fluence est obtenue en utilisant la luminosité intégrée et un facteur de conversion déterminé grâce à des simulations FLUKA [91, 92, 93] et Pythia 8 [94, 95, 96].

Un autre ingrédient essentiel à la digitisation est la modélisation du champs électrique attendu à l'intérieur du capteur pour une tension polarisante et une fluence données. Le champs électrique est calculé en utilisant des simulations TCAD (Technology Computed Aided Design). Le modèle de Hambourg [85] est utilisé pour émuler le phénomène d'anncaling (recuit).

Les porteurs de charges créés par le passage d'une MIP à l'intérieur du capteur sont exposés à la dérive selon les lignes de champs électriques, à la diffusion ainsi qu'à la déflexion (de l'angle de Lorentz  $\theta_L$ ) causée par la présence d'un champs magnétique. Les porteurs de charges peuvent également être piégés à l'intérieur de la bande interdite si le capteur a été exposé aux radiations. La charge piégée induit une charge (qui peut être évaluée en utilisant le potentiel de Ramo [77]) sur l'électrode du capteur qui est inférieure à ce qui aurait été obtenu si elle avait pu dériver jusqu'à l'électrode. La charge résiduelle, accumulée par l'électrode du module est alors convertie en ToT (Time-over-Threshold [78]). Le groupement de hits adjacents temporellement et spatialement ("clusterisation") est ensuite effectuée.

### Cartes du champs électrique

Des cartes de champs électriques ont été simulées pour les quatre couches de pixels du détecteur actuel et pour différentes étapes en termes de fluence (jusqu'à  $8.1 \times 10^{14} \text{ n}_{\text{eq}}/\text{cm}^2$  pour l'IBL correspondant au taux de fluence prédit pour la fin de 2018) et de tension de polarisation (jusqu'à 400V pour l'IBL et la B-Layer). Les cartes de champs électriques ont été simulées en utilisant des simulations TCAD (Silvaco [97] pour les capteurs planaires et Synopsis [98] pour les capteurs 3D). Les modèles utilisés pour simuler l'impact des dommages des rayonnements sur les capteurs sont le modèle de Perugia pour les capteurs 3D et le modèle de Chiochia [100] pour les capteurs planaires.

Le modèle de Chiochia [100] contient deux niveaux de défauts à l'intérieur de la bande interdite : un niveau de piégeage accepteur et un niveau de piégeage donneur avec des énergies d'activation respectives de  $E_c - 0.52 \text{ eV}$  et de  $E_v + 0.48 \text{ eV}$  ( $E_c$  étant l'énergie de la



bande de conduction et  $E_v$  l'énergie de la bande de Valence). Les autres paramètres de ce modèle sont les sections efficaces de capture de trous et électrons pour les niveaux accepteurs et donneurs ainsi que la concentration d'accepteur et de donneurs.

La Figure 4.2 (a/b) présente un profil du champs électrique pour quatre fluences différentes à 80V/150V. Avant irradiation, le champs électrique est quasi linéaire : la déplétion commence de la face arrière vers l'implant pixellaire. Après l'inversion du type de dopage due à l'exposition à une certaine dose de fluence, le maximum du champs électrique change de côté et se trouve désormais près de la face avant.

Une étude sur les incertitudes sur les différents paramètres du modèle a été menée : une incertitude de 10% a été ajoutée sur la concentration de donneur et d'accepteur ( $N_T^A$  and  $N_T^D$ ) ainsi que sur les sections efficaces de captures des trous et des électrons ( $\sigma_e^A, \sigma_h^A, \sigma_e^D, \sigma_h^D$ ). L'incertitude sur l'énergie effective de défauts a été établie à 0.4% ce qui correspond à 10% de l'énergie thermique  $kT$ . De cette étude sur les incertitudes, deux observations peuvent être formulées :

- Le champs électrique est hautement dépendant des variations de l'énergie effective des défauts, modérément dépendant des variations de la concentration des accepteurs et des donneurs et peu dépendant des variations des sections efficaces de captures de porteurs de charges.
- La variation des observables accepteurs est plus importantes que celles observées pour les donneurs, ce qui peut être expliqué par le fait que les niveau accepteur est plus près du niveau intrinsèque que celui du donneur.

## Validation du modèle

Pour valider le modèle de digitisation des dommages de rayonnements, l'efficacité de collection de charge obtenue grâce au digitizer a été comparée aux données obtenues pendant le Run2. Sept étapes du Run2 sont considérées avec des conditions de fluence et de tension polarisante opérationnelle différentes pour les 4 couches de pixels du détecteur. Les tensions de déplétion s'échelonnent entre 80 V et 400 V, la plus haute valeur de fluence considérée est de  $8.1 \times 10^{14}$  n<sub>eq</sub>/cm<sup>2</sup>. L'étape 0 correspond à la configuration ou il n'y a pas de radiation damage pour les 4 couches. L'étape 1 correspond au début du Run2 ou seul les trois couches pixellaires les plus externes (B-Layer, Layer 1 and 2) avait déjà accumulé de la fluence lors du Run1. L'étape 2 correspond au conditions an termes de fluence et de tension de polarisation obtenue vers le milieu de 2016 après avoir accumulé 15 fb<sup>-1</sup> du Run2. Les étapes 3 et 4 correspondent aux conditions à la fin de 2016 respectivement avant et après les modification de tension de polarisation du B-Layer et du Layer 1. L'étape 5 correspond à la fin de 2017 (75 fb<sup>-1</sup>). L'étape 6 présente les valeurs extrapolées de fluence qui seront atteintes à la fin de 2018.

## Efficacité de collection de charge

L'efficacité de collection de charge est utilisée pour valider la simulation des dommages des rayonnement en le comparant avec les données actuelles de l'IBL. La Figure B.1 présente une estimation de l'efficacité de collection de charge (ratio de la moyenne des distributions de cluster charge) pour les quatre couches du détecteur à pixels et pour les sept étapes considérés. La variation de collection de charge suit les variations de fluence et de tension polarisante pour les données et pour les simulations. A la fin du Run2, l'efficacité de collection de charge simulée atteint  $\simeq 89\%$  pour la Couche 2,  $\simeq 86\%$  pour la Couche 1,  $\simeq 78\%$  pour le B-Layer et  $\simeq 73\%$  pour l'IBL. Les données de l'IBL et celles simulées sont en bonne adéquation même si les simulations semblent donner de meilleurs résultats que les données à la fin de 2016 et 2017, ce qui peut être expliqué par le fait que les variations en terme de configuration des modules et variations de la température ne sont pas encore implémentés dans la digitisation.

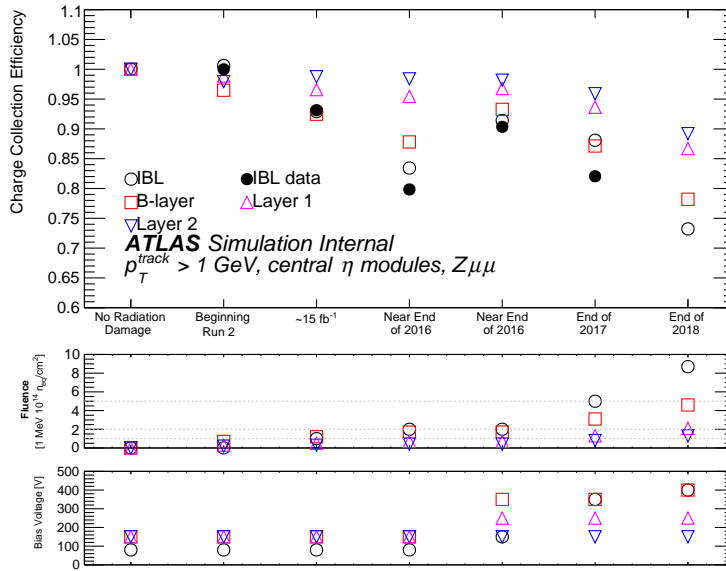


FIGURE B.1 – Efficacité de collection Charge pour les quatre couche du détecteur à pixel d'ATLAS, seul les modules centraux sont considérés. Les variations en termes de fluence et de tension de polarisation sont aussi indiquées.

## Propriétés des traces

Le modèle de digitisation des dommages des rayonnements ayant été validé par la comparaison de l'efficacité de collection de charge entre data et MC, le digitizer peut être utilisé pour investiguer l'effet des dommages des rayonnements sur les propriétés des traces. La résolution spatiale des plans de détecteurs ainsi que le taux de fausses traces ont été étudiées avec des simulations Zmumu. Le  $p_T$  des traces considérées étant bas, les traces sont sujettes à la diffraction multiple, ce qui impacte les résultats. Une augmentation de la fluence se traduit par une dégradation de la résolution spatiale. Pour conclure sur l'impact des rayonnements sur les propriétés des traces et par la suite sur l'étiquetage des jets de b, des lots de données

---

$t\bar{t}$  (statistiquement plus importants et avec un  $p_T$  plus important) sont actuellement en cours de préparation.

## Capteurs planaires à pixels en silicium

Le travail principal entrepris lors de cette thèse a été de tester et d’analyser les performances des productions de capteurs en silicium à pixels planaires, développés conjointement par le LPNHE et la fonderie FBK. Différents capteurs ont été testés après avoir reçu différentes doses d’irradiation et leurs performances en terme d’efficacité de reconstruction de charge et d’efficacité de reconstruction de hits sont présentés dans cette section.

### Présentation des capteurs

Pour être efficace dans l’environnement hautement radiatif du HL-LHC, le détecteur à pixel d’ATLAS doit être amélioré. Le LPNHE, la fonderie FBK et l’INFN sont associés dans la production et le développement de capteurs en silicium à pixel planaire. La technologie Active edge, ou capteur à bords actifs, est utilisée dans une partie des capteurs considérés. Cette technologie permet de réduire la zone non instrumentée en bordure des capteurs et d’augmenter ainsi, l’acceptance géométrique globale du détecteur. Les trois productions de capteurs n-on-p ont été testées en faisceaux après avoir reçu différentes doses d’irradiation. Chaque capteur a été relié à son électronique de lecture (puce électronique FE-I4B [46]) via bump-bonding à IZM Berlin<sup>1</sup>. Chaque capteur à pixel est composé d’une matrice de 336 rangées et 80 colonnes de pixels rectangulaires qui ont pour dimensions  $50\text{ }\mu\text{m} \times 250\text{ }\mu\text{m}$ . Les caractéristiques des trois productions sont présentées dans le tableau B.1.

L’épaisseur de capteurs varie d’une production à l’autre. la première production (capteurs LPNHE5 et LPNHE7) est constituée de capteurs de  $200\text{ }\mu\text{m}$  d’épaisseur, alors que la seconde (capteurs W30 et W80) ainsi que la troisième production sont constituées de capteur de  $130\text{ }\mu\text{m}$  ou  $100\text{ }\mu\text{m}$ . Les capteurs de la deuxième et troisième production sont plus fins, ce qui permet de mitiger l’impact des radiations sur leur efficacité. La première et troisième productions de capteurs sont des capteurs à bords actifs, réalisés grâce à la technique de DRIE (Deep reactive ion etching). Deux designs différents ont été étudiés : un bord actif classique, consistant en une unique tranchée faisant le tour du capteur pour la première production ; un bord actif en créneaux pour la troisième production, qui est en réalité composée de deux bords actifs segmentés faisant le tour du capteur. La technologie à bords actifs permet de réduire la zone non instrumentée en bordure du capteur grâce à la technique DRIE qui permet de garder l’intégrité du cristal, contrairement à une découpe classique par scie rotative en diamant qui engendre généralement des craquelures et des défauts dans le silicium. La taille de l’implant est de l’ordre de  $30\text{ }\mu\text{m}$  dans la direction courte du pixel et de  $230\text{ }\mu\text{m}$  dans la direction longue du pixel comme présenté dans la Figure B.2. Deux

---

<sup>1</sup>Fraunhofer-Institut für Zuverlässigkeit und Mikrointegration IZM - Gustav-Meyer-Allee 25, 13355 Berlin, Germany

TABLE B.1 – Caractéristiques des trois productions de capteurs. Le système de polarisation fait référence au processus de polarisation lors des phases de test avant bump-bonding. TM est l’abréviation de Temporary Metal et PT fait référence à Punch-Through. Les deux distances données pour le capteur M1.4 de la troisième production font référence aux distances aux bord actif intérieurs et extérieurs.

	Production 1		Production 2		Production 3
Nom des modules	LPNHE 5	LPNHE7	W30	W80	M1.4
Epaisseur (μm)	200	200	100	130	130
Active edge	Classique		Non		Créneaux
Nombre d’anneaux de garde	0	2	5	2	0
Distance au bord actif (μm)	100		-		37 and 52
P-stop	Yes	No	No		Yes
Système de polarisation	TM		PT		TM
Irradiation maximale( n <sub>eq</sub> /cm <sup>2</sup> )	Non irradié		1.4 × 10 <sup>16</sup>		2.7 × 10 <sup>15</sup>
Tension de déplétion (V)	Avant irradiation : 20 V				

techniques de polarisation sont utilisées pour polariser le capteur avant bump-bonding. Les productions 1 et 3 utilisent une bande de métal temporaire qui relie entre elles les rangées de la matrice pixellaire. La production 2 utilise une technique dite de punch-through qui implique l’utilisation d’une structure permanente qui dégrade l’efficacité de reconstruction des hits.

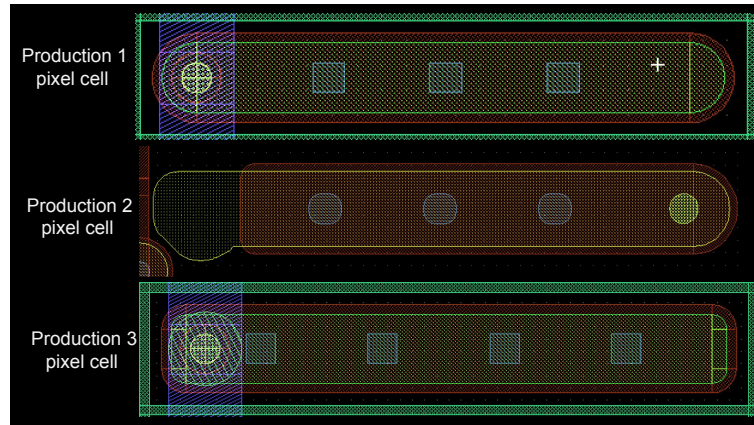


FIGURE B.2 – Détails d’un pixel des trois productions.

### Performances de capteurs fins et irradiés de la seconde production.

Deux capteurs de la deuxième production (W80 et W30) ont été irradiés à de hautes fluences, comparable à celles attendues dans le cadre du HL-LHC. En terme de résistance aux ra-

diations, ATLAS ITk demande au moins 97% d'efficacité de reconstruction de charge après irradiation. Pour atteindre cet objectif, le capteur doit être capable d'atteindre une tension de déplétion importante sans déclencher de décharges entre le capteur polarisé et l'électronique de lecture qui est à la terre, ainsi le capteur est recouvert d'une fine couche de passivation (BCB).

## Efficacité de collection de charge

La Figure B.3 présente l'efficacité de collection de charge pour différentes fluences. Les quatre

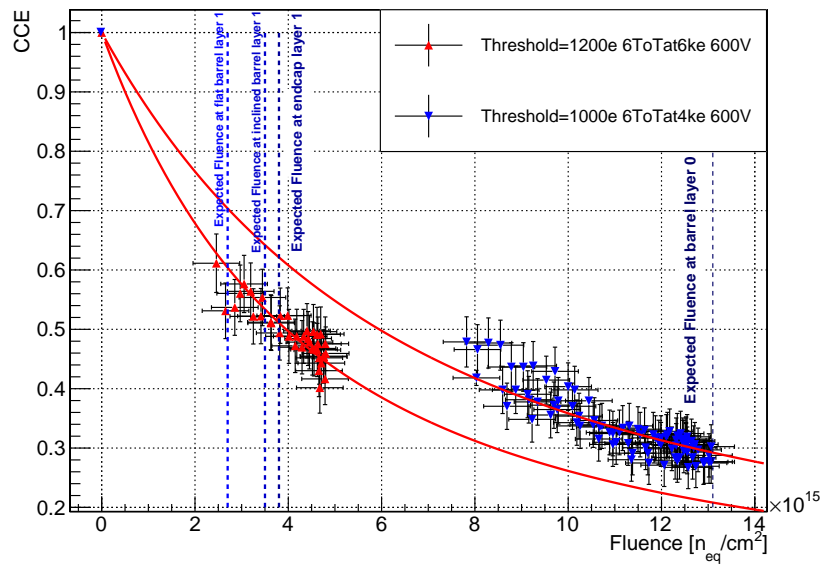


FIGURE B.3 – Efficacité de collection de charge extrapolée pour deux configurations différentes. Chaque distribution a été extrapolée avec une fonction de Hecht.

lignes verticales en pointillés représentent la limite en fluence attendue à la fin de la durée de vie de quatre partie du détecteur à pixel de l'ITk :

- La fluence attendue ( $2.7 \times 10^{15} \text{ n}_{\text{eq}}/\text{cm}^2$ ) dans la Couche 1 (deuxième couche en partant du point de collision) dans sa partie centrale.
- La fluence attendue ( $3.5 \times 10^{15} \text{ n}_{\text{eq}}/\text{cm}^2$ ) dans la partie inclinée de la Couche 1.
- La fluence attendue ( $3.8 \times 10^{15} \text{ n}_{\text{eq}}/\text{cm}^2$ ) dans la partie bouchon de la Couche 1.
- La fluence attendue ( $13.1 \times 10^{15} \text{ n}_{\text{eq}}/\text{cm}^2$ ) dans la partie centrale de la Couche 0 (la plus proche du point d'interaction)

Pour 1000 électrons de seuil et considérant les trois fluence attendue dans la Couche 1, l'efficacité de collection de charge est supérieure à 60%. A une fluence de  $1.3 \times 10^{16} \text{ n}_{\text{eq}}/\text{cm}^2$ , la fluence attendue dans la partie centrale de la Couche 0 après avoir collecté  $2000 \text{ fb}^{-1}$ ,

l'efficacité de collection de charge est inférieure à 30 %. L'utilisation de capteurs fins permet de garantir une efficacité de collection de charge comparable à celle de l'IBL en fin de vie, mais exposé à un ordre de magnitude en plus en terme de fluence.

### Efficacité de reconstruction de hits

L'efficacité de reconstruction de hits est présentée dans le tableau B.2 pour différentes fluence at plusieurs configurations en termes de seuil et de calibration en ToT. Les différentes fluence considérées correspondent aux fluences attendues dans les différentes couches de l'ITk. Quelques soit la configuration, l'efficacité est supérieure à 97% pour toutes les fluences correspondant aux fluence accumulées dans la deuxième couche la plus interne (Couche 1) du détecteur à pixels d'ITk. La limite donnée en terme d'efficacité de reconstruction de hits par ITk étant 97 %, les capteurs fins de la seconde production sont de bons candidats pour la Couche 1. Concernant la couche pixellaire la plus interne, la Couche 0, l'efficacité de reconstruction de hits est trop basse (88.6%), les capteurs de la deuxième production ne sont donc pas de bons candidats pour cette couche. Il est d'ailleurs prévu d'utiliser des capteurs 3D, plus résistants aux radiations dans cette partie du détecteur.

TABLE B.2 – Efficacité de reconstruction de hits extrapolée aux différentes fluences maximales attendues dans les couches de l'ITk.

<b>Fluence (<math>10^{15}</math> n<sub>eq</sub>/cm<sup>2</sup>)</b>	<b>2.7</b>	<b>3.5</b>	<b>3.8</b>	<b>7.45</b>	<b>13.1</b>
Seuil (électrons)	1200	1200	1200	1000	1000
Calibration en ToT (ToT correspondant aux électrons)	6at6	6at6	6at6	6at4	6at4
<b>Extrapolated Hit Efficiency (%)</b>	<b>98.6</b>	<b>97.6</b>	<b>97.2</b>	<b>97.0</b>	<b>88.6</b>

L'utilisation d'un seuil plus bas permettrait certainement de gagner en efficacité de reconstruction de hits.

### Performances des capteurs à bords fins

Le développement de capteurs aux bord réduits est nécessaire pour assurer une couverture géométrique optimale. La première production de capteurs possède des bords actifs et deux options en termes de nombre d'anneaux de garde : 0 ou 2. Le module M1.4 de la production 3 possède une version différente de bord actifs : deux tranchées discontinues enserrant le capteur à respectivement 37 et 52  $\mu\text{m}$  du dernier pixel. Un tel design permet de se passer de l'utilisation d'une galette de support.

L'efficacité de reconstruction de hits en bordure du capteur est présentée pour les deux capteurs de la première production en Figure B.4 (depuis [81]). Grace à la technologie active edge, les deux capteurs sont efficaces même dans la zone non instrumentée : l'efficacité de reconstruction de hits est plus grande que 50% jusqu'à environ 90  $\mu\text{m}$  du dernier pixel, à

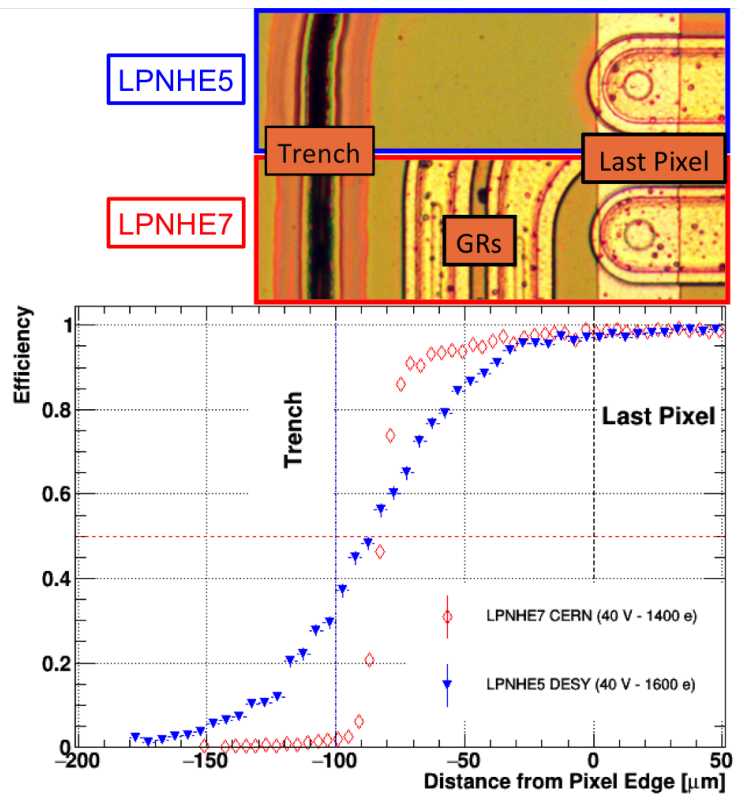


FIGURE B.4 – Efficacité en bordure du capteur pour LPNHE5 (pas de GRs - marqueurs pleins) et LPNHE7 (2 GRs - marqueurs ouverts)



seulement 10  $\mu\text{m}$  de la tranchée. La présence d’anneaux de garde et d’un bord actif permet d’avoir une bonne efficacité en bordure du capteur grâce à l’extension latérale de la déplétion et également d’augmenter la valeur de la tension d’avalanche. Ce résultat est prometteur pour les capteur à bords actifs et anneaux de garde en milieu radiatifs.

Un des capteurs de la troisième production, M1.4 a été irradié à KIT [128] pour atteindre une fluence de  $2.7 \times 10^{15} \text{ n}_{\text{eq}}/\text{cm}^2$ . Après irradiation, la tension d’avalanche du capteur a été estimée à 90-95 V, ce qui est relativement bas et est une preuve du dysfonctionnement du capteur. La Figure B.5 compare les performances en terme d’efficacité en bordure du capteur avant et après irradiation. Même dans le cas d’une tension d’avalanche prématurée, les performances du capteur en terme d’efficacité au bord sont similaire à celle obtenues avant irradiation. Pour un seuil de 1000 électrons, l’efficacité est supérieure à 50% jusqu’à 44  $\mu\text{m}$  du dernier pixel.

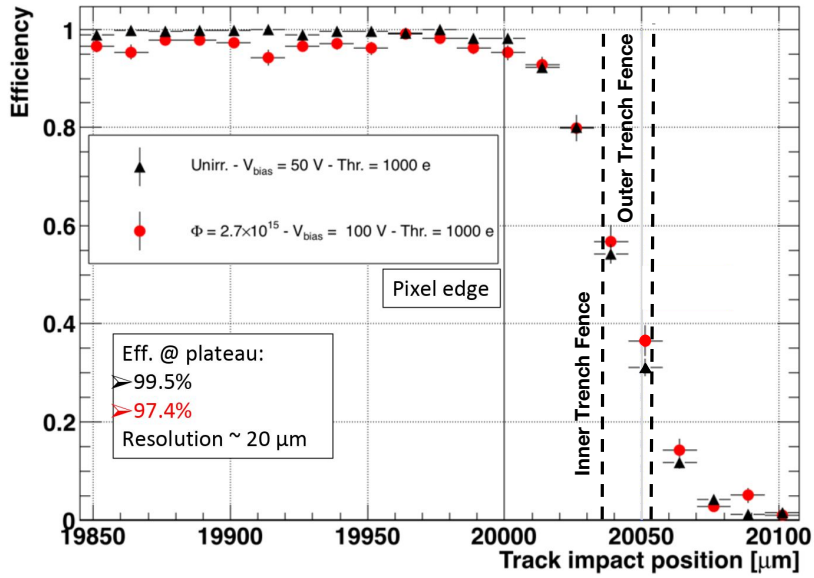


FIGURE B.5 – Comparaison de l’efficacité de reconstruction en bordure du capteur avant et après irradiation.

## Structure polarisante et implantation pixellaire

La Figure B.6 présente l’efficacité intra-pixellaire pour les trois productions et trois différentes fluences : non irradié, irradié à  $3 \times 10^{15} \text{ n}_{\text{eq}}/\text{cm}^2$  et irradié à  $1 \times 10^{16} \text{ n}_{\text{eq}}/\text{cm}^2$ . L’efficacité intra-pixellaire pour des capteurs non irradiés de la première et troisième production est très homogène grâce à l’utilisation de bandes de métal temporaires pour polariser le capteur durant les phases de tests, avant d’être relié à son électronique de lecture. La structure punch-through de la production 2 dégrade sévèrement l’efficacité en bordure du capteur. La comparaison des productions 1 et 3 irradiées à environ  $3 \times 10^{15} \text{ n}_{\text{eq}}/\text{cm}^2$  montre que l’efficacité est plus importante lorsqu’on utilise une solution de polarisation temporaire métallique plutôt qu’une technique punch-through. L’utilisation d’un implant plus large pour



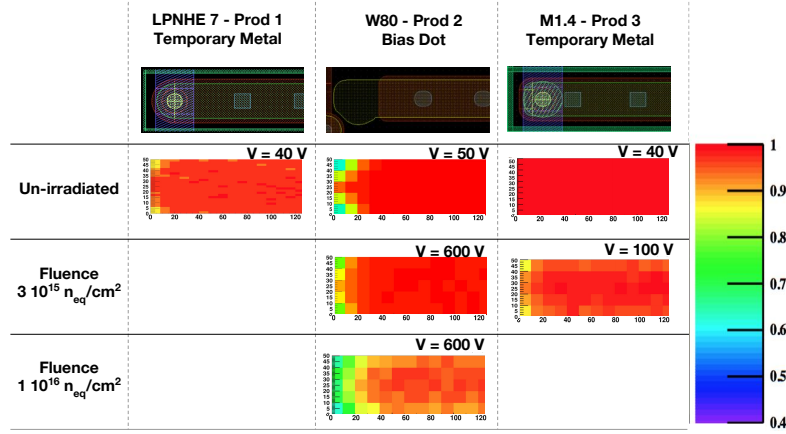


FIGURE B.6 – Efficacité intra-pixellaire présentée à l’intérieur d’une demi cellule pour trois capteurs issus des trois productions testées. Trois fluences différentes ont été considérée. Un schéma du pixel est proposée dans la partie haute de la figure.

les capteurs de la troisième production résulte en une augmentation de l’efficacité dans les coins du pixels.

## Amélioration des algorithmes de b-tagging

La production de b-hadrons au LHC est conséquente et l’un des principaux défis de la chaîne d’analyse d’ATLAS est la capacité d’identifier des b-hadrons ainsi que leur produits de désintégration. L’identification de b-jets est appelée b-tagging [63]. Avec l’augmentation de la statistique pendant la phase à haute luminosité du LHC, la source dominante d’incertitudes pour de nombreuses analyses de physique ne sera plus la statistique mais les incertitudes systématiques. Les incertitudes liées au b-tagging entrant dans le calcul d’incertitudes systématiques, l’optimisation des performances du b-tagging pourrait avoir un impact décisif sur les canaux de recherche impliquant des quarks b. Parmi ces canaux physiques, le couplage du Higgs avec lui même, en particulier avec des quarks b dans les états finaux.

Une partie de mon travail de thèse fut basé sur l’optimisation des algorithmes d’étiquetage des b-jet pour ITk. J’ai travaillé plus particulièrement sur l’optimisation de l’algorithme SV1 et sur les performances de b-tagging à haut  $p_T$ .

Le B-tagging exploite les caractéristiques de la désintégration des b-hadrons : grande masse du b-hadron ; présence d’un vertex secondaire du fait de la durée de vie relativement longue des b-hadrons ; traces avec des grands paramètres d’impacts transverses ( $d_0$ ) et longitudinaux ( $z_0 \sin(\theta)$ ).

Les performances de b-tagging s’exprime en terme d’efficacité de b-tagging (fraction de véritables b-jets étiquetés comme tels) et de c et light jet "mis-tag rate" qui sont les jets issus de la désintégrations de c ou light hadrons faussement identifiés comme b-jets. Les light (contenant des quarks u, d, s ou gluons) et c mis-tag rate sont évalués pour une efficacité de

b-tagging (working point). Un working point classiquement considéré dans les analyses de physiques d'ATLAS et qui sera utilisés dans la discussions suivante est 70%.

Il existe trois types d'algorithmes de b-tagging : les algorithmes basés sur les paramètres d'impact (IP3D...), les algorithmes basés sur les vertex secondaires (SV1) et les algorithmes reposant sur la topologie de désintégration des b-hadrons (JetFitter).

Les résultats de ces trois types d'algorithmes sont assemblés ensemble grâce à des techniques multivariées [150] (réseaux de neurones ou arbres de décision boosté) pour discriminer les b-jets des c et light jets.

### Algorithmes de b-tagging basés sur la reconstruction de vertex secondaires

L'étiquetage des jets de b en utilisant les vertex secondaires [149] est possible grace à l'algorithme SV1. Plusieurs étapes successives sont nécessaires :

- Sélection de traces à l'intérieur d'un jet : Plusieurs critères en terme de nombre de hits requis dans les différents détecteurs (pixels, SCT) sont définies, ainsi que des coupures sur les paramètres d'impact.
- Formation de tout les vertex contenant deux traces possible à l'intérieur du jet
- Sélection sur le liste de vertex : le premier critère est que la distance entre le vertex secondaire est principal soit importante. Les vertex correspondant à des interactions hadroniques avec la matière ou provenant de la désintégration de  $K_s$  or  $\Lambda$  ou de conversion de photons sont écartés.
- Fusion des vertex contenant deux traces en vertex secondaires contenant plusieurs traces.
- Utilisation d'une méthode likelihood pour discriminer les b-jets des c-jets ou light-jets. Pour construire la fonction de densité de probabilité, quatre observables sont utilisées : la masse invariante de toutes les particules provenant du vertex secondaire, le ratio de la somme des énergies des traces à l'intérieur du vertex secondaire et de toutes les traces à l'intérieur du jet, le nombre de vertex de deux traces sélectionnés dans le jet, l'angle entre la direction du jet et la direction de l'axe reliant vertex primaire et vertex secondaire.

### Optimisation de l'algorithme SV1 pour ITk

L'algorithme SV1 a été développé pour être utilisé dans les conditions actuelles de prise de données. Pour le rendre performant dans les conditions du HL-LHC, des modifications ont été apportées : la première étant d'intégrer la nouvelle géométrie de l'ITk dans le code. Cette modification a permis de supprimer les évènements provenant de l'interaction hadronique avec les différentes parties du détecteur. Comme présenté en Figure B.7, la suppression

de vertex correspondant à des couches du détecteur permet de réduire d'au moins 20% le nombre de light jets faussement étiqueté comme b-jets sur tout le spectre en  $p_T$ , et de façon significative dans la région  $0.5 < |\eta| < 3.5$ .

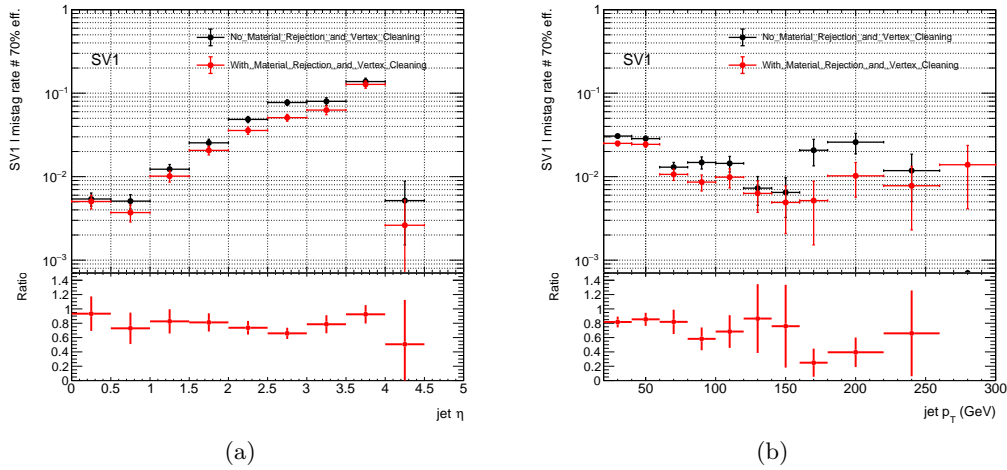


FIGURE B.7 – Taux de Light jets faussement étiqueté comme des jets de b en fonction de  $\eta$  (a) and  $p_T$  (b) avec (marqueurs rouges) et sans (marqueurs noirs) suppression de vertex secondaire correspondant à des couches du détecteur.

Un autre axe d'optimisation du détecteur a été le test de différentes options de sélection de traces : le nombre de hits requis dans le détecteur ( $\text{SiCuts} = 7, 9$  ou  $11$ ) ainsi que la borne inférieure en  $p_T$  (700, 900 et 1100 MeV). La Figure B.8 présente le taux de light jets faussement étiqueté comme b-jets en fonction de  $\eta$  (a) and  $p_T$  (b) pour les trois configurations. Les coupures les plus sévères ( $p_T > 1100$  MeV et  $\text{SiCuts} = 11$ ) donne de meilleurs résultats au moyen et grand  $\eta$  ainsi que sur l'intégralité du spectre en  $p_T$ .

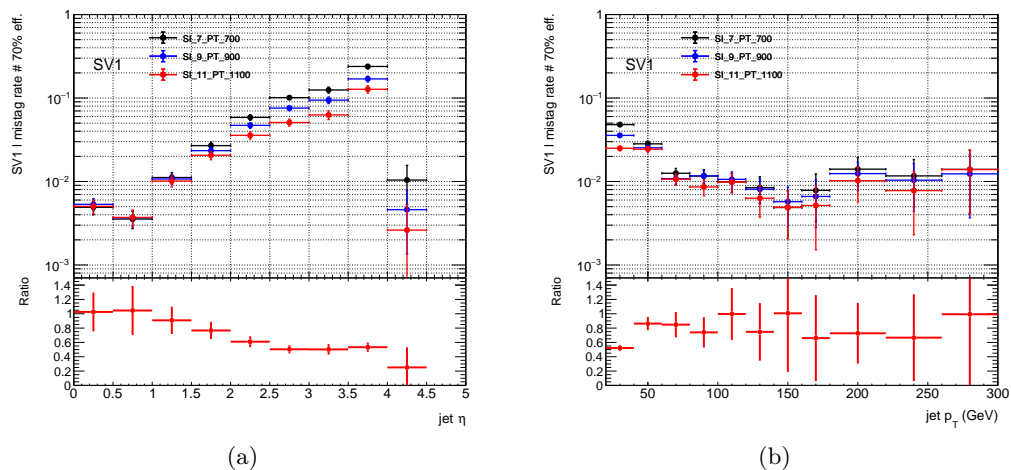


FIGURE B.8 – Taux de Light jets faussement étiqueté comme des jets de b en fonction de  $\eta$  (a) and  $p_T$  (b) pour plusieurs critères de sélection

Cette tendance est confirmée par la Figure B.9 qui présente le taux de mis-identification de light jets en fonction de l'efficacité de reconstruction des jets de b. La configuration ( $\text{SiHitsCuts} = 11$  and  $p_T\text{Cuts} = 1100$  MeV) permet une décroissance de 30 % du taux de

mis-identification de light jets en jet de b comparé à la configuration ( $\text{SiHitsCuts} = 7$  et  $p_T\text{Cuts} = 700$  MeV).

L'algorithme SV1 est un puissant outil pour réduire la contamination de light jets. Il sera utilisé conjointement avec la version d'IP3D optimisée pour ITk au sein d'algorithmes multivariés.

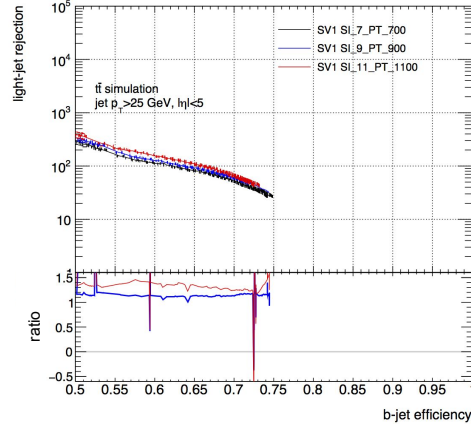


FIGURE B.9 – Taux de rejet des light jets en fonction de l'efficacité de reconstruction de b-jets.

# List of figures

1.1	From [8] Higgs potential for a 125 $GeV$ higgs boson with a vacuum expectation value (vev) of $v = 246\ GeV$ . $-\mu^2 < 0, \lambda > 0$ , the minimum of the potential is at $ \Phi  = \frac{v}{\sqrt{2}} \simeq 174\ GeV$ . . . . .	13
1.2	Higgs production channels considered at LHC. [22, 23] . . . . .	17
1.3	(a) Higgs cross section at 13 TeV proton-proton energy collision for various Higgs masses. (b) Higgs cross sections for a 125 GeV Higgs for different $\sqrt{s}$ [22].	18
1.4	Higgs branching ratios [23]. . . . .	19
2.1	Scheme of the CERN accelerator complex [28] . . . . .	22
2.2	LHC and High Luminosity LHC (HL-LHC) timeline [31]. . . . .	23
2.3	Left: Integrated luminosity for each year with also referenced the energy in the center of mass. Right: Distribution of the mean number of interactions per bunch crossing vs luminosity for the 2015-2018 (up to the 12 <sup>th</sup> of june) pp collision data at $\sqrt{s}=13\ TeV$ . [33] . . . . .	24
2.4	SM cross section production for several final states [34] . . . . .	25
2.5	Mass of the Higgs boson obtained by ATLAS experiment with the dataset collected in Run1 and Run2 on the two channels $H \rightarrow \gamma\gamma$ and $H \rightarrow ZZ \rightarrow 4\ leptons$ [36]. . . . .	25
2.6	The ATLAS detector [37] . . . . .	27
2.7	r and z dependency of the radial (Br) and axial (Bz) magnetic field components in the inner detector cavity, at fixed azimuth. (From [6]). . . . .	27
2.8	Inner Detector barrel section [37] . . . . .	28
2.9	Scheme of a barrel module of the electromagnetic calorimeter [50]. . . . .	31
2.10	Run2 Trigger overview [54]. . . . .	32

2.11	Perigée representation [58] . . . . .	33
2.12	Comparison of $d_0$ resolution with and without the IBL over the full $\eta$ range (a) and at low $p_T$ (0.4 GeV to 20 GeV)(b). From [60]. . . . .	34
2.13	Comparison of $z_0$ resolution with and without the IBL over the full $\eta$ range (a) and at low $p_T$ (0.4 GeV to 20 GeV)(b). From [60]. . . . .	34
2.14	Illustration of merged cluster phenomenon. The different colors account for signals from the passage of different charged particles. From [57]. . . . .	36
2.15	Comparison of track reconstruction efficiency for two track criteria over the full $\eta$ range (a) and $p_T$ range (b). From [60]. . . . .	37
3.1	PN junction. Scheme from [70]. . . . .	45
3.2	FEI4 Block diagram of the analog processing of the signal (from [46]) . . . .	49
3.3	Charge collection mechanism of an hybrid planar pixel sensor (left) and of a 3D pixel sensor (right). . . . .	50
3.4	Sections (not to scale) of an IBL-like n-in-n hybrid planar pixel sensor (a) and of an ITk-like n-in-p hybrid planar pixel sensor (b). For the IBL like module, the thickness of the sensor is 200 $\mu\text{m}$ and the pitch 250 $\mu\text{m} \times 50 \mu\text{m}$ ; For the ITk-like module, the thickness of the sensor will be around 100 $\mu\text{m}$ and the pitch will be either 50 $\mu\text{m} \times 50 \mu\text{m}$ or 25 $\mu\text{m} \times 100 \mu\text{m}$ . . . . .	51
3.5	Scheme of the edge of a sensor without Active edge (Left) and with Active edge (Right). $a$ is the size of the dead area and $d$ represents the distance between the last pixel and the end of the lateral depletion. . . . .	52
3.6	Defect overview from [83]. The $+/-$ legend indicates if the defect is charged at room temperature. Contributions of the point defects are represented in blue and cluster contributions (extended defects) are represented in red. . . .	54
3.7	Displacement damage in Silicon for different particles as a function of their energy [84]. . . . .	55
3.8	Type inversion of a n-type bulk into a p-type bulk [85] . . . . .	57

4.1	Schematic diagram of the radiation damage digitizer physics processes (from [89]). A planar pixel sensor (either IBL planar or B-Layer, Layer1 or Layer 2 planar pixel sensor) bump-bonded to its electronics read-out chip is presented. A crossing MIP creates electron hole pairs along its paths which are moving according to various contributions including drift along the electric field lines, deflection by the Lorentz angle caused by the magnetic field, thermal diffusion and charge trapping implied by radiation damaged induced states in the silicon bulk. Eventually, the remaining induced charge is digitized by the electronics and converted into Time-over-Threshold (ToT). . . . .	60
4.2	Electrical field in planar sensors (a) at 80 V, (b) at 150 V and 3D pixel sensors (c). For 3D sensor, the top plot is the electrical field before irradiation at 20 V and the bottom plot after receiving a fluence of $5 \times 10^{14} \text{ n}_{eq}/\text{cm}^2$ at 40 V. For planar pixel sensors, 4 fluence configurations are investigated: un-irradiated (black line), irradiated at $1 \times 10^{14} \text{ n}_{eq}/\text{cm}^2$ (red), $2 \times 10^{14} \text{ n}_{eq}/\text{cm}^2$ (blue), $5 \times 10^{14} \text{ n}_{eq}/\text{cm}^2$ (green). From [89]. . . . .	62
4.3	TCAD Electric field maps vs sensor bulk depth. A variation of the defect energy by $\pm 0.4\%$ is presented for a fluence of $\Phi = 2 \times 10^{14} \text{ n}_{eq}/\text{cm}^2$ . Plots a and b (respectively c and d) shows the evolution of the acceptor (donor) energy. The bias voltage is either 80 V (a and c) or 150 V (b and d). . . . .	65
4.4	TCAD Electric field maps vs sensor bulk depth. A variation of the electron and hole capture cross sections $\sigma_{e,h}$ by $\pm 10\%$ is presented for a fluence of $\Phi = 2 \times 10^{14} \text{ n}_{eq}/\text{cm}^2$ . Plots a, b, c, and d (respectively e, f, g and h) show the evolution of the acceptor (donor) capture cross sections. The capture cross sections for electrons (respectively holes) are presented in Figure a, b, e and f (respectively c, d, g and h). The bias voltage is either 80 V (a, c, e and g) or 150 V (b, d, f and h). . . . .	66
4.5	TCAD Electric field maps vs sensor bulk depth. A variation of the acceptor/donor concentration by $\pm 10\%$ is presented for a fluence of $\Phi = 2 \times 10^{14} \text{ n}_{eq}/\text{cm}^2$ . Plots a and b (respectively c and d) show the evolution of the acceptor(donor) concentrations. The bias voltage is either 80 V (a and c) or 150 V (b and d). . . . .	67
4.6	Summary plot for radiation damage testbeam . . . . .	69
4.7	Charge chunking unsmearing. This figure shows the normalized charge collected vs time to electrode. The red and blue curve are the collected charge respectively with/without unsmearing. The pink and green curve are the induced charge by trapped carriers respectively with/without unsmearing. The three plots are considering different numbers of sub-charges (chunks): the left plot shows results for 10 chunks, the middle one for 100 chunks and the right one for 1000 chunks. . . . .	70

4.8	Trapping effect on induced charge in a 3D sensor exposed at a fluence of $1 \times 10^{16} \text{ n}_{eq}/\text{cm}^2$ and biased at 260 V. The left plot shows the induced charge at trap location for three electrons created in the upper half part. The right plot is a 2D map in the XY plane of the weighting potential for two simulated 3D columns. . . . .	70
4.9	Charge collection efficiency comparison between data and simulation in Allpix standalone simulation [101]). The red dots represent data during the Run2. .	71
4.10	Distribution of the mean cluster size in the $z$ direction for the four ID pixel layers and the seven Run2 benchmarks considered. $Z \rightarrow \mu\mu$ samples are considered. The evolution in bias voltage and fluence are reported on the two bottom plots. . . . .	74
4.11	Distribution of the mean cluster size in the $\phi$ direction for the four ID pixel layers and the seven Run2 benchmarks considered. The evolution in IBL effective angle (absolute difference between the tilt angle and the Lorentz angle), bias voltage and fluence are reported on the three bottom plots. . . . .	75
4.12	Distribution of the mean total cluster size for the four ID pixel layers and the seven Run2 benchmarks considered. The evolution in bias voltage and fluence are reported on the two bottom plots. . . . .	76
4.13	IBL Cluster Charge distribution reported for the seven Run2 benchmarks considered. The top ratio plot (blue markers) presents the ratio of the beginning of Run2 benchmark over the "no radiation damage" benchmark (benchmark 0). The bottom ratio plot (yellow markers) presents the ratio of the end of 2018 benchmark over the beginning of Run2 benchmark. . . . .	77
4.14	Distribution of the mean cluster charge for the four ID pixel layers and the seven Run2 benchmarks considered. The evolution in bias voltage and fluence are reported on the two bottom plots. . . . .	78
4.15	Charge collection efficiency for the four ID pixel layers central $\eta$ modules and the seven Run2 benchmarks considered. The evolution in bias voltage and fluence are plotted on the two bottom plots. IBL data are also presented . .	79
4.16	Charge collection efficiency for the four ID pixel layers using $VH \rightarrow b\bar{b}$ samples. Central $\eta$ modules and the seven Run2 benchmarks are considered. The evolution in bias voltage and fluence are plotted on the two bottom plots. IBL data are also presented . . . . .	80
4.17	Distribution of the reconstructed tracks $p_T$ (a and c) and over the $\eta$ spectrum (b and d). $Z \rightarrow \mu\mu$ samples (a and b) and $VH \rightarrow b\bar{b}$ (c and d) samples are considered. . . . .	81



4.18	Distribution of the unbiased residuals RMS in the short pixel direction for the four ID pixel layers and the seven Run2 benchmarks considered. The evolution in cluster size in $\phi$ , effective angle for the IBL, bias voltage and fluence are plotted in the bottom plots. The following tracks selection criteria is considered: $p_T > 20$ GeV. . . . .	82
4.19	. . . . .	83
4.20	Distribution of the unbiased residuals RMS in the long pixel direction for the four ID pixel layers and the seven Run2 benchmarks considered. The evolution in bias voltage and fluence are plotted in the two bottom plots. The following tracks selection criteria is considered: $p_T > 20$ GeV. . . . .	83
4.21	Tracks fake rate for the seven Run2 benchmarks considered. The evolution in bias voltage and fluence are reported in the two bottom plots. . . . .	84
5.1	HL-LHC planned instantaneous peak luminosity (red dots) and integrated luminosity (blue line) [108] . . . . .	88
5.2	Fluence simulation in an ITk pixel section [107]. . . . .	90
5.3	ITk inclined layout scheme [107] . . . . .	91
5.4	The red part represents the ITk pixel detector, the blue one represents the ITk strips detector. . . . .	91
5.5	Material budget comparison between Run2 in red and ITk layout in blue.[107] . . . . .	92
5.6	ITk pixel layout simulation from [107]. The ITk pixel layout is divided in several parts. Parts 1 (flat barrel), 2 (inclined barrel rings) and 3 (end-caps rings) and their symmetric are the Inner pixel system. It is limited by the Inner Support Tube (IST), represented in magenta on the Figure. Part 4 and 5 form the Outer pixel barrel: L2 and L3 are on the same double sided longeron, whereas L4 is on a single sided longeron. Part 6 is the outer pixel end-caps. . . . .	95
5.7	ITk Track efficiency and fake rate compare to Run2 for $t\bar{t}$ samples. From [107]. . . . .	96
5.8	Comparison of c-jet and light-jet rejection vs b-jet efficiency between Run2 and ITk [107]. . . . .	97
5.9	Comparison of converted photons fractions between Run2 and ITk. Photon conversion identification efficiency for ITk [107]. . . . .	98
5.10	Width of $h \rightarrow ZZ \rightarrow 4\mu$ and $h \rightarrow \mu\mu$ invariant mass for ITk layout (plain markers) and Run2 (dashed markers) [107]. . . . .	99
5.11	HH branching ratios coupling [117] . . . . .	99

6.1	Section of a pixel sensor, not to scale. . . . .	104
6.2	Details of the pixel cell for the three LPNHE/FBK productions. . . . .	104
6.3	(a) Scheme of a depth cut of the edge area of an active edge sensor from the first production, the bias tab is only on one edge of the device. (b) SEM picture of a test trench structure. From [119]. . . . .	105
6.4	Microscope picture of corners of the three bump-bonded sensors of the first production: LPNHE5 (left), LPNHE4 (middle) and LPNHE7 (right). The black line at the top and on the right is the trench. The shortest distance from the pixels to the trench is 100 $\mu\text{m}$ for all the three sensors. For LPNHE4 there is one GR surrounding the pixel matrix; for LPNHE7 there are two GRs.	106
6.5	Details of a pixel of the first production . . . . .	106
6.6	Current-Voltage curves for test structures featuring different number of GRs. The innermost GR, if present, was kept at ground voltage. The shortest distance from the pixels to the trench is 100 $\mu\text{m}$ . The measurement for the test structure with 2 GRs was taken at a lower temperature with respect to the other two samples. . . . .	107
6.7	Wafer from the $n-on-p$ planar technology production [121] whose layout was mainly based on ATLAS FE-I4 and CMS PSI46 [122] designs. The red rectangle encircles one pixel sensors compatible with the FE-I4 readout chip. . . . .	107
6.8	Pixel details of the second production. At the bottom left, part of the bias dot and metal bias line can be seen. . . . .	108
6.9	Projections of the proton beam profile used at CERN IRRAD to irradiate the W80 module. Left: horizontal direction; right: vertical direction. A gaussian fit is superimposed. The (0,0) position correspond to the nominal beam center.	109
6.10	Fluence profile for W80 module after the the first (Left plot) and second irradiation step (Right plot). The area reported corresponds to the surface of the pixel module. . . . .	109
6.11	Current-Voltage curves of W80 sensor after a fluence of $3 \times 10^{15} \text{ n}_{\text{eq}}/\text{cm}^2$ (green markers) and after an cumulative fluence of $1 \times 10^{16} \text{ n}_{\text{eq}}/\text{cm}^2$ (blue and yellow markers). The temperature is indicated in the legend. . . . .	110
6.12	Sensor power dissipation curves of W80 sensor after a fluence of $3 \times 10^{15} \text{ n}_{\text{eq}}/\text{cm}^2$ (green markers) and after a fluence of $1.1 \times 10^{16} \text{ n}_{\text{eq}}/\text{cm}^2$ (blue, yellow and red markers). The green, blue and yellow markers gives results obtained at $\simeq -40^\circ\text{C}$ . . . . .	112

6.13	Details of the third production staggered edge. The Figure (a) presents a large view of one of the corner of M1.4 sensor. In Figure (b) the pixel to edge distances, the edge pitch and the segments dimensions are reported. . . . .	112
6.14	Pixel scheme of the third production. . . . .	113
6.15	Current-Voltage curves of M1.4 before and after irradiation. . . . .	114
6.16	Sensor Power dissipation curve of M1.4 before and after irradiation. . . . .	114
6.17	IV curves of RD53A compatible sensors. Two pixel pitch options are considered: $25\text{ }\mu\text{m} \times 100\text{ }\mu\text{m}$ (a) and $50\text{ }\mu\text{m} \times 50\text{ }\mu\text{m}$ (b, c, d). Two wafer technologies are considered: SiSi (a and b) and SOI (a, c and d). The bias range goes from 0 to 200V and the current scale (which is logarithmic) goes from $10^{-10}$ to $10^{-4}$ A. The legend compiles the various wafer names. . . . .	115
6.18	ToT scheme with HitDiscCnfg discussion . . . . .	117
7.1	Scheme of DESY beam production for testbeam . . . . .	121
7.2	Hit map of a tested sensor in beam. On the abscissa is the pixel column index, on the ordinate axis is the pixel row index. (Left) the beam is focused on the center of the sensor; (right) the beam is focused on the edge, which allows to perform edge efficiency scan. The area where hits are seen is a $1\text{ cm}^2$ rectangle and correspond to the area of the trigger scintillator. . . . .	124
7.3	Left: residual distribution for clusters of 1 pixel cell fitted with a box function convoluted with a Gaussian. Right: residual distribution in logarithmic scale of two pixels clusters, fitted with the sum of two Gaussians. Data were taken at CERN-SPS, hence the multiple scattering contribution is small ( $4\mu\text{m}$ ). The threshold was 1400 electrons, the ToT tuning was 7 ToT corresponding to 1400 electrons and the sensor was biased at 40V. . . . .	126
7.4	Residual distribution of LPNHE7 for all clusters in the short pixel direction ( $50\text{ }\mu\text{m}$ pitch). The RMS of the residual is about $11.5\text{ }\mu\text{m}$ . Data were taken at CERN-SPS, hence the contribution from pointing resolution convoluted with the multiple scattering is small ( $\sim 5\mu\text{m}$ ). The threshold was 1400 electrons, the ToT tuning was 7 ToT corresponding to 1400 electrons and the sensor was biased at 40V. . . . .	127
7.5	Left: residual distribution for all cluster sizes in the short pixel direction (Y). Right: residual distribution for clusters of 1 pixel cell in Y direction fitted with a box function convoluted with a Gaussian. Data were taken at DESY, hence the multiple scattering contribution is important. . . . .	127

- 7.6 Global hit efficiency for the 2 sensors (LPNHE7 and LPNHE5), for various bias points, threshold configurations (1600 or 1400 electrons) and beam tests (CERN or DESY). *Edge/Center* identifies data taken when the beam was focused at the detector periphery/center. The uncertainties are dominated by the systematics from the reconstruction software. . . . . 128
- 7.7 Hit map of W80. The Down and Up ROI are visible respectively in the left/right plots. . . . . 130
- 7.8 Average ToT profiles for the two ROI. The threshold, ToT tuning and bias voltage are indicated in the legend box. All distribution are fitted with a polynomials of degree two (red lines). . . . . 131
- 7.9 Horizontal (a) and vertical (b) fluence profiles with and without fluence peak constraint. The blue/red and green/yellow points represent data taken in the Up/Down ROI. . . . . 131
- 7.10 average ToT distribution vs fluence for three different bias voltages. The left/right plot is without/with fluence peak constraint. The horizontal/vertical bin label in the legend means that the fluence and average ToT have been extracted from an horizontal/vertical profile of the Down ROI. . . . . 132
- 7.11 Cluster ToT map (a) and ToT horizontal profiles for the reference DUT (un-irradiated). . . . . 132
- 7.12 ToT distribution for thin sensors with 3 different irradiations and configurations: (a) W30 before irradiation, threshold of 1200e, ToT gain of 6ToT for 6000 electrons; (b) W80 irradiated at  $3 \times 10^{15}$  n<sub>eq</sub>/cm<sup>2</sup>, threshold of 1200e, ToT gain of 6ToT for 6000 electrons; (c) W80 irradiated at  $1 \times 10^{16}$  n<sub>eq</sub>/cm<sup>2</sup>, threshold of 1000e, ToT gain of 6ToT for 4000 electrons. The Mean true ToT value are reported below each plot. HDC refers to the HitDiscConfig register. 134
- 7.13 ToT distribution for thin un-irradiated sensor (blue) biased at 150 V and for thin irradiated at  $3 \times 10^{15}$  n<sub>eq</sub>/cm<sup>2</sup> sensors biased at 600 V (red). The fit consists in a Landau convoluted with a Gaussian. . . . . 135
- 7.14 Average ToT vs Fluence for two sets of tuning: Threshold = 1200 electrons, 6ToT at 6000 electrons (150V un-irradiated and 600V irradiated) and Threshold = 1 000 electrons, 6ToT at 4000 electrons (600V) . . . . . 136
- 7.15 ToT distribution (a) for W80 thin sensor irradiated at  $1 \times 10^{16}$  n<sub>eq</sub>/cm<sup>2</sup>. Five bias voltages between 400 V and 600V were considered (black 400 V, blue 450 V, green 500 V, orange 550 V, red 600 V), the threshold was set to 850 electrons. All the distribution are fitted by a gaussian convoluted with a landau and the MPV of the ToT distribution is extracted an reported in the bottom plot, uncertainties on the MPV are obtained by changing the fit range. 137

7.16	Average ToT distribution vs fluence for 3 different bias voltages. The horizontal/vertical bin label in the legend means that the fluence and average ToT have been extracted from an horizontal/vertical profile of the region of interest.	138
7.17	average ToT distribution vs fluence for 2 different threshold tunings. The horizontal/vertical bin label in the legend means that the fluence and average ToT have been extracted from an horizontal/vertical profile of the region of interest (Down or Up).	138
7.18	Charge to ToT calibration curves for three sets of tuning and threshold. Curves in black, red and magenta are obtained for the same tuning values (threshold of 1000 electrons and ToT calibration of 6 ToT corresponding to 4000 electrons). Dashed lines represents a $\pm 500e$ uncertainty.	139
7.19	Collected charge vs Fluence for two sets of tuning: Threshold=1200e, 6ToT at 6ke (150V, un-irradiated and 600V, irradiated) and Threshold=1000e, 6ToT at 4ke, 600V.	140
7.20	Charge collection efficiency extrapolation for two sets of tuning: Threshold=1200e, 6ToT at 6000e and Threshold=1000e, 6ToT at 4000e. Expected end-of-lifetime fluences for ITk are also indicated.	141
7.21	(a) CCE expected at the end of Run2 with current IBL sensors, compared to (b) charge collected efficiency obtained for 2 sets of fluence at the end of ITK lifetime for the second layer (red), and for the first layer (blue) at mid luminosity course, if production2-like sensors were considered. The lines are the result of a fit with Hecht formula.	143
7.22	Hit efficiency for thin irradiated sensors. The red triangles are for sensor irradiated at an average fluence of $1 \times 10^{16} \text{ n}_{eq}/\text{cm}^2$ and the blue ones at an average fluence of $3 \times 10^{15} \text{ n}_{eq}/\text{cm}^2$ . Threshold and gain are indicated in the upper box.	143
7.23	Hit efficiency for thin irradiated sensors. The blue triangles are for sensor irradiated at $1 \times 10^{16} \text{ n}_{eq}/\text{cm}^2$ and the red ones at $3 \times 10^{15} \text{ n}_{eq}/\text{cm}^2$ . The black square represents data for a thin un irradiated sensor. Threshold and gain are indicated in the box.	144
7.24	Edge efficiency profiles for LPNHE5 (no GRs - full markers) and LPNHE7 (2 GRs - open markers). Laboratory were the data were taken, device bias voltage and threshold are indicated too. The horizontal dashed line marks the 50%-point efficiency. The devices photograph on top helps in visualizing which physical area of the pixel is related to the efficiency profile.	146
7.25	Numerical simulation of the electric field. Left: 0 GRs; right: 2 GRs. The simulated bias voltage value was 40 V.	147
7.26	Comparison of edge efficiency profile of LPNHE7 for several bias voltages	148

7.27	Comparison of edge efficiency profile before and after irradiation of one sensor of the third production (M1.4). Data were taken at DESY . . . . .	149
7.28	Comparison of edge efficiency profile of irradiated M14 for three bias voltages (90 V, 100 V and 110 V). The two black dashed lines represents the 2 edge fences, the thin dark line at 20000 $\mu\text{m}$ represents the virtual limit of the last pixel. (a) presents results for a threshold of 1000 electrons and a ToT gain of 8 ToT for 4000 e;(b) presents results for a threshold of 1200 electrons and a ToT gain of 6 ToT for 6000 e . . . . .	151
7.29	Two dimensional edge efficiency profile for M1.4 at 40 V after irradiation (data taken at CERN-SPS). The white rectangles correspond to trench segments. .	152
7.30	Edge efficiency profiles intersecting respectively the first fence of edge (a) and the second one (b). . . . .	152
7.31	Graphical representation of the simulated 3D structure. The visible part of the mesh grid is superimposed. . . . .	153
7.32	Simulation in 3D of the electric field in the edge area for 50V (un-irradiated sensor). The pink color correspond to a null electric field. One can notice that the electric field is 0 in the trench. . . . .	153
7.33	Numerical simulation of the electric field (a, c and e) and of the Holes concentration (b, d and f). The a, b/c, d/e, f plots represent respectively the electric field or hole concentration at a depth of 10/65/120 $\mu\text{m}$ under the surface of the sensor. This simulation was obtained for a bias voltage of 50 V. . . . .	155
7.34	Numerical simulation of the electric field for different trenches in Y. The black curves intersects the innermost staggered trench whereas the red one intersects the outermost ring of trench. The left/right/bottom plots represents the electric field at a depth of 10/65/120 $\mu\text{m}$ under the surface of the sensor. .	156
7.35	In pixel efficiency presented in a half pixel cell for the three sensors. Results are presented for 3 different fluences when available. A scheme of the pixel is presented in the top part of the figure. . . . .	157
8.1	B-hadron decay, salient features. From [145]. . . . .	160
8.2	Extended (a) and Inclined (b) layouts. . . . .	164
8.3	Comparison of the light mis-tag rate vs $\eta$ (a) and vs $p_T$ (b) for two layout options. The Mv2c20 tagger is here considered. At the bottom the ratio of inclined over extended is presented. . . . .	165

8.4	Comparison of the c-jet mis-tag rate vs $\eta$ (a) and vs $p_T$ (b) for two layout options. The Mv2c20 tagger is here considered. At the bottom the ratio of inclined over extended is presented. . . . .	165
8.5	Distribution of two-track vertices (n2t) for b-jets and light flavour jets, with (plain lines) and without (dashed lines) the cleaning step . . . . .	168
8.6	Comparison of the transverse distance between the secondary vertex and the primary vertex associated with/without material rejection and vertex cleaning.	169
8.7	Light mis-tag rate vs $\eta$ (a) and $p_T$ (b) with (red markers) and without (black markers) vertex cleaning and material rejection. At the bottom, the ratio of light mis-tag rate with over without material rejection and vertex cleaning is reported. . . . .	169
8.8	Comparison of the secondary vertex mass distribution (a,b), number of two tracks vertices (c,d), energy fraction (e,f), vs $\eta$ (a, c, e) or $p_T$ (b, d, f). Three tracks selection criteria are considered: SiHitsCuts = 7 and $p_TCuts$ = 700 MeV; SiHitsCuts = 9 and $p_TCuts$ = 900 MeV; SiHitsCuts = 11 ; $p_TCuts$ = 1100 MeV . . . . .	172
8.9	Comparison of number of two tracks vertices candidates (a)/ number of tracks per secondary vertex (b) for various tracking cuts scenari ( SiHitsCuts = 7 and $p_TCuts$ = 700 MeV; SiHitsCuts = 9 and $p_TCuts$ = 900 MeV; SiHitsCuts = 11 ; $p_TCuts$ = 1100 MeV). . . . .	173
8.10	Secondary vertex reconstruction rate for b-jets(a), c-jets (b) and light flavour jets (c). Three tracks selection criteria are considered: SiHitsCuts = 7 and $p_TCuts$ = 700 MeV; SiHitsCuts = 9 and $p_TCuts$ = 900 MeV; SiHitsCuts = 11 ; $p_TCuts$ = 1100 MeV. The top/bottom ratio plots represents respectively the ratio of the (9,900)/(11,1100) configurations with the (7,700) one. . . . .	174
8.11	Light mistag rate for various tracking cuts tested: SiHitsCuts = 7 and $p_TCuts$ = 700 MeV; SiHitsCuts = 9 and $p_TCuts$ = 900 MeV; SiHitsCuts = 11 and $p_TCuts$ = 1100 MeV. In the ratio plot, the red markers represents the ratio of the config (11,1100) with respect to the (7,700) configuration. . . . .	175
8.12	Light jet rejection vs b-jet efficiency. Various cuts on $p_T$ (PtCuts) and Silicon hits cuts (SiCuts, including the pixel hits and the SCT hits) have been investigated. The black/blue/red curves shows performance for the following couples of SiCuts and PtCuts: 7&700 , 9&900 and 11&1100. In the ratio plot, the blue/red curve represents the ratio of the config (11,1100)/(9,900) with respect to the (7,700) configuration. . . . .	175
8.13	Light-flavour jet mis-tag rate vs jet $p_T$ for MV taggers for the intermediate ITK layout using $Z'$ samples of masses ranging from 1 TeV to 5 TeV and $t\bar{t}$ samples. (b) presents a zoom on the $p_T$ region around 300 GeV. . . . .	177

A.1	Graphical representation of the simulated 3D structure. The visible part of the mesh grid is superimposed. . . . .	183
A.2	Graphical representation of the doping regions of the simulated 3D structure. The picture correspond to a region at depth $Z=0.2 \mu\text{m}$ . . . . .	184
B.1	Efficacité de collection Charge pour les quatre couche du détecteur à pixel d'ATLAS, seul les modules centraux sont considérés. Les variations en termes de fluence et de tension de polarisation sont aussi indiquées. . . . .	190
B.2	Détails d'un pixel des trois productions. . . . .	192
B.3	Efficacité de collection de charge extrapolée pour deux configurations différentes. Chaque distribution a été extrapolée avec une fonction de Hecht. . .	193
B.4	Efficacité en bordure du capteur pour LPNHE5 (pas de GRs - marqueurs pleins) et LPNHE7 (2 GRs - marqueurs ouverts) . . . . .	195
B.5	Comparaison de l'efficacité de reconstruction en bordure du capteur avant et après irradiation. . . . .	196
B.6	Efficacité intra-pixellaire présentée à l'intérieur d'une demi cellule pour trois capteurs issus des trois productions testées. Trois fluences différentes ont été considérée. Un schéma du pixel est proposée dans la partie haute de la figure.	197
B.7	Taux de Light jets faussement étiqueté comme des jets de b en fonction de $\eta$ (a) and $p_T$ (b) avec (marqueurs rouges) et sans (marqueurs noirs) suppression de vertex secondaire correspondant à des couches du détecteur. . . . .	199
B.8	Taux de Light jets faussement étiqueté comme des jets de b en fonction de $\eta$ (a) and $p_T$ (b) pour plusieurs critères de sélection . . . . .	199
B.9	Taux de rejet des light jets en fonction de l'efficacité de reconstruction de b-jets.	200



# Bibliography

- [1] Morad Aaboud et al. Observation of Higgs boson production in association with a top quark pair at the LHC with the ATLAS detector. 2018. URL <https://cds.cern.ch/record/2621167>.
- [2] ATLAS Collaboration. Observation of  $H \rightarrow b\bar{b}$  with the ATLAS detector. Technical Report ATLAS-COM-CONF-2018-039, CERN, Geneva, Jul 2018. URL <https://cds.cern.ch/record/2628337>.
- [3] Gaston Bachelard. *La formation de l'esprit scientifique*. Paris: Librairie philosophique J. Vrin, 5e édition, 1967. Collection: Bibliothèque des textes philosophiques., 1934.
- [4] CERN. URL <https://home.cern/fr>.
- [5] Oliver Brüning, Paul Collier, P Lebrun, Stephen Myers, Ranko Ostojic, John Poole, and Paul Proudlock. *LHC Design Report*. CERN Yellow Reports: Monographs. CERN, Geneva, 2004. URL <https://cds.cern.ch/record/782076>.
- [6] ATLAS Collaboration. The ATLAS Experiment at the CERN Large Hadron Collider. *Journal of Instrumentation*, 3(08):S08003, 2008. doi: 10.1088/1748-0221/3/08/S08003. URL <http://stacks.iop.org/1748-0221/3/i=08/a=S08003>.
- [7] A.Pich. The Standard Model of Electroweak Interactions. *arXiv:1201.0537v1*, 2012, IFIC, University of Valencia, Spain.
- [8] Heather E Logan. TASI 2013 lectures on Higgs physics within and beyond the Standard Model. *arXiv:1406.1786*, 2014.
- [9] S. L. Glashow. Partial Symmetries of Weak Interactions. *Nucl. Phys.*, 22:579–588, 1961. doi: 10.1016/0029-5582(61)90469-2.
- [10] Steven Weinberg. A model of leptons. *Phys. Rev. Lett.*, 19:1264–1266, Nov 1967. doi: 10.1103/PhysRevLett.19.1264. URL <https://link.aps.org/doi/10.1103/PhysRevLett.19.1264>.
- [11] Abdus Salam. Weak and Electromagnetic Interactions. *Conf. Proc.*, C680519:367–377, 1968.
- [12] Hideki Yukawa. On the interaction of elementary particles. i. *Proceedings of the Physico-Mathematical Society of Japan. 3rd Series*, 17:48–57, 1935.

- [13] Nicola Cabibbo. Unitary symmetry and leptonic decays. *Phys. Rev. Lett.*, 10:531–533, Jun 1963. doi: [10.1103/PhysRevLett.10.531](https://doi.org/10.1103/PhysRevLett.10.531). URL <https://link.aps.org/doi/10.1103/PhysRevLett.10.531>.
- [14] Makoto Kobayashi and Toshihide Maskawa. CP Violation in the Renormalizable Theory of Weak Interaction. *Prog. Theor. Phys.*, 49:652–657, 1973. doi: [10.1143/PTP.49.652](https://doi.org/10.1143/PTP.49.652).
- [15] C. Patrignani et al. Review of Particle Physics. *Chin. Phys.*, C40(10):100001, 2016. doi: [10.1088/1674-1137/40/10/100001](https://doi.org/10.1088/1674-1137/40/10/100001).
- [16] R et al Aaij. Amplitude analysis of  $B^+ \rightarrow j/\psi \phi K^+$  decays. *Phys. Rev. D*, 95:012002, Jan 2017. doi: [10.1103/PhysRevD.95.012002](https://doi.org/10.1103/PhysRevD.95.012002). URL <https://link.aps.org/doi/10.1103/PhysRevD.95.012002>.
- [17] R. et al Aaij. Observation of  $j/\psi \phi$  structures consistent with exotic states from amplitude analysis of  $B^+ \rightarrow j/\psi \phi K^+$  decays. *Phys. Rev. Lett.*, 118:022003, Jan 2017. doi: [10.1103/PhysRevLett.118.022003](https://doi.org/10.1103/PhysRevLett.118.022003). URL <https://link.aps.org/doi/10.1103/PhysRevLett.118.022003>.
- [18] The LHCb Collaboration. Observation of five new narrow  $\Omega_c^0$  states decaying to  $\Xi_c^+ K^-$ . *Phys. Rev. Lett.*, 118:182001, May 2017. doi: [10.1103/PhysRevLett.118.182001](https://doi.org/10.1103/PhysRevLett.118.182001). URL <https://link.aps.org/doi/10.1103/PhysRevLett.118.182001>.
- [19] *LHCb experiment*, . URL <https://lhcb.cern.ch/>.
- [20] ATLAS Collaboration. Observation of a new particle in the search for the Standard Model Higgs boson with the ATLAS detector at the LHC. *Physics Letters B*, 716(1): 1 – 29, 2012. ISSN 0370-2693. doi: <https://doi.org/10.1016/j.physletb.2012.08.020>. URL <http://www.sciencedirect.com/science/article/pii/S037026931200857X>.
- [21] the CMS Collaboration. Observation of a new boson at a mass of 125 GeV with the CMS experiment at the LHC. *Physics Letters B*, 716(1):30–61, sep 2012. doi: [10.1016/j.physletb.2012.08.021](https://doi.org/10.1016/j.physletb.2012.08.021). URL <https://doi.org/10.1016/j.physletb.2012.08.021>.
- [22] LHC Higgs cross sections working group, . URL <https://twiki.cern.ch/twiki/bin/view/LHCPhysics/LHCHXSWG#Documentation>.
- [23] D. de Florian et al. Handbook of LHC Higgs Cross Sections: 4. Deciphering the Nature of the Higgs Sector. 2016. doi: [10.23731/CYRM-2017-002](https://doi.org/10.23731/CYRM-2017-002).
- [24] W. James Stirling. Progress in Parton Distribution Functions and implications for LHC. In *Proceedings, 38th International Symposium on Multiparticle Dynamics (ISMD 2008): Hamburg, Germany, September 15-20, 2008*, pages 46–55, 2009. doi: [10.3204/DESY-PROC-2009-01/41](https://doi.org/10.3204/DESY-PROC-2009-01/41), [10.3360/dis.2008.4](https://doi.org/10.3360/dis.2008.4). URL <https://inspirehep.net/record/805147/files/arXiv:0812.2341.pdf>. [46(2008)].
- [25] *AEGIS experiment*. URL <https://aegis.web.cern.ch/aegis/>.
- [26] *ISOLDE experiment*. URL <http://isolde.web.cern.ch/>.

- 
- [27] *LHC closer*. URL [https://www.lhc-closer.es/taking\\_a\\_closer\\_look\\_at\\_lhc/0.lhc\\_running](https://www.lhc-closer.es/taking_a_closer_look_at_lhc/0.lhc_running).
- [28] Julie Haffner. The CERN accelerator complex. Complexe des accélérateurs du CERN. Oct 2013. URL <https://cds.cern.ch/record/1621894>. General Photo.
- [29] *CMS experiment*. URL <https://cms.web.cern.ch/>.
- [30] *ALICE experiment*. URL <https://home.cern/fr/about/experiments/alice>.
- [31] URL <https://project-hl-lhc-industry.web.cern.ch/content/project-schedule>.
- [32] Stefan Maettig, J Haller, and T Pauly. Luminosity Measurements with the ATLAS Detector, Jun 2012. URL <https://cds.cern.ch/record/1513982>. Presented 06 Aug 2012.
- [33] The ATLAS Collaboration. Luminosity Public Results Run2, . URL [https://twiki.cern.ch/twiki/bin/view/AtlasPublic/LuminosityPublicResultsRun2#Luminosity\\_summary\\_plots\\_for\\_201](https://twiki.cern.ch/twiki/bin/view/AtlasPublic/LuminosityPublicResultsRun2#Luminosity_summary_plots_for_201).
- [34] The ATLAS Collaboration. Summary plots from the ATLAS Standard Model physics group , . URL <https://atlas.web.cern.ch/Atlas/GROUPS/PHYSICS/CombinedSummaryPlots/SM/>.
- [35] The ATLAS collaboration. Evidence for the  $H \rightarrow b\bar{b}$  decay with the ATLAS detector. *JHEP*, 12:024, 2017. doi: [10.1007/JHEP12\(2017\)024](https://doi.org/10.1007/JHEP12(2017)024).
- [36] Measurement of the Higgs boson mass in the  $H \rightarrow ZZ^* \rightarrow 4\ell$  and  $H \rightarrow \gamma\gamma$  channels with  $\sqrt{s}=13\text{TeV}$   $pp$  collisions using the ATLAS detector. Technical Report ATLAS-CONF-2017-046, CERN, Geneva, Jul 2017. URL <http://cds.cern.ch/record/2273853>.
- [37] The ATLAS TDAQ Collaboration. The atlas data acquisition and high level trigger system. *Journal of Instrumentation*, 11(06):P06008, 2016. URL <http://stacks.iop.org/1748-0221/11/i=06/a=P06008>.
- [38] ATLAS Collaboration. Atlas magnet system: Technical design report. *1. Tech. rep. CERN- LHCC-97-18.*, 1997. URL <https://cds.cern.ch/record/338080>.
- [39] Douglas Schaefer. The ATLAS Diamond Beam Monitor: luminosity Detector on the LHC. Technical Report ATL-INDET-PROC-2015-009, CERN, Geneva, Jul 2015. URL <https://cds.cern.ch/record/2034225>.
- [40] Peter Jenni, Marzio Nessi, and Markus Nordberg. Zero Degree Calorimeters for ATLAS. Technical Report LHCC-I-016. CERN-LHCC-2007-001, CERN, Geneva, Jan 2007. URL <http://cds.cern.ch/record/1009649>.
- [41] L Fabbri. Forward Detectors in ATLAS: ALFA, ZDC and LUCID. Apr 2009. URL <https://cds.cern.ch/record/1172844>. DIS09. Start date 26/04/2009.
- [42] G. Aad, M. Ackers, F.A. Alberti, M. Aleppo, G. Alimonti, et al. ATLAS pixel detector electronics and sensors. *JINST*, 3:P07007, 2008. doi: [10.1088/1748-0221/3/07/P07007](https://doi.org/10.1088/1748-0221/3/07/P07007).

- [43] The ATLAS Collaboration. ATLAS insertable b-layer technical design report. Technical report, CERN, 2010. URL <http://cdsweb.cern.ch/record/1291633/files/ATLAS-TDR-019.pdf>.
- [44] Abbott, B. and others. Production and Integration of the ATLAS Insertable B-Layer. *JINST*, 13(05):T05008, 2018. doi: [10.1088/1748-0221/13/05/T05008](https://doi.org/10.1088/1748-0221/13/05/T05008).
- [45] Sherwood I. Parker, Christopher J. Kenney, and Julie Segal. 3-D: A New architecture for solid state radiation detectors. *Nucl. Instrum. Meth.*, A395:328–343, 1997. doi: [10.1016/S0168-9002\(97\)00694-3](https://doi.org/10.1016/S0168-9002(97)00694-3).
- [46] M. Garcia-Sciveres et al. The FE-I4 pixel readout integrated circuit. *Nucl. Instrum. Meth.*, A636:S155–S159, 2011. doi: [10.1016/j.nima.2010.04.101](https://doi.org/10.1016/j.nima.2010.04.101).
- [47] I. Peric et al. *Nucl. Instr. and Meth. A*, 565(1):178 – 187, 2006.
- [48] Georges Aad et al. Operation and performance of the ATLAS semiconductor tracker. *JINST*, 9:P08009, 2014. doi: [10.1088/1748-0221/9/08/P08009](https://doi.org/10.1088/1748-0221/9/08/P08009).
- [49] E. Abat et al. The ATLAS Transition Radiation Tracker (TRT) proportional drift tube: Design and performance. *JINST*, 3:P02013, 2008. doi: [10.1088/1748-0221/3/02/P02013](https://doi.org/10.1088/1748-0221/3/02/P02013).
- [50] *ATLAS liquid-argon calorimeter: Technical Design Report*. Technical Design Report ATLAS. CERN, Geneva, 1996. URL <http://cds.cern.ch/record/331061>.
- [51] G. Aad et al. Expected Performance of the ATLAS Experiment - Detector, Trigger and Physics. 2009.
- [52] *ATLAS tile calorimeter: Technical Design Report*. Technical Design Report ATLAS. CERN, Geneva, 1996. URL <https://cds.cern.ch/record/331062>.
- [53] *ATLAS muon spectrometer: Technical Design Report*. Technical Design Report ATLAS. CERN, Geneva, 1997. URL <https://cds.cern.ch/record/331068>.
- [54] The ATLAS Collaboration. Performance of the ATLAS Trigger System in 2015. Performance of the ATLAS Trigger System in 2015. *Eur. Phys. J. C*, 77 (CERN-EP-2016-241. 5):317. 76 p, Nov 2016. URL <https://cds.cern.ch/record/2235584>. 77 pages in total, author list starting page 61, 50 figures, 1 table. Published in *Eur. Phys. J. C*. All figures including auxiliary figures are available at <http://atlas.web.cern.ch/Atlas/GROUPS/PHYSICS/PAPERS/TRIG-2016-01/>.
- [55] M Shochet, L Tompkins, V Cavaliere, P Giannetti, A Annovi, and G Volpi. Fast TracKer (FTK) Technical Design Report. Technical Report CERN-LHCC-2013-007. ATLAS-TDR-021, Jun 2013. URL <https://cds.cern.ch/record/1552953>. ATLAS Fast Tracker Technical Design Report.
- [56] Markus Elsing. Tracking at the LHC. page lectures given at the university of Friburg, 2016.

- 
- [57] ATLAS Collaboration. Performance of the atlas track reconstruction algorithms in dense environments in lhcb run 2. *The European Physical Journal C*, 77(10):673, Oct 2017. ISSN 1434-6052. doi: [10.1140/epjc/s10052-017-5225-7](https://doi.org/10.1140/epjc/s10052-017-5225-7). URL <https://doi.org/10.1140/epjc/s10052-017-5225-7>.
- [58] Shingo Kazama. *Object Reconstruction*, pages 55–69. Springer Japan, Tokyo, 2016. ISBN 978-4-431-55657-2. doi: [10.1007/978-4-431-55657-2\\_5](https://doi.org/10.1007/978-4-431-55657-2_5). URL [https://doi.org/10.1007/978-4-431-55657-2\\_5](https://doi.org/10.1007/978-4-431-55657-2_5).
- [59] Maurice Garcia-Sciveres and Norbert Wermes. A review of advances in pixel detectors for experiments with high rate and radiation. *Reports on Progress in Physics*, 81(6):066101, 2018. URL <http://stacks.iop.org/0034-4885/81/i=6/a=066101>.
- [60] Track Reconstruction Performance of the ATLAS Inner Detector at  $\sqrt{s} = 13$  TeV. Technical Report ATL-PHYS-PUB-2015-018, CERN, Geneva, Jul 2015. URL <http://cds.cern.ch/record/2037683>.
- [61] Improved electron reconstruction in ATLAS using the Gaussian Sum Filter-based model for bremsstrahlung. Technical Report ATLAS-CONF-2012-047, CERN, Geneva, May 2012. URL <https://cds.cern.ch/record/1449796>.
- [62] G Borissov, D Casper, K Grimm, S Pagan Griso, L Egholm Pedersen, K Prokofiev, M Rudolph, and A Wharton. Atlas strategy for primary vertex reconstruction during run-2 of the lhcb. *Journal of Physics: Conference Series*, 664(7):072041, 2015. URL <http://stacks.iop.org/1742-6596/664/i=7/a=072041>.
- [63] ATLAS Collaboration. Performance of b-jet identification in the atlas experiment. *Journal of Instrumentation*, 11(04):P04008, 2016. URL <http://stacks.iop.org/1748-0221/11/i=04/a=P04008>.
- [64] ATLAS Collaboration. Measurement of the  $\Lambda_b^0$  lifetime and mass in the atlas experiment. *Phys. Rev. D*, 87:032002, Feb 2013. doi: [10.1103/PhysRevD.87.032002](https://doi.org/10.1103/PhysRevD.87.032002). URL <https://link.aps.org/doi/10.1103/PhysRevD.87.032002>.
- [65] *Pythia*. URL [home.thep.lu.se/Pythia/](http://home.thep.lu.se/Pythia/).
- [66] GEANT4 Collaboration. GEANT4: A Simulation toolkit. *Nucl. Instrum. Meth.*, A506:250–303, 2003. doi: [10.1016/S0168-9002\(03\)01368-8](https://doi.org/10.1016/S0168-9002(03)01368-8).
- [67] *ROOT Data Analysis Framework*, <https://root.cern.ch/>. URL <https://root.cern.ch/>.
- [68] L. Rossi, P. Fischer, T. Rohe, and N. Wermes. *Pixel detectors: From fundamentals to applications*. Springer Science & Business Media, 2006. doi: <https://doi.org/10.1007/3-540-28333-1>.
- [69] Gerhard Lutz. *Semiconductor Radiation Detectors*. Springer Berlin Heidelberg, 2007. doi: [10.1007/978-3-540-71679-2](https://doi.org/10.1007/978-3-540-71679-2). URL <https://doi.org/10.1007/978-3-540-71679-2>.

- [70] M. Krammer. Silicon detectors, 2010-11. URL [http://www.hephy.at/fileadmin/user\\_upload/Lehre/Unterlagen/Praktikum/Halbleiterdetektoren.pdf](http://www.hephy.at/fileadmin/user_upload/Lehre/Unterlagen/Praktikum/Halbleiterdetektoren.pdf).
- [71] L. Landau. On the energy loss of fast particles by ionization. *J. Phys.(USSR)*, 8: 201–205, 1944.
- [72] S. Terzo. *Development of radiation hard pixel modules employing planar n-in-p silicon sensors with active edges for the ATLAS detector at HL-LHC*. PhD thesis, Technische Universitat Munchen, Max-Planck-Institut fur Physik, 2015. URL <https://sterzo.web.cern.ch/>.
- [73] Hans Bichsel. Straggling in thin silicon detectors. *Rev. Mod. Phys.*, 60:663–699, Jul 1988. doi: 10.1103/RevModPhys.60.663. URL <https://link.aps.org/doi/10.1103/RevModPhys.60.663>.
- [74] S Meroli, D Passeri, and L Servoli. Energy loss measurement for charged particles in very thin silicon layers. *Journal of Instrumentation*, 6(06):P06013, 2011. URL <http://stacks.iop.org/1748-0221/6/i=06/a=P06013>.
- [75] P. Shulek et al. Fluctuations of ionization loss. *Sov. J. Nucl. Phys.* 4 (1967) 400.
- [76] The ATLAS Collaboration. Cluster Properties and Lorentz Angle Measurement in the 4-Layer Pixel Detector Using Cosmic Rays. Technical Report ATL-PHYS-PUB-2015-012, CERN, Geneva, Jun 2015. URL <http://cds.cern.ch/record/2020918>.
- [77] S. Ramo. Currents induced by electron motion. *Proceedings of the IRE* 27 (1939) 584.
- [78] I. Kipnis et al. A time-over-threshold machine: the readout integrated circuit for the babar silicon vertex tracker. *IEEE Transactions on Nuclear Science* 44 (1997) 289.
- [79] G Lindström, S Watts, and F Lemeilleur. 3rd RD48 status report: the ROSE collaboration (R&D on silicon for future experiments), Dec 1999. URL <https://cds.cern.ch/record/421210>.
- [80] J. Lange, G. Giannini, S. Grinstein, M. Manna, G. Pellegrini, D. Quirion, S. Terzo, and D. Vázquez Furelos. Radiation hardness of small-pitch 3d pixel sensors up to a fluence of  $3 \times 10^{16}$  n eq /cm<sup>2</sup>. *Journal of Instrumentation*, 13(09):P09009, 2018. URL <http://stacks.iop.org/1748-0221/13/i=09/a=P09009>.
- [81] M. Bomben, A. Ducourthial, A. Bagolini, M. Boscardin, L. Bosisio, G. Calderini, L. D’Eramo, G. Giacomini, G. Marchiori, N. Zorzi, A. Rummler, and J. Weingarten. Performance of active edge pixel sensors. *Journal of Instrumentation*, 12(05):P05006, 2017. URL <http://stacks.iop.org/1748-0221/12/i=05/a=P05006>.
- [82] M. Bruzzi and M. Moll. Technical report, CERN, 2007. URL <http://cdsweb.cern.ch/record/1082083/files/RD50statusreport.pdf>. RD50 status report.
- [83] Ioana Pintilie On behalf of the RD50 Collaboration. Experimental techniques for defect characterization of highly irradiated materials and structures. *PoS(Vertex 2016)033*, The 25th International workshop on vertex detectors September 26-30, 2016, La Biodola, Isola d’Elba, ITALY.



- 
- [84] A.Vasilescu (INPE Bucharest) and G.Lindstroem (University of Hamburg). Displacement damage in Silicon online compilation. 2000. URL <http://sesam.desy.de/members/gunnar/Sidfuncs.html>.
- [85] M. Moll. *Radiation Damage in Silicon Particle Detectors*. PhD thesis, Hamburg, 1999. URL <https://mmoll.web.cern.ch/mmoll/thesis/>.
- [86] G Kramberger, V Cindro, I Mandic, M Mikuz, and M Zavrtanik. Effective trapping time of electrons and holes in different silicon materials irradiated with neutrons, protons and pions. Technical Report ATL-INDET-2002-006, CERN, Geneva, Jan 2001. URL <https://cds.cern.ch/record/684161>.
- [87] C. Abellan Beteta, M. Atzeni, V. Battista, A. Bursche, B. Dey, A. Dosil Suarez, C. El-sasser, A. Fernandez Prieto, J. Fu, E. Graverini, I. Komarov, E. Lemos Cid, F. Lionetto, A. Mauri, A. Merli, P.R. Pais, E. Perez Trigo, M. del Pilar Peco Regales, P. Stefko, O. Steinkamp, B. Storaci, and M. Tobin. Monitoring radiation damage in the LHCb Tracker Turicensis. Technical Report arXiv:1809.05063, Sep 2018. URL <https://cds.cern.ch/record/2638494>. \* Temporary entry \*.
- [88] Radiation effects at the LHC experiments and impact on operation and performance. URL <https://indico.cern.ch/event/695271/overview>.
- [89] Mathieu Benoit, Marco Bomben, Rebecca Carney, Gilberto Giugliarelli, Tommaso Lari, Lingxin Meng, Benjamin Philip Nachman, Lorenzo Rossini, Veronica Wallangen, Julien-christopher Beyer, Audrey Ducourthial, Anna Macchiolo, Javier Llorente Merino, Paul Miyagawa, Ian Dawson, Nick Dann, and Cinzia Da Via. Modeling Radiation Damage Effects for Pixel Sensors in the ATLAS Detector. Technical Report ATL-COM-INDET-2017-011, CERN, Geneva, Mar 2017. URL <https://cds.cern.ch/record/2255825>.
- [90] A. Ducourthial. Modeling radiation damage to pixel sensors in the atlas detector. *Journal of Instrumentation*, 13(03):C03046, 2018. URL <http://stacks.iop.org/1748-0221/13/i=03/a=C03046>.
- [91] A Ferrari, Paola R Sala, A Fassò, and Johannes Ranft. *FLUKA: A multi-particle transport code (program version 2005)*. CERN, Geneva, 2005. URL <https://cds.cern.ch/record/898301>.
- [92] Giuseppe Battistoni, S. Muraro, Paola R. Sala, Fabio Cerutti, A. Ferrari, Stefan Roesler, A. Fasso, and J. Ranft. The FLUKA code: Description and benchmarking. *AIP Conf. Proc.*, 896:31–49, 2007. doi: 10.1063/1.2720455. [,31(2007)].
- [93] Radiation background simulations for run2. URL [https://twiki.cern.ch/twiki/bin/viewauth/Atlas/RadiationBackgroundSimulationsRun2#13\\_TeV\\_simulations\\_corresponding](https://twiki.cern.ch/twiki/bin/viewauth/Atlas/RadiationBackgroundSimulationsRun2#13_TeV_simulations_corresponding).
- [94] Torbjorn Sjöstrand, Stephen Mrenna, and Peter Z. Skands. PYTHIA 6.4 Physics and Manual. *JHEP*, 05:026, 2006. doi: 10.1088/1126-6708/2006/05/026.

- [95] Summary of ATLAS Pythia 8 tunes, 2012. URL <https://cds.cern.ch/record/1474107>.
- [96] Torbjorn Sjöstrand, Stefan Ask, Jesper R. Christiansson, Richard Corke, Nishita Desai, Philip Ilten, Stephen Mrenna, Stefan Prestel, Christine O. Rasmussen, and Peter Z. Skands. An Introduction to PYTHIA 8.2. *Comput. Phys. Commun.*, 191:159, 2015. doi: [10.1016/j.cpc.2015.01.024](https://doi.org/10.1016/j.cpc.2015.01.024).
- [97] *Silvaco International Inc.*, 4701 Patrick Henry Drive, Bldg 2 Santa Clara, CA 95054. URL <http://www.silvaco.com/>.
- [98] Synopsys, Mountain View, California (USA). URL <http://synopsys.com>.
- [99] F. Moscatelli, D. Passeri, A. Morozzi, R. Mendicino, G. F. Dalla Betta, and G. M. Bilei. Combined bulk and surface radiation damage effects at very high fluences in silicon detectors: Measurements and tcad simulations. *IEEE Transactions on Nuclear Science*, 63(5):2716–2723, 2016. ISSN 0018-9499. doi: [10.1109/TNS.2016.2599560](https://doi.org/10.1109/TNS.2016.2599560).
- [100] V Chiochia et al. A double junction model of irradiated silicon pixel sensors for lhc. *Nucl. Instr. and Meth. A*, 568(1):51 – 55, 2006. ISSN 0168-9002. doi: [10.1016/j.nima.2006.05.199](https://doi.org/10.1016/j.nima.2006.05.199). New Developments in Radiation Detectors.
- [101] John Idarraga and Mathieu Benoit. Generic Geant4 implementation for pixel detectors. *The AllPix Simulation Framework*, page [twiki.cern.ch:AllPix], 2006.
- [102] Athena software. URL <https://atlassoftwaredocs.web.cern.ch/athena/>.
- [103] ATLAS Collaboration. A neural network clustering algorithm for the atlas silicon pixel detector. *Journal of Instrumentation*, 9(09):P09009, 2014. doi: [10.1088/1748-0221/9/09/P09009](https://doi.org/10.1088/1748-0221/9/09/P09009). URL <http://stacks.iop.org/1748-0221/9/i=09/a=P09009>.
- [104] HL-LHC Project. URL <http://hilumilhc.web.cern.ch/about/hl-lhc-project>.
- [105] S. McMahon, P. Allport, H. Hayward, and B. Di Girolamo. Initial Design Report of the ITk: Initial Design Report of the ITk. Technical Report ATL-COM-UPGRADE-2014-029, CERN, Geneva, Oct 2014. URL <https://cds.cern.ch/record/1952548>.
- [106] ATLAS Collaboration. *Technical Design Report for the ATLAS ITk Strip Detector*. Number ATL-COM-UPGRADE-2017-006. Geneva, Mar 2017. URL <https://cds.cern.ch/record/2256817>.
- [107] ATLAS Collaboration. Technical Design Report for the ATLAS ITk Pixel Detector. Technical Report ATL-COM-ITK-2018-019, CERN, Geneva, Mar 2018. URL <https://cds.cern.ch/record/2310230>.
- [108] S. McMahon, P. Allport, H. Hayward, and B. Di Girolamo. Initial Design Report of the ITk: Initial Design Report of the ITk. Technical Report ATL-COM-UPGRADE-2014-029, CERN, Geneva, Oct 2014. URL <https://cds.cern.ch/record/1952548>.
- [109] Collaboration ATLAS. Letter of Intent for the Phase-II Upgrade of the ATLAS Experiment. Technical Report CERN-LHCC-2012-022. LHCC-I-023, CERN, Geneva, Dec 2012. URL <https://cds.cern.ch/record/1502664>. Draft version for comments.



- 
- [110] ATLAS Collaboration. Technical Proposal: A High-Granularity Timing Detector for the ATLAS Phase-II Upgrade. Technical Report ATL-COM-LARG-2018-008, CERN, Geneva, Mar 2018. URL <https://cds.cern.ch/record/2310228>. Draft of Technical Proposal for circulation to ATLAS.
- [111] Maurice Garcia-Sciveres. The RD53A Integrated Circuit. Technical Report CERN-RD53-PUB-17-001, CERN, Geneva, Oct 2017. URL <https://cds.cern.ch/record/2287593>.
- [112] Advacam. URL <http://advacam.com>.
- [113] CNM. URL <http://www.imb-cnm.csic.es/index.php/en/projects>.
- [114] FBK. URL <https://www.fbk.eu/en/>.
- [115] Sintef. URL <https://www.sintef.no/en/silicon-radiation-sensors/>.
- [116] VTT. URL <https://www.vttmemsfab.fi/technology-applications/silicon-detectors/>.
- [117] J Alison. Experimental Studies of hh. Oct 2014. URL <http://cds.cern.ch/record/1952581>.
- [118] M Bomben, A Bagolini, M Boscardin, L Bosisio, G Calderini, J Chauveau, G Giacomini, A La Rosa, G Marchiori, and N Zorzi. Electrical characterization of thin edgeless n-on-p planar pixel sensors for atlas upgrades. *Journal of Instrumentation*, 9 (05):C05020, 2014. URL <http://stacks.iop.org/1748-0221/9/i=05/a=C05020>.
- [119] M. Bomben et al. Development of Edgeless n-on-p Planar Pixel Sensors for future ATLAS Upgrades. *Nucl. Instr. and Meth. A*, 712:41–47, 2013.
- [120] E. Vianello et al. Optimization of double-side 3d detector technology for first productions at FBK. In *Nuclear Science Symposium and Medical Imaging Conference (NSS/MIC), 2011 IEEE*, pages 523–528, 2011.
- [121] G.-F. Dalla Betta, M. Boscardin, M. Bomben, M. Brianzi, G. Calderini, G. Darbo, R. Dell’Orso, A. Gaudiello, G. Giacomini, R. Mendicino, M. Meschini, A. Messineo, S. Ronchin, D.M.S. Sultan, and N. Zorzi. The infn-fbk “phase-2” r&d program. *Nucl. Instr. and Meth. A*, 824:388 – 391, 2016. ISSN 0168-9002. doi: [10.1016/j.nima.2015.08.074](https://doi.org/10.1016/j.nima.2015.08.074). Frontier Detectors for Frontier Physics: Proceedings of the 13th Pisa Meeting on Advanced Detectors.
- [122] H. Chr. Kastli, M. Barbero, W. Erdmann, Ch. Hormann, R. Horisberger, D. Kotlinski, and B. Meier. Design and performance of the CMS pixel detector readout chip. *Nucl. Instrum. Meth.*, A565:188–194, 2006. doi: [10.1016/j.nima.2006.05.038](https://doi.org/10.1016/j.nima.2006.05.038).
- [123] H Spieler. Semiconductor detector systems. pages 1–512, 01 2007.
- [124] MPG ATLAS group private communications.

- [125] A Chilingarov. Temperature dependence of the current generated in si bulk. *Journal of Instrumentation*, 8(10):P10003–P10003, oct 2013. doi: [10.1088/1748-0221/8/10/p10003](https://doi.org/10.1088/1748-0221/8/10/p10003). URL <https://doi.org/10.1088/1748-0221/8/10/p10003>.
- [126] Natascha Savic, J. Beyer, A. Macchiolo, and R. Nisius. Investigation of thin n-in-p planar pixel modules for the ATLAS upgrade. *JINST*, 11(12):C12008, 2016. doi: [10.1088/1748-0221/11/12/C12008](https://doi.org/10.1088/1748-0221/11/12/C12008).
- [127] S. Ronchin et al. Edgeless planar pixel sensors with atlas and cms designs produced by fbk-cmm, 2017. URL <https://indico.cern.ch/event/587631/contributions/2471721/>. 12th Trento Workshop on Advanced Silicon Radiation Detectors.
- [128] Irradiation Center Karlsruhe. URL [https://www.etp.kit.edu/english/irradiation\\_center.php](https://www.etp.kit.edu/english/irradiation_center.php).
- [129] The FE-I4B Collaboration. The FE-I4B Integrated Circuit Guide. 2012.
- [130] H. Jansen, S. Spannagel, et al. Performance of the EUDET-type beam telescopes. *EPJ Techniques and Instrumentation*, 3(1):7, 2016. ISSN 2195-7045. doi: [10.1140/epjti/s40485-016-0033-2](https://doi.org/10.1140/epjti/s40485-016-0033-2). URL <http://dx.doi.org/10.1140/epjti/s40485-016-0033-2>.
- [131] A. Gerbershagen on behalf of CERN Experimental Areas Group. Overview over cern sps test beams. In *6th beam telescope and test beam workshop*, 2018, Zurich.
- [132] Ralf Diener, Norbert Meyners, and Marcel Stanitzki. The DESY II Test Beam Facility – Status and Future. 6th Beam Telescopes and Test Beam Workshop 2018, Zürich (Switzerland), 16 Jan 2018 - 19 Jan 2018, Jan 2018. doi: [10.3204/PUBDB-2018-01077](https://doi.org/10.3204/PUBDB-2018-01077). URL <http://bib-pubdb1.desy.de/record/400024>.
- [133] R. L. Gluckstern. Effect of multiple scattering on measurement of track momentum and direction. *Nuclear Instruments and Methods*, 56:145–147, January 1967. doi: [10.1016/0029-554X\(67\)90271-6](https://doi.org/10.1016/0029-554X(67)90271-6).
- [134] C. Hu-Guo et al. First reticule size maps with digital output and integrated zero suppression for the EUDET-JRA1 beam telescope. *Nucl. Instr. Meth. A*, 623(1): 480 – 482, 2010. ISSN 0168-9002. doi: [http://dx.doi.org/10.1016/j.nima.2010.03.043](https://doi.org/10.1016/j.nima.2010.03.043). URL <http://www.sciencedirect.com/science/article/pii/S0168900210006078>. 1st International Conference on Technology and Instrumentation in Particle Physics.
- [135] *RCE, the Reconfigurable Cluster Element*. URL <https://rceproject.web.cern.ch/>.
- [136] M. Backhaus et. al. Development of a versatile and modular test system for ATLAS hybrid pixel detectors. *Nucl. Instr. Meth. A*, 650(1):37 – 40, 2011. ISSN 0168-9002. doi: [http://dx.doi.org/10.1016/j.nima.2010.12.087](https://doi.org/10.1016/j.nima.2010.12.087). URL <http://www.sciencedirect.com/science/article/pii/S0168900210028676>. International Workshop on Semiconductor Pixel Detectors for Particles and Imaging 2010.
- [137] *Eutelescope*. URL <http://eutelescope.web.cern.ch/>.

- 
- [138] V. Blobel. Millepede II: Linear Least Squares Fits with a Large Number of Parameters. 3rd LHC Detector Alignment Workshop CERN 2009. URL <https://indico.cern.ch/event/50502/timetable/?view=standard>.
- [139] *Tbmon2*. URL <https://bitbucket.org/TBmon2/tbmon2/overview>.
- [140] Hecht K. Zum mechanismus des lichtelektrischen primärstromes in isolierenden kristallen. *Zeit. Physik*. 1932;77:235.
- [141] Schwarz and Russe. Semi-empirical equations for electron velocity in silicon. *IEEE Trans. Electron Devices Vol. 30, No. 12 (1983): 1634-1639*.
- [142] A. Ducourthial, M. Bomben, G. Calderini, G. Marchiori, L. D'Eramo, I. Luise, A. Bagolini, M. Boscardin, L. Bosisio, G. Darbo, G.-F. Dalla Betta, G. Giacomini, M. Meschini, A. Messineo, S. Ronchin, and N. Zorzi. Thin and edgeless sensors for atlas pixel detector upgrade. *Journal of Instrumentation*, 12(12):C12038, 2017. URL <http://stacks.iop.org/1748-0221/12/i=12/a=C12038>.
- [143] STControl Eudaq. URL <https://github.com/eudaq/eudaq/releases>.
- [144] Benjamin Philip Nachman, Lorenzo Rossini, Marco Bomben, Tommaso Lari, Anna Macchiolo, Audrey Ducourthial, Lingxin Meng, Mathieu Benoit, Julien-christopher Beyer, Rebecca Carney, Nick Dann, Ian Dawson, Cinzia Da Via, Gilberto Giugliarelli, Paul Miyagawa, and Veronica Wallangen. Pixel Radiation Damage Plots for Workshop. Technical Report ATL-COM-INDET-2018-013, CERN, Geneva, Apr 2018. URL <https://cds.cern.ch/record/2311989>.
- [145] Ian Connelly. Performance and calibration of b-tagging with the ATLAS experiment at LHC Run-2. Technical Report ATL-PHYS-PROC-2016-193, CERN, Geneva, Nov 2016. URL <https://cds.cern.ch/record/2229557>.
- [146] Optimisation of the ATLAS  $b$ -tagging performance for the 2016 LHC Run. Technical Report ATL-PHYS-PUB-2016-012, CERN, Geneva, Jun 2016. URL <https://cds.cern.ch/record/2160731>.
- [147] Identification of Jets Containing  $b$ -Hadrons with Recurrent Neural Networks at the ATLAS Experiment. Technical Report ATL-PHYS-PUB-2017-003, CERN, Geneva, Mar 2017. URL <https://cds.cern.ch/record/2255226>.
- [148] G Piacquadio and C Weiser. A new inclusive secondary vertex algorithm for b-jet tagging in ATLAS. *Journal of Physics: Conference Series*, 119(3):032032, jul 2008. doi: 10.1088/1742-6596/119/3/032032. URL <https://doi.org/10.1088/1742-6596/119/3/032032>.
- [149] Secondary vertex finding for jet flavour identification with the ATLAS detector. Technical Report ATL-PHYS-PUB-2017-011, CERN, Geneva, Jun 2017. URL <https://cds.cern.ch/record/2270366>.
- [150] Expected performance of the ATLAS  $b$ -tagging algorithms in Run-2. Technical Report ATL-PHYS-PUB-2015-022, CERN, Geneva, Jul 2015. URL <https://cds.cern.ch/record/2037697>.